Insights into Structural Dynamics of Avian Cryptochromes



Laila M. N. Shah

St. Cross College

University of Oxford

A thesis submitted for the degree of

Doctor of Philosophy

Michaelmas Term 2025

Acknowledgements

This thesis would not exist without the many people who have made the past four years the best to date.

I would like to start by acknowledging my supervisor, Prof. Justin Benesch, as well as Prof. Peter Hore, who has acted as an honorary supervisor to me. They have allowed me to undertake an incredible project that has been both challenging and deeply rewarding. I would also like to thank my master's supervisor, Dr Eamonn Reading, who encouraged me to apply to Oxford and first introduced me to mass spectrometry. Through their mentorship and support, I have grown in confidence both in and out of the lab and developed a genuine passion for science.

I also want to thank the Benesch Group for their warmth, wisdom and support over the past few years. I first began working on this project with Dr Angela Gehrckens, who taught me the value of collaboration, many of the quirks of mass spectrometry and, most importantly, how to work in the dark! I, of course, could not have completed this DPhil without my partner in crime, Olav Johannessen. The many late-night experiments listening to Latin jazz, conference trips and endless amounts of support and silliness have given me a friend for life. I also want to thank Neel Sen for all his valuable input in the lab and the many hours he has spent with me trying to write HDX code (one day we'll release HDeXplore!). I would also like to thank Fran for all her advice, Alex for the fun nights out and Konstantin, Sulaiman, Amida, Siong Chen, Hannah, Clare and all the previous members of the Benesch Group for their support. I would especially like to thank Dr Ellie Holden and Dr Valeria Calvaresi for teaching me to love (?) HDX. I could not think of a better support group; they have made the many hours spent dealing with comms errors, tuning ECD cells and even a trip to Dundee infinitely more bearable. I also wish to thank Pip Benjamin, who has endlessly entertained me with his compositions, dry humour and hermeneutic labour. I want to thank the many friends in Oxford who made it a home, my St Cross friends, especially Katie, Harald and Ana, for countless bops, game nights and for discovering all of Oxford's quirks together, as well as the many others I've met through the Bossaphonik gang, Lamby council and all those I've spent many an evening with.

I couldn't get through the acknowledgements section without saying something about my best friends. Mia...I genuinely don't have the words to express what

you've done for me. I can't even begin to recount the memories we've made or the laughter we've shared. Seeing your face almost every day has kept me sane, we are the perfect codependence and I am so unbelievably lucky to have a friend like you. Megan, there's nobody I'd rather drive to Manchester and back for at midnight. I am so grateful for the spontaneous trips to Oxford when I needed company most, they really meant the world to me. Kiera, your confidence, determination and positivity have impressed me to no end. You truly are an inspiration. Sophia, there's no one I would rather go to for advice; your wisdom and endless kindness make you the best friend I could hope for. Clare, you're the kind of friend who proves that distance means nothing, your generosity and strength mean more to me than I can say. Bryan, you've made these last six months so different; I can't thank you enough for the little trips, constant jokes, care and joy you've brought into my life. The unconditional love and support I've received from all of you (even when I'm wrong!), have made me feel like the luckiest person in the world.

Finally, to my parents, I can't thank you enough for everything you've done for me. Whether it's science, music, Trini and Palestinian culture, generosity, love or simply your outlook on life, you are my greatest inspirations. You've truly allowed me to grow over the past few years and I wouldn't be the person I am today without you. You've shown me that it's possible to balance work, hobbies and fun, and to live life to the fullest. For that, I will always be grateful. I know I have big boots to fill, but I hope that I will reach there one day. I also have to thank our pets: Sophie, my beloved childhood cat; Rami, who has brought chaos into our lives over the past year; and, of course, our three chickens, Catty, Boots and Betty.

With all the suffering in the world, I am grateful and unbelievably lucky to have lived with immense privilege through education, safety, security and love. Thank you again to those who have been a part of my life over the past four years.

"I may not have gone where I intended to go, but I think I have ended up where I needed to be."

— Douglas Adams, The Long Dark Tea-Time of the Soul

Statement of Originality

This thesis describes research carried out in the Department of Physical and Theoretical Chemistry at the University of Oxford between October 2021 and October 2025. It centres on the structural and dynamic characterisation of avian cryptochrome 4a proteins, with a particular focus on understanding their conformational responses to light and magnetic stimuli. All data presented were acquired, processed and analysed by me unless explicitly stated otherwise in the main text or figure captions. All figures were prepared from my own data and analyses, except where specific collaborative contributions are noted. Chapters describing the PCO4 and some of the Cry4a studies include collaborative work with Dr Rebecca Latter and Dr Angela Gehrckens, respectively, and contributions have been acknowledged accordingly.

This thesis is an original account of my research and writing. No part of it has been submitted, in whole or in part, for any degree, diploma, or other academic qualification at any other institution.

Laila M. N. Shah
October 2025

Abstract

This thesis investigates how light influences the structure and dynamics of avian cryptochrome 4a proteins, which are thought to contribute to the magnetic compass of migratory birds. Using hydrogen–deuterium exchange mass spectrometry in combination with complementary mass-spectrometric approaches, it examines how photoexcitation of the flavin cofactor induces conformational change and how this response differs across species and mutants.

The first study develops and validates using hydrogen–deuterium exchange mass spectrometry on a well-characterised plant enzyme, *Arabidopsis thaliana* Plant Cysteine Oxidase 4. This work, published in the *Journal of Biological Chemistry*, demonstrates that ligand binding can stabilise flexible elements within the enzyme and establishes the experimental framework for subsequent protein dynamics studies.

The main body of the thesis focuses on European robin cryptochrome 4a, revealing that light activation induces local structural stabilisation linked to the flavin adenine dinucleotide cofactor. Targeted mutations show that both the cofactor and specific residues involved in the electron transfer chain are required to transmit photochemical changes into wider structural responses, providing experimental evidence for how electron transfer couples to conformational dynamics.

A comparative analysis of cryptochrome 4a from robin, chicken and quail demonstrates that this light-responsive behaviour is conserved across species, although the strength of the effect varies. The results indicate that photochemically driven conformational change is not uniquely linked to migratory behaviour but reflects broader species-specific adaptations.

Overall, this work establishes hydrogen–deuterium exchange mass spectrometry as a powerful method for investigating cryptochrome structure and dynamics and offers new insight into how light-driven reactions are translated into structural signals within biological photoreceptors.

Contents

List of Figures

List of Abbreviations

1 Introduction to Magnetoreception and Cryptochromes 1
- 1.1 Motivation . . . 1
- 1.2 Magnetoreception . . . 2
  - 1.2.1 The Earth's Magnetic Field and Migration . . . 3
- 1.3 Putative Magnetoreceptors . . . 5
  - 1.3.1 Magnetite . . . 6
  - 1.3.2 Cryptochromes . . . 7
  - 1.3.3 The Radical Pair Mechanism . . . 10
- 1.4 Previous Work . . . 14
- 1.5 Summary . . . 19

2 Technical Background on Mass Spectrometry 21
- 2.1 Motivation . . . 22
- 2.2 Mass Spectrometry Workflows . . . 22
- 2.3 Native Mass Spectrometry . . . 23
  - 2.3.1 Historical Development of Native Mass Spectrometry . . . 23
- 2.4 Mass Spectrometry Workflow . . . 25
  - 2.4.1 Sample Preparation . . . 25
  - 2.4.2 Electrospray Ionisation . . . 27
  - 2.4.3 Ion Transmission . . . 28
  - 2.4.4 Mass Filtering/ Selection . . . 30
  - 2.4.5 Ion Fragmentation . . . 30
  - 2.4.6 Mass Analysers . . . 32
  - 2.4.7 Relevance to Cryptochrome Studies . . . 34
- 2.5 Hydrogen-Deuterium Exchange Mass Spectrometry (HDX-MS) . . . 34
  - 2.5.1 The History of HDX-MS . . . 34
  - 2.5.2 Exchange Kinetics . . . 35
- 2.6 Typical Workflow . . . 40

2.6.1 Sample Preparation . . . 40
2.6.2 Labelling . . . 40
2.6.3 Quenching the Exchange Reaction . . . 42
2.6.4 Proteolytic Digestion . . . 43
2.6.5 Desalting and Separation . . . 43
2.6.6 Mass Spectrometric Analysis . . . 44
2.6.7 Data Processing and Uptake Calculation . . . 44
2.6.8 Scrambling and ECD Fragmentation . . . 46
2.6.9 Alternate Workflow: Pulsed Labelling . . . 47
2.6.10 Limitations . . . 49
2.7 Summary . . . 51

3 HDX as a Tool for Elucidating Conformational Changes 53
3.1 Abstract . . . 53
3.2 Plant Cysteine Oxidase (PCO4) . . . 54
3.3 Rationale for Using HDX-MS . . . 56
3.4 Experimental Design . . . 58
3.5 Results . . . 59
3.5.1 Visualising HDX Data . . . 59
3.5.2 Coverage and Dynamics . . . 60
3.5.3 Differential HDX . . . 64
3.6 Discussion and Conclusions . . . 71
3.7 Materials and Methods . . . 71
3.7.1 Synthesis of Peptidomimetics . . . 71
3.7.2 In Vitro Activity Assays . . . 72
3.7.3 HDX-MS . . . 73

4 Characterising Robin Cryptochrome 4a 75
4.1 Abstract . . . 76
4.2 Robin Cryptochrome (*Er*Cry4a) as a model system . . . 76
4.2.1 Cryptochrome Structure . . . 78
4.3 Dynamic Regions of *Er*Cry4 Wild Type . . . 81
4.4 Light Induced Effects . . . 84
4.4.1 404-412 . . . 90
4.4.2 α22 . . . 93
4.4.3 Phosphate Binding Loop and Protrusion Loop . . . 95
4.5 Refolding Experiments (Pulsed Labelling HDX) . . . 99
4.6 ECD analysis of the PBL . . . 101
4.6.1 Intrinsic rates . . . 103
4.6.2 Kinetic fitting of experimental exchange rates . . . 104

4.6.3 Protection factors (PFs) . . . 106
4.6.4 Residue-level localisation . . . 107
4.6.5 Interpretation . . . 109
4.7 Magnet-Induced Differences . . . 111
4.8 Conclusions . . . 114
4.9 Materials and Methods . . . 116
4.9.1 Materials . . . 116
4.9.2 HDX-MS . . . 116
4.9.3 Native Mass Spectrometry . . . 118
4.9.4 Data Analysis . . . 119

5 The Effect of Mutations on Robin Cryptochrome 4a 121
5.1 Abstract . . . 122
5.2 Apo Protein (R356E) . . . 123
5.2.1 Global Dynamics . . . 124
5.2.2 Response to Stimuli . . . 126
5.3 TrpD Mutant (W369F) . . . 129
5.3.1 Response to Stimuli . . . 131
5.4 Triple Mutant (C317R/Y319F/W369F) . . . 133
5.4.1 Global Dynamics . . . 133
5.4.2 Response to Stimuli . . . 135
5.5 Comparative Discussion . . . 136
5.5.1 Phosphate Binding Loop . . . 136
5.5.2 Protrusion Loop . . . 138
5.5.3 α22 . . . 139
5.5.4 Putative Dimer Region . . . 140
5.5.5 Mutation Region . . . 141
5.5.6 Discussion . . . 141
5.6 Conclusions . . . 143
5.7 Materials and Methods . . . 144
5.7.1 Materials . . . 144
5.7.2 HDX-MS . . . 145
5.7.3 Native Mass Spectrometry . . . 146
5.7.4 Data Analysis . . . 146

6 Comparative Study of Avian Cryptochromes across Robin, Chicken and Quail (*Er*Cry4a, *Gg*Cry4a and *Cc*Cry4a) 149

6.1 Abstract . . . 150
6.2 Introduction . . . 150
6.2.1 Chicken Cryptochrome (*Gg*Cry4a) . . . 152
6.2.2 Quail Cryptochrome (*Cc*Cry4a) . . . 154
6.2.3 Structure and Sequence Similarity . . . 155
6.3 Motivation . . . 161
6.4 Comparisons of Wild Types . . . 162
6.5 Comparisons of TrpD Mutants . . . 165
6.6 Comparisons of TrpD / Y319F Mutants . . . 169
6.7 Important Regions . . . 170
6.7.1 Phosphate-Binding Loop . . . 170
6.7.2 Protrusion Loop . . . 174
6.7.3 α22 . . . 176
6.7.4 Potential Dimer Region . . . 179
6.7.5 Mutation Region . . . 181
6.8 Magnet-Induced Effects . . . 183
6.9 Discussion . . . 183
6.9.1 Residue Distances from FAD Across Species . . . 184
6.9.2 Kinetics in the *Cc*Cry4a CTT . . . 187
6.10 Conclusions . . . 190
6.11 Materials and Methods . . . 192
6.11.1 Materials . . . 192
6.11.2 HDX-MS . . . 192
6.11.3 Native Mass Spectrometry . . . 194
6.11.4 Data Analysis . . . 194

7 Final Conclusions and Outlook 197

7.1 Summary of Principal Findings . . . 198
7.2 Insights from Mutational Studies . . . 198
7.2.1 R356E (Apo Protein) . . . 199
7.2.2 W369F (TrpD Mutant) . . . 199
7.2.3 C317R/Y319F/W369F (Triple Mutant) . . . 199
7.3 Comparative Dynamics Across Species . . . 200
7.4 Mechanistic Interpretation . . . 201
7.5 Future Directions . . . 201
7.5.1 Membrane Association . . . 202
7.5.2 Interaction Partners . . . 203

7.5.3 Post-Translational Modifications 203
7.5.4 Residue-Level Experiments 204
7.6 Concluding Remarks 204

Appendices

A Appendices **207**
A.1 Chapter 4 207
A.2 Chapter 5 209
A.3 Chapter 6 213

References **235**

List of Figures

1.1 The Earth's Magnetic Field 4
1.2 The Radical Pair Mechanism 11
1.3 Electron Transfer Chain 13
1.4 The Radical Pair Mechanism in Cryptochromes 14
1.5 *Dm*Cry Structural Changes 18

2.1 QE and ToF 26
2.2 ESI Models 28
2.3 Quadrupole 30
2.4 Orbitrap 33
2.5 HDX exchange mechanisms 36
2.6 pH dependence of HDX 37
2.7 HDX exchange regimes 38
2.8 HDX Workflow 41
2.9 Exchangeable amides in the peptide backbone 42
2.10 Fragment ion types in MS/MS 45
2.11 Pulsed-labelling HDX workflows 48

3.1 PCO4 Crystal Structure 56
3.2 PCO4 Coverage 61
3.3 PCO4 Heatmap 62
3.4 PCO4 Heatmap on Structures 62
3.5 PCO4 15s Heatmap 63
3.6 PCO4 1h Heatmap 64
3.7 *At*PCO4 DifferentialHeatmap 65
3.8 *At*PCO4 Woods Plot 66
3.9 *At*PCO4 HDX Data on Structures 67
3.10 PCO4 15 s differential HDX–MS map 69
3.11 PCO4 60 min differential HDX–MS map 70

4.1 ErCry4a Structure 78
4.2 ErCry4a Sequence with Secondary Structure 79
4.3 HDX–MS uptake heatmap for *Er*Cry4a 83

4.4 Structural mapping of HDX–MS uptake in *Er*Cry4a 84
4.5 Differential HDX–MS heatmap for LS vs DS 86
4.6 Woods plot for LS vs DS comparison 87
4.7 Volcano plot for LS vs DS comparison 88
4.8 Structural mapping of significant peptides, LS vs DS 89
4.9 HDX–MS uptake plot for peptide 404–412 91
4.10 Native MS of *Er*Cry4a 92
4.11 HDX–MS uptake plots for α22 93
4.12 PBL uptake plots 95
4.13 PL uptake plots 96
4.14 AF2–AF3 comparison of the PBL 97
4.15 Position of the PBL in pigeon Cry4 98
4.16 Interacting residues between the PBL and PL in *Er*Cry4a 99
4.17 PBL pulsed-labelling plots 100
4.18 PL pulsed-labelling plots 100
4.19 Formation of c and z ions in ECD fragmentation 102
4.20 Kex Fitting 104
4.21 Fragment level protection factor 106
4.22 Residue level protection factors 108
4.23 Residue level free energies 110
4.24 Differential HDX–MS heatmap for LSM vs LS 112
4.25 Volcano plot for LSM vs LS comparison 113
4.26 Light Determination 117
4.27 Magnetic Strength Determination 117

5.1 ErCry4 Structure 122
5.2 Comparison of HDX profiles in wild-type and apo Cry4a. 125
5.3 HDX of apo Cry4a (LS vs DS). 126
5.4 HDX of apo Cry4a (LSM vs LS). 127
5.5 HDX heatmap of apo Cry4a. 128
5.6 HDX heatmap of W369F (TrpD) mutant. 130
5.7 Light–dark comparison for W369F. 131
5.8 Light+magnet comparison for W369F. 132
5.9 HDX heatmap of triple mutant. 134
5.10 Woods plots for triple mutant. 135
5.11 Heatmap of all mutants 137
5.12 HDX uptake in the phosphate-binding loop. 138
5.13 HDX uptake in the protrusion loop. 139
5.14 HDX uptake in α22. 140
5.15 HDX uptake of residues 404-412. 141

5.16 HDX uptake of residues 362-369. 142

6.1 Phylogenetic tree of robin, chicken, quail and selected outgroups . . 152
6.2 Bird Sequence Alignment 157
6.3 Aligned predicted structures of Cry4a proteins 159
6.4 AlphaFold3 models of Cry4a proteins 160
6.5 Overall deuterium uptake across species 163
6.6 Light-induced differences in wild-type Cry4a proteins 164
6.7 TrpD mutant comparison across species 166
6.8 Woods plots for TrpD mutants across species 168
6.9 Absence of light-dependent peptides in Y319F/W369F double mutants 171
6.10 Light-induced uptake behaviour of the PBL across Cry4a species . . 172
6.11 Light-induced uptake behaviour of the PL across Cry4a species . . . 175
6.12 Light-induced uptake behaviour of α22 across Cry4a species 177
6.13 Relative uptake of residues 404–412 across Cry4a species 180
6.14 Relative uptake of residues 362–369 across Cry4a species 182
6.15 Residue distances from FAD across species 185
6.16 Residue composition of the PBL across species 186
6.17 Residue variation near the TrpC–TrpD region 186
6.18 EXX behaviour in the C-terminal tail of quail Cry4a 188

A.1 Woods plots of *Er*Cry4a WT 208
A.2 Woods plots of *Er*Cry4a W369F 210
A.3 Woods plots of *Er*Cry4a C317R/Y319F/W369F 211
A.4 Woods plots of *Er*Cry4a R356E 212
A.5 Woods plots of *Cc*Cry4a WT 214
A.6 Woods plots of *Cc*Cry4a W369F 215
A.7 Woods plots of *Cc*Cry4a Y319F/W369F 216
A.8 Woods plots of *Gg*Cry4a WT 217
A.9 Woods plots of *Gg*Cry4a W369F 218
A.10 Woods plots of *Gg*Cry4a Y319F/W369F 219
A.11 RFU overview of *Er*Cry4a 220
A.12 RFU at 15s for *Er*Cry4a 221
A.13 RFU at 1 min for *Er*Cry4a 222
A.14 RFU at 5 min for *Er*Cry4a 223
A.15 RFU at 30 min for *Er*Cry4a 224
A.16 RFU overview of *Cc*Cry4a 225
A.17 RFU at 15s for *Cc*Cry4a 226
A.18 RFU at 1 min for *Cc*Cry4a 227
A.19 RFU at 5 min for *Cc*Cry4a 228

A.20 RFU at 30 min for *Cc*Cry4a 229
A.21 RFU overview of *Gg*Cry4a 230
A.22 RFU at 15s for *Gg*Cry4a 231
A.23 RFU at 1 min for *Gg*Cry4a 232
A.24 RFU at 5 min for *Gg*Cry4a 233
A.25 RFU at 30 min for *Gg*Cry4a 234

List of Abbreviations

AF2 . . . . . AlphaFold2

AF3 . . . . . AlphaFold3

APBS . . . . . Adaptive Poisson-Boltzmann Solver

Apo . . . . . Apo protein (without FAD co-factor)

***At*PCO4** . . . *Arabidopsis thaliana* Plant Cysteine Oxidase 4

BME . . . . . β-Mercaptoethanol

CcCry4a . . . *Coturnix coturnix* Cryptochrome 4a (quail)

CID . . . . . Collision-Induced Dissociation

CTT . . . . . C-Terminal Tail

Cry . . . . . Cryptochrome

DS . . . . . Dark State

DSM . . . . . Dark + Magnet State

DMSO . . . . . Dimethyl Sulphoxide

ECD . . . . . Electron Capture Dissociation

ETD . . . . . Electron Transfer Dissociation

***Er*Cry4a** . . . European robin (*Erithacus rubecula*) cryptochrome 4a

ESI . . . . . Electrospray Ionisation

EX1/EX2 . . . Hydrogen–Exchange Kinetic Regimes

EXX . . . . . Mixed Hydrogen–Exchange Kinetic Regime

FAD . . . . . Flavin Adenine Dinucleotide

FADH$^{\bullet}$ . . . . Flavin Semiquinone Radical

FADH^{-} . . . . Fully Reduced Flavin

FAD$^{\bullet -}$ . . . . . Anionic Semiquinone Flavin Radical

GgCry4a . . . *Gallus gallus* Cryptochrome 4a (chicken)

HCD . . . . . Higher-Energy Collision Dissociation

HDX . . . . . Hydrogen–Deuterium Exchange

HDX–MS . . . Hydrogen–Deuterium Exchange Mass Spectrometry

HPLC . . . . . High-Performance Liquid Chromatography

IMS . . . . . Ion Mobility Spectrometry

$\mathbf{k}_{\mathrm{int}}$ . . . . . Intrinsic Exchange Rate Constant

$\mathbf{k}_{\mathrm{obs}}$ . . . . . Observed Exchange Rate Constant

LC . . . . . Liquid Chromatography

LS . . . . . Light State

LSM . . . . . Light + Static Magnetic Field

MALDI . . . . Matrix-assisted Laser Desorption/Ionisation

MD . . . . . Molecular Dynamics

MS . . . . . Mass Spectrometry

MS/MS . . . . Tandem Mass Spectrometry

m/z . . . . . Mass-to-Charge Ratio

Native MS . . Native-State Mass Spectrometry

NCE . . . . . Normalised Collision Energy

Ni–NTA . . . . Nickel–Nitrilotriacetic Acid (affinity resin)

PBL . . . . . Phosphate-Binding Loop

PDB . . . . . Protein Data Bank

PF . . . . . Protection Factor

PHR . . . . . Photolyase Homology Region

PL . . . . . Protrusion Loop

PLGS . . . . . ProteinLynx Global Server (Waters data software)

PTM . . . . . Post Translational Modification

QE . . . . . Q-Exactive (Orbitrap mass spectrometer)

Q-ToF . . . . . Quadrupole Time-of-Flight

RF . . . . . Radio Frequency

RFU . . . . . Relative Fractional Uptake

RPM . . . . . Radical Pair Mechanism

S/N . . . . . Signal-to-Noise Ratio

SDS-PAGE . . Sodium Dodecyl Sulphate Polyacrylamide Gel Electrophoresis

SEC . . . . . Size-Exclusion Chromatography

SID . . . . . Surface-Induced Dissociation

SMALP . . . . Styrene-Maleic Acid Lipid Particle

TCEP . . . . . Tris(2-carboxyethyl)phosphine

ToF . . . . . Time-of-Flight (mass analyser)

TrpA–TrpD . Tryptophan Electron-Transfer Chain (residues A–D)

UHMR . . . . Ultra-High Mass Range (Thermo Orbitrap)

UVPD . . . . . Ultraviolet Photodissociation

W369F . . . . TrpD Mutant (Tryptophan-to-Phenylalanine mutation)

WT . . . . . Wild Type

Y319F . . . . . Tyrosine mutant (Tyrosine-to-Phenylalanine mutation)

"A well a everbody's heard about the bird
bird, bird, bird, bird is the word"

— The Trashmen via Megan Wilson

1

Introduction to Magnetoreception and Cryptochromes

Contents

1.1 Motivation 1
1.2 Magnetoreception 2
1.2.1 The Earth's Magnetic Field and Migration 3
1.3 Putative Magnetoreceptors 5
1.3.1 Magnetite 6
1.3.2 Cryptochromes 7
1.3.3 The Radical Pair Mechanism 10
1.4 Previous Work 14
1.5 Summary 19

1.1 Motivation

Migration is a widespread phenomenon across the animal kingdom, involving long-distance movements often carried out with remarkable precision [1, 2]. Each year, countless species undertake vast and often perilous journeys, guided by sensory systems that remain only partially understood. Birds, in particular, are capable of travelling thousands of kilometres with remarkable accuracy, even when deprived of familiar landmarks [3]. Their ability to orient and navigate over

such distances suggests the involvement of multiple sensory cues and specialised molecular mechanisms.

One explanation for this navigational ability is that some animals can detect the Earth's magnetic field and use it as a basis of a compass for orientation [4]. Behavioural studies provide strong evidence for such magnetoreception, yet its molecular basis remains unresolved [5–7]. Determining how organisms achieve magnetic sensitivity remains a central challenge in sensory biology.

In this thesis, I focus on cryptochromes, a class of light-sensitive proteins that have emerged as leading candidates for the compass magnetoreceptor. By probing their structural dynamics, I aim to reveal how light and magnetic cues might influence protein conformation and how such changes could form a step in a sensory pathway. Mass spectrometry provides a powerful means of investigating these dynamics, offering insights that are otherwise inaccessible.

1.2 Magnetoreception

Birds are able to use a variety of spatial and environmental cues, relying on prominent landscape features such as mountain ranges, rivers and coastlines to guide their routes [3]. They also use stellar patterns, olfactory signals and a time-compensated sun compass to maintain their bearings, integrating these inputs across a range of spatial and temporal scales [8–12].

Among these cues, the capacity to detect the Earth's magnetic field, known as magnetoreception, has attracted particular attention. This capacity appears to support the precise migratory behaviour seen in species such as sea turtles, salmon and songbirds, where individuals are able to return to specific breeding or wintering sites across vast distances [4, 13, 14]. Despite decades of study, the underlying mechanisms remain poorly understood. Unlike the familiar senses of sight, hearing or smell, magnetoreception lacks a clearly defined sensory organ or receptor structure, making it difficult to identify where and how magnetic information is detected.

Current hypotheses propose two main routes by which animals may sense the geomagnetic field. The first involves the presence of ferrimagnetic particles, such as

magnetite, that could act as microscopic compass needles within specialised receptor cells. The second relies on light-dependent radical-pair reactions in flavoproteins such as cryptochromes and DNA photolyases, in which magnetic interactions influence the spin states of photoinduced radicals [15–18]. Each mechanism offers a plausible explanation for certain behavioural and physiological observations, yet both face challenges in reconciling their predicted sensitivity and stability with the complexity of real biological systems. It is possible that different taxa employ distinct mechanisms or that more than one operate in parallel under different environmental conditions.

Research into magnetoreception has therefore developed into a multidisciplinary field at the intersection of behavioural ecology, molecular biology and quantum physics. Progress has been driven by the convergence of behavioural experiments, anatomical studies and biophysical modelling, each contributing complementary insights into how magnetic information could be detected and processed. Despite many remaining uncertainties, the search for the molecular basis of magnetoreception continues to reshape our understanding of sensory biology and the limits of biological detection. Understanding how animals perceive the geomagnetic field remains one of the most compelling challenges in modern biology, with implications that reach from quantum chemistry to global migration ecology.

1.2.1 The Earth's Magnetic Field and Migration

The Earth's magnetic field, also known as the geomagnetic field, is a pervasive and relatively stable environmental feature. It is generated by geodynamo processes in the planet's liquid outer core, where convective motions of molten iron and nickel create electrical currents, which in turn produce magnetic fields [19]. These fields combine to form a roughly dipolar global field, resulting in a magnetic north and south pole located near the geographic poles. While the field resembles that of a traditional bar magnet, it exhibits both spatial and temporal variations. These include local anomalies, drift, and, over long timescales, reversals of the poles [20].

The magnetic field is defined by several parameters: intensity, inclination and declination, as shown in Figure 1.1. Intensity refers to the field's strength, inclination describes the angle between the field lines and the Earth's surface and declination specifies the angle between magnetic north and true north. These parameters vary predictably with latitude, creating spatial gradients that can provide navigational information. For instance, inclination is close to 0° at the magnetic equator and approaches ±90° near the poles [21].

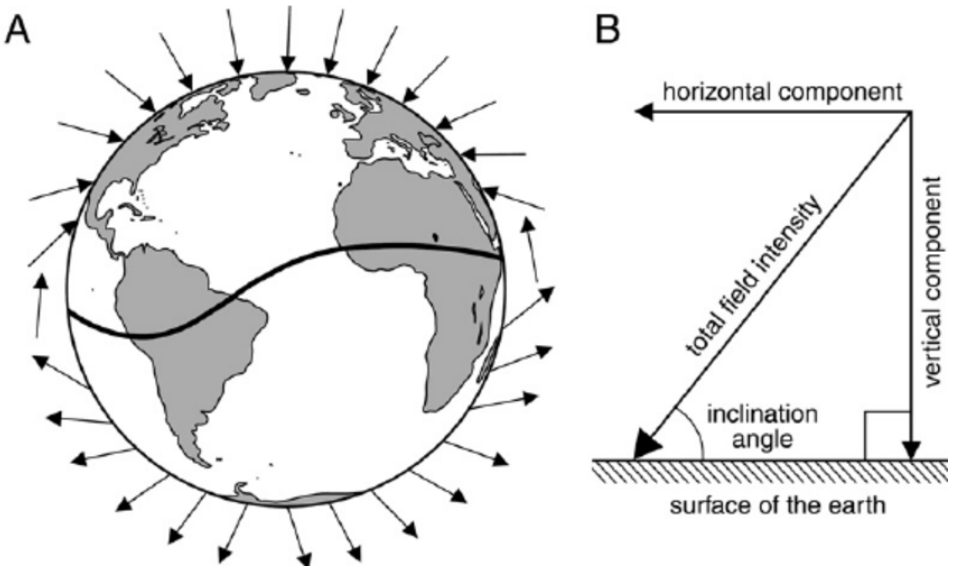


Figure 1.1: (A) Schematic of the Earth's magnetic field showing how field lines (arrows) intersect the Earth's surface. The angle formed between the field lines and the surface, known as the inclination, varies systematically with latitude. (B) Diagram illustrating properties of the Earth's magnetic field relevant to animal navigation. The field at any location can be described by its total intensity and inclination angle. Field intensity can be resolved into two vector components: horizontal and vertical intensity. Figures taken from Lohmann *et al.*[22].

Geomagnetic cues provide an important frame of reference for migratory species, particularly in environments lacking visual or topographical landmarks. Behavioural studies have shown that many species can detect magnetic inclination, using it as a directional cue for orientation [23–25]. Early experiments by Wiltschko and Merkel on European robins (*Erithacus rubecula*) first demonstrated that orientation behaviour could be influenced by magnetic fields [26]. Subsequent work established that the avian compass is based on the inclination of the Earth's magnetic field

(the angle between the field lines and the Earth's surface), rather than its polarity (the distinction between north- and south-pointing field directions) [4].

Further evidence for geomagnetic sensitivity comes from work by Lohmann *et al.*, who found that loggerhead turtle hatchlings adjusted their swimming direction when exposed to magnetic fields replicating those found in different oceanic regions [13]. These experiments suggest that turtles can use magnetic parameters to build a bi-coordinate map of their migratory range, though their mechanism likely differs from the light-dependent system proposed for birds and insects.

A complementary example is provided by Guerra *et al.*, who showed that monarch butterflies orient using an inclination compass dependent on light of wavelengths below 420 nm [27]. When deprived of blue light, the butterflies lost their directional preference, which was restored upon its reintroduction. Disruption of the antennae also abolished this behaviour, suggesting that cryptochromes within the antennal photoreceptors contribute to magnetic sensing.

These are just three examples from a vast and growing field that strongly supports the capability of certain animals to detect magnetic inclination and use it in constructing a magnetic map. Increasing evidence indicates that animals integrate magnetic information with other sensory inputs, including celestial and olfactory cues, which supports the existence of a multimodal navigational strategy [28, 29].

These examples illustrate that magnetic cues form a consistent part of the sensory landscape for many migratory species. The detection of magnetic inclination across diverse taxa implies the presence of molecular mechanisms capable of responding to weak geomagnetic fields. In birds and insects, evidence increasingly points to a light-dependent process, implicating photoreceptive proteins such as cryptochromes as potential magnetoreceptors.

1.3 Putative Magnetoreceptors

Building on the behavioural evidence for magnetic orientation, recent work has sought to uncover the molecular basis of magnetoreception. Several candidate mechanisms have been proposed, encompassing both light-dependent and light-independent

systems. Some are supported by behavioural and anatomical observations, while others remain largely theoretical.

1.3.1 Magnetite

Magnetite (Fe_3O_4) is a ferrimagnetic iron oxide mineral found in both geological and biological systems. Its strong magnetic properties have led to the proposal that biogenic magnetite could contribute to magnetoreception in animals [30]. Crystals synthesised by the organism may respond to the Earth's magnetic field through physical torque or alignment and this motion is thought to activate mechanosensitive channels or associated structures that transduce magnetic information into neural signals.

The first biological occurrence of magnetite was described by Blakemore, who observed intracellular, electron-dense particles responsible for magnetotaxis in bacteria [31]. These particles were later confirmed as magnetite organised in membrane-bound chains, or magnetosomes, which act as microscopic compass needles that align passively with the geomagnetic field [32, 33]. This passive alignment enables bacteria to follow magnetic field lines and locate optimal redox environments, providing an early demonstration of magnetic alignment in a living system and motivating searches for similar structures in animals.

Magnetite particles have since been identified in several vertebrates. In fish, they occur in specialised tissues of the olfactory epithelium, typically as single-domain crystals capable of moving within geomagnetic fields [34–36]. Juvenile salmon and rainbow trout both contain magnetite and can orient within artificial magnetic fields [34, 35]. Magnetic pulses can disrupt orientation in salmon, consistent with interference of these particles [37]. However, similar deposits have not been found in all taxa. For example, Keays *et al.* reported no magnetite-based structures in pigeons [38].

In birds, iron-rich dendritic structures in the upper beak of homing pigeons were once proposed as magnetoreceptors [39, 40]. Behavioural studies on Australian silvereyes showed that brief exposure to strong magnetic pulses caused temporary

disorientation, suggesting a magnetite-based intensity sensor linked to the trigeminal nerve [15, 41]. Subsequent analyses, however, revealed that these iron-rich cells were macrophages rather than sensory neurons, undermining this interpretation [38, 42]. Evidence for magnetite-based receptors in birds therefore remains inconclusive.

Although the precise transduction mechanism is unclear, plausible models suggest that torque on magnetite chains could modulate mechanically gated ion channels [30]. However, magnetite alone cannot explain the light-dependent orientation seen in many birds, implying that multiple mechanisms may coexist: a magnetite-based system may detect magnetic intensity or gradients, while a radical-pair mechanism in cryptochromes provides a light-dependent compass [43–45].

Magnetite remains a compelling model for light-independent magnetoreception, with strong support in fish but far less consistent evidence in birds and mammals. Its relevance across species remains uncertain and understanding its role will depend on combining behavioural, anatomical and biophysical evidence. A separate, light-dependent mechanism has been proposed involving cryptochromes.

1.3.2 Cryptochromes

Cryptochromes are flavoproteins found across the plant and animal kingdoms, where they are involved in a number of roles including circadian regulation and, potentially, magnetoreception. Originally identified as blue-light photoreceptors in plants, they have since been discovered in a wide range of animals, including insects, mammals and birds [46]. Within the retina, cryptochromes are thought to act as light-dependent magnetic sensors, making them the most experimentally supported candidates for a magnetic compass. They are closely related to DNA photolyases, a family of light-dependent DNA-repair enzymes and share many structural and mechanistic features with them [47]. The following sections examine their properties, photochemistry and proposed mechanisms in greater detail.

Cryptochrome Classes

Cryptochromes can be classified into several distinct functional subclasses.

Type-1 cryptochromes, such as *Drosophila melanogaster* cryptochrome (*Dm*Cry), are widespread in insects and other invertebrates, where they primarily function as photoreceptors that entrain the circadian clock [48]. Type-1 cryptochromes bind flavin adenine dinucleotide (FAD) and can also associate with a secondary antenna chromophore, such as 5,10-methenyltetrahydrofolate [49]. In *Drosophila*, light-activated cryptochrome binds directly to the clock protein Timeless (TIM), targeting it for proteasomal degradation [50]. This process resets the balance of clock proteins and synchronises the circadian clock with the day–night cycle. Knockout studies have shown that in the absence of cryptochrome, flies are unable to synchronise their circadian rhythms to light, confirming its essential role within the *Drosophila* clock [51].

Beyond its circadian function, *Dm*Cry has also been implicated in light-dependent magnetoreception, as it can form long-lived radical pairs that may be influenced by the Earth's magnetic field [52, 53]. Behavioural studies indicate that cryptochrome-deficient flies lose the ability to detect and respond to magnetic fields under blue light, whereas wild-type flies can orient within magnetic field mazes under full-spectrum illumination; this response disappears when wavelengths below 420 nm are blocked [53]. When cryptochrome expression was restored in previously deficient flies, magnetic responsiveness returned, further supporting its role as the primary magnetosensor [54].

However, more recent work by Bassetto *et al.* failed to reproduce magnetically induced behavioural responses in *Drosophila*, casting doubt on earlier findings [55]. Hydrogen–deuterium exchange mass spectrometry (HDX–MS) studies of *Dm*Cry have nevertheless demonstrated conformational changes in the presence of blue light, suggesting that the C-terminal tail participates in forming a signalling state [56]. Mutations disrupting the electron-transfer chain attenuate these light-induced conformational changes, highlighting their importance for photoactivation. Given

the close relevance of this work to the experiments presented in this thesis, the *Dm*Cry study will be discussed in greater detail later in this chapter.

Type 2 cryptochromes (mammalian-like) are generally light-insensitive, as they do not stably bind FAD. They form complexes with Period (PER) proteins that associate with the CLOCK–BMAL1 transcription factor complex to repress their own gene transcription, thereby closing the circadian feedback loop [57]. This process is independent of light, as type 2 cryptochromes lack efficient photoreduction activity [58]. Although they retain a vestigial flavin-binding pocket, indicating that ancestral forms likely bound FAD and were light sensitive, type 2 cryptochromes now function primarily as circadian repressors rather than as candidates for magnetoreception [59].

CRY-DASH cryptochromes were first identified in *Arabidopsis* and serve as a functionally different class of cryptochrome within bacteria, plants, fungi and some non-mammalian vertebrates [60]. Structurally, they retain the canonical photolyase homology domain and are able to bind FAD but lack the C-terminal tail extension seen in other cryptochromes [61]. Although CRY-DASH proteins retain the ability to repair UV-induced lesions in single-stranded DNA and RNA *in vitro*, their physiological function *in vivo* remains unclear. Since they cannot repair double-stranded genomic DNA, it is uncertain whether this activity represents their true biological function or is due to their photolyase ancestry [62].

Beyond these subclasses, a further lineage of cryptochromes, Cry4, has emerged in birds. Unlike mammalian cryptochromes, Cry4 is light sensitive, expressed in the retina and shows properties consistent with a role in magnetoreception, making it a prime candidate for an avian magnetic compass [17, 63]. Its proposed characteristics and structural properties will be discussed below.

Cryptochrome 4a

Cry4 exists as two isoforms, Cry4a and Cry4b, which result from alternative splicing of the same gene. Cry4b contains an additional exon encoding 29 amino acids compared to Cry4a and exhibits variable expression rates over a 24-hour period, with mRNA levels peaking in the afternoon and decreasing at night [64]. In contrast,

Cry4a expression remains stable throughout the day and night, supporting its proposed role as a magnetoreceptor rather than as a clock protein. The localisation of Cry4a in double cones and long-wavelength-sensitive single cones in European robins further supports this interpretation, as these photoreceptors are systematically arranged across the retina and could facilitate detection of the direction of the Earth's magnetic field [65]. Cry4a has been identified in numerous bird species, including European robins, chickens and quails, as well as in fish, amphibians, reptiles and other vertebrates [17, 64, 66, 67].

Cry4a possesses a canonical photolyase homology region (PHR) that binds FAD, a cofactor essential for photochemical activity. This region contains a conserved tetrad of tryptophan residues that establish an electron-transfer chain initiating radical-pair formation upon blue light excitation. Purified Cry4a exhibits blue light-dependent photochemistry and demonstrates magnetic field effects on radical-pair intermediates [17]. Additionally, spectroscopic studies have confirmed the formation of long-lived flavin radicals under blue light in near-physiological buffer conditions.

1.3.3 The Radical Pair Mechanism

The radical pair mechanism (RPM) is a quantum mechanical process whereby weak magnetic fields can influence the outcome of biochemical reactions. A hypothesis based on the RPM has emerged as the leading theory for the physical origin of magnetoreception in migratory animals, particularly in birds [16, 68, 69]. The RPM hypothesis proposes that magnetic sensitivity may arise from light-induced electron transfer reactions in specialised molecules which form spin-correlated radical pairs whose reaction dynamics can be influenced by external magnetic fields. The general principle of the RPM, illustrated in Figure 1.2 is as follows: two reactants (denoted as A and B) are exposed to light, leading to the excitation of B. This then triggers electron transfer from the donor (A) to the acceptor (B). Since the precursor is in the singlet ground state, conservation of spin angular momentum dictates that the initial radical pair is also formed in a singlet state.

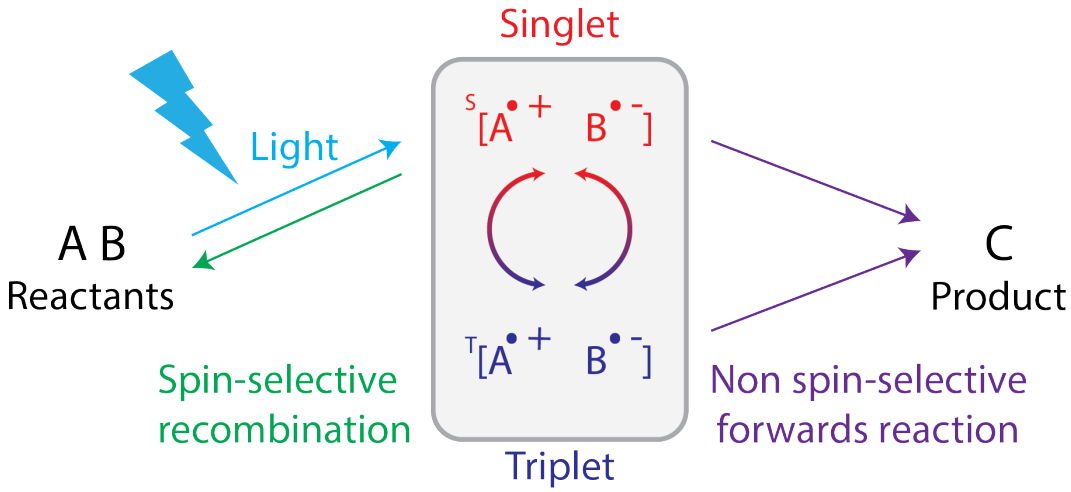


Figure 1.2: General reaction scheme illustrating the radical pair mechanism. Photoexcitation of the acceptor (B) triggers electron transfer from the donor molecule (A), producing a radical pair that can interconvert between singlet and triplet states. The reaction proceeds via spin-selective recombination to the ground state or via a non-spin-selective forward reaction to form product (C). The yields of these pathways are influenced by the Earth's magnetic field. Figure adapted from Hore and Mouritsen [16].

Spin refers to the intrinsic angular momentum carried by electrons. Each electron can occupy one of two states, often described as "up" (↑) or "down" (↓). If the unpaired electron spins, one in each radical, are opposed, the pair forms a singlet (S) state.

$$|\mathrm{S}\rangle = \frac{1}{\sqrt{2}}\left(|\uparrow\downarrow\rangle - |\downarrow\uparrow\rangle\right) \tag{1.1}$$

Like the singlet, the triplet states can also be expressed as linear combinations of the spin-up and spin-down basis states:

$$|\mathrm{T}_0\rangle = \frac{1}{\sqrt{2}}\left(|\uparrow\downarrow\rangle + |\downarrow\uparrow\rangle\right) \tag{1.2}$$

$$|\mathrm{T}_+\rangle = |\uparrow\uparrow\rangle \tag{1.3}$$

$$|\mathrm{T}_-\rangle = |\downarrow\downarrow\rangle \tag{1.4}$$

Singlet–triplet interconversion is driven by hyperfine interactions between the unpaired electron spins and nearby nuclear spins. Because the electrons carry magnetic moments, they also couple to an external magnetic field, which further

influences these spin dynamics. Hyperfine interactions are anisotropic, so their effects on the spin dynamics depend on the orientation of the radical pair relative to the magnetic field. This orientation dependence changes the rates and extent of singlet–triplet interconversion, which in turn alters the populations of spin states and the resulting reaction product yields. As a result, radical pair chemistry becomes sensitive to magnetic field direction, providing the physical basis of a radical pair compass.

Usually, the Earth's magnetic field of about 50 μT would be considered too weak to affect biochemical reactions, since the typical magnetic interaction energies are roughly a million times smaller than the thermal energy ($k_{\mathrm{B}}T$) of biological molecules [16]. However, radical pairs exist in a highly non-equilibrium state, forming immediately after photoexcitation. Granted a long enough spin-coherence time, their evolution is not dictated by thermodynamics but by coherent spin dynamics, whereby the electron spins remain correlated and can interconvert between singlet and triplet states.

The application of the RPM to magnetoreception dates back to 1978, when Schulten *et al.* first proposed that singlet–triplet interconversion could be influenced by the Earth's magnetic field in a biologically relevant way [68]. Their theory suggested that if radical pairs were generated in specific molecular orientations within an organism, then the anisotropy of hyperfine interactions could allow sensitivity to the direction of the geomagnetic field. Within cryptochromes, the magnetically sensitive spin correlated radical pairs are formed as follows [69, 70]. In its resting state, FAD, located in the centre of the cryptochrome, is in its fully oxidised form ($\mathrm{FAD_{ox}}$), in a singlet ground state. In the presence of blue light, the flavin is excited into a higher energy singlet state. The excited FAD is a strong oxidant and can then accept an electron from a nearby tryptophan termed Trp_A. This begins a series of stepwise electron transfers across a chain of tryptophans ending in Trp_D and, in some cases, also a nearby tyrosine as shown in Figure 1.3. The initial electron transfer produces $\mathrm{FAD}^{\bullet -}$ and $\mathrm{TrpH}^{\bullet +}$. As mentioned, these radical pairs then interconvert between singlet and triplet states under the influence of hyperfine

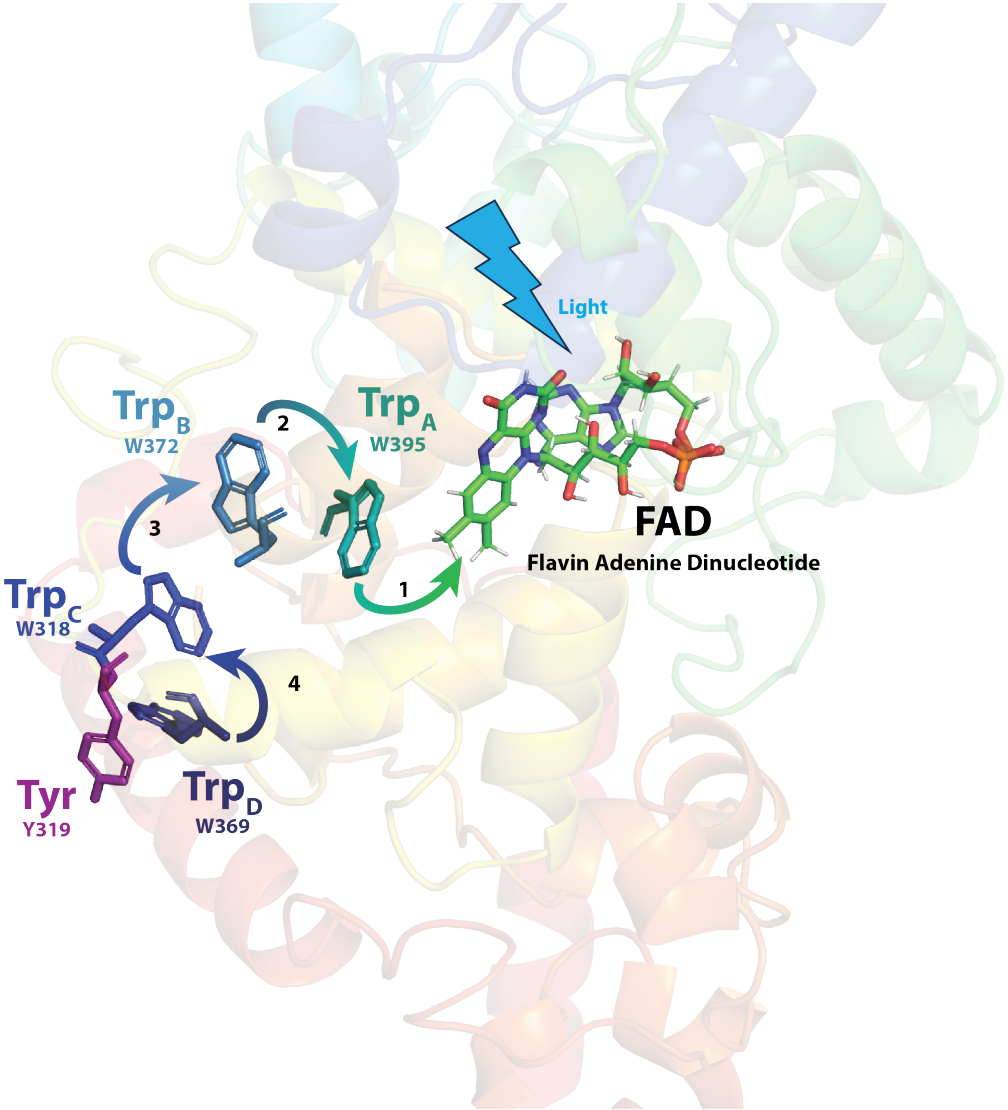


Figure 1.3: The electron-transfer chain, shown here using a European robin Cry4a homology model, depicts photoactivation of FAD followed by sequential electron transfers that generate a long-lived radical pair between FAD and TrpD, potentially involving a nearby tyrosine.

and Zeeman interactions, which can bias the reaction outcomes and may ultimately yield a signalling state in the protein. This process is illustrated in Figure 1.4.

The radical pair mechanism offers a plausible explanation for how weak magnetic fields can affect biological systems through changes in radical pair spin dynamics. In the case of animal magnetoreception, it provides a mechanism for light-activated molecular reactions to be influenced by the Earth's magnetic field and, in turn, to shape behavioural responses. This idea has developed into an active area of

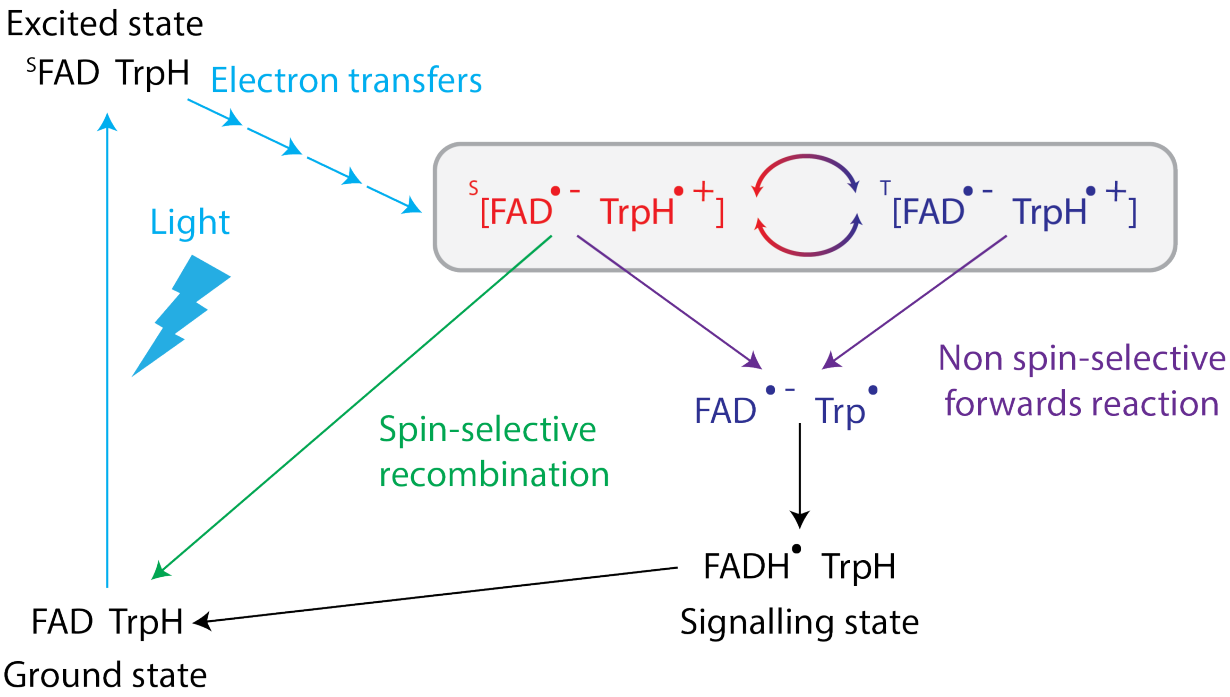


Figure 1.4: Radical pair mechanism in cryptochromes. Ground-state FAD is photoexcited, initiating a series of electron transfers that generate a long-lived radical pair. This radical pair can interconvert between singlet and triplet states under the influence of the Earth's magnetic field, modulating the yield of signalling states. Figure adapted from Hore and Mouritsen [16].

research, both theoretically and experimentally and underpins much of the work presented in this thesis. However, the RPM does not explain how these initial quantum events are coupled to structural changes in the protein or to downstream signalling pathways. These later steps are less well understood but are essential for linking molecular spin chemistry to physiology and behaviour.

This thesis focuses on the structural response of Cry4a to light and magnetic stimuli. Through HDX–MS, I characterise conformational changes that may connect radical-pair formation to downstream signalling processes.

1.4 Previous Work

This section reviews landmark studies on Cry4a to contextualise the research presented in this thesis within the broader scientific literature.

A pivotal study by Xu *et al.* demonstrated that recombinant European robin Cry4a (*Er*Cry4a), when purified and exposed to blue light *in vitro*, undergoes light-driven radical-pair reactions that are magnetically sensitive at millitesla field strengths [17]. Although the signal-to-noise ratio did not permit detection of effects at Earth-strength fields, the findings provided direct evidence that Cry4a exhibits the photochemical properties expected of a magnetically sensitive flavoprotein. Through systematic substitution of tryptophan residues with phenylalanine along the electron transfer chain, Xu *et al.* showed that Trp_A to Trp_D are essential for generating and maintaining magnetically sensitive radical pairs. These results demonstrated that the tryptophan chain plays a central role in shaping radical pair dynamics and thereby the magnetic response of Cry4a. In the same study, comparative assays indicated that Cry4a from non-migratory species such as chicken and pigeon produced substantially weaker or no detectable magnetic field effects under equivalent conditions.

However, more recent in-depth studies of chicken (*Gallus gallus*) Cry4a have reported magnetic field effects that are comparable to, and in some cases greater than, those observed for European robin Cry4a [71]. In particular, mutation of the fourth tryptophan produced a pronounced change in magnetic sensitivity, consistent with the strong influence of this residue reported previously for robin Cry4a. This result indicates that the final tryptophan strongly shapes the magnetic response by influencing radical pair lifetimes and interconversion. The study also showed that substitutions previously associated with migratory adaptation (R317C and E320K) had little impact on magnetic sensitivity, suggesting that interspecies differences may instead arise from factors beyond the immediate radical-pair chemistry, such as interaction partners, oligomeric state, or retinal environment [71].

Recent work has shown that Cry4a is not confined to a monomeric state but can readily form dimers, stabilised by non-covalent contacts and in some cases by disulphide linkages [72]. Cross-linking experiments and computational modelling identified several plausible dimerisation sites, including regions close to the FAD-binding site and the tryptophan tetrad, raising the possibility that oligomerisation

could influence radical-pair formation. These findings highlight quaternary structure as a potentially important factor in magnetoreception, suggesting that Cry4a may function in higher-order assemblies in the retina. In the context of the present work, however, all HDX-MS measurements were carried out on monomeric Cry4a and the structural dynamics discussed therefore relate specifically to the conformational properties of individual subunits, without the additional complexity introduced by oligomerisation.

HDX-MS has been extensively applied to the algal cryptochrome/photolyase *Chlamydomonas reinhardtii* cryptochrome *Cra*Cry, a protein capable of both DNA repair and photoreception [73]. Using a custom-built light chamber, these experiments compared *Cra*Cry in oxidised and photoreduced states to identify regions of the protein that change upon blue light excitation. The data showed that the C-terminal extension interacts with the PHR, masking the DNA-binding site and that this interaction loosens after illumination. Increased exchange was also observed in a loop where the final tryptophan of the electron transfer chain sits, as well as in an adjacent helix. These results provided some of the first direct evidence that cryptochromes undergo localised conformational changes upon photoactivation.

More recently, time-resolved ion mobility MS has been used to capture these transitions in real time, allowing structural changes in *Cra*Cry to be followed directly after blue-light excitation [74]. This study revealed light-induced rearrangements involving the α22 helix and the attached C-terminal extension, governed by proton-coupled electron transfer at residues D321 and D323. Mutational analysis showed that disruption of these interactions modulates the kinetics of structural switching between dark and lit states, establishing the α22–PHR interface as a key element in signalling-state formation.

Although *Cra*Cry differs from avian Cry4a in its overall structure, the general principles are highly relevant. These studies demonstrate how light modulates flexibility within the electron-transfer chain and adjacent secondary structures and how redox changes control access to functional domains through movement of the C-terminal region. Cry4a lacks such an extended C-terminal tail, yet similar

light-dependent shifts are predicted to occur in loops and helices surrounding the FAD pocket and tryptophan tetrad. The (*Cra*Cry) studies therefore provide a methodological and conceptual reference for interpreting the value of HDX–MS in capturing subtle structural changes and for analysing the conformational dynamics observed in avian Cry4a.

A closely related subject is *Dm*Cry, which has also been studied using HDX-MS [56]. As stated previously, *Dm*Cry is a type-1 cryptochrome, potentially implicated in magnetoreception through various biochemical and behavioural studies. The HDX–MS experiments achieved 77% sequence coverage of *Dm*Cry. Coverage was comprehensive across most of the PHR and the extended C-terminal region. However, two critical loops, the phosphate-binding loop (PBL, residues 249–263) and the protrusion loop (PL, residues 288–306), were not covered by any peptides. This limitation meant that loop dynamics had to be inferred indirectly or supplemented with molecular dynamics (MD) simulations. Despite these gaps in coverage, the HDX data provided clear evidence of light-dependent conformational changes. Within the C-terminal tail (CTT), particularly across the helices α22 and α23, low uptake was observed in the dark state, whereas illumination led to a significant increase in deuterium incorporation. This was of note as the spectra acquired over this region displayed EX1 kinetics (explained in depth in Chapter 2.7), which can be the sign of an unfolding event or larger-scale structural rearrangement. Within this study, it was proposed that the CTT detaches or unfolds, causing a transition to an 'open' state consistent with a population of higher deuterium uptake. Illumination also affected regions of the protein that lie beneath α22 and α23 in the dark state. Peptides from α16, normally shielded by the C-terminal helices, showed increased uptake once these helices detached, indicating that previously buried surfaces became solvent-exposed. In addition to this, light-dependent changes were observed in α4 and in the loop connecting α14 and α15.

Although these effects were less pronounced than those observed for α22/α23, they demonstrate that the structural response extends beyond the immediate proximity to the flavin pocket and C-terminal region. To gain a deeper understanding

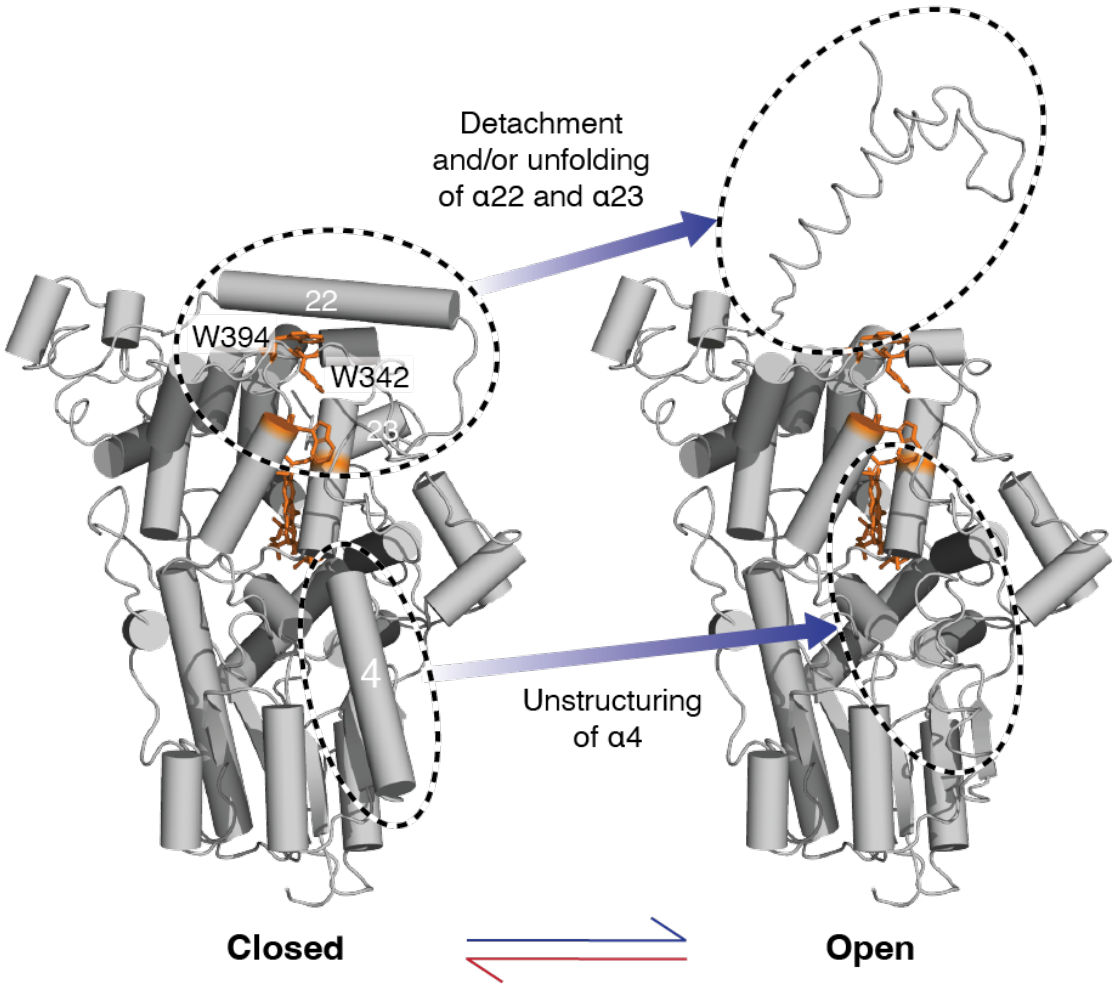


Figure 1.5: Proposed structural states of *Drosophila melanogaster* cryptochrome (*Dm*Cry) used to interpret HDX data. Structures of a closed state (left) and an open state (right) are shown. In the light-induced open state, helices α22 and α23 are proposed to detach and/or unfold, exposing previously buried regions such as loop L14-15 and helix α16, leading to increased solvent accessibility. Illumination also appears to destabilise helix α4, consistent with HDX data showing marked differences between light and dark states in the wild type. Figure taken from Chandler *et al.* [56].

of the loops and regions not covered in the HDX experiments, MD simulations were conducted on *Dm*Cry. In the light state simulations, the PBL adopted a short helical turn and moved closer to the FAD, whereas the PL moved towards helix α6. As a result of these loop displacements, the interactions holding α22 and α23 towards the central part of the protein are disrupted. In effect, the simulations provided a structural trigger that explains the HDX observation of α22/α23 release: reduction of FAD alters loop conformations, which in turn weakens C-terminal anchoring

(Figure 1.5). The MD trajectories also showed that the final tryptophan (W394) fluctuated more in the light state, adopting conformations that left it more exposed to solvent compared with the dark state. To test whether the conformational switch depends on the electron transfer chain, two variants were examined: W342F TrpC and W394F TrpD. In W394F, the light-induced uptake changes in $\alpha22/\alpha23$ observed in the wild-type were abolished. In W342F, the effect was strongly reduced but still detectable, particularly in $\alpha23$. These results demonstrate that the structural response is critically dependent on the final tryptophan and, more broadly, on an intact electron-transfer chain in a similar manner to (*Cra*Cry). These experiments establish that blue light causes conformational changes in *Dm*Cry that can be captured directly by HDX-MS and rationalised by MD simulations. This provides a clear methodological and conceptual precedent for my work carried out on avian Cry4a within this thesis, where similar HDX approaches are used to probe light-dependent dynamics in a protein more directly implicated in magnetoreception.

1.5 Summary

This section has shown that, although magnetoreception is well established across several taxa, its molecular basis remains unresolved. The Earth's magnetic field provides spatially informative cues, such as inclination, intensity and polarity. Many species, particularly migratory birds, appear able to detect and use the Earth's magnetic field strength and inclination for orientation and navigation. A few candidate mechanisms have been proposed to explain this ability, including magnetite-based receptors. However, light-dependent magnetoreception mediated by cryptochromes still remains the most experimentally supported model. Cry4a stands out as the most likely candidate as it is able to form long-lived radical pairs and has been shown to display magnetic field sensitivity. Previous studies have demonstrated light-induced effects on other cryptochromes, which give a strong basis to the study of avian cryptochromes within this thesis. Having established this biological and mechanistic foundation, the following section introduces mass spectrometry-based approaches for studying Cry structure and dynamics. These

techniques enable detailed characterisation of protein conformations, thereby offering experimental insight into the molecular features underlying magnetoreception.

"All you really need to know for the moment is that the universe is a lot more complicated than you might think, even if you start from a position of thinking it's pretty damn complicated in the first place."

— Douglas Adams via Mia Whitefield

2

Technical Background on Mass Spectrometry

Contents

2.1 Motivation 22
2.2 Mass Spectrometry Workflows 22
2.3 Native Mass Spectrometry 23
2.3.1 Historical Development of Native Mass Spectrometry . . 23
2.4 Mass Spectrometry Workflow 25
2.4.1 Sample Preparation 25
2.4.2 Electrospray Ionisation 27
2.4.3 Ion Transmission 28
2.4.4 Mass Filtering/ Selection 30
2.4.5 Ion Fragmentation 30
2.4.6 Mass Analysers 32
2.4.7 Relevance to Cryptochrome Studies 34
2.5 Hydrogen-Deuterium Exchange Mass Spectrometry (HDX-MS) 34
2.5.1 The History of HDX-MS 34
2.5.2 Exchange Kinetics 35
2.6 Typical Workflow 40
2.6.1 Sample Preparation 40
2.6.2 Labelling 40
2.6.3 Quenching the Exchange Reaction 42
2.6.4 Proteolytic Digestion 43
2.6.5 Desalting and Separation 43
2.6.6 Mass Spectrometric Analysis 44
2.6.7 Data Processing and Uptake Calculation 44
2.6.8 Scrambling and ECD Fragmentation 46

2.6.9 Alternate Workflow: Pulsed Labelling 47
2.6.10 Limitations 49
2.7 Summary 51

2.1 Motivation

Understanding how cryptochromes respond structurally to light and magnetic stimuli requires methods capable of monitoring proteins in solution under conditions close to their native state. To address this, a mass spectrometry (MS)–based strategy was developed combining native MS and hydrogen–deuterium exchange MS (HDX–MS). Native MS provides information on cofactor binding, oligomeric state and overall integrity, while HDX–MS enables site-resolved mapping of solvent accessibility and conformational flexibility. These techniques allow light- and magnetically induced changes to be characterised without the need for crystallisation or labelling with external probes.

2.2 Mass Spectrometry Workflows

Mass spectrometry workflows are broadly divided into top-down, middle-down and bottom-up approaches, each differing in the level of structural information retained [75, 76].

In top-down MS, intact proteins are ionised and analysed directly without prior digestion, preserving post-translational modifications (PTMs) and noncovalent interactions where conditions permit. This enables the characterisation of proteoforms, domain organisation and global conformational states [77].

By contrast, bottom-up MS involves proteolytic digestion, typically with pepsin under quench conditions, to produce overlapping peptides that are analysed by LC–MS. This workflow is the foundation of most HDX studies, as it enables site-resolved measurement of deuterium incorporation and the identification of locally flexible regions [78, 79].

Middle-down MS lies between these, using limited proteolysis or specialised proteases (e.g. OmpT) to generate larger fragments or domains. This reduces spectral complexity compared with top-down analysis while maintaining broader structural context than conventional bottom-up approaches [80, 81].

Each workflow therefore offers complementary insights into protein structure and dynamics. Top- and middle-down analyses are especially suited for studying proteoforms and domain-level conformational states, whereas bottom-up HDX–MS remains the preferred approach for quantifying localised protection and detecting condition-dependent structural changes.

2.3 Native Mass Spectrometry

Biological MS is used across the life sciences to identify and analyse proteins, peptides, metabolites, lipids and nucleic acids and has become a central tool for exploring molecular structure and interactions [82, 83].

Native MS extends these applications by enabling the analysis of intact proteins and complexes under conditions that preserve their non-covalent interactions [77, 84]. By maintaining near-physiological buffers and avoiding denaturing agents, native MS captures folded conformations and bound ligands directly, providing information on stoichiometry, subunit composition and conformational heterogeneity [85–87]. This approach is increasingly used to probe assembly and stability of protein complexes in structural biology [88, 89].

In this work, native MS was used to verify FAD binding, assess oligomeric state and monitor for degradation before and after other experiments. These measurements ensured that subsequent HDX and fragmentation analyses were carried out on intact, well-defined species.

2.3.1 Historical Development of Native Mass Spectrometry

Native MS developed from advances in soft ionisation that made it possible to transfer intact biomolecules and complexes into the gas phase without disrupting their non-covalent interactions. Before these techniques were introduced, MS was

used mainly to measure the masses of small organic compounds, while high-resolution MS and tandem MS provided elemental composition and structural information through accurate mass measurements and fragmentation [82].

The development of soft ionisation in the late 1980s transformed what could be studied by MS. Electrospray ionisation (ESI) was introduced as a means of generating ions directly from solution, while matrix-assisted laser desorption/ionisation (MALDI) provided an alternative approach for analysing larger molecules [90–92]. In MALDI, the analyte is mixed with a matrix that absorbs laser energy and transfers charge during desorption. ESI instead creates charged droplets from solution that evaporate until ions are released. As ESI produces multiply charged ions, it allows high-mass species to be detected within the limited m/z range of most analysers and underpins all of the approaches used in this thesis.

The importance of these developments was recognised when the 2002 Nobel Prize in Chemistry was awarded jointly to John Fenn and Koichi Tanaka for the development of ESI and MALDI, which made it possible to analyse biological macromolecules by MS. Their work opened the field to proteins, nucleic acids and large non-volatile compounds that had previously been inaccessible to MS-based analysis.

By the early 1990s, studies showed that non-covalent assemblies such as protein–ligand and protein–protein complexes could survive transfer into the gas phase, establishing that ESI could preserve native-like structures [93, 94].

Major progress in the early 2000s came from improvements in instrumentation. The introduction of the quadrupole time of flight (Q-ToF) enabled high-mass ions to be transmitted efficiently while retaining good resolution [95]. Controlling gas pressure and ion optics was also shown to be essential for maintaining complex integrity. Improvements in source design and sample preparation soon followed, expanding the range of systems accessible to native MS and helping to establish it as a core technique in structural biology [85, 89, 96].

At the same time, new fragmentation and activation methods were developed to explore subunit interactions and complex formation. Collision-induced dissociation

(CID) became especially useful for ejecting subunits or ligands without fully unfolding the complex, providing information on connectivity and binding strength [97]. In contrast, electron-capture dissociation (ECD) introduced a nonergodic mechanism in which low-energy electrons induce backbone cleavage while leaving non-covalent contacts intact. This allowed direct probing of structural organisation and residue-specific protection within protein complexes [98, 99].

Data processing has also evolved to keep up with instrumentation. Manual peak assignment gave way to automated deconvolution and tools such as UniDec allowed complex spectra to be converted into mass distributions using a Bayesian model [100]. This made it possible to analyse large datasets consistently and opened the way for high-throughput studies of heterogeneous systems.

Native MS has since moved from proof-of-principle experiments to an established method for studying biomolecular assemblies. It is now used to determine oligomeric states, identify binding partners, map substructures and explore large complexes in detail.

2.4 Mass Spectrometry Workflow

This section outlines how analytes are prepared, ionised and transmitted through a mass spectrometer. It describes the main instrumental components with reference to the systems used in this work: the Q Exactive UHMR (Thermo Fisher Scientific), the Synapt G2-Si Q-ToF (Waters) (Figure 2.1) and the Select Series Cyclic IMS Q-ToF (Waters). These instruments are applied throughout this thesis for both native MS and HDX-MS experiments.

2.4.1 Sample Preparation

To obtain clean spectra suitable for deconvolution, careful sample preparation is essential. The analyte is typically buffer exchanged into a volatile electrolyte that maintains near-physiological properties while removing non-volatile salts, detergents and other additives that can suppress ionisation or cause adduct formation [85, 101]. In practice within the experiments undertaken in this thesis, proteins are handled

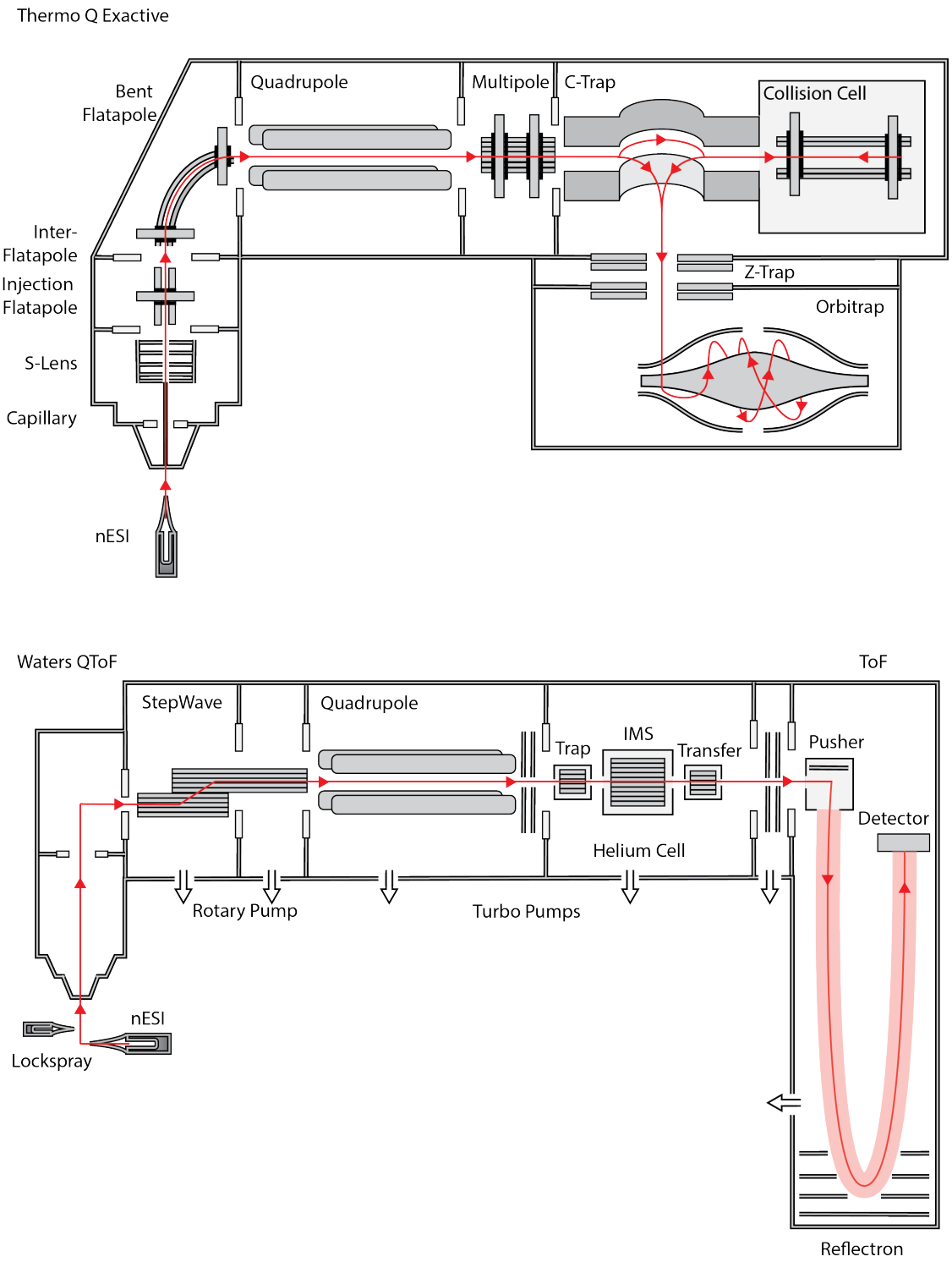


Figure 2.1: Schematic comparison of ion transmission in a quadrupole–Orbitrap (Q Exactive UHMR, top) and a quadrupole–time-of-flight (Q-ToF, bottom) mass spectrometer. Both systems use similar front-end ion optics and quadrupole selection, but differ in the analyser and detection stages, where ions are either trapped and oscillated in an Orbitrap or accelerated through a flight tube for time-of-flight measurement.

in the dark and kept on ice as much as possible to minimise aggregation, co-factor reduction, photodegradation or dimerisation. Samples are then buffer exchanged into 200 mM ammonium acetate at pH 7, a volatile electrolyte that removes residual salts and reducing agents such as BME prior to electrospray [88, 102].

2.4.2 Electrospray Ionisation

ESI uses a strong electrical potential to transfer ions from solution into the gas phase. The sample is buffer-exchanged into a volatile electrolyte and loaded into a gold-coated capillary that has been clipped to form a small aperture. When a high voltage is applied between the emitter and the mass spectrometer inlet, electrostatic forces counteract the surface tension of the liquid and create a Taylor cone at the tip of the capillary [103]. The electric field at the cone tip generates a fine spray of charged droplets that are drawn into the inlet. As the solvent evaporates, the droplets shrink and the charge density rises until the electrostatic repulsion balances the surface tension of the liquid. This balance, known as the Rayleigh limit, defines the maximum charge that a droplet of radius R can sustain [104].

$$Q_{\mathrm{R}} = 8\pi\sqrt{\varepsilon_0\,\gamma\,R^3} \tag{2.1}$$

Rayleigh charge limit for a conducting spherical droplet, where Q_{R} is the maximum stable charge (C), R is the droplet radius (m), γ is the surface tension ($N\,m^{-1}$), and ε_0 is the vacuum permittivity ($C^2\,N^{-1}\,m^{-2}$).

Once this limit is exceeded, droplets undergo Coulombic fission, producing smaller droplets that continue to evaporate and divide until free analyte ions are released and transmitted into the mass spectrometer [105]. The specific mechanism by which ions emerge from the final droplets is explained by three complementary models: the ion evaporation model (IEM), the charged residue model (CRM) and the chain ejection model (CEM) shown in Figure 2.2.

The IEM proposes that strong electric fields at the droplet surface eject small previously solvated ions directly into the gas phase[106]. This mechanism explains the abundance of low-mass, singly charged species. The CRM involves progressive

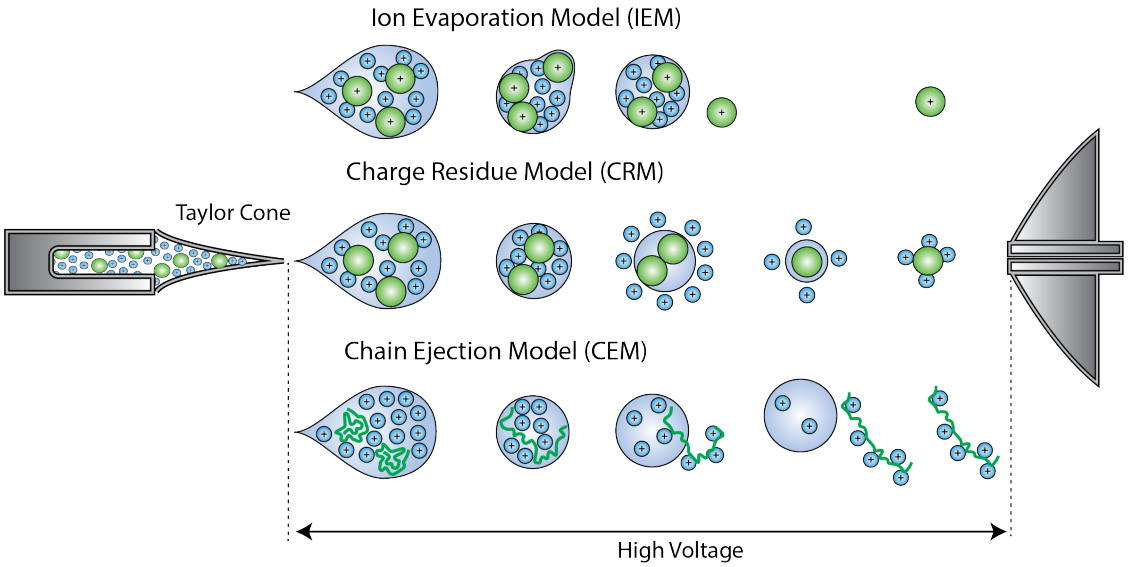


Figure 2.2: Schematic illustration of the ion evaporation (IEM), charged residue (CRM) and chain ejection (CEM) models. IEM describes the direct ejection of solvated ions from the droplet surface, CRM involves complete desolvation of charged droplets until a single analyte remains and CEM depicts the sequential extrusion of unfolded protein chains from the droplet.

evaporation and repeated Coulombic fission until the remaining droplet contains a single analyte molecule, which is released once the solvent has fully evaporated [107]. This process accounts for the multiple charge states observed for compact, folded proteins without fragmentation [108]. The CEM describes ion formation from unfolded or denatured proteins that migrate to the droplet surface due to their hydrophobic character. One terminus is expelled first, followed by sequential extrusion of the remaining chain until the entire protein is released [109].

The instruments used in this work employ nano-electrospray ionisation (nESI), which uses emitters with tip diameters of only a few micrometres instead of the 100 μm typical of conventional ESI. This reduces flow rate, limits sample consumption and improves desolvation efficiency for low-concentration samples [110–112].

2.4.3 Ion Transmission

Before reaching the mass analyser, ions pass through a series of transfer and focusing components designed to remove residual solvent and neutral species while maintaining an ion beam. The analyte enters the ion source through a heated

capillary that helps to desolvate and is guided towards the S-lens via the ion transfer tube. The S-lens is a radio-frequency (RF) stacked-ring ion guide composed of alternating ring electrodes that progressively narrow along the ion path [113]. By alternating the phase of the applied voltage, the S-lens focuses ions into a stable beam while acting as a vacuum barrier between the high-pressure source region and the lower-pressure ion optics. The applied RF amplitude can be tuned to favour transmission of different m/z ranges, with higher values improving transmission of high-mass ions [114].

Within Q Exactive instruments (Thermo Fisher Scientific), the focused beam then enters the injection flatapole, another RF ion guide formed from a square array of flat electrodes. In the Q Exactive UHMR, this region can perform in-source trapping where the injection flatapole is momentarily pulsed to a negative potential while the inter-flatapole remains at a high positive potential, allowing temporary accumulation and cooling of ions before release [115]. Once released, the desolvated ion packet is transferred to the bent flatapole, which applies both an axial DC field and RF confinement to guide ions through a 90° turn. Neutral molecules and residual droplets cannot follow this trajectory and are pumped away, improving the overall signal-to-noise ratio.

The Waters Q-ToF instruments use a comparable but distinct front-end configuration. Ions are first produced by an orthogonal ZSpray source, in which the spray is directed at right angles to the inlet, aiding removal of neutrals and droplets before transmission. The resulting ion beam then enters the StepWave region, a two-stage stacked-ring ion guide that captures ions in the lower section and actively transfers them to the upper guide while neutrals are removed [116]. Downstream of this, the T-Wave system accumulates, transmits and, when required, fragments ions. The T-Wave consists of a series of ring electrodes that generate travelling DC pulses, creating a moving potential wave that propels ions through the device. Separate sections act as a trap, an ion-mobility separator and a transfer region, allowing both cooling and controlled fragmentation where necessary.

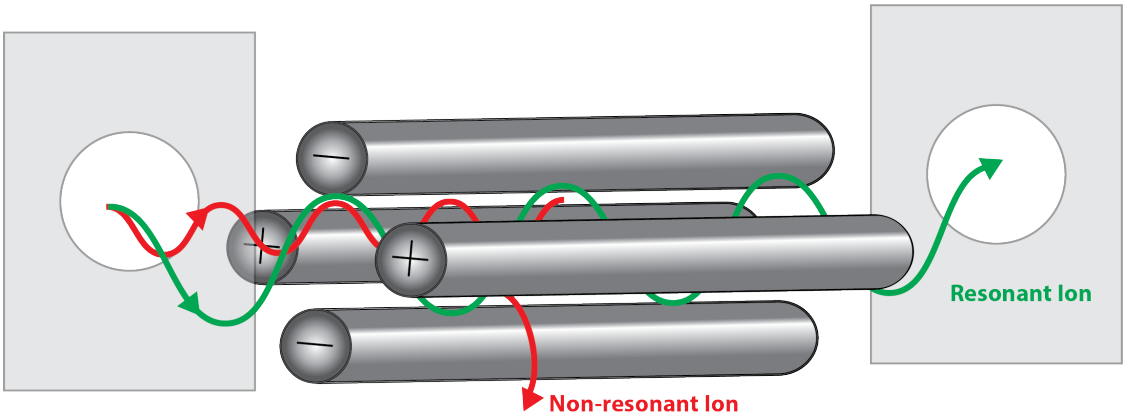


Figure 2.3: Schematic of a quadrupole mass filter showing the arrangement of four parallel rods with alternating radio-frequency (RF) and direct-current (DC) potentials. Only ions with a stable trajectory for a given m/z ratio pass through to the detector.

2.4.4 Mass Filtering/ Selection

In most MS instruments, mass selection is carried out using a quadrupole (Figure 2.3). Quadrupoles transmit ions that have stable trajectories under the applied RF and DC voltages; ions with unstable trajectories strike the metal rods and are not transmitted [117]. A quadrupole comprises of four parallel metal rods arranged in opposite pairs, with each pair electrically connected. When an RF potential is applied to the two pairs, which are 180° out of phase (typically with a superimposed DC component), one pair is positive while the other is negative, generating the oscillating field that defines the mass-stability window. For a given RF and DC, ions within a narrow m/z window will travel through the quadrupole towards the collision cell analyser. The quadrupole can be used to isolate a precursor for MS/MS but can also be used to focus and transmit ions more efficiently.

2.4.5 Ion Fragmentation

After mass filtering, selected ions can be fragmented to obtain structural or compositional information. This is achieved through a range of activation methods that transfer energy to the ions, either through collisions, photons or electrons. The most widely used approach is CID, where ions collide repeatedly with a neutral gas and convert kinetic energy into internal energy that breaks the weakest bonds. On Q Exactive instruments this process is implemented as higher-energy collisional

dissociation (HCD) in a multipole collision cell [118, 119]. Either selected precursors or the full ion population are accelerated into the cell and collide with nitrogen. The energy transferred during these collisions can cause local unfolding and charge migration, leading to asymmetric dissociation where one subunit is ejected with a higher charge while the remaining assembly becomes charge reduced and shifts to higher m/z [120]. This behaviour reflects how charge is distributed across the complex and can be used to infer interface strength and subunit stability. The collision energy is controlled using the normalised collision energy (NCE) parameter, which scales with m/z and instrument voltages to maintain consistent fragmentation across charge states [119]. For very high-mass ions, heavier gases such as xenon can be used within the HCD cell to increase momentum transfer and enhance dissociation or desolvation [121]. Following activation, fragments are returned to the C-Trap, cooled and then analysed in the Orbitrap at high resolution.

Other than CID, several other activation methods have been developed that provide complementary information. Infrared multiphoton dissociation (IRMPD) and ultraviolet photodissociation (UVPD) both use photon energy to excite ions and generate characteristic fragmentation patterns [122]. UVPD is particularly effective for mapping modifications or probing backbone flexibility due to its ability to access higher energy states. Electron-based approaches such as electron capture dissociation (ECD) and electron transfer dissociation (ETD) instead induce fragmentation through electron capture or transfer to multiply charged ions, cleaving the peptide backbone while retaining weaker noncovalent interactions and PTMs [98]. These are especially useful in top-down and HDX workflows, where maintaining native-like conformations is critical. Surface-induced dissociation (SID) takes a different approach, accelerating ions into a rigid surface to fragment large assemblies through impulsive energy transfer rather than gradual heating. The resulting fragments often retain subunit connectivity, providing a direct view of complex architecture [123]. These approaches allow fragmentation behaviour to be tuned depending on whether local, sequence-level or global complex information is required.

2.4.6 Mass Analysers

Mass analysers separate ions according to their m/z, while detectors measure the resulting signal to generate a mass spectrum. Different analyser designs provide trade-offs between resolution, sensitivity, dynamic range and scan speed.The instruments used in this thesis were the Q Exactive UHMR, which employs an Orbitrap analyser and the Synapt G2-Si and Xevo, both of which use time-of-flight (ToF) analysers. These two technologies are among the most widely applied in structural and native MS, each offering distinct advantages depending on the experiment.

The Orbitrap is an electrostatic trap that measures ion oscillation frequency rather than direct impact on a detector [124] (Figure 2.4). Ions are injected from the C-Trap into the electrostatic field surrounding a central spindle-shaped electrode, where they follow stable orbital trajectories while oscillating harmonically along the trap axis. The axial oscillation frequency is inversely proportional to the square root of m/z. Rather than striking a detector, the motion of the trapped ions induces an image current on the split outer electrodes, which is amplified and recorded as a time-domain transient to generate the mass spectrum. Fourier transformation converts this transient into a frequency-domain spectrum and through calibration, these frequencies are converted into m/z values. The precision of frequency measurement determines both resolving power and mass accuracy, with typical Orbitraps achieving sub-ppm precision under optimal conditions [119, 121]. The high stability of the electrostatic field and the absence of active RF confinement make the Orbitrap particularly suitable for high-resolution analysis of intact proteins and large assemblies. Its design allows for long transient acquisition and tuneable resolution, enabling users to balance scan speed against resolving power depending on experimental requirements [125].

In contrast, the ToF analyser separates ions based on the time they take to travel through a field-free region after acceleration [126]. Ions accelerated through the same potential difference receive identical kinetic energy; therefore, their velocities depend on their m/z, with lighter ions arriving at the detector earlier than heavier

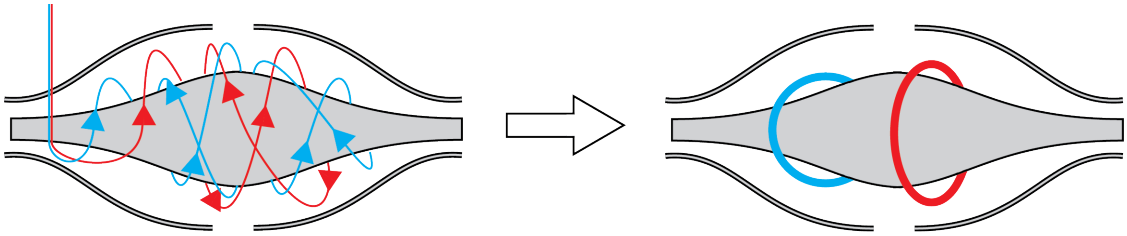


Figure 2.4: Schematic of the Orbitrap mass analyser. Ions injected from the C-Trap orbit a central spindle electrode and oscillate along its axis. The axial oscillation frequency, proportional to m/z, is measured as an image current on the outer electrodes and Fourier-transformed to obtain the mass spectrum.

ones. Since ESI generates a continuous beam, it must be divided into discrete packets of ions that are pulsed orthogonally into the flight tube. As these packets drift through the field-free region, small variations in initial kinetic energy can cause peak broadening. To correct for this, modern ToF instruments use a reflectron, an electrostatic mirror that compensates for these differences by forcing faster ions to travel a slightly longer path, refocusing ions of the same m/z and improving resolution. The final signal is produced when ions strike the detector, generating a voltage pulse proportional to ion abundance. The time-of-flight is then converted into m/z values using the known acceleration voltage and flight length.

ToF analysers combine fast spectral acquisition with wide dynamic range, which is essential for time-resolved or mobility-separated measurements. As they use pulsed ion packets, they can also be easily integrated with ion mobility spectrometry (IMS), enabling simultaneous determination of drift time and m/z [127, 128]. In the Waters Synapt and Xevo platforms, travelling-wave ion mobility (TWIMS) modules can be used before to ToF, separating ions by their collision cross section before mass analysis. This combination has been instrumental in probing conformational heterogeneity in proteins and complexes, complementing the high precision of Orbitrap-based measurements.

While both analysers perform mass measurement, their operating principles and strengths are different. The Orbitrap offers extremely high resolution and mass accuracy, precise charge-state determination and the potential for charge-detection operation in the UHMR [129]. These capabilities make it ideal for characterising

intact proteins, large complexes and assemblies with fine isotopic or charge-state detail. In contrast, the ToF provides rapid acquisition, high transmission efficiency and compatibility with IMS and HDX workflows, features critical for time-resolved experiments. In practice within the experiments carried out in this thesis, the Thermo Fisher Orbitrap platforms were used for native MS experiments, while Waters Q-ToF instruments were used for HDX-MS.

2.4.7 Relevance to Cryptochrome Studies

Native MS provides a direct way to examine the behaviour of avian cryptochromes in solution and to test whether the protein retains the expected properties after purification. It was used to check identity, detect and quantify monomer–dimer equilibria or higher-order assemblies and assess binding to cofactors such as FAD or to other partners. As the measurements are made under conditions that preserve the folded state and key noncovalent interactions, native MS can capture changes in assembly or conformation that are likely to be important for cryptochrome function and its proposed role in magnetoreception.

2.5 Hydrogen-Deuterium Exchange Mass Spectrometry (HDX-MS)

To investigate these structural changes in greater detail and follow differences in local flexibility, HDX-MS is used throughout this work as the principal tool for analysing conformational dynamics.

2.5.1 The History of HDX-MS

The study of hydrogen exchange in proteins dates back to the 1950s, when Linderstrøm-Lang and colleagues at the Carlsberg Laboratories began exploring it following Pauling's discovery of the α-helix and β-sheet [130, 131]. They reasoned that hydrogen bonding within regular secondary structure would slow the rate of exchange of backbone amide hydrogens. To test this, they deuterated proteins such as insulin in solution, froze and lyophilised them and then rehydrated under

controlled conditions before separating the material on density gradients [132]. Exchange rates were determined by measuring density shifts over time and fitting the resulting data to first-order rate constants. These early studies established that exchange rates depended on both pH and temperature [133].

The main limitation of these early measurements was the lack of residue-specific information. This changed in the 1980s with the development of high-field multidimensional NMR, which made it possible to assign individual backbone amides and follow their exchange after transfer into deuterated buffer [134]. Comparing experimental rates to intrinsic exchange rates allowed calculation of protection factors, providing direct information on structure and stability [78].

The emergence of ESI in the early 1990s opened the possibility of coupling hydrogen exchange to MS. Zhang and Smith first demonstrated that amide exchange could be measured by proteolysis followed by LC-MS analysis and this approach was later applied to myoglobin [135, 136]. This established the basis of the modern "bottom-up" HDX-MS workflow: labelling in deuterated buffer, quenching, pepsin digestion followed by LC-MS measurement [137].

Since then, HDX-MS has become a widely used approach for studying conformational change, ligand binding and structural dynamics in solution [138]. It has been particularly valuable for analysing membrane proteins, where conventional methods struggle due to low solubility and the effects of detergents on ionisation and digestion. Progress in this area has come from using more MS-compatible membrane mimetics such as nanodiscs and detergent-free systems including SMALPs and SMILPs, which preserve a native-like lipid environment while maintaining spectral quality.

2.5.2 Exchange Kinetics

HDX-MS probes protein structure and dynamics by monitoring the exchange of backbone amide hydrogens with deuterium when a protein is exposed to a deuterated solvent [139]. As deuterium is heavier than hydrogen (2.0014 Da vs 1.0078 Da), incorporation results in a measurable mass increase [137]. Amide hydrogens exchange on an experimentally accessible timescale and are highly sensitive to changes in

secondary structure, making them reliable indicators of local stability. The rate of exchange depends both on the intrinsic chemical step and on transient structural fluctuations that expose the amide to solvent. The intrinsic step proceeds through three catalytic routes: acid, base and water catalysis as illustrated below (Figure 2.5).

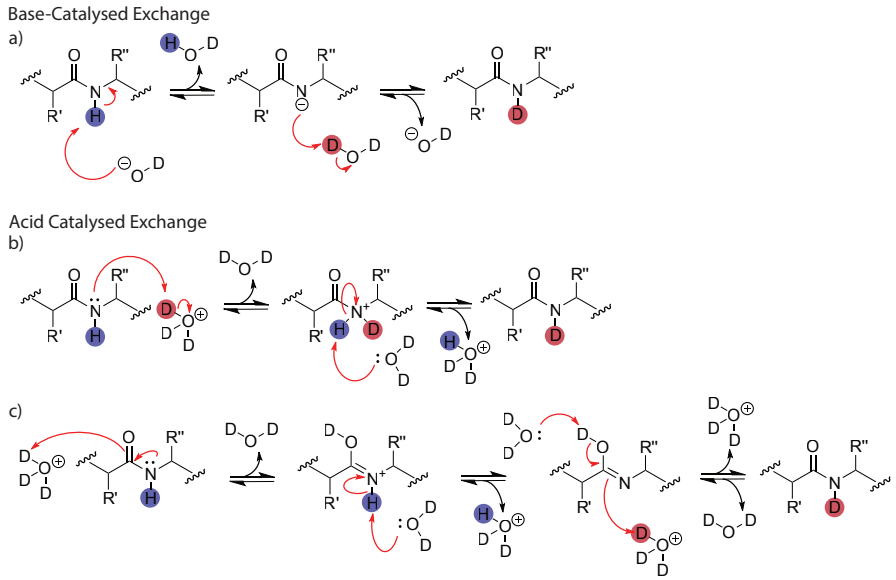


Figure 2.5: Mechanisms of acid-, base- and water-catalysed HDX. Adapted from Narang *et al.* [139].

In the base-catalysed mechanism, a deuterated hydroxide ion abstracts the amide proton, generating an anionic nitrogen that is subsequently reprotonated by D^+ from solvent. Acid catalysis proceeds either through protonation of the amide nitrogen by D_3O^+, forming a cationic intermediate, or by protonation of the carbonyl oxygen, which increases the acidity of the adjacent NH group and promotes deprotonation. Both routes lead to the incorporation of deuterium via reprotonation by D_3O^+. The neutral, water-catalysed mechanism involves a water molecule acting as a weak base to abstract the amide proton, with a second water molecule often assisting in proton transfer. Although water itself is a poor proton donor and acceptor, its autoionisation into H_3O^+ and OH^- makes it integral to all three catalytic routes.

Berger *et al.* investigated the pH dependence of exchange in poly-DL-alanine and identified a minimum rate at pH 2.5 [141] (Figure 2.6). This principle forms the basis of the quench conditions used in modern HDX workflows. As most biological HDX

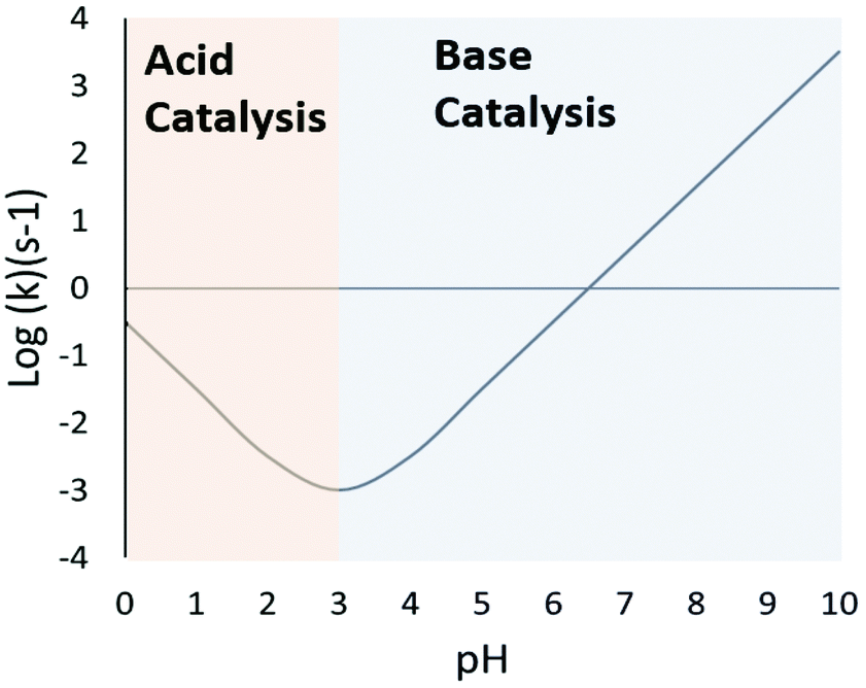


Figure 2.6: Dependence of the intrinsic exchange rate (k_{int}) on pH, showing acid, base and water catalysis. The minimum exchange rate occurs near pH 2.5-3, where acid and base contributions are balanced. Reproduced from Brown *et al.* [140].

experiments are conducted near pH 7-8 to approximate physiological conditions, the reactions are typically dominated by base catalysis.

$$k_{\text{int}} = k_{\text{acid}}[\text{H}^+] + k_{\text{base}}[\text{OH}^-] + k_{\text{water}} \tag{2.2}$$

Here k_{int} represents the intrinsic chemical exchange rate for an unprotected amide at the specific pH and temperature; k_{acid}, k_{base} and k_{water} are the rate constants for the three catalytic pathways.

Exchange within folded proteins also depends on transient structural fluctuations that briefly expose protected sites. This behaviour is described by a the following model [132, 142]:

$$\text{NH}_{\text{closed}} \underset{k_{closed}}{\overset{k_{open}}{\rightleftharpoons}} \text{NH}_{\text{open}} \xrightarrow[\text{D}_2\text{O}]{k_{\text{int}}} \text{ND}_{\text{open}} \underset{k_{open}}{\overset{k_{closed}}{\rightleftharpoons}} \text{ND}_{\text{closed}} \tag{2.3}$$

Here $\text{NH}_{\text{closed}}$ denotes a non-exchanging, hydrogen-bonded state and NH_{open} a transiently accessible state. Structural breathing motions cause transitions between

these states, governed by k_{open} and k_{closed}.

The observed rate of exchange, k_{HX}, depends on these three constants and under native conditions is given by [78]:

$$k_{\mathrm{HX}} = \frac{k_{open} \times k_{\mathrm{int}}}{k_{closed} + k_{\mathrm{int}}} \tag{2.4}$$

Two kinetic regimes are commonly observed as illustrated in Figure 2.7 [143]. The predominant regime, EX2, occurs when closing is faster than chemical exchange ($k_{closed} \gg k_{\mathrm{int}}$). In this case, the structure opens and closes many times before exchange occurs, producing a single isotopic distribution that gradually shifts to higher m/z with time.

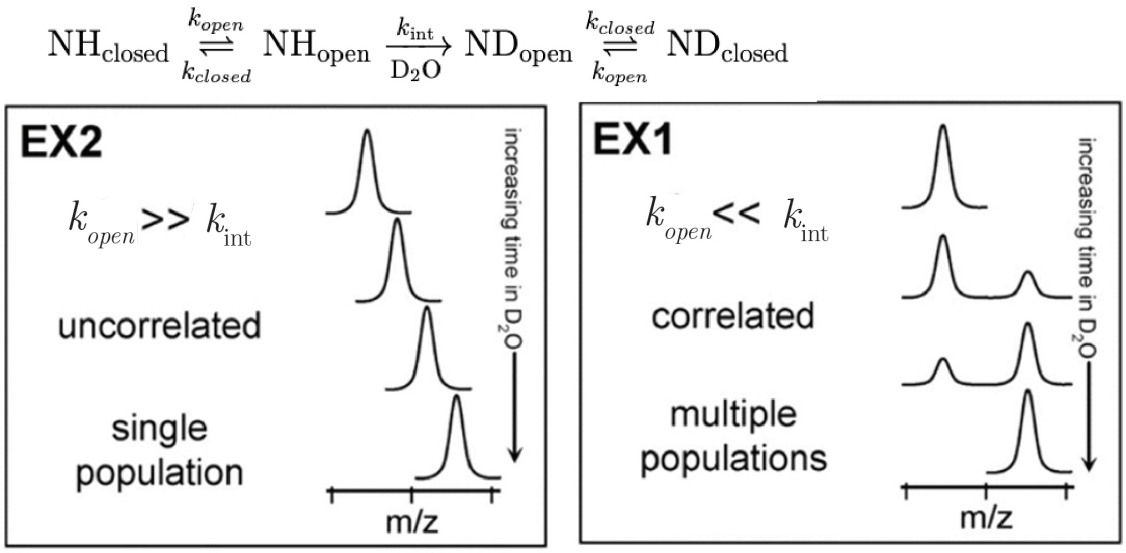


Figure 2.7: Comparison of EX2 and EX1 hydrogen–deuterium exchange regimes. In EX2 (left), the rate of structural closing (k_{closed}) is much faster than the chemical exchange rate (k_{int}), so multiple opening and closing events occur before exchange. The population remains uncorrelated, producing a single isotopic envelope that gradually shifts to higher m/z with time. In EX1 (right), the refolding rate (k_{closed}) is slower than the chemical exchange rate (k_{int}), meaning that once a region opens it fully exchanges before refolding. This gives rise to correlated exchange and two distinct populations corresponding to unexchanged and fully exchanged species, producing a characteristic bimodal pattern. Adapted from Weis *et al.* [143].

In contrast, EX1 exchange occurs when the closing rate is slower than chemical exchange ($k_{closed} \ll k_{\mathrm{int}}$). Here the region unfolds, exchanges completely and then

refolds before the next opening event. This produces a bimodal isotope pattern with one population corresponding to unexchanged, folded molecules and another to fully exchanged, refolded species. Over time, the high-m/z peak increases as more molecules undergo complete exchange. Quantifying these populations provides a measure of the conformational transition rate. EX1 behaviour often reflects cooperative structural rearrangements, such as helix or domain unfolding and can reveal functionally relevant motions [143–145].

Intrinsic exchange rates also vary according to amino acid type and local sequence. Each residue has its own k_{int}, primarily determined by the preceding residue and, to a lesser extent, the following one [146, 147]. These effects arise from inductive and hydrogen-bonding influences on the amide's acidity and basicity. Proline is non-exchangeable because it lacks a backbone amide hydrogen, while N-terminal residues exchange too rapidly to be treated by the same model.

The ratio of the intrinsic rate to the experimentally observed rate gives the protection factor, which quantifies how much structure or hydrogen bonding slows exchange:

$$P(i) = \frac{k_{\mathrm{int}}(i)}{k_{\mathrm{obs}}(i)} \tag{2.5}$$

Typical P values range from approximately 1 for disordered or solvent-exposed regions to 10^3–10^6 for highly protected helices or sheets. The corresponding equilibrium free energy for opening can then be calculated, assuming EX2 kinetics:

$$\Delta G_{\mathrm{op}}(i) = RT \ln P(i) = -RT \ln K_{\mathrm{op}}(i) \tag{2.6}$$

Relationship between the protection factor $P(i)$, the equilibrium constant for local opening $K_{\mathrm{op}}(i)$ and the corresponding free energy change $\Delta G_{\mathrm{op}}(i)$. Here, $\Delta G_{\mathrm{op}}(i)$ represents the Gibbs free energy change associated with transient exposure of site i to solvent ($\mathrm{J\,mol^{-1}}$); R is the universal gas constant (8.314 J $\mathrm{mol^{-1}}$ $\mathrm{K^{-1}}$); T is the absolute temperature (K); and $P(i)$ and $K_{\mathrm{op}}(i)$ are dimensionless. This relationship provides a quantitative link between exchange kinetics and local stability under native conditions.

2.6 Typical Workflow

Conventional HDX tends to follow a controlled workflow where the protein is prepared in a stable buffer, labelled in D_2O, quenched, digested under quench conditions, separated using LC-MS and finally subjected to data processing and statistical testing (Figure 2.8). Throughout, it is important to maintain pH and temperature conditions to minimise back exchange and carry over. The steps in a typical workflow are described in detail below:

2.6.1 Sample Preparation

Before exchange, the protein of interest is purified and buffer exchanged into a deuterium-compatible solution. In this work, proteins were stored in 20 mM Tris, 200 mM NaCl and 10 mM β-mercaptoethanol (BME) at pH 8. The slightly basic conditions maintain the solubility and stability of flavoproteins such as cryptochromes, preventing the acid-induced FAD loss that can lead to aggregation. The inclusion of NaCl provides moderate ionic strength to suppress non-specific protein–protein interactions, while BME keeps cysteines in their reduced state, minimising disulphide cross-linking and favouring a monomeric form. Samples are stored and handled in the dark to preserve the redox state of FAD. Immediately before labelling, the protein is diluted in the same buffer to a final concentration of approximately 15 μM, providing sufficient signal in the resulting spectra.

2.6.2 Labelling

To determine deuterium uptake, an initial control experiment is performed under identical conditions but without deuterium. The protein is first diluted in an equilibration buffer containing 5 mM KH_2PO_4 in H_2O at pH 7.0. Labelling is then initiated by diluting the sample into a deuterated buffer of the same composition prepared in D_2O at pD 7.0 (corresponding to pH 6.6), giving a final D_2O fraction of 92% to minimise back-exchange.

During labelling, solvent-accessible backbone amide hydrogens exchange with deuterium (Figure 2.9). Proline residues do not contribute to exchange since the

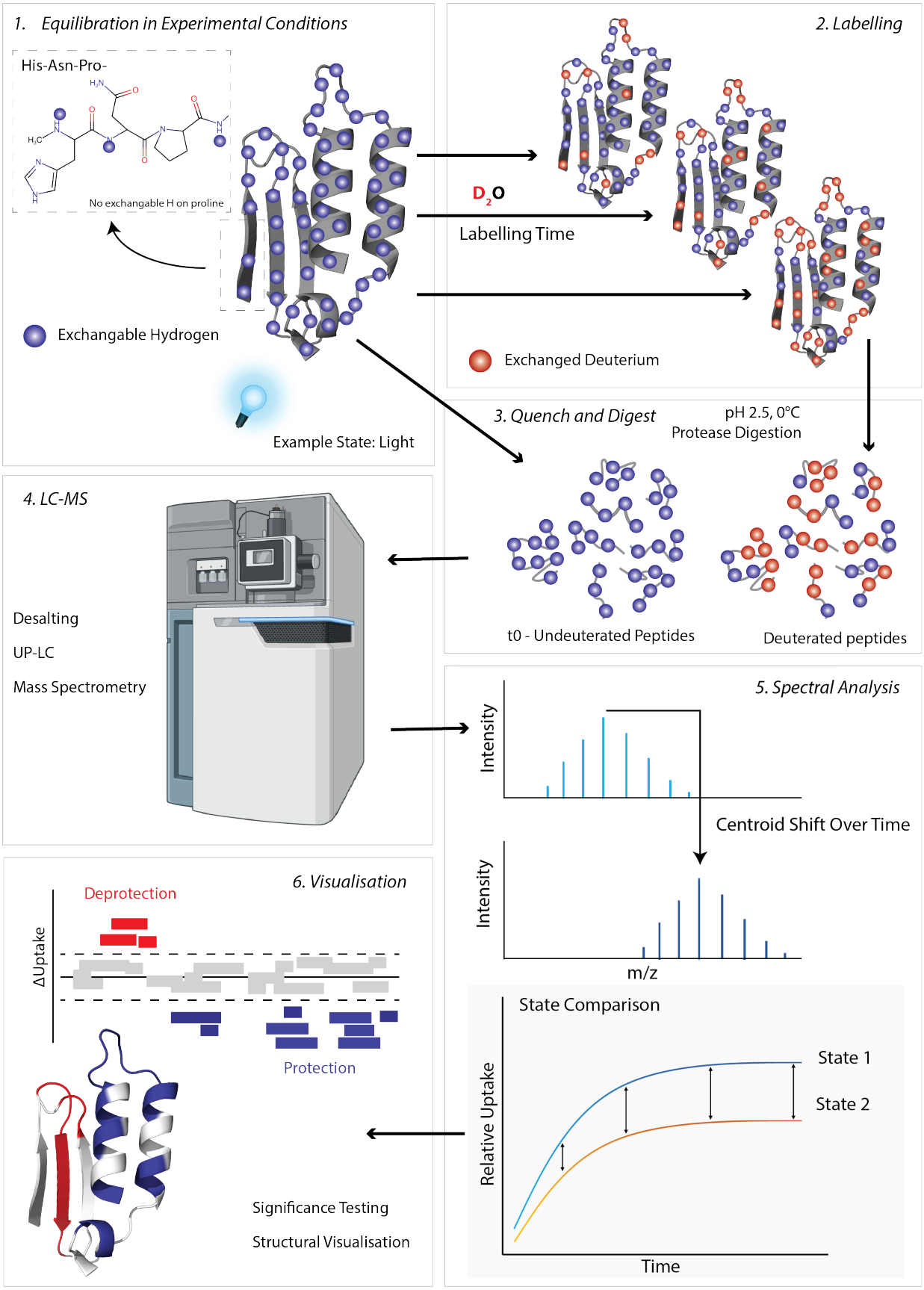


Figure 2.8: Proteins are incubated in D_2O, quenched, digested and analysed by LC–MS. Isotopic shifts reveal deuterium uptake, which can be plotted over time or mapped onto structures to show protected (blue) and deprotected (red) regions.

amide nitrogen is covalently bound within the pyrrolidine ring. As a result, the number and rate of exchangeable sites are dictated by protein structure, hydrogen bonding and solvent accessibility.

Back-exchange refers to the replacement of incorporated deuterium with hydrogen during labelling, quenching, digestion, or LC–MS analysis due to the presence of aqueous solvents [138, 144]. This process reduces the apparent mass increase and can make regions appear more protected than they are. Labelling reactions are carried out at multiple time points (15 s, 1 min, 5 min and 30 min) to generate uptake curves, with each time point acquired in quadruplicate to ensure sufficient reproducibility for statistical analysis.

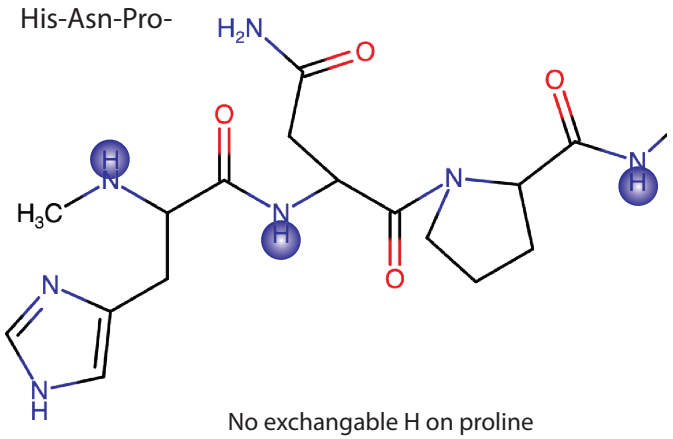


Figure 2.9: Example peptide (His–Asn–Pro) showing exchangeable backbone amide hydrogens (blue spheres). Proline does not contribute an exchangeable amide hydrogen because its backbone nitrogen is incorporated into the pyrrolidine ring and is bonded to carbon atoms rather than carrying an N-H proton. Only solvent-accessible amides contribute to measurable deuterium uptake.

2.6.3 Quenching the Exchange Reaction

Exchange is stopped by rapidly lowering both the pH and temperature through a 1:1 dilution with ice-cold 50 mM KH_2PO_4 in H_2O at pH 1.9 containing 1 M guanidinium chloride (GdnCl) at 0°C. This treatment reduces the pH to approximately 2, close to the minimum of the intrinsic HDX rate, while the temperature drop further suppresses exchange. The inclusion of GdnCl assists in partial unfolding of the protein, improving the efficiency of subsequent pepsin digestion.

2.6.4 Proteolytic Digestion

Following the quenching step, the proteins are digested under the same acidic conditions to generate peptides suitable for LC–MS analysis while minimising back-exchange. Pepsin is most often used for this purpose as it remains active at pH 2–3 and tolerates low temperatures. Unlike enzymes such as trypsin that recognise specific residues (Lys/Arg), pepsin has broad substrate specificity and cleaves adjacent to bulky hydrophobic residues including Phe, Leu, Tyr and Trp. Therefore, it produces a dense mixture of overlapping peptides typically 5–25 amino acids in length rather than a single predictable set. The high redundancy of these peptides improves spatial resolution in HDX mapping.

To reduce back-exchange and enhance reproducibility, pepsin is commonly immobilised on a column and incorporated online before the trap column. In this work, digestion was initially performed using a Waters Enzymate column but later switched to a home-packed column prepared following Rand Group protocols to improve sequence coverage [148]. Other acid-stable proteases such as aspergillopepsin, rhizopuspepsin and nepenthesin can be used individually or alongside pepsin to complement its cleavage preferences and extend coverage into regions under-represented in peptic fragments.

Online digestion was carried out for two minutes on the Synapt G2-Si and three minutes on the Select Series Cyclic IMS to generate a high number of peptides while limiting back-exchange. Blank injections were run between samples to monitor carry-over, ensuring that any apparent EX1 kinetics did not arise from residual peptides. Successful digestion yields a reproducible peptide map with extensive overlap and high sequence coverage across the protein.

2.6.5 Desalting and Separation

After proteolysis, peptides are separated by liquid chromatography under cooled conditions to minimise back-exchange. The chromatographic flow path, including the trap and analytical columns, is maintained at low temperature throughout the run. Peptides are first loaded onto a short trap column for desalting, then

eluted onto an analytical column using a gradient between solvent A (H_2O with 0.1% formic acid) and solvent B (acetonitrile with 0.1% formic acid). This gradient separates peptides according to their hydrophobicity and chain length, producing narrow, well-resolved peaks suitable for downstream MS analysis.

2.6.6 Mass Spectrometric Analysis

Spectra are acquired in positive ion mode with source conditions tuned for gentle transmission. A lock-mass reference is sampled every 30 seconds to maintain mass accuracy across runs and replicates. Peptides are ionised by ESI to generate multiply charged ions that are transmitted through the instrument as described earlier in this chapter.

Both the Synapt G2-Si and the Select Series Cyclic instruments include ion-mobility capability. On the G2-Si, ions first pass through a helium cell for collisional cooling, then through a nitrogen TWIMS cell. The drift time, or the time taken for an ion to pass through the cell, depends on its size, shape and charge, providing an additional dimension of separation that helps resolve co-eluting peptides. In the Cyclic, ions are injected into a circular travelling-wave mobility cell and can be directed through the cell multiple times to enhance resolution. Increasing the number of passes improves the separation of closely related conformers. Although this capability can assist deconvolution of overlapping peptides, it was not used in these datasets as chromatographic separation was sufficient.

Undeuterated runs are acquired with fragmentation to obtain MS^E data for peptide identification and sequence assignment. The resulting identifications and retention times are then used to map deuterated peptides. Labelling experiments are performed without fragmentation to prevent H/D scrambling.

2.6.7 Data Processing and Uptake Calculation

Undeuterated peptides from the MS^E runs were identified using ProteinLynx Global Server (PLGS, Waters). PLGS detects peptides by correlating low-energy precursor and elevated-energy fragment data to reconstruct product-ion spectra based on

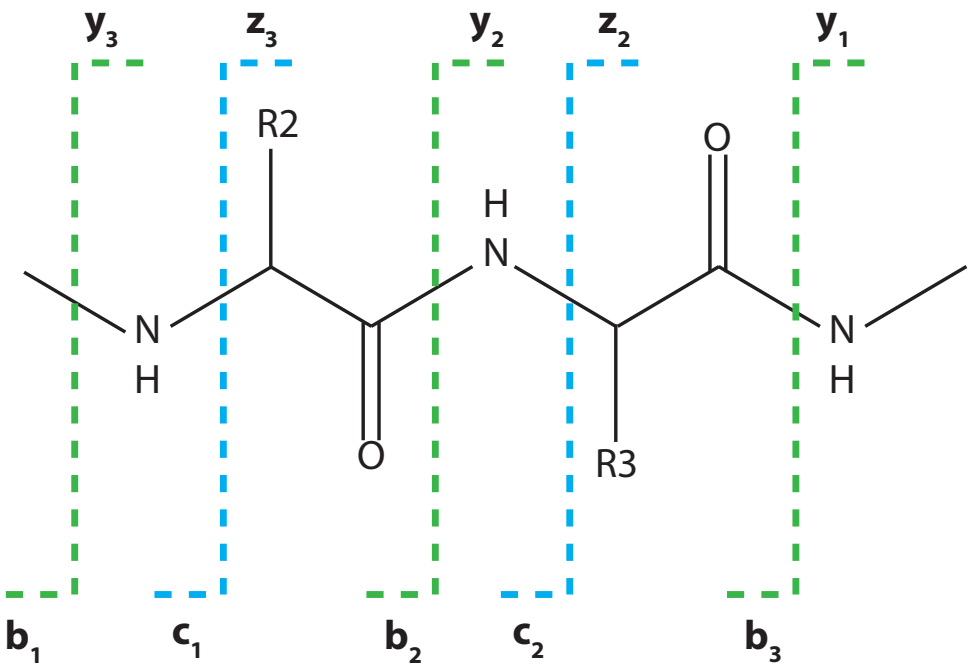


Figure 2.10: Schematic representation of backbone fragmentation in MS/MS. CID and HCD produce b and y ions through cleavage of the amide bond, whereas ECD and ETD generate c and z ions via cleavage of the N–C_α bond.

chromatographic co-elution [149]. The resulting fragment ions are matched to theoretical b/y ions from an *in silico* digest of the supplied FASTA sequence using the Ion Accounting algorithm. Peptides are scored according to the proportion of observed fragment intensity explained by theoretical ions within a user-defined mass tolerance, generating a list of confidently identified sequences with associated charge states, masses and retention times. These data form the input for deuterium uptake analysis.

Deuterium incorporation was quantified using DynamX 3.0 (Waters), which extracts isotopic envelopes for each identified peptide and charge state. The centroid mass of each envelope is calculated across the labelling time course to yield the mean mass shift relative to the undeuterated reference [79, 137]. Replicate data are combined to generate mean uptake values and standard deviations for each peptide at each time point. DynamX automatically aligns chromatographic retention times

between replicates, filters data according to signal intensity and retention-time deviation and corrects for global back-exchange where required.

Processed data were subsequently imported into Deuteros 2.0 for statistical comparison and visualisation [150]. Deuteros performs pairwise testing between experimental conditions (for example, light vs dark or wild-type vs mutant) using Welch's two-sample t-test at each peptide and time point. Welch's test does not require equal variances between groups, making it suitable for HDX measurements where replicate variability may differ [151]. The null hypothesis states that the mean deuterium uptake of a peptide under two conditions is equal; a low p-value indicates a statistically significant difference in uptake between conditions. Significance is typically assessed at $p < 0.01$ or $p < 0.05$ and peptides passing this threshold are highlighted in Woods or volcano plots to visualise regions of differential exchange.

Woods plots display per-peptide differences in deuterium uptake along the sequence, whereas volcano plots combine effect size (uptake difference) and significance ($-\log_{10}(p)$) to highlight regions of interest. Deuteros also calculates confidence intervals for mean uptake using standard error propagation from replicate centroid masses [79, 150]. This framework provides a rigorous statistical approach for distinguishing genuine structural perturbations from random variability in the HDX measurements. The resulting datasets can then be mapped onto structural models to interpret local flexibility and conformational changes, as detailed in later chapters.

2.6.8 Scrambling and ECD Fragmentation

In HDX–MS, scrambling refers to the gas-phase redistribution of labile hydrogens and deuteriums during or before fragmentation [152, 153]. When this occurs, the spectra no longer reflect the true solution-phase deuterium uptake, giving a misleading impression of local exchange. Under CID or HCD conditions, ions gain vibrational energy that promotes intramolecular proton transfer along the backbone and side chains, disrupting site-specific labelling of deuterated amides. The resulting b/y fragments therefore display a scrambled deuterium pattern. The extent of scrambling increases under harsher source conditions such as higher temperatures,

elevated cone voltages, longer trapping times, or stronger collisional activation, all of which raise internal vibrational energy.

To minimise scrambling, electron-based fragmentation methods such as ECD and electron transfer dissociation ETD are used [154]. These techniques induce fast backbone cleavage that generates c/z ions before hydrogen migration can occur, preserving the original solution-phase labelling pattern. The resulting c and z ions report deuterium uptake at successive residues, allowing near–amino-acid resolution when differences between adjacent fragments are compared [98, 152]. In ECD, a multiply charged peptide or protein ion captures a low-energy electron to form a radical cation which then cleaves at the N–C_α bond:

$$[\mathrm{M}{+}n\mathrm{H}]^{n+} + e^- \;\rightarrow\; [\mathrm{M}{+}n\mathrm{H}]^{(n-1)+\bullet} \xrightarrow{\text{fast}} c_n \;+\; z^{\bullet}_{N-n} \tag{2.7}$$

Here, n is the precursor charge and N the sequence length; c_n and $z^{\bullet}_{N-n}$ are the complementary backbone fragments produced by N–C_α bond cleavage. Comparative studies have shown that ECD and ETD preserve site specificity and reduce scrambling far more effectively than CID or HCD, providing more accurate localisation of exchange sites [98, 152]. In practice, ECD HDX–MS/MS targets selected peptides under gentle conditions to produce c and z ions suitable for residue-level mapping of deuterium uptake.

2.6.9 Alternate Workflow: Pulsed Labelling

Pulsed-labelling HDX experiments provide a complementary means of probing conformational dynamics by decoupling structural exchange from the duration of solvent exposure. Unlike continuous labelling, where uptake is monitored over a series of time points to produce kinetic curves that can reveal EX1 or EX2 exchange regimes, pulsed labelling fixes the exchange window and instead varies the conformational state of the protein prior to the pulse (Figure 2.11)[131, 145].

In practice, the protein is equilibrated under defined conditions, such as under blue light or in darkness for specific durations to establish distinct conformational populations. Each sample is then exposed to deuterated buffer for a single, identical

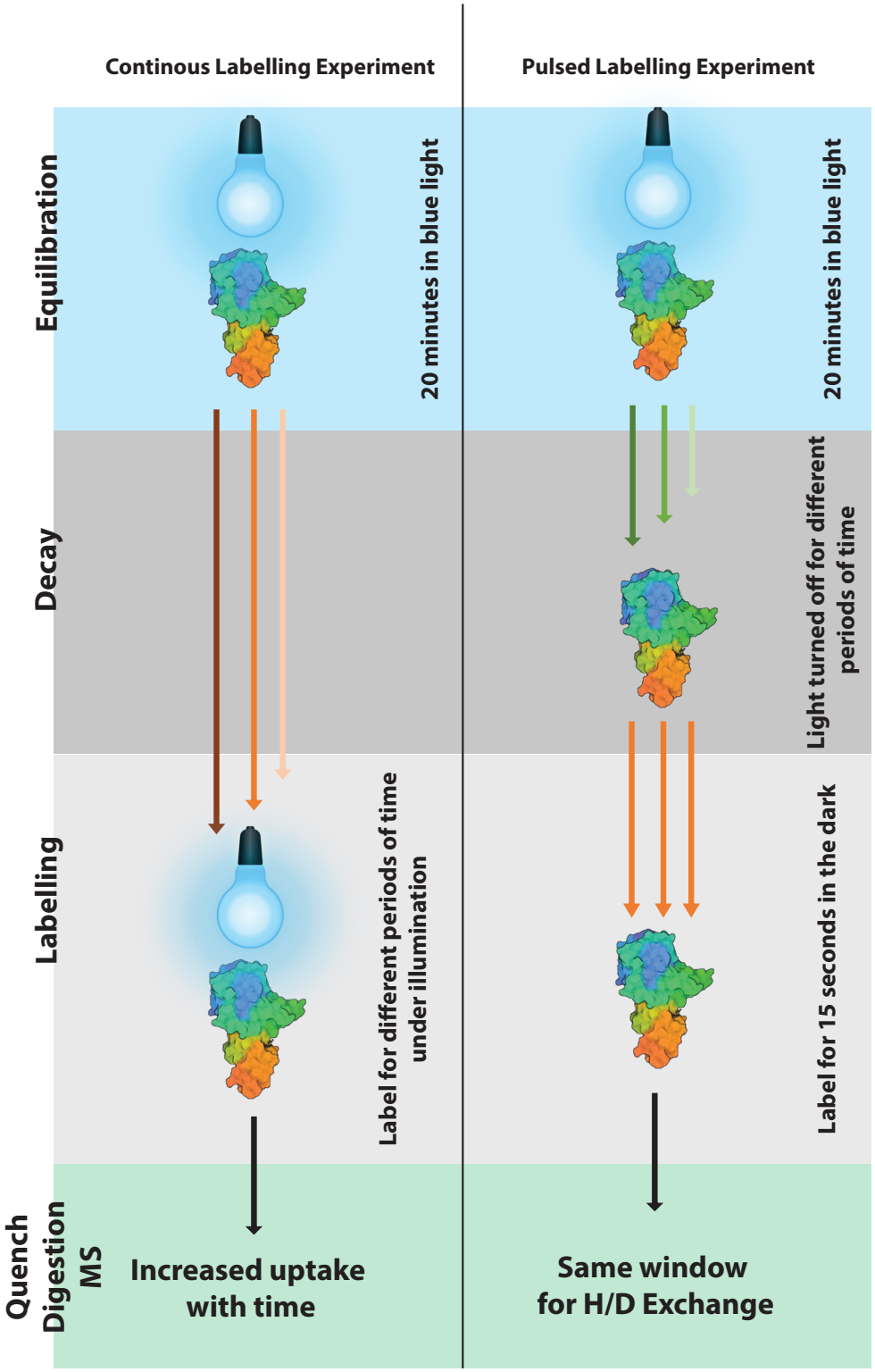


Figure 2.11: Comparison of continuous (left) and pulsed (right) labelling HDX workflows. In the continuous approach, proteins are labelled for increasing durations under a single condition (for example, sustained illumination), yielding time-dependent uptake curves that report on protection and conformational dynamics. In the pulsed approach, samples are first equilibrated under different conditions (for example, varying dark recovery times), then subjected to a single, identical deuterium pulse of fixed duration. Differences in uptake therefore reflect the conformational ensemble at the moment of labelling rather than cumulative exchange time.

pulse under constant D_2O fraction, pD and temperature, followed immediately by quenching. As all samples share the same labelling duration, any difference in deuterium uptake reflects the fraction of exchange-competent states present at the time of the pulse rather than changes in intrinsic exchange kinetics [144].

Pulse durations are typically chosen to be short enough to minimise back-exchange and prevent large-scale unfolding while still providing measurable uptake, generally on the order of seconds to minutes [79, 145]. This approach is particularly suited to capturing transient or light-induced structural rearrangements, where conformational changes occur faster than the time resolution of traditional continuous HDX. In this work, the pulsed-labelling design was used to compare structural states of cryptochromes immediately after photoactivation, offering a snapshot of early dynamic intermediates that would otherwise be averaged out in a conventional time-course experiment.

2.6.10 Limitations

Although HDX–MS is a powerful technique for probing protein structure and dynamics, several caveats must be considered, particularly when it is applied to complex or heterogeneous systems.

Conventional HDX workflows provide information at the peptide level rather than at individual amino acids. As described in the workflow section, pepsin and other acid-stable proteases typically generate peptides of 5–25 residues, meaning that uptake is averaged across all amides within a peptide. Consequently, localised changes in flexibility or solvent exposure can be masked if only a small subset of residues within a peptide undergo significant exchange. Overlapping peptides can help to refine these regions, but high redundancy is not always achieved. Fragmentation-based methods such as ECD or ETD can resolve deuterium uptake to individual amides, though these experiments are technically demanding and usually applied to selected peptides only [98, 143].

A major challenge in HDX experiments is back-exchange involving the loss of incorporated deuterium during quenching, digestion, chromatography, or ionisation

due to exposure to H_2O-based solvents. Back-exchange reduces the apparent mass shift and therefore underestimates the true extent of uptake [137]. While careful control of pH, temperature and timing can minimise this effect, it cannot be eliminated entirely. For this reason, HDX studies often use differential approaches in which two or more states are compared directly. Provided back-exchange is consistent between conditions, relative uptake differences remain meaningful even if absolute deuteration levels are underestimated.

HDX–MS reports on ensemble-averaged behaviour rather than on single structural states. Each uptake curve represents the weighted contribution of all conformations present in solution. When multiple states coexist or interconvert on comparable timescales, the observed kinetics reflect a mixture of exchange rates rather than a single defined process [131]. This averaging can obscure rare or transient intermediates, which may only become apparent using specialised designs such as pulsed labelling or global fitting of kinetic models. Similarly, proteins undergoing large conformational rearrangements can display composite uptake curves that represent overlapping structural transitions rather than a discrete unfolding event.

Experimental conditions have a pronounced influence on exchange behaviour. Parameters such as pH, temperature and buffer composition directly affect the intrinsic chemical exchange rate (k_{ch}). For instance, increasing temperature accelerates exchange, whereas salts, cofactors, or reducing agents can alter protein stability and hence solvent accessibility [79]. Even small deviations can lead to measurable differences in apparent protection. It is therefore essential to maintain tightly controlled conditions and to treat comparisons between independent datasets with caution. This is particularly relevant for photoreceptors such as cryptochromes, where buffer composition not only affects global stability but can also influence the redox state of the FAD cofactor.

Finally, HDX–MS remains a low-throughput and experimentally sensitive technique. Reproducibility can be affected by subtle differences in digestion efficiency, peptide carry-over, or chromatographic performance. To distinguish genuine

structural differences from noise or artefacts, experiments should include multiple replicates, blank injections and robust statistical analysis [140]. Each stage of the workflow requires careful optimisation and reliable interpretation depends on consistent experimental control and critical evaluation of the resulting data.

2.7 Summary

Both native MS and HDX–MS have been central to the experimental work described in this thesis. Native MS provided key information on FAD binding, oligomeric state, interaction partners and sample integrity following extended HDX experiments. HDX–MS, in turn, revealed the conformational dynamics underlying cryptochrome function. By combining conventional HDX–MS with pulsed-labelling experiments and ECD fragmentation, it was possible to resolve structural changes with improved temporal and spatial precision, offering deeper insight into how cryptochromes respond to light and other perturbations. The results of these analyses are presented in Chapters 4.9.4 and 5.7.4.

"Flowers are restful to look at.
They have neither emotions nor conflicts."

— Sigmund Freud via Olav Johannessen

3

HDX as a Tool for Elucidating Conformational Changes

Contents

3.1 Abstract 53
3.2 Plant Cysteine Oxidase (PCO4) 54
3.3 Rationale for Using HDX-MS 56
3.4 Experimental Design 58
3.5 Results 59
3.5.1 Visualising HDX Data 59
3.5.2 Coverage and Dynamics 60
3.5.3 Differential HDX 64
3.6 Discussion and Conclusions 71
3.7 Materials and Methods 71
3.7.1 Synthesis of Peptidomimetics 71
3.7.2 In Vitro Activity Assays 72
3.7.3 HDX-MS 73

3.1 Abstract

This chapter introduces HDX–MS as a structural tool for investigating protein conformational dynamics, using *Arabidopsis thaliana* Plant Cysteine Oxidase 4 (PCO4) as a model system. PCOs catalyse oxygen-dependent oxidation of N-terminal cysteine residues on group VII ethylene response factors (ERF-VIIs), acting

as biochemical oxygen sensors in plants. Although crystal structures have revealed the core architecture of PCOs, they provide only static snapshots of a protein family whose catalytic function depends on dynamic flexibility, particularly within surface loops surrounding the substrate channel. To address this, HDX–MS was applied to determine whether substrate-like peptidomimetics can induce conformational rearrangements that correlate with the enhanced catalytic activity observed in biochemical assays.

The study, published in the *Journal of Biological Chemistry*, demonstrates that binding of a substrate-mimicking peptide promotes protection of a flexible hairpin loop adjacent to the active site and concurrent deprotection of neighbouring regions associated with the putative oxygen-entry tunnel [155]. These opposing changes indicate a concerted rearrangement consistent with ligand-induced priming of the enzyme, in which stabilisation of the substrate-binding loop is coupled to increased accessibility for oxygen diffusion. Additional protection at distal, partially disordered segments suggests subsequent global ordering of the enzyme following initial peptide engagement.

Beyond providing a detailed mechanism for activity enhancement in PCO4, this work establishes HDX–MS as a powerful approach for detecting subtle, functionally relevant motions in solution that are inaccessible to crystallography. The methodological framework developed here underpins the more complex applications of HDX–MS presented in later chapters, where it is used to interrogate light-dependent structural dynamics in avian cryptochromes.

3.2 Plant Cysteine Oxidase (PCO4)

Oxygen availability is a fundamental constraint on biological systems and organisms have evolved specialised mechanisms to sense and respond to fluctuations in oxygen concentration. In plants, oxygen levels vary with environmental stresses such as flooding and during developmental processes including seed germination and growth. Restricted gas diffusion within tissues generates localised hypoxic regions and adaptation to altered oxygen availability occurs primarily at the transcriptional

level through the action of oxygen-responsive transcription factors [156, 157]. In *Arabidopsis thaliana*, these are classified as group VII Ethylene Response Factors (ERF-VIIs), which induce expression of genes required for metabolic adjustment to hypoxia, including those involved in glycolysis and fermentative ATP production [158, 159].

When oxygen is abundant, the N-terminal cysteine of ERF-VIIs is oxidised to cysteine-sulphinic acid. This modification enables subsequent arginylation by arginyltransferases, ubiquitination by the E3 ligase PRT6 and degradation of the transcription factor via the proteasome [160–162]. The oxidation reaction is catalysed by the Plant Cysteine Oxidases (PCOs), which couple their enzymatic activity directly to molecular oxygen and thus function as biochemical oxygen sensors. Through this mechanism, PCOs ensure that hypoxia signalling is rapidly down-regulated when oxygen levels recover [163, 164].

PCOs are non-haem iron-dependent thiol dioxygenases belonging to the cupin superfamily. Structural studies of Arabidopsis isoforms PCO2, PCO4 and PCO5 have revealed a conserved jelly-roll β-barrel fold with an Fe(II) ion coordinated by a facial triad of histidines at the active site [165, 166]. This architecture resembles that of mammalian thiol dioxygenases such as cysteamine dioxygenase, but includes adaptations that allow recognition of protein substrates rather than small molecules [167]. Despite these structural insights, the mechanisms underlying substrate specificity and the influence of peptide binding on enzyme flexibility remain poorly defined. Notably, PCO catalytic activity is enhanced by preincubation with substrate peptides or synthetic analogues, suggesting that ligand binding may stabilise specific conformational states and modulate turnover.

Beyond their enzymatic role, PCOs have attracted increasing interest due to their relevance to plant stress tolerance. Flooding, which produces hypoxic soil conditions, is predicted to become more frequent and severe under climate change. Modulating PCO activity has therefore been proposed as a strategy to pre-adapt crops for submergence tolerance by stabilising ERF-VII transcription factors and sustaining hypoxia-responsive gene expression [168, 169]. Both genetic and chemical approaches

to modify PCO function are under investigation with the goal of improving crop resilience and food security [170, 171]. Understanding how PCOs recognise and respond to substrates is thus of both mechanistic and agricultural importance.

These considerations establish PCO4 as a suitable model for probing the relationship between structure, flexibility and activity. From an experimental perspective, PCO4 is a soluble, well-characterised enzyme with high-resolution structural data available (Figure 3.1), providing an ideal foundation for examining how substrate-like binding events influence protein dynamics [165].

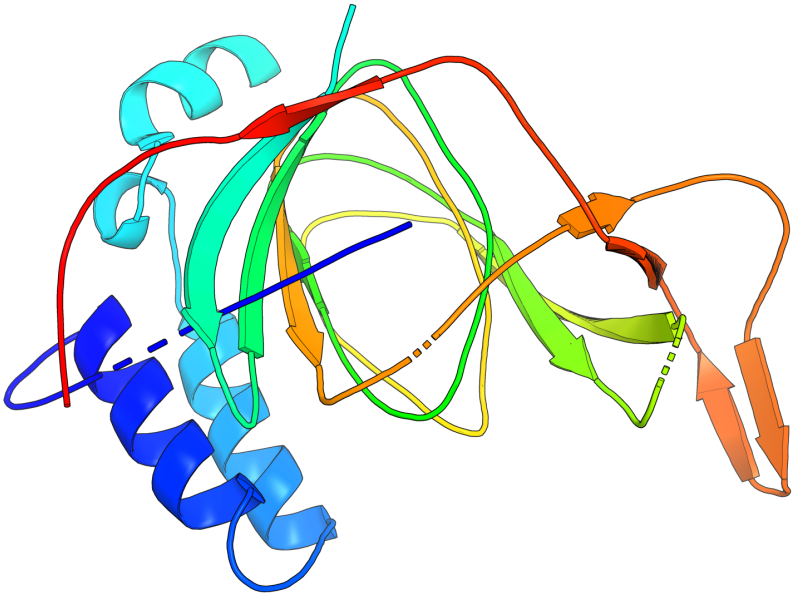


Figure 3.1: Crystal structure of *At*PCO4 (PDB 6S7E) [165].

3.3 Rationale for Using HDX-MS

Understanding how enzymes respond structurally to ligand binding requires methods that can probe both conformational dynamics and static structure. For PCOs, crystallographic studies have elucidated their overall fold and active site organisation

[165, 166]. However, these studies capture only a single conformational state. Flexible surface loops and other dynamic regions of PCOs are often unresolved in crystal structures, making their structure and function harder to understand. These unresolved regions are hypothesised to contribute significantly to substrate recognition and regulation of enzymatic activity. Therefore, additional techniques are needed to investigate protein motions and conformational changes in solution.

HDX-MS is particularly well-suited to this problem since it can be used to study the dynamics of proteins. In brief, the method monitors the exchange of labile backbone amide hydrogens with deuterium when a protein is exposed to D_2O-containing buffer. The rate of exchange reflects local structural dynamics, as it depends on both solvent accessibility and the stability of hydrogen bonding within secondary structure elements [78]. Regions that become more solvent-exposed or dynamic exchange more rapidly, while regions that are buried or structurally protected exchange more slowly. By comparing deuterium uptake patterns under different conditions, HDX-MS can identify localised conformational changes across a protein.

The central mechanistic question addressed in this study was whether substrate-like peptidomimetics could induce a conformational shift in PCO4, thereby priming the enzyme for enhanced activity. This hypothesis arose from biochemical observations showing that preincubation with such peptides unexpectedly increased catalytic turnover rather than inhibiting it. Crystallographic studies have been unable to resolve whether substrate binding leads to structural priming, as all available PCO structures represent ligand-free forms. Alternative techniques such as NMR, although powerful for studying dynamics, are impractical for a protein of this size without isotope labelling and would not permit systematic comparison across multiple binding conditions.

Continuous HDX–MS was therefore employed to characterise conformational changes in solution under near-native conditions. Its sensitivity to dynamic and partially disordered regions makes it particularly suited to probing flexible elements such as the hairpin loop spanning residues 182–190 in *Arabidopsis thaliana* PCO4

(*At*PCO4), which is predicted to contribute to substrate recognition and specificity [166, 167]. Docking studies place this loop near the substrate channel, suggesting that ligand binding may alter its conformation. By monitoring time-dependent deuterium uptake, HDX–MS enabled detection of subtle loop rearrangements and provided a structural framework to interpret the observed kinetic enhancement following peptide preincubation.

As well as investigating the mechanism of PCO4 activation, this study also establishes HDX–MS as a practical workflow for investigating conformational dynamics in solution, an approach subsequently extended to the light-dependent behaviour of avian cryptochromes in later chapters.

3.4 Experimental Design

Full experimental details are provided in the Materials and Methods section at the end of this chapter, but as this chapter serves as an introduction, the workflow will be described in brief within this section.

Recombinant *At*PCO4 was expressed and purified in *E. coli* by Dr Rebecca Latter (see Materials and Methods for details). This experiment compared the conformational behaviour of *At*PCO4 in the presence and absence of a peptidomimetic analogue of the ERF-VII N-terminal sequence. Peptidomimetic 9 (Pep9) was previously shown to induce near-maximal activity enhancement in biochemical assays and was therefore selected for investigation. *At*PCO4 was preincubated with the peptidomimetic at a 1:1000 molar ratio (enzyme to peptide) for 6 min before labelling. Preincubation was necessary because enzymatic assays indicated that activity enhancement depended on a period of substrate or analogue binding prior to catalysis. Control experiments lacking peptidomimetic were conducted under identical conditions to allow for comparative analysis to identify regions of change. The experiment followed a conventional HDX workflow as described in Chapter 2.7. To capture long-lived structural dynamics, the protein was labelled for 15 s, 1 min, 5 min, 30 min and 60 min timepoints. This range of timepoints

was chosen to encompass the expected exchange kinetics of both flexible loops (fast-exchanging) and more protected secondary structure elements (slow-exchanging). Each timepoint was performed in triplicate to ensure reproducibility.

3.5 Results

3.5.1 Visualising HDX Data

Peptide assignment in DynamX involves matching deuterated spectra to identified undeuterated peptide sequences based on retention time, charge state and mass accuracy. After preliminary assignments, the user manually curates the dataset to ensure the correct isotope distributions have been selected. This curation prevents artefacts from overlapping isotopic envelopes, poorly resolved spectra or incorrect charge state assignments. Peptides exhibiting ambiguous or overlapping spectral features, particularly where multiple overlapping peptides give conflicting uptake profiles, were excluded to maintain data quality. This approach ensures that only high-confidence peptides are used in subsequent uptake calculations and statistical comparisons.

Before presenting the detailed results, it is useful to outline how HDX-MS data is typically displayed and interpreted. Exchange kinetics are monitored at the peptide level, with uptake curves showing the increase in relative deuterium incorporation over time. When comparing two conditions, differences in uptake are often summarised as ΔRFU (difference in relative fractional uptake between states). To calculate the RFU, the uptake value (in Daltons) of the corresponding peptide is divided by the theoretical maximum uptake for that peptide, defined as the number of exchangeable backbone amide hydrogens, excluding the N-terminal amine and proline residues. This normalisation allows uptake values to be compared across peptides of different lengths and sequences.

$$\text{RFU} = \frac{\text{Uptake (Da)}}{\text{Maximum uptake (Da)}} \tag{3.1}$$

where RFU denotes the relative fractional uptake.

$$\Delta\text{RFU} = \text{RFU}_{\text{state 1}} - \text{RFU}_{\text{state 2}} \tag{3.2}$$

These datasets can be visualised in several complementary ways. Throughout this chapter, blue shading indicates regions that take up less deuterium and are therefore more protected, often corresponding to more stable secondary structure or stronger hydrogen bonding. In contrast, red denotes areas that exchange more readily and are consequently more flexible or solvent-exposed. Differential heatmaps provide a rapid overview of uptake behaviour across the protein and at different time points, highlighting broad regions of protection or deprotection. To assess statistical significance, ΔRFU values can be displayed in volcano or Woods plots, which emphasise peptides showing meaningful structural change. Finally, mapping these differences onto crystal structures or AlphaFold models places the observed dynamics in a spatial context, linking local fluctuations in deuterium uptake to specific structural elements within *At*PCO4.

3.5.2 Coverage and Dynamics

Figure 3.2 shows a coverage map obtained after the spectra were manually curated in DynamX. The results led to the successful identification of 55 peptides, spanning 97.5% of the protein with an average redundancy of 3.04. This indicates that each residue was, on average, covered by three independent peptides. This high level of redundancy provides robustness to subsequent analyses and helps mitigate ambiguity caused by localised inconsistencies in peptide behaviour. At this stage, it is important to consider whether regions of interest in the protein are sufficiently covered by the peptides obtained. If this is not the case, coverage may be optimised by using an alternative quench or a different or complementary protease.

PCO4 heatmaps demonstrate that the protein contains distinct regions with markedly different exchange profiles (Figure 3.3). Overall, the deuterium uptake pattern aligns with expectations for a folded globular protein: the termini and loop regions undergo rapid exchange, whereas structured domains such as α helices and β sheets remain strongly protected. This contrast is reflected in the red colouring

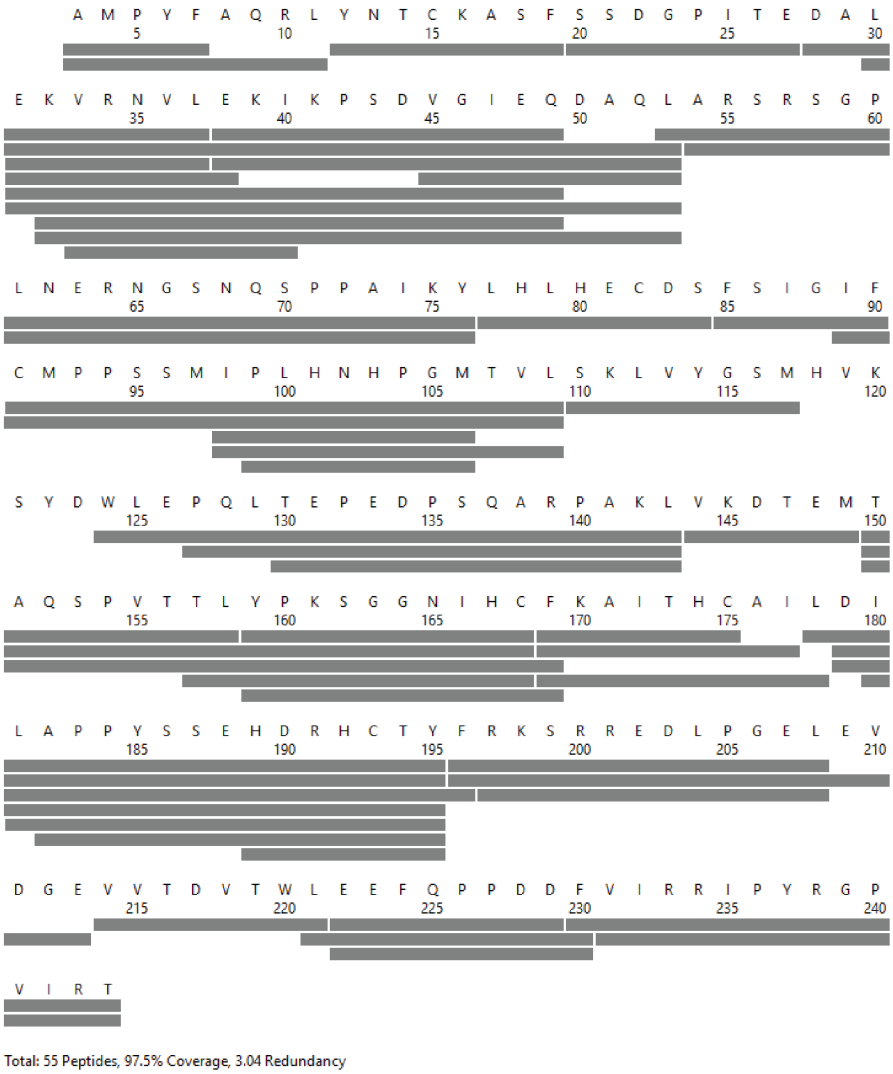


Figure 3.2: Coverage map of *At*PCO4. Grey bars indicate correctly identified peptides along the amino acid sequence. Plot generated in DynamX 3.0.

at the N- and C-terminal ends and in regions corresponding to surface loops, while the protein core is generally pale, indicative of limited deuterium incorporation even after prolonged labelling times.

Prominent dynamic regions include the first ∼10 residues at the N-terminus and the final C-terminal segment beyond residue 230. Both show high uptake at all timepoints, consistent with an unstructured region or conformational mobility. Several internal loop elements are also highly exchange-prone, notably residues 55–70 and 125–133, as well as a highly dynamic segment between residues 20–30. These loops incorporate deuterium rapidly from the earliest timepoints and remain

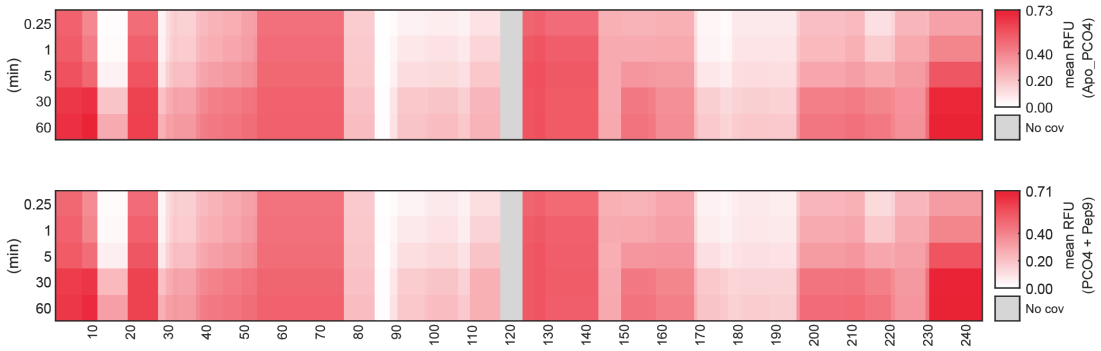


Figure 3.3: Barcode plot showing RFU across *At*PCO4 alone (top) and in the presence of Pep9 (bottom). A white-to-red colour scale indicates the extent of deuterium uptake over time, with red corresponding to higher uptake. Grey regions denote areas without peptide coverage.

strongly labelled throughout the experiment. Importantly, the 55–70 and 126–133 segments coincide with regions that are absent in the crystal structure, reinforcing the view that missing density reflects genuine flexibility in solution rather than artefacts of crystallisation.

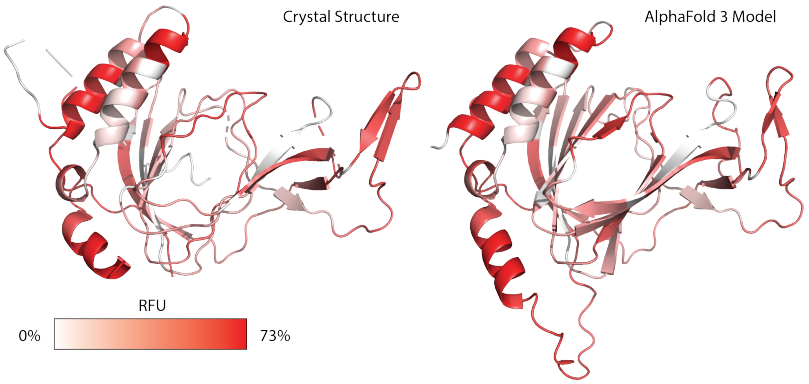


Figure 3.4: Heatmaps mapped onto the PCO4 crystal structure (left) and the AlphaFold3 model (right). The white-to-red colour scale represents RFU, with white indicating lower and red indicating higher levels of exchange.

Mapping the uptake data onto structural models provides a complementary perspective. In the crystal structure, protected regions are concentrated around the β-sheet barrel and associated helices, whereas poorly resolved loops correspond to highly dynamic segments in the HDX data. AlphaFold predictions allow visualisation

of these unresolved loops, confirming their high uptake. Figure 3.4 illustrates this at the one-hour timepoint, showing that uptake is concentrated in the termini and loops, while the core β-barrel remains largely protected.

In contrast, the most protected regions are consistently located in the structural core. Examples include residues 30–50, 75–100 and 170–200, which encompass α helices and β strands within the protein core. These elements exhibit only minimal uptake even after one hour, consistent with stable hydrogen bonding and restricted solvent accessibility. The preservation of these protected regions throughout the labelling window underlines the structural integrity of the PCO4 fold.

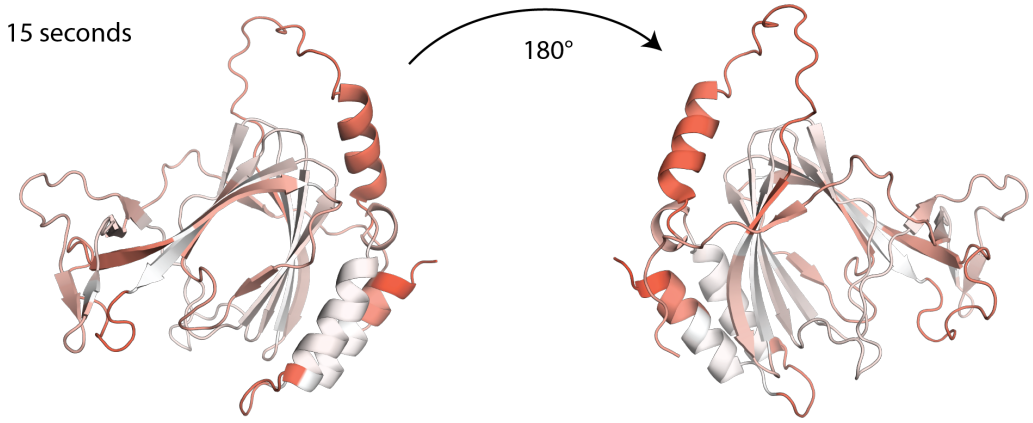


Figure 3.5: RFU values mapped onto *At*PCO4 at the 15-second timepoint. Figure reproduced from Latter *et al.*[155].

Timepoint-specific visualisations emphasise the kinetic aspects of exchange. At 15 seconds (Figure 3.5), the majority of the protein is still largely unlabelled, with the central β-sheet barrel remaining pale. The only strongly labelled regions at this stage are the termini, particularly the C-terminal tail, consistent with their intrinsic disorder.

By one hour (Figure 3.6), uptake has spread further into peripheral helices and loops, while the core β strands remain largely protected. Several loop elements adjacent to helices show higher uptake at this later stage, reflecting slower exchange in partially stabilised regions. Notably, the N-terminal α helix exhibits a gradient of uptake along its length: the base remains relatively protected, whereas the

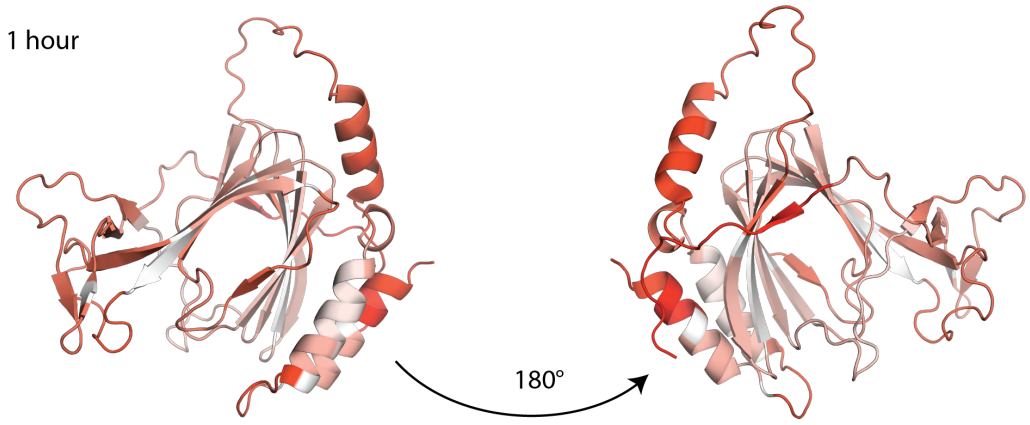


Figure 3.6: RFU values mapped onto *At*PCO4 the one-hour timepoint. Figure reproduced from Latter *et al.*[155].

tip shows increased incorporation, suggesting fraying or partial flexibility within an otherwise ordered helix.

Together, these data reveal a protein architecture in which a well-protected β-barrel core is flanked by dynamic termini and interspersed with flexible loops.

3.5.3 Differential HDX

The comparative HDX-MS analysis of *At*PCO4 with and without Pep9 reveals a reproducible and localised set of conformational differences. These changes are centralised around flexible loops adjacent to the substrate-binding channel and the proposed O_2-tunnel, suggesting that peptidomimetic binding alters the structural dynamics of *At*PCO4 in a way that primes the enzyme for enhanced catalytic turnover.

The initial overview is shown in Figures 3.7 and 3.9, which compares uptake profiles of *At*PCO4 in the presence and absence of Pep9 across all time points without any statistical testing. This analysis demonstrates that larger differences are confined to a small number of regions rather than distributed uniformly throughout the protein, showing localised effects of binding. Statistical analyses reveal four regions which are consistently altered: residues 51–72 and 176–193, which exhibit

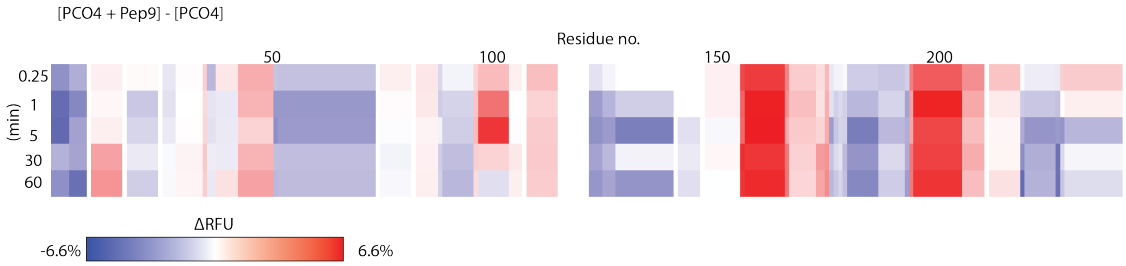


Figure 3.7: Differential heatmap ([PCO4 + Pep9] - [PCO4]) of *At*PCO4 across the amino acid sequence. Blue regions indicate increased protection upon addition of Pep9, whereas red regions indicate increased deprotection.

protection (negative ΔRFU) and residues 147–175 and 194–210, which become deprotected (positive ΔRFU) (Figure 3.8).

The 176–193 region is of particular interest as it encompasses the hairpin loop (residues 182–190), a flexible element near the substrate binding channel. Protection here could mean that binding of Pep9 restricts conformational flexibility in this region, shielding backbone amides from solvent exchange. This is in agreement with docking simulations reported, which positioned both RAP2.12-derived peptides and peptidomimetic 10 in the substrate channel with direct interactions in this region. Protection of residues 51–72 is also observed. Although this region is distant from the catalytic site, its reproducible reduction in uptake implies that peptidomimetic binding has allosteric consequences extending beyond the immediate channel. The functional role of this region is not yet clear, but its stabilisation remains a consistent feature of the dataset.

In contrast, the neighbouring loops spanning residues 147–175 and 194–210 display increased deuterium uptake in the presence of Pep9, indicating greater solvent accessibility and flexibility. The 147–175 segment contributes to the putative O_2 tunnel and its deprotection suggests enhanced dynamics that may facilitate oxygen entry into the buried active site. The 194–210 loop, located on the opposite side of the hairpin, shows a similar increase in exchange, consistent with a hinge-like motion in which stabilisation of the central hairpin is balanced by mobilisation of its adjacent loops.

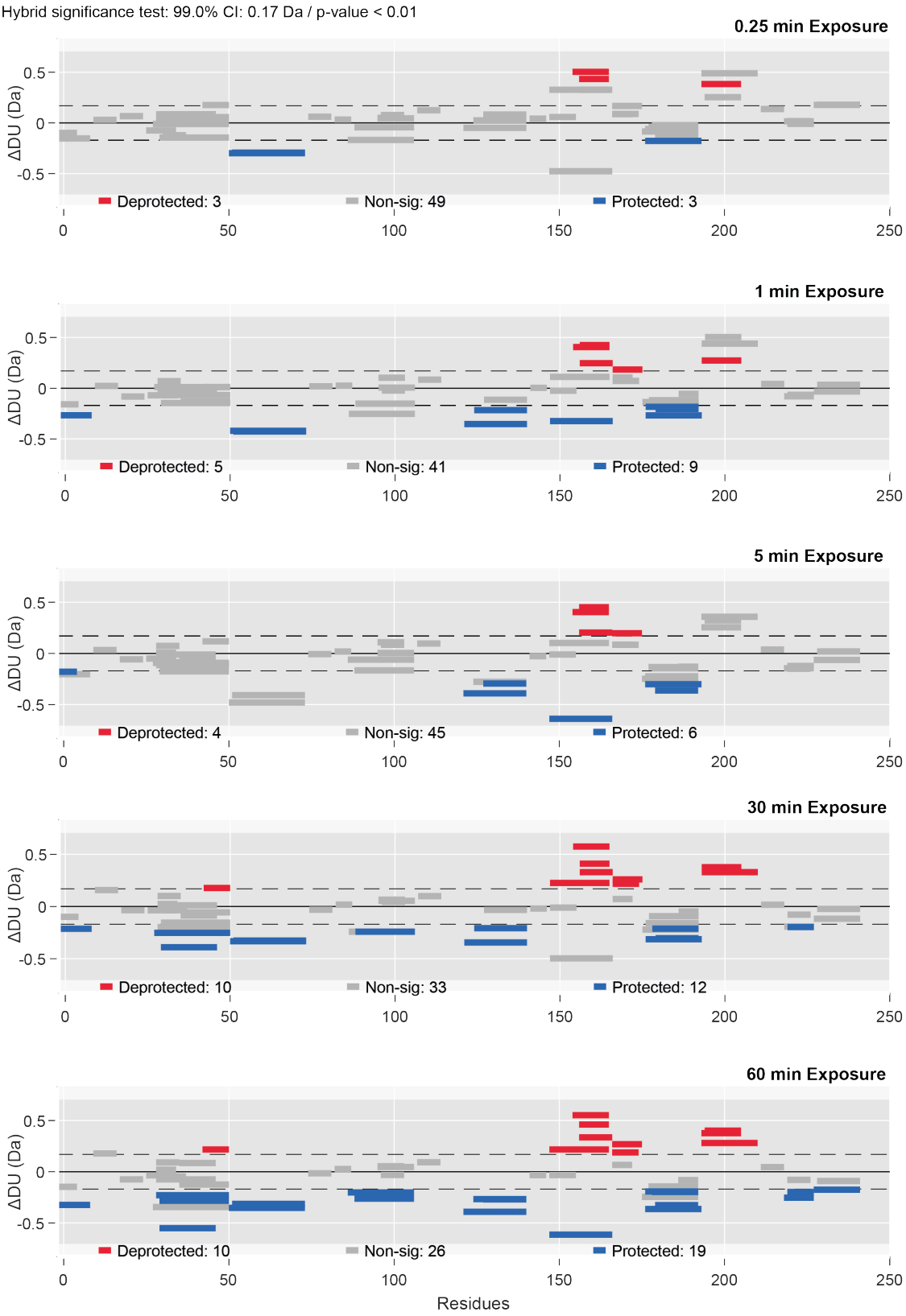


Figure 3.8: Peptides showing statistically significant changes upon addition of Pep9 to *At*PCO4 are displayed in Woods plots, from the earliest time point (15 seconds, top) to the latest (60 minutes, bottom). Blue indicates peptides that become protected in the presence of Pep9, red indicates peptides that are deprotected and grey denotes peptides that do not meet the significance threshold.Figure reproduced from Latter *et al.*[155].

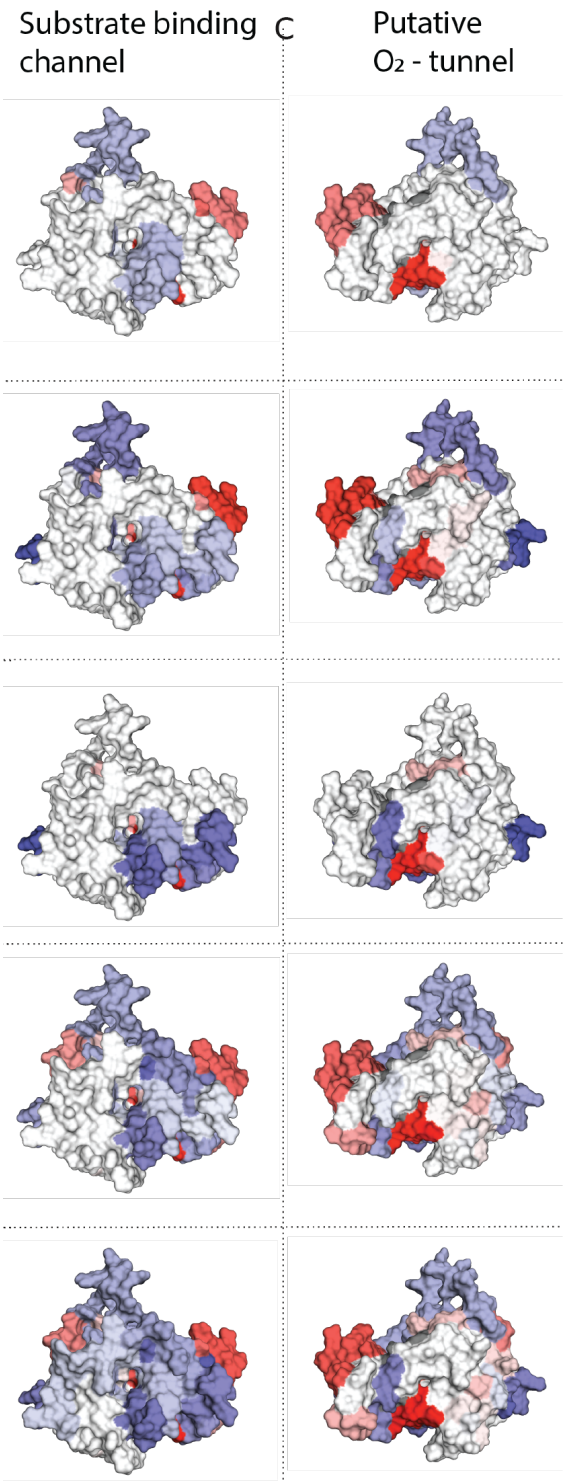


Figure 3.9: Peptides showing statistically significant changes upon addition of Pep9 to *At*PCO4 are mapped onto surface representations, from the earliest time point (15 seconds, top) to the latest (60 minutes, bottom). Blue indicates peptides that become protected in the presence of Pep9, red indicates peptides that are deprotected and grey denotes peptides that do not meet the significance threshold.Figure reproduced from Latter *et al.*[155].

These regions of change can then be plotted on the structures. At the shortest exposure (15 s; Figure 3.10), protection of the hairpin loop (176–193) is already apparent, indicating that this interaction forms immediately upon pre-incubation with Pep9. Protection persists throughout the entire time course, including the longest labelling period shown in Figure 3.11), consistent with a stable interaction.

The flanking loops (147–175 and 194–210) also show significant increases in exchange from the earliest time points onwards. Their behaviour contrasts with the hairpin itself, while the central loop becomes more structured, the adjacent loops become more dynamic. This pattern underlines the idea of a concerted rearrangement rather than a localised stabilisation.

At 60 min, three additional regions exhibit significant protection: residues 1–8, 121–140 and 218–227. These segments are partially or fully disordered in AlphaFold models. The gain of protection at long labelling times suggests that these disordered loops acquire structure or form intramolecular contacts following peptidomimetic binding. This delayed protection supports a sequential mechanism: immediate stabilisation of the hairpin loop is followed by longer-timescale ordering of distal regions, consolidating the primed conformation of *At*PCO4.

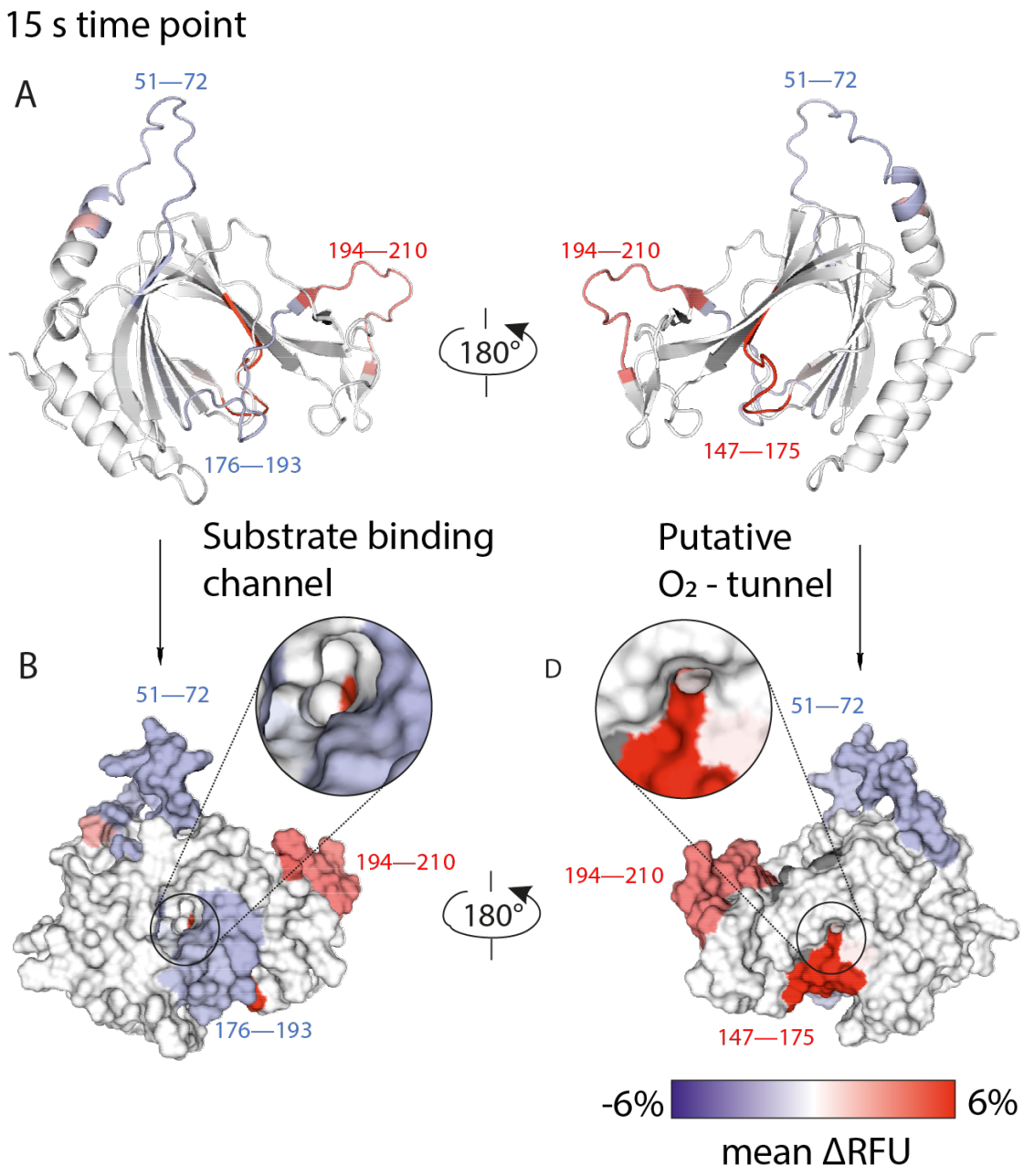


Figure 3.10: Differential HDX–MS analysis of *At*PCO4 at 15 s following incubation with Pep9. (A,B) Cartoon and surface representations coloured by ΔD uptake (peptide-bound minus apo), highlighting early protection and deprotection events. Regions showing decreased exchange (protection) are indicated in blue and regions showing increased exchange (deprotection) in red. Insets show regions of interest.Figure reproduced from Latter *et al.*[155].

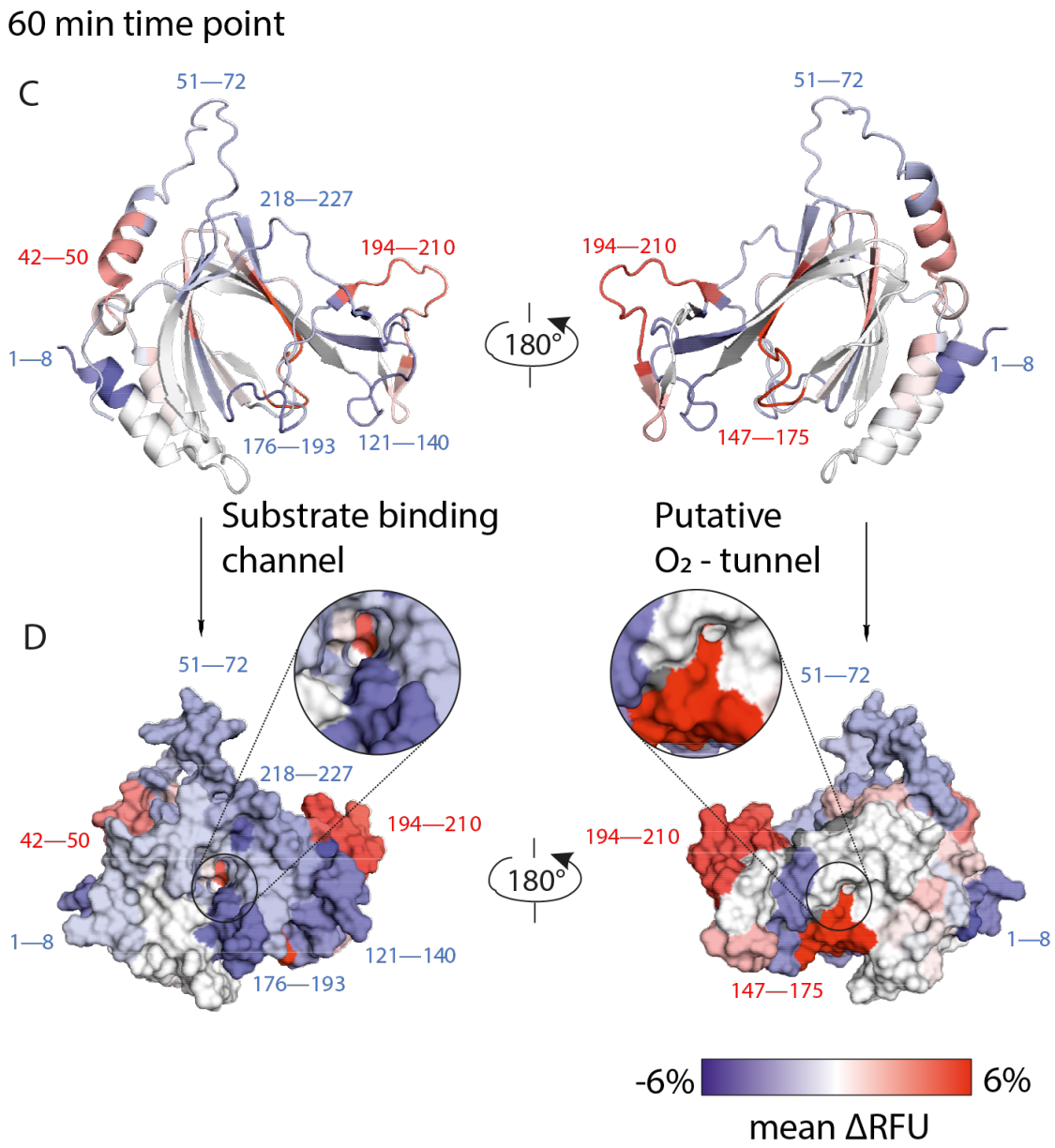


Figure 3.11: Differential HDX–MS analysis of *At*PCO4 at 60 min following incubation with Pep9. (A,B) Cartoon and surface representations coloured by ΔD uptake (peptide-bound minus apo), highlighting early protection and deprotection events. Regions showing decreased exchange (protection) are indicated in blue and regions showing increased exchange (deprotection) in red. Insets show regions of interest.Figure reproduced from Latter *et al.*[155].

3.6 Discussion and Conclusions

The HDX-MS results provide structural support for the biochemical observation that Pep9 enhances *At*PCO4 activity. The observed protection of the hairpin loop implies that Pep9 makes contacts with this region to hold it in place above the substrate channel, mimicking the stabilisation expected during substrate entry and thereby maintaining the integrity of the binding pocket. Simultaneous deprotection of the O_2-tunnel loop (147–175) indicates greater flexibility and solvent accessibility, consistent with facilitated oxygen entry through the tunnel. The delayed emergence of protection in disordered loops (1–8, 121–140, 218–227) suggests that once the hairpin is engaged, a cascade of structural ordering propagates through the protein, leading to a globally more ordered, catalytically favourable state. This may represent conformational priming where the binding of substrate-like peptides induces stabilisation of the hairpin loop and mobilisation of surrounding gating loops, thereby promoting a more active conformation of the enzyme. This interpretation also aligns with docking results, which positioned peptidomimetic 10 and RAP2.12 peptides in the substrate channel, supported by hydrogen-bonding interactions at Asp176 and Tyr182. Therefore, the HDX-MS data, together with docking and biochemical assays, provide a consistent mechanistic picture: peptidomimetic binding stabilises critical structural motifs at the substrate channel while enhancing flexibility of access routes for oxygen, priming *At*PCO4 for rapid turnover upon substrate introduction.

3.7 Materials and Methods

Adapted from Latter*et al.* [155].

3.7.1 Synthesis of Peptidomimetics

Carried out by Dr Rebecca Latter. $RAP2.1_{22–17}$ was purchased from GL Biochem. All peptidomimetics were chain assembled on Rink amide resin using microwave-assisted SPPS on a Liberty Blue peptide synthesizer (CEM Corporation) with the

equivalent ratio of [5]:[5]:[7.5] of [Fmoc-protected amino acid]:[DIC]:[Oxyma Pure] at 50 °C for 10 min. The final amino acid was coupled by manual SPPS with the equivalent ratio of [2]:[2]:[3.5] of [Fmoc-protected amino acid]:[HATU]:[DIPEA] overnight. Full conversion was checked by the Kaiser test.

Peptides were cleaved from resin using 0.5% TIPS and 0.5% H_2O in TFA.

Following TFA removal, the resultant residue was suspended in cold Et_2O and centrifuged for 5 min in a 5804R centrifuge (Eppendorf). The white to yellow precipitate was washed twice with cold Et_2O and centrifuged again before being dissolved in a mixture of ACN in H_2O and purified using preparative reverse-phase HPLC (RP-HPLC) with a gradient of buffer A and buffer B from 20% B to 70% over 40 min at 4 mL min^{-1} using a Gemini 10 µm NX-C18 110 Å LC column (Phenomenex).

Analytical RP-HPLC was carried out on a Gemini 5 µm C18 110 Å LC column (Phenomenex) at a flow rate of 1 mL min^{-1}. Analytical injections were monitored at 215 nm.

3.7.2 In Vitro Activity Assays

Carried out by Dr Rebecca Latter.

Recombinant *At*PCO4 was expressed using BL21(DE3) *E. coli* cells containing the plasmid pET-28a(+)-His-THROMBIN-*At*PCO4 and purified using Ni^{2+}-affinity and size-exclusion chromatography. WT *At*PCO4 was purified using this method.

WT *At*PCO4 reactivity towards Pep9 was assessed by incubating 0.5 µM recombinant enzyme with 200 µM Pep9 in assay buffer (50 mM Bis-tris propane, 40 mM NaCl, pH 8) supplemented with 20 µM $FeSO_4$, 1 mM ascorbate and 5 mM TCEP, at 25 °C for 20 min before quenching in 5% (v/v) formic acid.

To determine *At*PCO4 catalytic activity towards $RAP2.1_{22–17}$ in the presence and absence of Pep9, mixtures of (i) recombinant enzyme with either 0 or 400 µM Pep9 in assay buffer supplemented with $FeSO_4$ and ascorbate and (ii) $RAP2.1_{22–17}$ in assay buffer supplemented with TCEP, were incubated separately at 25 °C for 6 min. Equal volumes of mixtures (i) and (ii) were then combined, achieving the

desired reaction concentrations (0.5 µM recombinant enzyme, 20 µM RAP2.1$_{22–17}$, 0 or 200 µM Pep9, 20 µM $FeSO_4$, 1 mM ascorbate, 5 mM TCEP) and initiating the reaction. Reaction samples taken at 0 s, 30 s, 60 s, 90 s, 2 min, 5 min, 10 min, 15 min and 20 min intervals were quenched in 5% (v/v) formic acid.

To test the significance of the Pep9–*At*PCO4 preincubation step, the method above was modified so that either 0 or 400 µM Pep9 was instead included in mixture (ii). Mixtures were again incubated separately at 25 °C for 6 min before being combined in equal volumes, initiating the reaction. Samples were taken and quenched in 5% (v/v) formic acid.

3.7.3 HDX-MS

Recombinant *At*PCO4 was expressed using BL21(DE3) *E. coli* cells containing the plasmid pET-28a(+)-His-TEV-AtPCO4 and purified as described above and in (61) but with the addition of a TEV protease cleavage step to remove the N-terminal His6 tag prior to size exclusion chromatography (cleavage of the His6 tag and use of a codon optimised sequence promoted molecular weight homogeneity of peptide fragments). AtPCO4 was either preincubated in the presence (1:1000 AtPCO4-to-peptidomimetic 9) or absence of peptidomimetic 9 for 6 min before 5 µL was diluted in 55 µL deuterated buffer (5 mM potassium phosphate in D_2O, pD = 7.4) at rt to achieve 15 µM AtPCO4 and a labelling solution of 92% D_2O. Samples were then incubated for 15 s, 60 s, 5 min, 30 min and 60 min and then quenched with an ice-cold H_2O buffer (50 mM potassium phosphate, pH = 1.9) of equal volume. Control (0s) experiments were performed by adding 55 µL of a non-deuterated equilibrium buffer (5 mM potassium phosphate in H_2O, pH = 7.4) to dilute a recombinant AtPCO4 sample to 15 µM, this was immediately followed by quenching. The pH of the quenched solution was 2.5 at 0 °C. This was injected into an on-line HDX manager (Trajan Scientific and Medical) set to 0 °C. The sample was injected onto a 50 µL sample loop before passing over a protease column (packed in-house (2mm x 2 cm) with immobilised pepsin (Thermo Scientific), at 20 °C using an isocratic H_2O 0.1% (v/v) formic acid solution at a flow rate of

200 µL/min. Peptide products were collected on a trapping column (VanGuard ACQUITY C18 BEH 2.1 × 5 mm; Waters), at 0 °C. After 3 min collection and de-salting, peptides were eluted onto an analytical column for separation using a reverse-phase gradient with a flow rate of 80 µL/min. The elution profile using a H_2O (A) ACN (B) 0.1% (v/v) formic acid gradient was as follows: 1-7 min, 92% (A) to 65% (A); 7-8 min, 5% (A) to 5% (A); 8-10 min hold at 5% (A). This was followed by a saw tooth gradient between 95% and 5% (A) for 10 min to backflush the columns between proteins runs. This was then followed by a re-equilibration period of 2 min at 92% (A). The analytical flow rate was 40 µL/min and was electrosprayed into a Cyclic IMS QTOF MS (Waters) for mass analysis. Sample handling was automated using a robotic liquid handling HDX3 system (Trajan Scientific and Medical) to ensure reproducible timings. Instrument conditions were as follows: capillary 3.0 kV, sample cone 30 V, source offset 30 V. The source temperature was set to 80 °C, the desolvation temperature was 150 °C and the desolvation gas flow was 600 L/hr, nebuliser gas 6.5 L/hr, trap collisional energy 6 V, transfer collisional energy 4 V. Spectra were acquired between 50 - 2000 m/z. LeuEnk was used as an internal calibrant and acquired every 30 s. 0 s MSE data was acquired for peptide mapping where the transfer collisional energy is ramp from 20 V-30 V and sample cone is overridden to 50 V. Peptides were identified from MS/MS data collected from the control runs and processed using Protein Lynx Global Server 3.0 (Waters). This was then used to create a database on DynamX 3.0 (Waters) to assign spectra from the labelling runs using the following parameters; minimum sequence length 5, maximum sequence length 25, minimum fragmentation products per amino acid 0.2, maximum MH+ Error (ppm) 5 and file threshold 3. The automated peak analysis was then verified manually to remove any noisy, overlapping or ambiguous charge states and peptides. The change in deuterium uptake was then calculated by comparing the shift in m/z over time to the non-deuterated control. This data was then exported and statistically analysed using Deuteros 2.0 (Andy Lau) and visualised using PyMOL (Schrodinger).

"Total ion count
Total ion count"

— A robin via Clare Brown

4

Characterising Robin Cryptochrome 4a

Contents

4.1 Abstract 76
4.2 Robin Cryptochrome (*Er*Cry4a) as a model system . . 76
4.2.1 Cryptochrome Structure 78
4.3 Dynamic Regions of *Er*Cry4 Wild Type 81
4.4 Light Induced Effects 84
4.4.1 404-412 90
4.4.2 α22 93
4.4.3 Phosphate Binding Loop and Protrusion Loop 95
4.5 Refolding Experiments (Pulsed Labelling HDX) 99
4.6 ECD analysis of the PBL 101
4.6.1 Intrinsic rates 103
4.6.2 Kinetic fitting of experimental exchange rates 104
4.6.3 Protection factors (PFs) 106
4.6.4 Residue-level localisation 107
4.6.5 Interpretation 109
4.7 Magnet-Induced Differences 111
4.8 Conclusions 114
4.9 Materials and Methods 116
4.9.1 Materials 116
4.9.2 HDX-MS 116
4.9.3 Native Mass Spectrometry 118
4.9.4 Data Analysis 119

4.1 Abstract

This chapter presents a detailed HDX–MS characterisation of European robin cryptochrome 4a (*Er*Cry4a), establishing it as the reference system for subsequent comparative studies. The protein was analysed under four conditions: light (LS), dark (DS), light with magnetic field (LSM) and dark with magnetic field (DSM), using conventional HDX-MS, pulsed-labelling HDX and electron-capture dissociation.

HDX–MS revealed a well-protected β-sheet core surrounded by flexible helical regions. Illumination produced reproducible protection in the PBL, PL, α22 and regions associated with the dimer interface, identifying these as light-responsive structural elements. Under the conditions tested, static magnetic fields produced no measurable changes in solvent accessibility. This suggests that any magnetic effects, if present, operate on a different timescale or magnitude from the photosensitive effects and therefore do not give rise to detectable conformational rearrangements in these experiments.

Pulsed-labelling experiments showed that light-induced stabilisation of the PBL and PL is reversible, relaxing to the dark-state ensemble within hours after illumination. Residue-level mapping of exchange within the PBL using ECD revealed moderate, position-dependent protection consistent with transient local structuring. These results define *Er*Cry4a as a structurally and dynamically well-characterised reference for investigating light-dependent conformational responses in avian cryptochromes.

4.2 Robin Cryptochrome (*Er*Cry4a) as a model system

The European robin is a key species in magnetoreception research owing to its well-characterised migratory and orientation behaviour. It breeds across temperate Europe and migrates south in winter, following regular seasonal routes that are also observed in captive orientation experiments. Migrating robins kept under laboratory

conditions show nocturnal restlessness (*Zugunruhe*) in their migratory direction, providing a clear behavioural indicator of compass use [172].

The European robin was the first species in which the avian magnetic compass was shown to be inclination-based rather than polarity-based. Experiments by Wolfgang and Roswitha Wiltschko demonstrated that robins reversed their orientation when either the vertical or the horizontal component of the geomagnetic field was inverted, but not when both were inverted [4]. This established that migratory birds use the inclination of field lines as a compass cue, a finding later confirmed in other species [3, 21].

Robins also exhibit a wavelength-dependent magnetic response, maintaining orientation under short-wavelength illumination but losing it under longer wavelengths [173]. Although these effects are often attributed to the absorption characteristics of flavin cofactors, the correspondence is only approximate. Orientation has been reported under green light up to 565 nm, where fully oxidised FAD shows little absorption, suggesting that the underlying photoreceptive mechanism may involve additional chromophore states or redox forms [69, 174, 175].

The European robin was also among the first avian species in which Cry4 expression was mapped in the retina [65, 176]. Cry4 localises to double cones and long-wavelength-sensitive single cones, which are systematically arranged across the retina and well positioned to integrate compass information with visual input. The Cry4a isoform is expressed at stable levels throughout the day and night, indicating that it is unlikely to have a circadian function. Its expression varies seasonally, with higher levels observed during spring and autumn migration [64], consistent with a role in migration-related signalling rather than daily timekeeping. This combination of spatial and temporal expression patterns further establishes the robin as a leading model for linking molecular mechanisms to migratory orientation.

Decades of behavioural, physiological and molecular research on the European robin provide a depth of context rarely available for other migratory birds. This foundation allows new molecular insights into *Er*Cry4a to be interpreted within a

well-defined behavioural framework, reinforcing the robin's value as a benchmark species for magnetoreception research.

The robin, therefore, provides a powerful system in which physiological light conditions, molecular photochemistry and orientation behaviour can be integrated.

4.2.1 Cryptochrome Structure

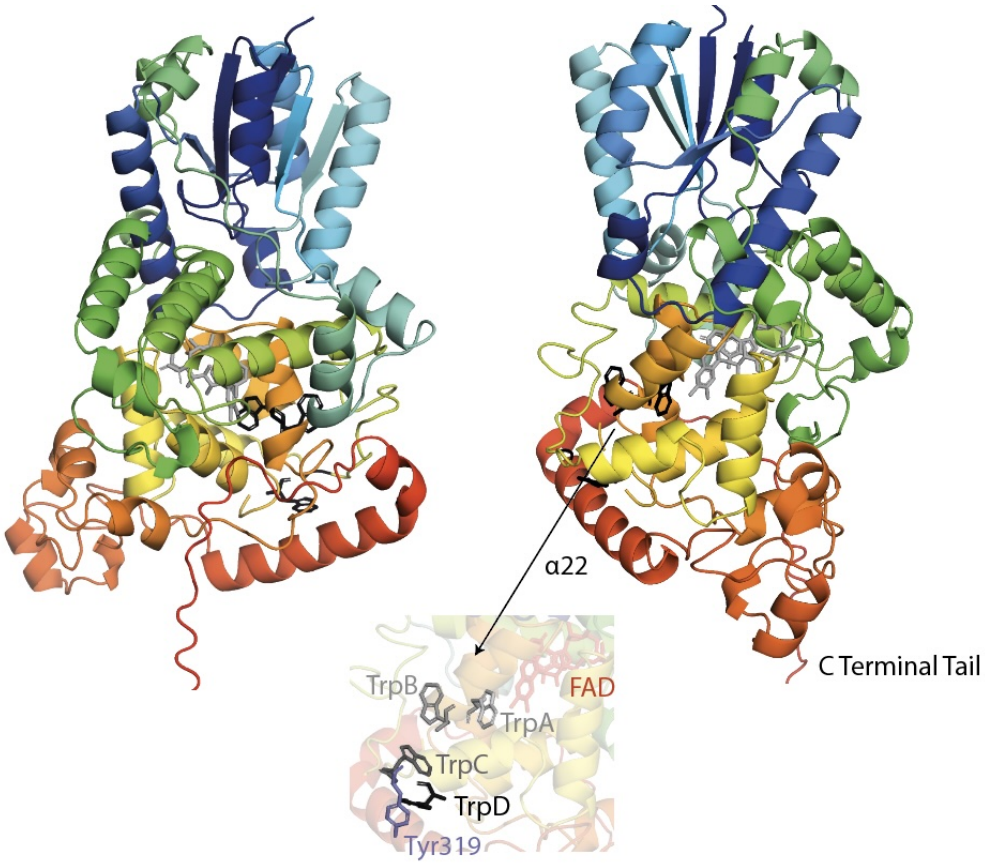


Figure 4.1: Predicted structure of *Er*Cry4a generated using AlphaFold 3. The conserved tryptophan tetrad is highlighted in a gradient from grey (TrpA) to black (TrpD), illustrating the sequential electron-transfer pathway. The non-covalently bound FAD cofactor is shown in orange.

*Er*Cry4a adopts the canonical PHR fold that defines the cryptochrome–photolyase family. The protein consists of a compact α/β domain and an extended helical domain. The predicted three-dimensional structure is shown in Figure 4.1 and the correspondence between sequence and secondary structure elements is illustrated in Figure 4.2. These representations highlight the conserved organisation of the

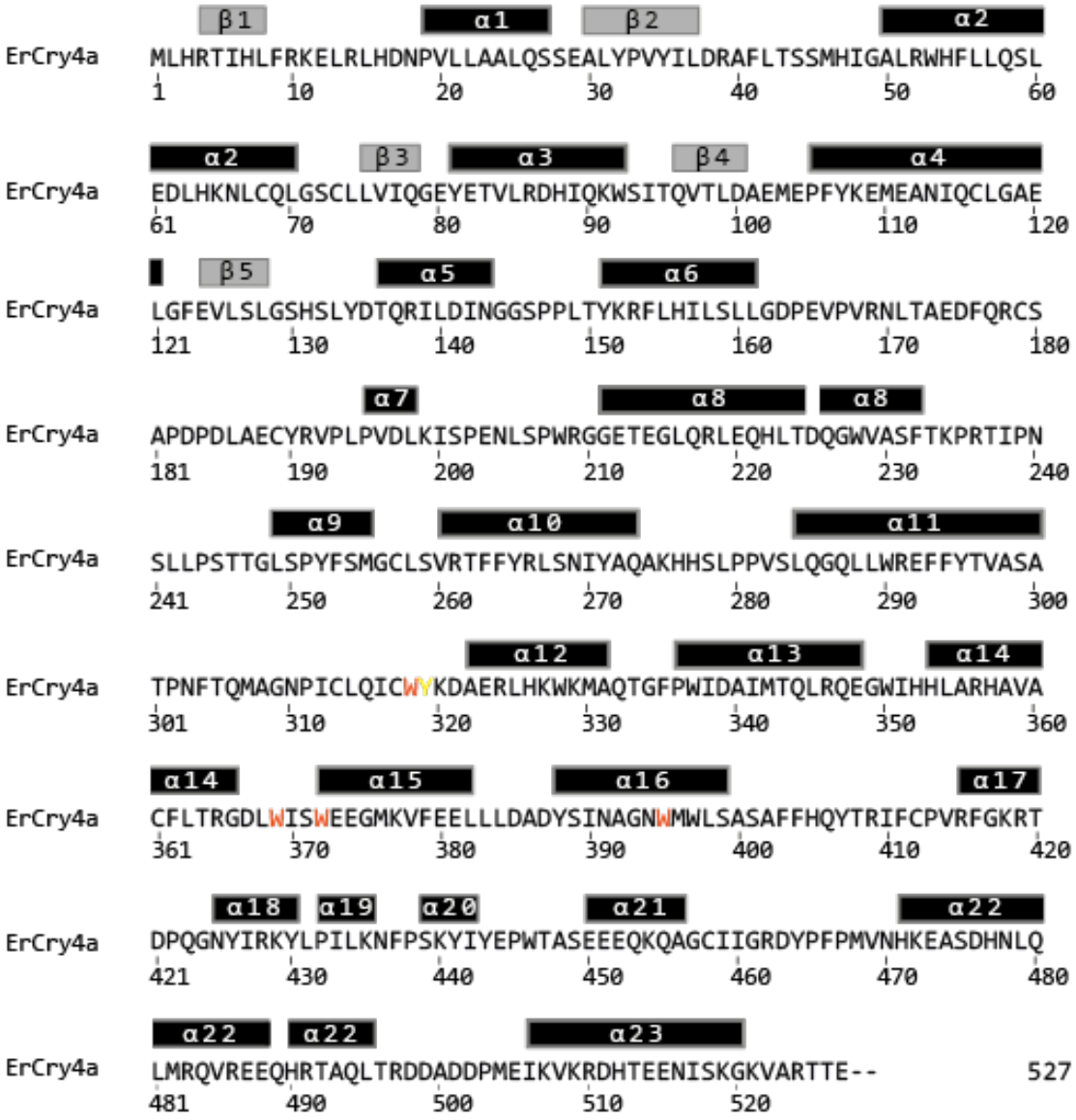


Figure 4.2: Amino acid sequence of *Er*Cry4a with secondary structure elements mapped. β-strands and α-helices are indicated above the sequence.The tryptophan residues forming the electron-transfer chain (TrpA–TrpD; W318, W372, W395 and W369) are shown in red and tyrosine (Y319) is highlighted in yellow.

PHR and provide the structural framework for interpreting the dynamic analyses presented in this chapter.

The PHR constitutes the majority of *Er*Cry4a and is organised into two subdomains [72, 177]. The N-terminal subdomain adopts the characteristic dinucleotide-binding (Rossmann-like) fold of the cryptochrome–photolyase family, consisting of a central parallel β-sheet core flanked by α-helices [47]. This configuration is highly conserved across photolyases and cryptochromes and plays a central role in stabilising FAD binding and maintaining enzymatic function [178]. In *Er*Cry4a, this domain extends approximately to residue 150 and encompasses the β-sheet elements.

The C-terminal subdomain is predominantly α-helical and forms a compact structure. This region shapes the specialised FAD-binding cavity, where the non-covalently bound flavin lies at the interface between the two PHR subdomains: the isoalloxazine ring is buried within the α-helical domain, while the adenine moiety extends toward the α/β domain [177]. This organisation, supported by AlphaFold predictions and biophysical characterisation of *Er*Cry4a, provides the structural basis for the flavin's redox chemistry and photochemistry [16, 179]. Time-resolved crystallographic studies of related photolyases further show that this helical subdomain can undergo conformational changes during electron transfer, suggesting that the equivalent region in *Er*Cry4a may also participate in light-driven structural rearrangements [180].

Central to the proposed magnetosensory function of *Er*Cry4a is a conserved tryptophan tetrad that mediates electron transfer from the protein surface to the photoexcited FAD [17]. The four residues, W395 (TrpA), W372 (TrpB), W318 (TrpC) and W369 (TrpD), are arranged in a chain that enables sequential electron transfers following blue-light excitation. TrpA, located adjacent to the flavin, initiates the radical-pair cascade, TrpB and TrpC provide intermediate steps and TrpD, positioned closest to the protein surface, acts as the terminal electron donor in the pathway.

Tyr319 lies in close proximity to TrpD (approximately 3.9 Å), enabling contribution towards the electron transfer chain [181]. This additional redox-active

residue is thought to extend the lifetime of magnetically sensitive radical-pair states and thereby enhance the protein's capacity for magnetic sensing. The conservation of both the tryptophan tetrad and Tyr319 across avian cryptochromes highlights their likely functional importance in magnetoreception.

Extending beyond the structured PHR, *Er*Cry4a possesses a flexible CTT of around 30 residues (Figure 4.1). This extension is not found in canonical photolyases but occurs widely among cryptochromes, where its presence is conserved even though the sequence itself is highly variable. The CTT is thought to contribute to light-dependent conformational switching and to mediate interactions with downstream signalling partners [182]. Structural and biochemical evidence indicate that it undergoes light-induced rearrangements upon flavin photoreduction, transitioning from a docked state against the protein core to a released conformation that enables binding to target proteins and initiation of signalling cascades [178].

Recent studies using native mass spectrometry and chemical cross-linking have shown that *Er*Cry4a can form dimers through both covalent disulphide bonds and non-covalent interactions [72]. These oligomers have been proposed to contribute to cryptochrome function in other systems and may influence the magnetosensory properties of *Er*Cry4a, although their precise physiological relevance remains to be established.

4.3 Dynamic Regions of *Er*Cry4 Wild Type

The following sections present the results of HDX–MS experiments on *Er*Cry4a. Unless otherwise stated, all measurements were performed using the standard HDX–MS workflow described in Chapters 2 and 3, ensuring consistency and comparability across datasets. The initial continuous-labelling HDX–MS experiments on wild-type *Er*Cry4a were performed by my colleague Dr Angela Gehrckens. The global and differential uptake data shown here are based on her measurements, which I subsequently re-analysed to ensure consistency with the processing methods used throughout this thesis. I also repeated the continuous-labelling experiments and carried out the pulsed-labelling HDX analyses myself. Four experimental states

were examined: the light state (LS), the dark state (DS), the light state in the presence of a static magnetic field (LSM) and the dark state with magnetic-field exposure (DSM). These conditions were designed to probe both light-dependent conformational changes and potential magnetic-field effects.

As a first step, the overall deuterium uptake of *Er*Cry4a was characterised in each of these four states, providing a baseline comparison of protein dynamics before turning to more detailed analyses at the peptide and regional levels. Figures 4.3 and 4.4 summarise uptake values for overlapping peptides aligned along the primary sequence and mapped onto the protein structure, respectively.

Within the N-terminal region, deuterium uptake is relatively low, consistent with stable secondary structure characteristic of the canonical α/β-domain of the cryptochrome–photolyase family. Peptides spanning $\beta1$–$\beta3$ remain pale on the heatmap, indicating strong backbone protection from hydrogen bonding within the sheet.

In the extended helical domain, uptake patterns are more heterogeneous. Helices $\alpha3$–$\alpha6$ show intermediate protection, whereas $\alpha7$ and $\alpha8$ display higher uptake, consistent with increased flexibility in this region. Similar behaviour has been proposed to underlie light-induced conformational rearrangements in other cryptochromes [178].

In the later regions of the sequence, helices $\alpha12$–$\alpha16$ show very low uptake, consistent with a rigid helical core. In contrast, peptides spanning the terminal helices ($\alpha17$–$\alpha22$) display increased exchange, reflecting greater conformational flexibility in this region.

The most prominent feature of the heatmap is the C-terminal region, which shows a progressive increase in uptake toward the end of the sequence. This pattern indicates extensive solvent exposure and rapid exchange, consistent with an intrinsically disordered segment. In *Er*Cry4a, the graded rise from $\alpha22$ into the terminal extension suggests a gradual loss of secondary structure, culminating in a flexible tail that is highly susceptible to exchange and well positioned to mediate light-dependent regulatory interactions.

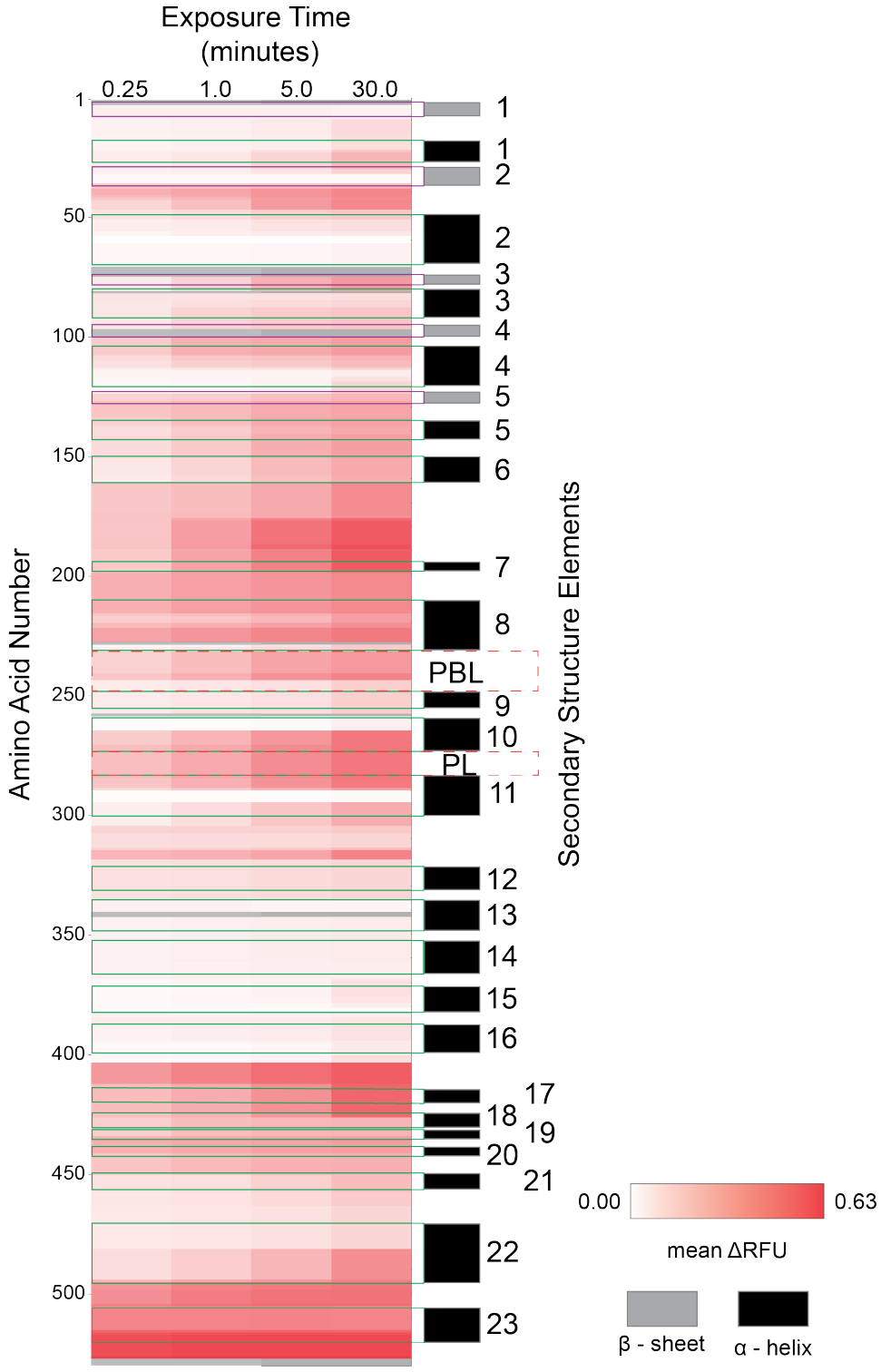


Figure 4.3: Heatmap showing deuterium uptake across overlapping peptides of wild-type *Er*Cry4a under standard HDX–MS conditions. Peptides are aligned along the primary sequence on the vertical axis and uptake is colour-coded according to the relative fractional uptake (RFU) scale from low (white) to high (red). Regions of minimal uptake correspond to protected regions, whereas higher uptake is observed in more accessible regions. This representation provides an overview of the global dynamics of *Er*Cry4a in the dark state.

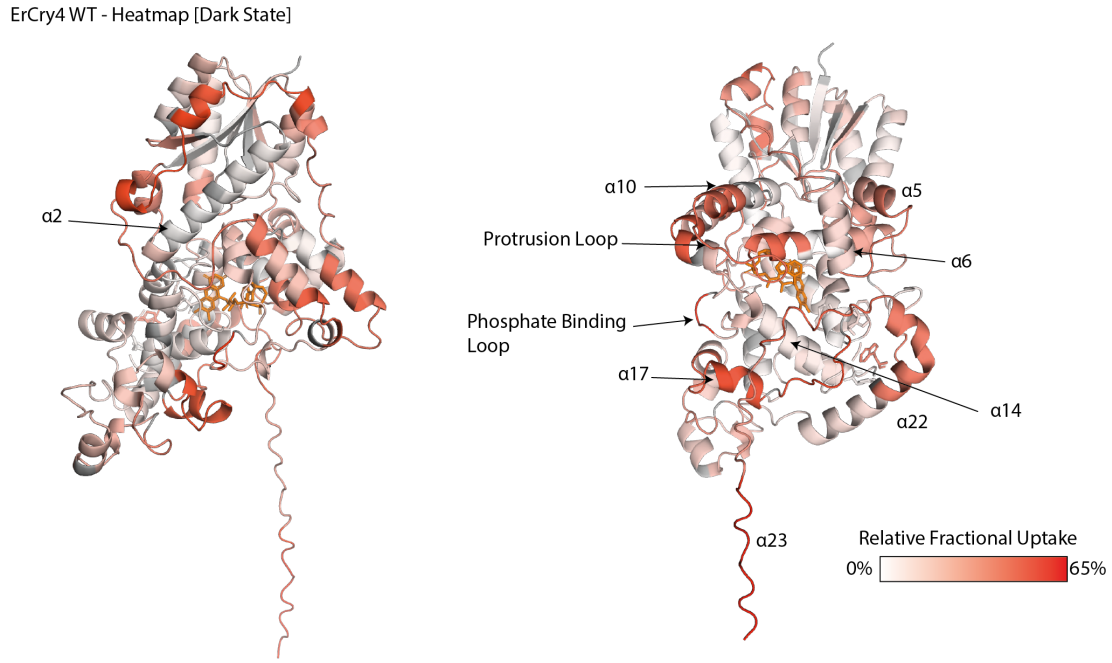


Figure 4.4: Deuterium uptake in wild-type *Er*Cry4a mapped onto the AlphaFold 3 structural model. Colour coding corresponds to the relative fractional uptake (RFU) scale from low (white) to high (red), providing a spatial representation of protection across the protein.

Overall, the HDX data provide a structural map of *Er*Cry4a dynamics. The central β-sheet forms a rigid core characteristic of the photolyase fold, while surrounding α-helices show variable stability, with some helices and adjoining loops exhibiting enhanced flexibility. Such mobility, particularly around the FAD-binding site, is likely to facilitate conformational changes linked to electron transfer and signalling. In contrast, the CTT is uniformly dynamic, consistent with its proposed role as a light-responsive regulatory element.

4.4 Light Induced Effects

Comparison of the light and dark states of *Er*Cry4a reveals distinct and reproducible differences in deuterium uptake, consistent with a conformational response to light. The differential heatmap (Figure 4.5) shows changes of up to $\pm 15\%$ RFU, with most of the protein remaining unchanged but several regions exhibiting significant light-dependent effects. These responses are localised primarily to the PBL, PL,

specific helices and near the CTT.

Across the N-terminal β-sheets and α-helices, uptake shows no significant light-induced differences. The β-sheets therefore appear largely unaffected by illumination, in contrast to neighbouring loops and selected helices that exhibit reproducible perturbations. This stability is consistent with crystallographic observations in plant and animal cryptochromes, where the β-sheets constitute a rigid structural core anchoring the FAD cofactor [183].

Statistical analysis using the hybrid significance test was applied to the differential HDX–MS data and the results were visualised in a Woods plot (Figure 4.6) and volcano plot (Figure 4.7). Across all representations, the PBL, PL and several C-terminal helices consistently exceeded the significance thresholds, confirming these regions as the principal sites of light-dependent conformational change. These significant peptides are mapped onto the *Er*Cry4a structural model in Figure 4.8, illustrating the spatial distribution of light-induced protection.

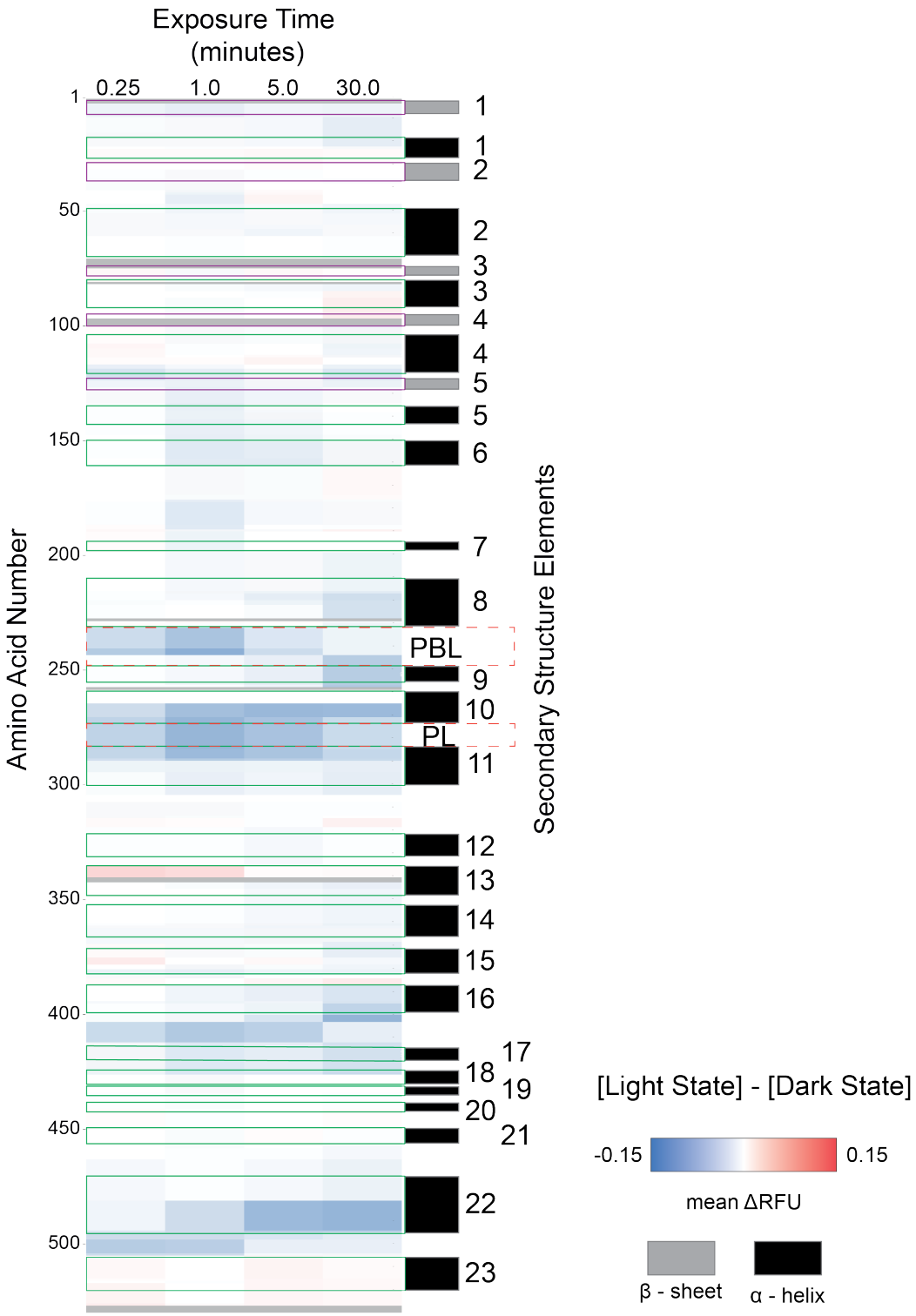


Figure 4.5: Differential HDX–MS heatmap comparing the light state (LS) with the dark state (DS). Colour coding represents the change in ΔRFU along the primary sequence: blue indicates reduced uptake in LS (greater protection), red indicates increased uptake in LS (reduced protection) and white denotes no significant difference. Several regions display reproducible light-induced protection, highlighting conformational changes in *Er*Cry4a associated with photoactivation.

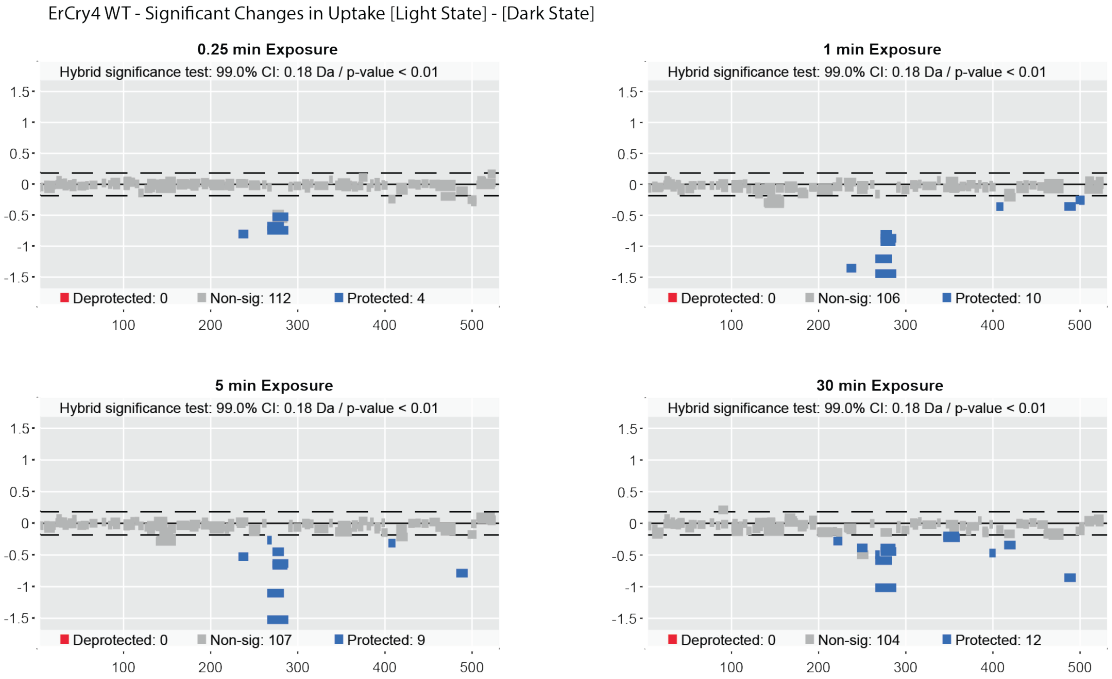


Figure 4.6: Woods plot of differential HDX–MS data comparing the light state (LS) with the dark state (DS) of wild-type *Er*Cry4a. Each bar represents the difference in deuterium uptake between conditions (ΔHDX) for an individual peptide across multiple time points. Significance was assessed using the hybrid significance test (99% confidence interval; ΔHDX threshold 0.18 Da; $p < 0.01$). Several peptides, particularly in the PBL, PL and terminal helices, exhibit statistically significant protection in the light state.

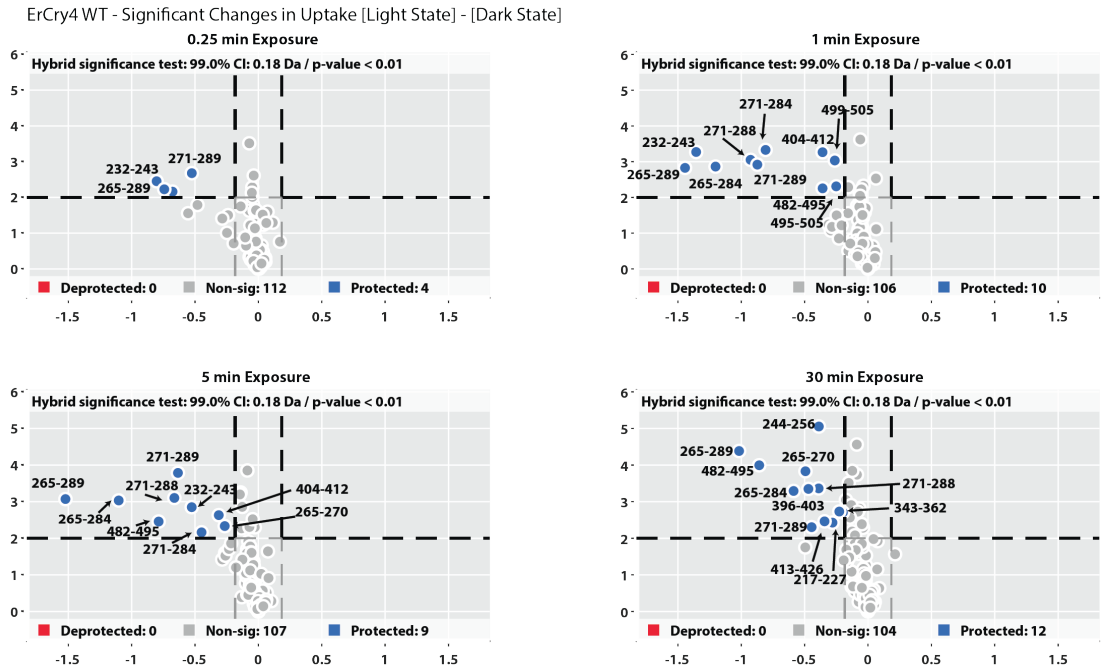


Figure 4.7: Volcano plot of differential HDX–MS results comparing the LS with the DS of wild-type *Er*Cry4a. Each point represents an individual peptide, plotted by the difference in uptake (ΔHDX, x-axis) against significance ($-\log_{10} p$, y-axis). The vertical lines indicate the ΔHDX threshold of 0.18 Da and the horizontal line marks the 99% confidence level ($p < 0.01$).

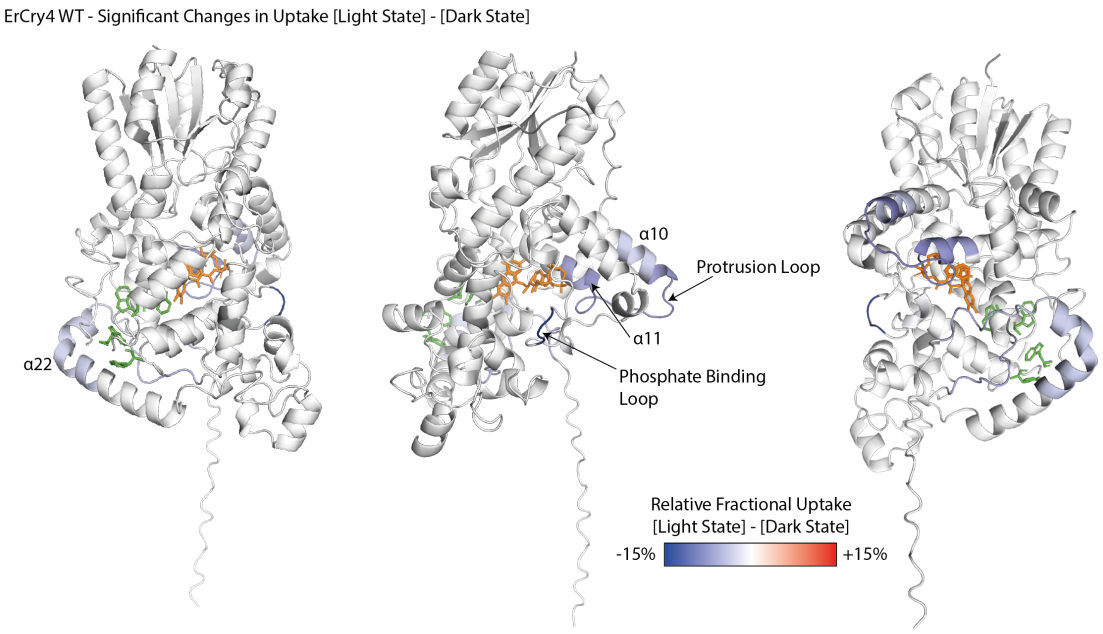


Figure 4.8: Significant light-induced differences in deuterium uptake mapped onto the AlphaFold 3 structural model of *Er*Cry4a. Peptides identified as significant by the hybrid significance test (99% confidence interval; ΔHDX threshold 0.18 Da; $p < 0.01$) are colour-coded by the magnitude and direction of change (blue = reduced uptake in LS, red = increased uptake in LS, white = no change). Light-dependent protection is localised to the PBL, PL and terminal helices, highlighting these regions as key sites of conformational rearrangement.

4.4.1 404-412

One region that shows reproducible light-induced protection in the HDX data is the peptide spanning residues 404–412 (Figure 4.9). Located in the C-terminal portion of the PHR domain, this region consistently displays reduced deuterium uptake in the LS across multiple labelling time points. Its behaviour is notable because it contains Cys412, identified by Hanić *et al.* as one of two cysteines (together with Cys317) most likely to form disulphide-linked dimers, with blue light proposed to promote this interaction [72]. Docking models from that study further positioned Cys412 within or adjacent to putative dimer interfaces, suggesting that this region may contribute to light-dependent oligomerisation of *Er*Cry4a.

The light-induced protection observed in this region could initially be interpreted as photoexcitation stabilising the peptide through incorporation into a dimer interface. However, this explanation is unlikely under the experimental conditions used as the HDX samples contained β mercaptoethanol (BME) to maintain cysteine residues in a reduced state, preventing covalent dimer formation. In addition, native mass spectrometry of the same preparations confirmed that *Er*Cry4a remained predominantly monomeric, with only small amounts of dimer detectable after more than three hours of incubation at room temperature, substantially longer than the protein was ever held during HDX labelling (Figure 4.10). Disulphide-linked dimerisation can therefore be excluded as the source of the protection observed in residues 404–412.

The protection of this peptide under predominantly monomeric conditions suggests the need for alternative explanations. One possibility is that photoexcitation promotes intramolecular packing involving Cys412 and neighbouring residues, thereby reducing local flexibility and solvent exposure. Another is that, although covalent dimerisation is prevented, this region may still engage in transient non-covalent contacts that shield the backbone. Such weak and reversible associations would be undetectable by native MS but could nonetheless appear in HDX as low level protection.

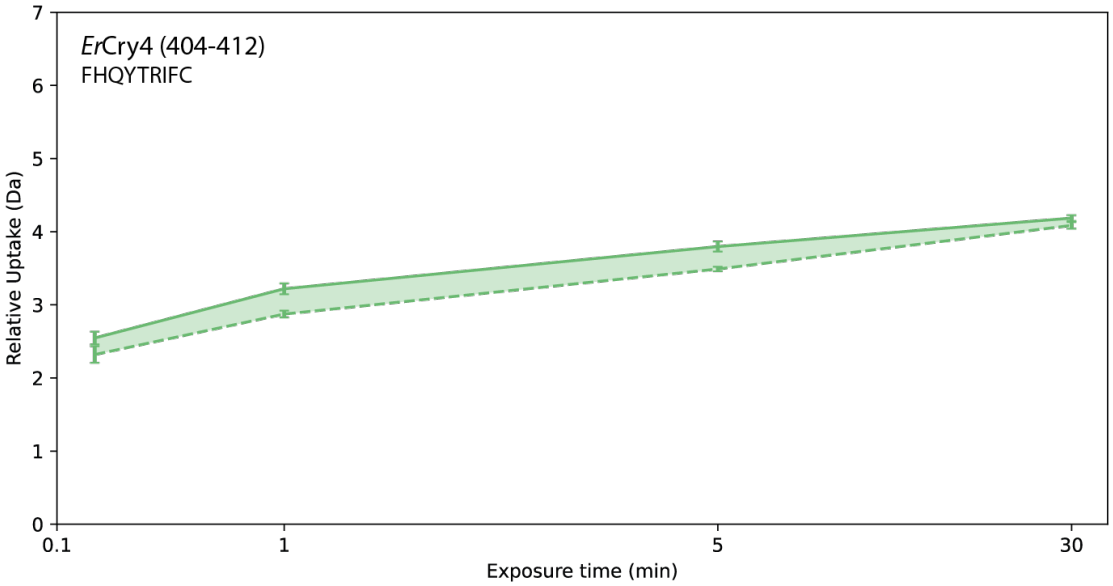


Figure 4.9: Deuterium uptake for peptide 404–412 of *Er*Cry4a under LS and DS conditions. Uptake is plotted as relative fractional uptake (RFU) against labelling time. The solid line represents the light state, the dashed line the dark state and the shaded region indicates the difference in uptake between conditions. This peptide displays significant light-dependent protection, consistent with conformational stabilisation in this region.

More broadly, the overlap with the dimerisation site identified by Hanić *et al.* suggests that residues 404–412 may function as a regulatory switch, comparable to mechanisms described in other cryptochromes. In plants, blue light promotes the assembly of photoactivated oligomers, with crystal and cryo-EM structures revealing extensive interfaces involving residues near the C-terminal region of the PHR [184, 185]. Although cysteines are not the sole drivers of oligomerisation in plant cryptochromes, these studies show that photoactivation can stabilise interface surfaces in a manner reminiscent of the protection observed here. In mammals, cysteines in the C-terminal lid region of cryptochromes, most notably Cys412 and Cys414 in mouse CRY1, have been implicated in modulating interactions with Period (PER) proteins, with evidence pointing to redox sensitivity as a key regulatory factor [59].

Therefore, these results indicate that the light-state protection of residues 404–412 in *Er*Cry4a reflects local stabilisation rather than dimerisation under our experimental conditions. The involvement of the same region in disulphide-linked

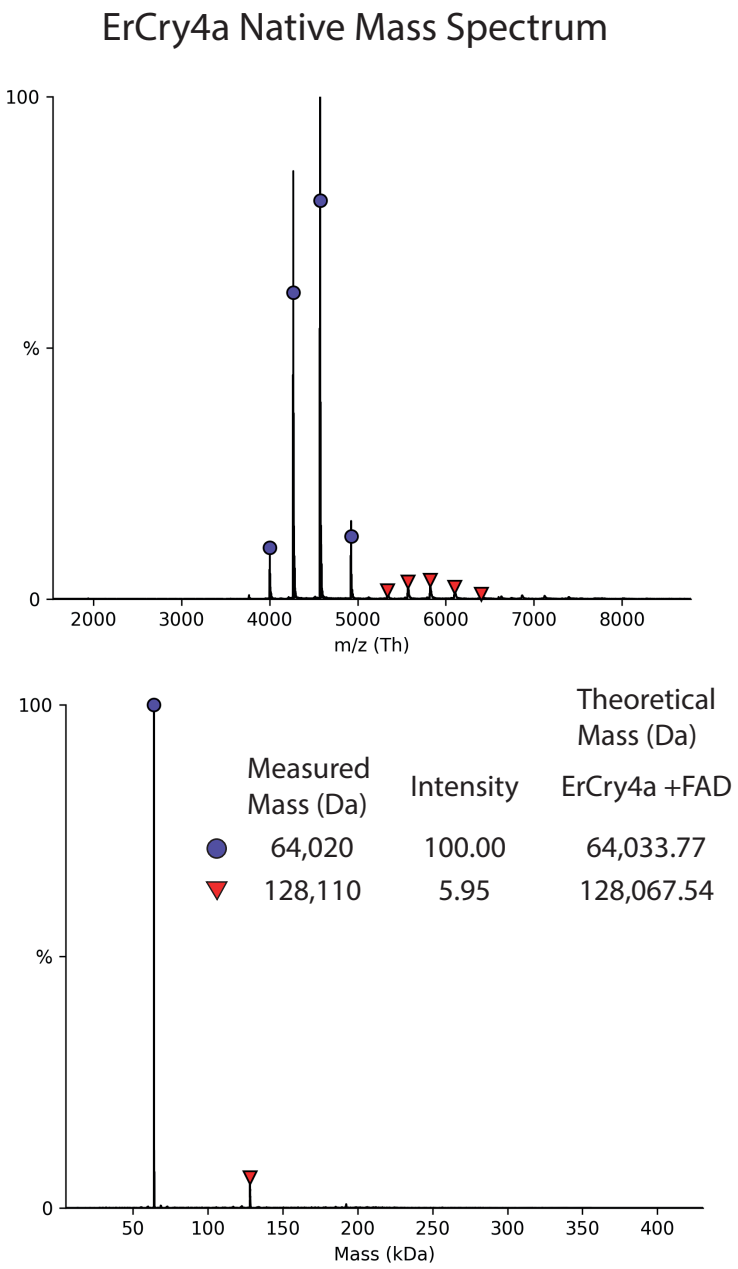


Figure 4.10: Native mass spectrum of wild-type *Er*Cry4a acquired under the same buffer conditions used for HDX–MS. The spectrum is dominated by monomeric species, with only low-intensity signals corresponding to dimers detectable after extended incubation. These data confirm that *Er*Cry4a is predominantly monomeric under the conditions used for HDX experiments, excluding disulphide-linked dimerisation as the source of protection in residues 404–412.

dimerisation in simulations and in redox-sensitive partner interactions in mammalian cryptochromes highlights its functional versatility and suggests that it may act as a context-dependent regulatory element.

4.4.2 α22

A notable feature of the dataset is the delayed protection of α22 at the C-terminus of the PHR domain in *Er*Cry4a (Figure 4.11). Unlike the PBL and PL, which show light-dependent differences within the earliest labelling intervals, peptides from α22 display significant protection only at later time points.

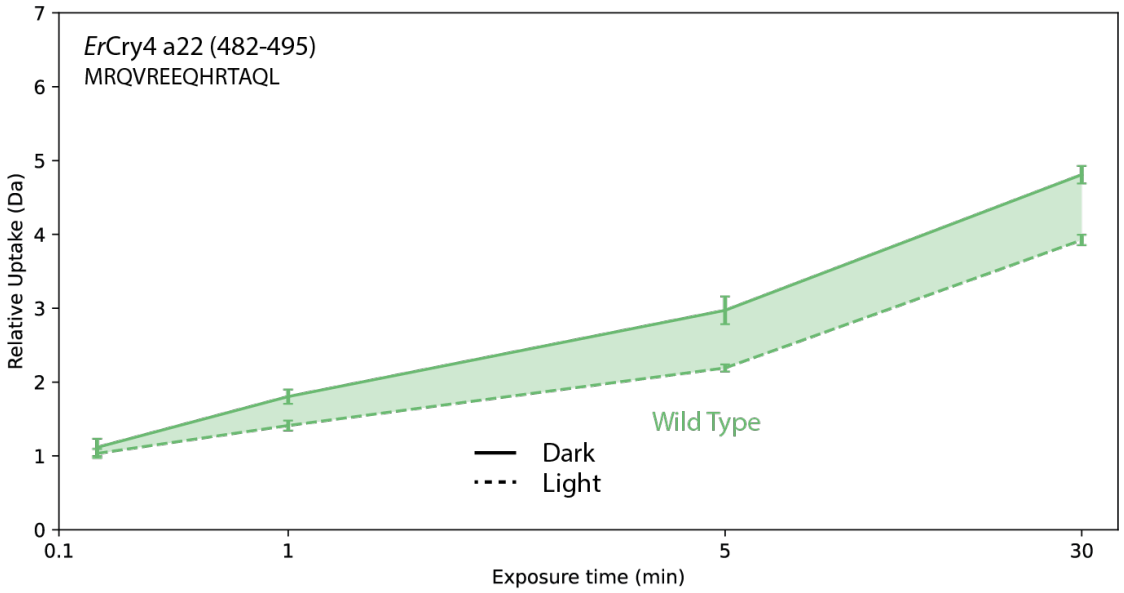


Figure 4.11: Deuterium uptake for the peptide within α22 in *Er*Cry4a. Uptake is plotted as relative fractional uptake (RFU) against labelling time. The solid line represents the light state (LS), the dashed line the dark state (DS) and the shaded region indicates the difference between them. Protection of α22 in the light state becomes evident only at later labelling times, consistent with delayed stabilisation of this helix relative to earlier light-responsive regions such as the PBL and PL.

Comparable behaviour has been reported in other cryptochromes. In *Cra*Cry from *Chlamydomonas reinhardtii*, Franz-Badur *et al.* identified an interaction network in which D321 and D323 form contacts with R485 and R492 on helix α22[73]. These interactions shield Y373 from solvent and help stabilise the electron-transfer chain. When light triggers formation of the $Y373^{\bullet}$ radical, the salt bridges are disrupted, increasing α22 mobility. *Cra*Cry contains three tryptophans (W322,

W376, W399) and one tyrosine (Y373) that together form an aromatic tetrad, with Y373 acting as the terminal electron donor. In contrast, *Er*Cry4a has a tryptophan tetrad (TrpA–TrpD, ending at W369) and an additional tyrosine (Y319) that can act as an auxiliary redox partner. The difference in their electron transfer chains may alter how charge transfer couples to structural change, consistent with the enhanced protection of α22 seen in the light state. Although α22 occupies a similar position in both proteins, the outcome of photoactivation differs: in *Cra*CRY, α22 becomes less protected (more mobile) in the light, whereas in *Er*Cry4a it becomes more protected (less mobile), reflecting differences in the organisation of the electron transfer chain.

Additional insight comes from *Drosophila melanogaster* cryptochrome (*Dm*Cry). Using HDX–MS, Chandler *et al.* observed EX1 kinetics in peptides spanning α22 and α23 [56]. EX1 behaviour, which reflects cooperative switching between discrete conformational states, indicates that light drives α22 into a dynamic equilibrium between open and closed forms. This contrasts with the more typical EX2 kinetics governed by local hydrogen-bond stability. The observation of EX1 therefore supports a model in which α22 undergoes a slow, concerted rearrangement consistent with its proposed role as a structural switch.

When compared directly, *Er*Cry4a shows a similar delayed onset of α22 protection, implying that its conformational response is either subtle or dependent on population shifts between flexible and stabilised states. This interpretation aligns with time-resolved X-ray scattering studies on *Dm*Cry by Berntsson *et al.*, which revealed ultrafast microsecond rearrangements around the flavin followed by slower millisecond-scale motions elsewhere in the protein [186]. The functional relevance of the delayed stabilisation seen in *Er*Cry4a becomes clearer when considered alongside structural and physiological data. In full-length *Dm*Cry, related C-terminal helices form contacts with the PHR domain to maintain cofactor geometry, underscoring their role in stabilising photoactive states. By analogy, light-induced protection of α22 in *Er*Cry4a may represent a locking step that stabilises the protein in a signalling-competent conformation and prevents premature reversion to the dark state. This interpretation is consistent with the slower exchange kinetics expected

for helices integrated into the hydrogen-bonding network of the protein core. At the physiological level, electrophysiological recordings in *Drosophila* show that cry-dependent membrane depolarisation is triggered within seconds of illumination and persists for nearly a minute, while behavioural assays reveal light-induced clock-resetting responses lasting much longer [187]. The delayed stabilisation of α22 in *Er*Cry4a occurs on a comparable timescale, suggesting that this helix contributes to maintaining the protein's active conformation between the initial photochemical event and the ensuing long-lived signalling state.

4.4.3 Phosphate Binding Loop and Protrusion Loop

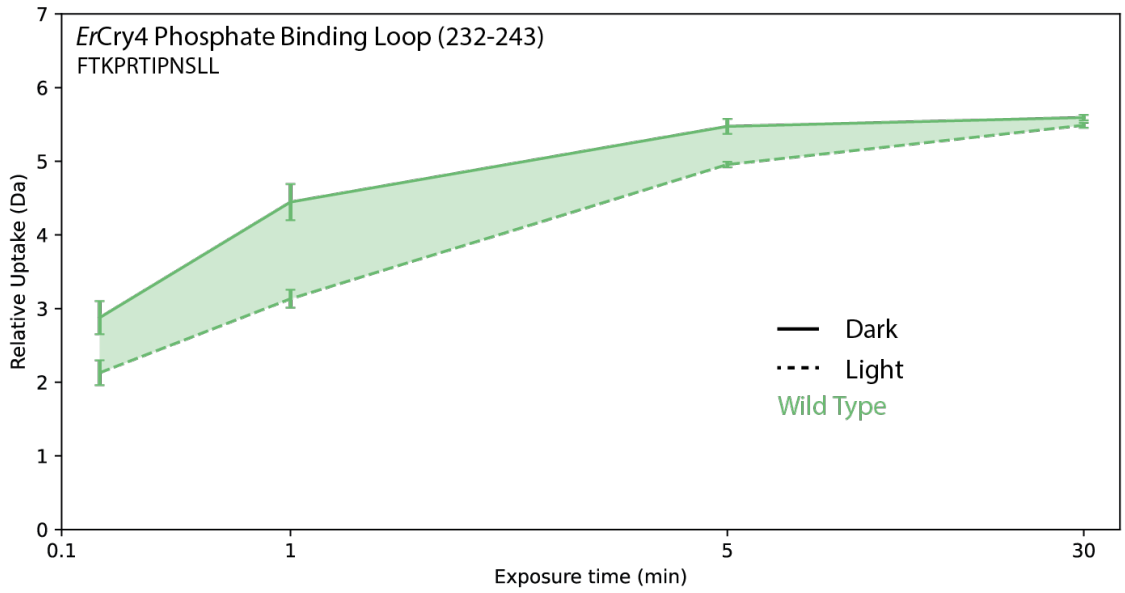


Figure 4.12: Deuterium uptake for peptides spanning the PBL of *Er*Cry4a. Uptake is shown as RFU against labelling time. The solid line represents DS, the dashed line LS and the shaded region indicates the difference between them. The PBL exhibits rapid light-induced protection detectable from the earliest 0.25 min time point. Error bars represent the standard deviation across four replicates.

The PBL exhibited the largest light-dependent difference in *Er*Cry4a, showing a significant decrease in deuterium uptake in LS relative to DS. This protection suggests that photoexcitation stabilises the loop, reducing solvent exchange and promoting additional local structure or interactions. Notably, structural predictions capture this region differently depending on the modelling algorithm, as

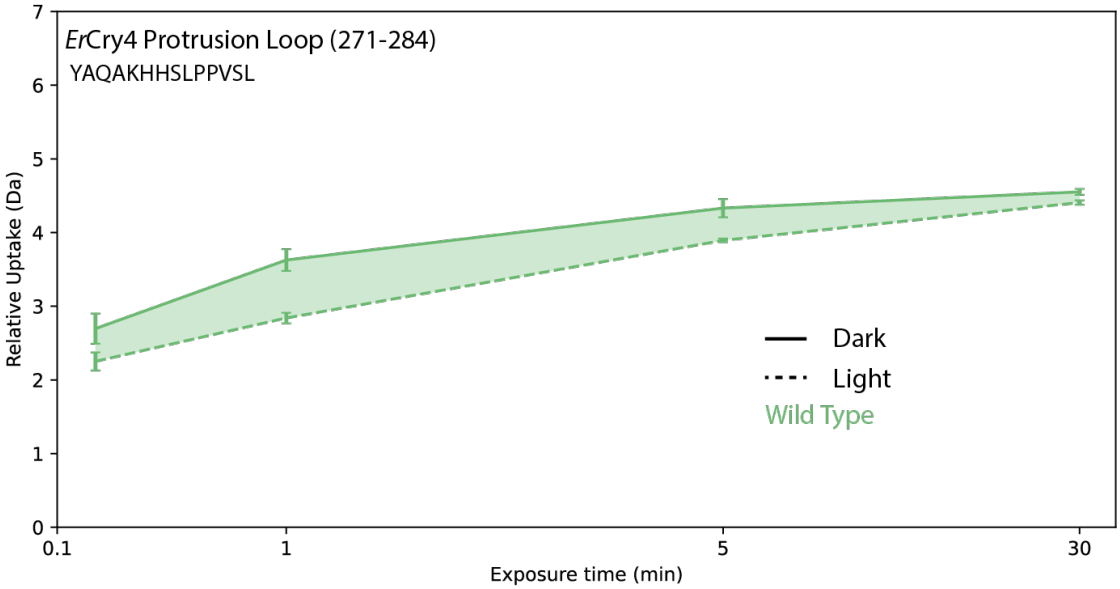


Figure 4.13: Deuterium uptake kinetics for peptides spanning the PL of *Er*Cry4a. Uptake is shown as RFU against labelling time. The solid line represents DS, the dashed line LS and the shaded region indicates the difference between them. The PL displays light-dependent protection apparent from the earliest 0.25 min time point. Error bars represent the standard deviation across four replicates.

illustrated in Figure 4.14, highlighting its sensitivity to both experimental and computational approaches.

In the AF2 model the PBL appears largely unstructured, lacking defined secondary elements. By contrast, AF3 predicts a more ordered configuration, with a central proline introducing a kink. As HDX is insensitive to proline itself, any stabilisation centred on this residue would be detected indirectly through reduced exchange in neighbouring amides. This raises the possibility that the light-induced protection of the PBL in *Er*Cry4a reflects a proline-anchored ordering similar to that captured by AF3, with the residue acting as a pivot point in the photo-activated state.

Molecular dynamics simulations of pigeon Cry4 by Schuhmann *et al.* offers a complementary perspective, suggesting that the PBL can act as a flexible gate that shifts its position in response to the redox state of the FAD (Figure 4.15) [188]. In their simulations, photoactivation induced loop movements that increased solvent access to the flavin pocket, interpreted as a gating motion regulating access to

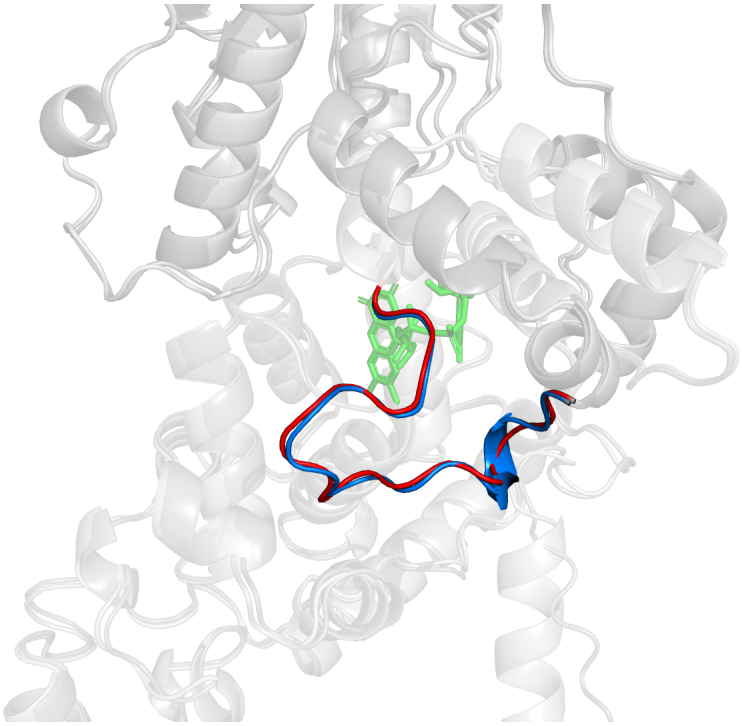


Figure 4.14: Comparison of AF2 (red) and AF3 (blue) structural models of *Er*Cry4a produced by Navoneel Sen. The PBL is highlighted, showing distinct conformations between the two predictions, consistent with its dynamic behaviour observed by HDX.

the cofactor environment. By contrast, our HDX data reveal a clear light-induced decrease in uptake, consistent with enhanced protection of the same loop in *Er*Cry4a. These outcomes are not necessarily contradictory as MD captures fast fluctuations and transient opening events, whereas HDX reports an ensemble average. If the light-activated PBL samples both open and closed states but predominantly adopts the closed conformation, HDX would show increased protection. Therefore, both approaches converge on the conclusion that the PBL is a light-sensitive structural element with a central role in cofactor gating, even though the balance of open versus closed conformations may differ between species and methodologies.

The structural basis for PBL mobility has been attributed to specific contacts between loop residues and the isoalloxazine and pyrophosphate moieties of FAD. In cryptochromes such as *At*Cry and *Dm*Cry, conserved residues form hydrogen bonds with the flavin ring, phosphate groups and adenine moiety, collectively stabilising loop position and regulating access to the cofactor [177, 178, 189, 190]. Light-induced changes in the redox state of FAD are likely to alter these interactions, producing the

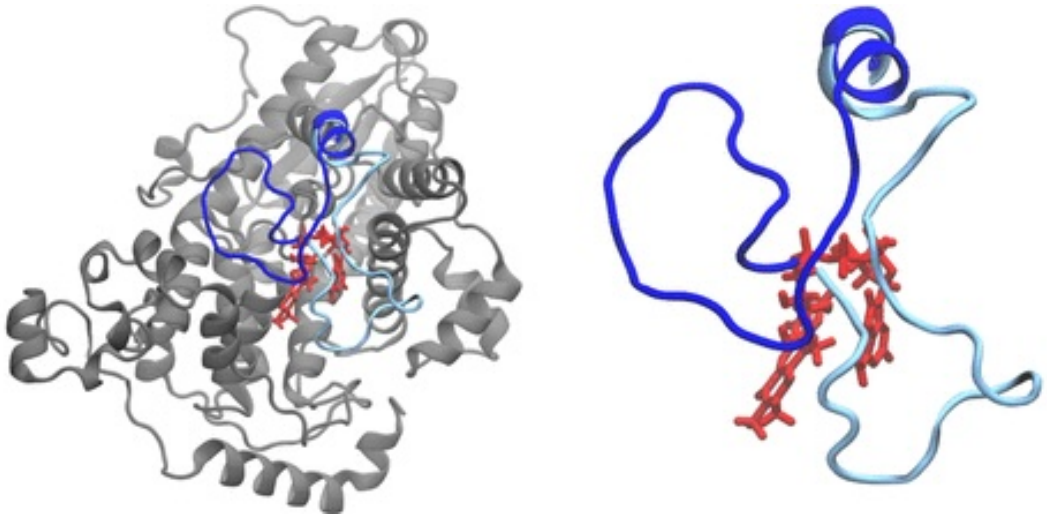


Figure 4.15: Figure reproduced from Schuhmann *et al.*, showing the position of the PBL in the dark (dark blue) and light (light blue) states relative to the FAD (red) in pigeon Cry4. The right-hand panel is an expanded view of the region on the left, highlighting the movement of the PBL upon illumination. [188]

more tightly packed conformation detected by HDX while still permitting transient loop opening events captured by MD simulations.

The PL provides a useful point of comparison. In *Er*Cry4a, this region also shows light-induced protection, although the effect is less pronounced than in the PBL. Schuhmann *et al.* likewise reported light-dependent changes in surface-exposed loops of pigeon Cry4, but in that case the response was an increase in flexibility rather than stabilisation. These apparently opposing outcomes can still be rationalised if the PBL and PL act as mechanically coupled elements. The two loops are positioned close together and share contacts such as those illustrated in Figure 4.16. In *Er*Cry4a, stabilisation of the PBL against the FAD could constrain its motion and simultaneously reduce solvent exposure of the PL, producing the correlated protection seen by HDX–MS. In pigeon Cry4, by contrast, photoactivation may relieve these contacts or redistribute strain in a way that enhances loop mobility. Such differences could arise from species-specific sequence variations or from distinct distributions of flavin redox intermediates. In both cases, the PBL and PL emerge as dynamically linked light-sensitive motifs that regulate access to the flavin cavity and mediate structural rearrangements within the protein.

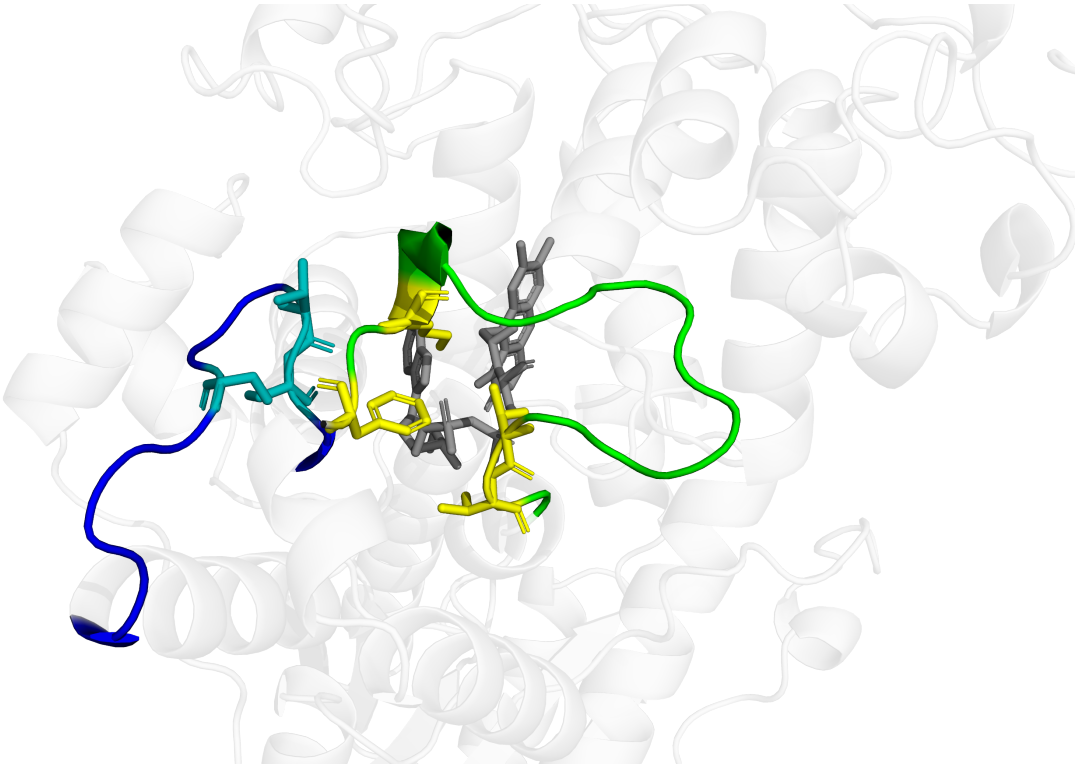


Figure 4.16: AF3 model of *Er*Cry4a showing residues that form putative contacts between the PBL and the PL. The PBL backbone is shown in green and the PL in blue. Contacting residues within the PBL (F232, K234, T246, T247) are shown as yellow sticks and those within the PL (S278, V282, S283) are shown as turquoise sticks. The FAD cofactor is shown in grey. This colour scheme highlights the residues that could form direct interactions between the two loops, which may contribute to light-dependent stabilisation of the PBL.

4.5 Refolding Experiments (Pulsed Labelling HDX)

To examine the reversibility of light-induced structural changes in cryptochrome, pulsed-labelling experiments were performed that highlighted two dynamic regions, the PBL and the PL. Both had shown strong, immediate responses in the continuous HDX time course, with significant protection detectable within the first 15 s of exchange. To test how stably these changes persist once the light stimulus is removed, samples were illuminated for 20 min to allow the protein to adopt a light-adapted state, then returned to darkness for recovery intervals ranging from 15 s to 3 h before applying a uniform 15 s deuterium pulse. This approach provides snapshots of the conformational ensemble at defined recovery points and allows monitoring of how quickly the protein relaxes towards the dark state.

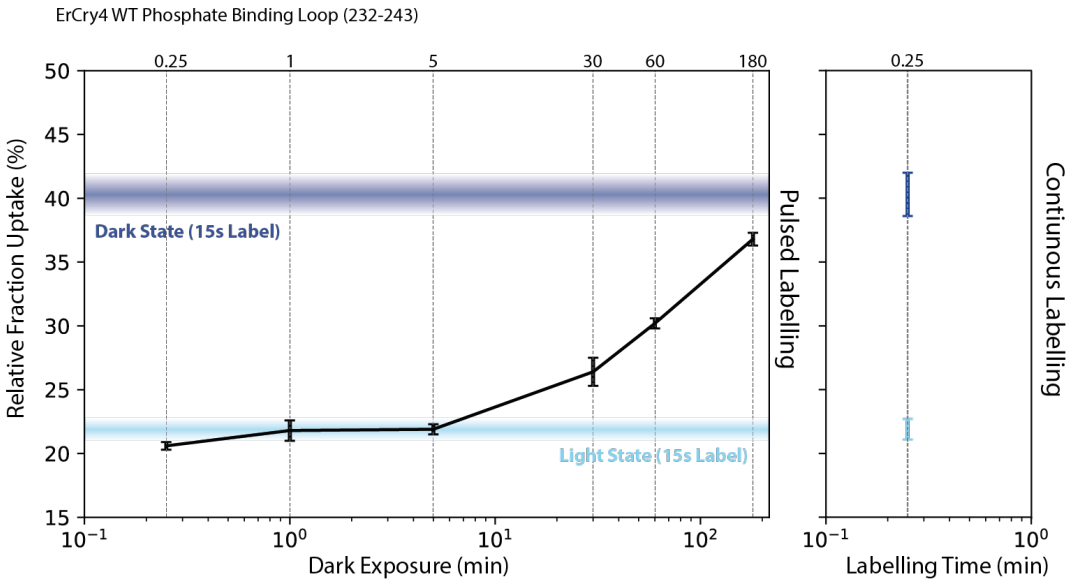


Figure 4.17: Pulsed-labelling HDX for the peptide covering the PBL of *Er*Cry4a (232-243). RFU is shown after a fixed deuterium pulse with varying dark-state recovery times. Curves are compared to DS (dark blue) and LS (light blue), allowing the transition of the peptide from LS back to DS to be monitored.

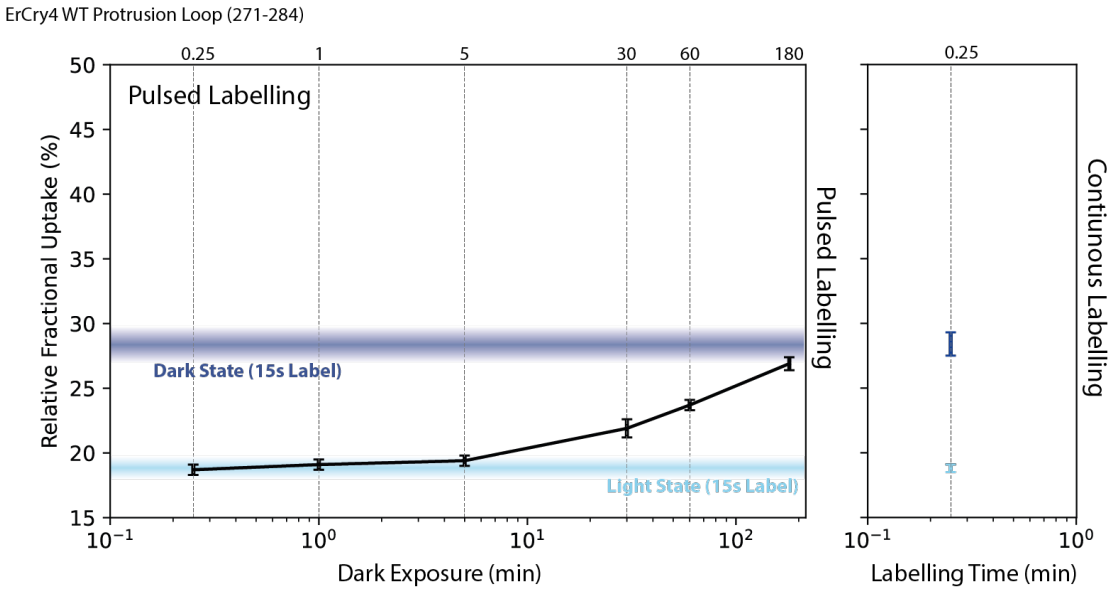


Figure 4.18: Pulsed-labelling HDX for the peptide covering the PL of *Er*Cry4a (271–284). RFU is shown after a fixed deuterium pulse with varying dark-state recovery times. Relative to the PBL, the PL displays weaker light-dependent protection.

The behaviour of the PBL in these experiments was particularly clear (Figure 4.17). Immediately after illumination, the PBL showed strong protection relative to DS, consistent with the continuous time course. After light removal, the loop remained protected for several minutes, showing little difference from the illuminated sample. Recovery towards the DS conformation became evident after about 5 min and continued progressively, following first-order kinetics with a time constant of approximately 83 min. This behaviour suggests that the PBL acts as a gating element that remains stabilised in the light-adapted state but can revert to a solvent-accessible conformation once illumination ceases.

The PL displayed a similar pattern but with a smaller magnitude (Figure 4.18). Protection in the light state was reproducible but consistently weaker than in the PBL, indicating a less pronounced stabilisation of the loop. Recovery followed comparable first-order behaviour, with a time constant of around 72 min and reached the DS baseline within the 3 h measurement window. The smaller magnitude but similar kinetics imply that the PL responds to changes in the flavin environment through contacts shared with the PBL but does not undergo as large a conformational shift.

The pulsed-labelling data show that both the PBL and PL undergo reversible, light-dependent structural changes with comparable relaxation rates. Their dynamic properties are consistent with their location at the entrance to the FAD pocket, where they likely regulate cofactor accessibility. The ability of these loops to switch between light and dark states on similar timescales suggests a finely tuned mechanism for resetting cryptochrome conformation in response to changing illumination.

4.6 ECD analysis of the PBL

To improve the localisation of protection seen within the PBL, the peptide [FTKPRTIPNSLL] was selected for HDX–ECD analysis across five labelling times (15 s, 1 min, 5 min, 30 min, 60 min). This sequence was chosen because it spans the central portion of the loop and had already shown light-dependent protection in the peptide-level HDX data, making it an ideal candidate for higher-resolution analysis. By

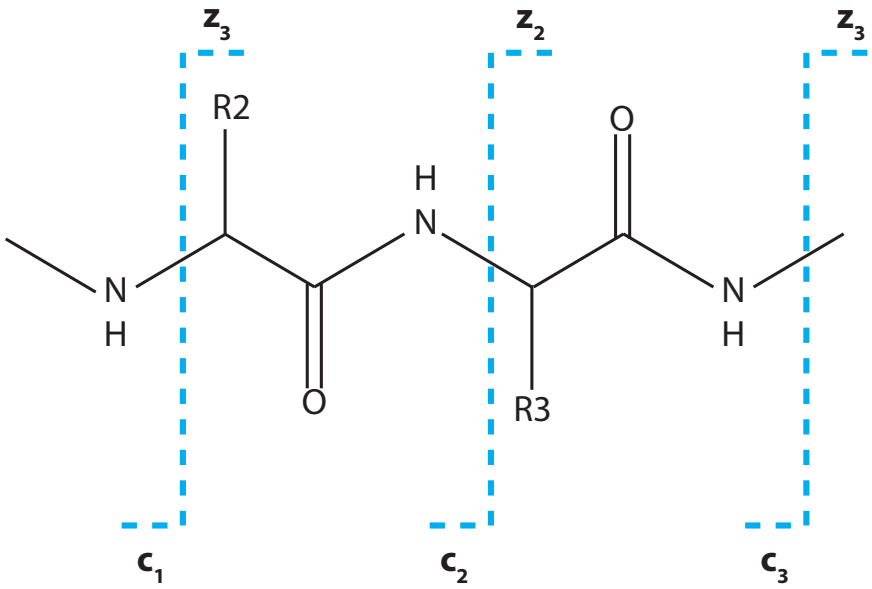


Figure 4.19: Schematic representation of backbone cleavage sites that generate c_n and z_n ions during electron-capture dissociation (ECD). Cleavage occurs at the N–C_α bond, producing an N-terminal c_n fragment (left of the break) and a complementary C-terminal z_n fragment (right of the break). The blue dashed boxes indicate the positions of successive c and z ions along the peptide backbone.

fragmenting the labelled peptide directly in the mass spectrometer, ECD generates a series of c- and z-ions that give values of deuterium uptake at successive backbone positions (Figure 4.19). Due to time constraints, only one replicate was acquired for each time point. As a result, subsequent fitting and the associated R^2 values are weaker than would ideally be desirable. Nevertheless, because protection factors are typically interpreted on an order of magnitude basis, the available data are still sufficient to extract meaningful trends and to identify the secondary structure characteristics of the regions examined.

In this case, c-ions from c4 through c11 were observed with sufficient intensity and reproducibility to provide near-continuous coverage across the peptide. The availability of this overlapping fragment series means that changes in uptake can be localised more precisely than at the peptide level, enabling a residue-by-residue view of how protection is distributed along the PBL. The data were subsequently fitted using a new beta-version software platform under development

at Waters Corporation, provisionally named NewMarket. As this software is still in development and details are not yet publicly available, the present study represents one of the first demonstrations of its application to residue-level HDX analysis.

4.6.1 Intrinsic rates

Table 4.1: Position-specific intrinsic exchange rates (k_{int}) for peptide FTKPRTIPNSLL. Each row shows the central residue (n) together with its flanking neighbours ($n-1$, $n+1$), including residues outside the peptide (S–1 upstream and P12 downstream). Non-exchangeable positions (F0, P3, P7) are listed for completeness but have no k_{int} values assigned.

$(n-1)$	n	$(n+1)$	k_{int} (s^{-1})
S–1	F0	T1	–
F0	T1	K2	2.3
T1	K2	P3	3.4
K2	P3	R4	–
P3	R4	T5	1.6
R4	T5	I6	3.3
T5	I6	P7	0.69
I6	P7	N8	–
P7	N8	S9	4.1
N8	S9	L10	11.0
S9	L10	L11	1.2
L10	L11	P12	0.38

As a first step, position-specific intrinsic rate constants (k_{int}) were calculated using the Nguyen/Bai spreadsheet formalism [146, 147]. These values predict the exchange behaviour of a fully unstructured peptide at the experimental pH and temperature. Non-exchangeable positions (the first amide and all prolines) were excluded, while all other residues were assigned rates according to their side-chain identity together with nearest-neighbour corrections derived from the flanking $n-1$ and $n+1$ residues. This ensures that each backbone amide is modelled with a context-dependent k_{int} rather than a simple residue-type average and accounts for sequence-specific influences that can significantly accelerate or decelerate intrinsic exchange. The resulting values are summarised in Table 4.1, where both the central residue and its adjacent neighbours are listed for clarity, including the flanking S–1 and P12 residues outside the analysed peptide.

The distribution of k_{int} values highlights several points. First, polar residues such as Ser9 are predicted to exchange extremely rapidly ($\sim$11 s^{-1}), reflecting their propensity for solvent exposure and weak hydrogen bonding in unfolded conformations. By contrast, hydrophobic positions such as Leu11 are predicted to exchange very slowly (< 0.5 s^{-1}), consistent with amides adjacent to bulky, non-polar side chains that disfavour transient solvent access. Second, the overall mean k_{int} across the sequence falls in the range 2–4 s^{-1}, consistent with moderately exposed sites under the experimental conditions. Finally, the variation across the sequence emphasises the importance of residue-specific corrections: neglecting nearest-neighbour effects would obscure these local differences and risk systematic bias in subsequent analyses.

4.6.2 Kinetic fitting of experimental exchange rates

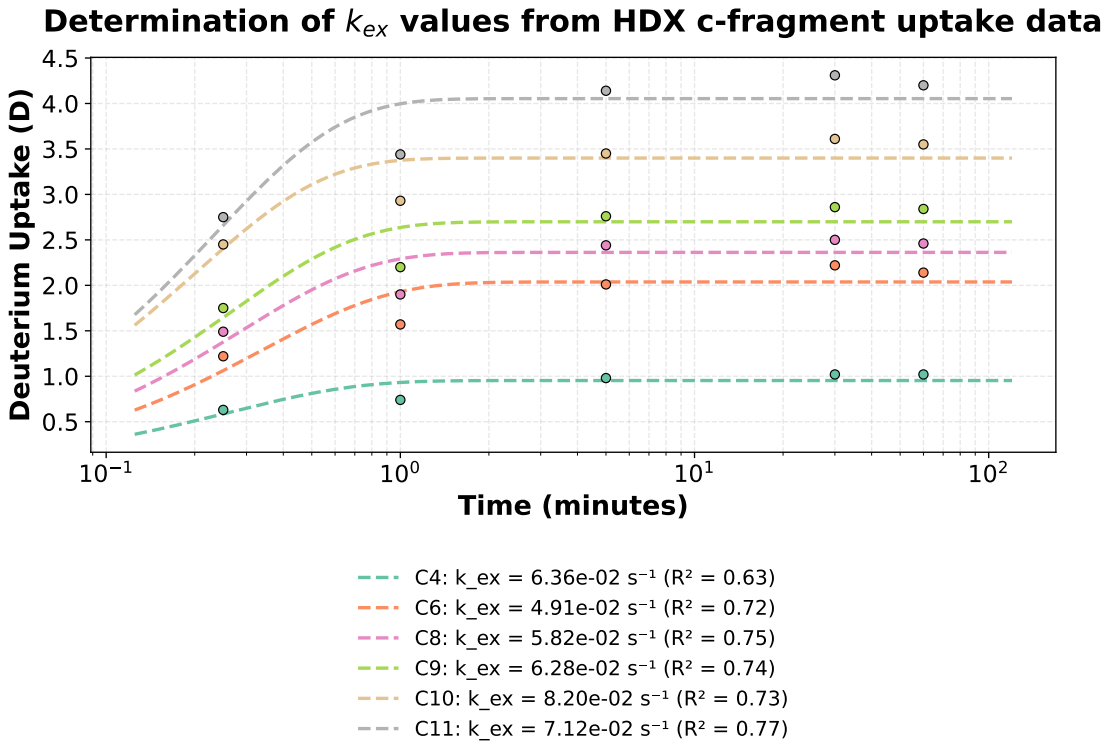


Figure 4.20: Experimental deuterium uptake data for *c*-ion fragments c4–c11 fitted to a single-exponential uptake model. Points represent measured uptake values; dashed lines indicate model fits. Reported k_{ex} values lie between 5×10^{-2} and 8×10^{-2} s^{-1}, with R^2 values from 0.63 to 0.77.

Experimental deuterium uptake curves for each *c*-ion fragment were fit to a single-exponential uptake model:

$$D(t) \;=\; D_{\max}\left(1 - e^{-k_{\mathrm{ex}}t}\right),$$

where k_{ex} is the apparent exchange rate constant and $D_{\max}$ the maximum deuterium incorporation. Rather than allowing $D_{\max}$ to vary freely, it was fitted to the experimentally observed uptake at the longest labelling point (60 min), corrected for back-exchange. This ensures that the regression is driven by the uptake profile rather than by arbitrary scaling and that the fitted k_{ex} values reflect the actual approach of each fragment towards its experimental plateau.

In the context of HDX, k_{ex} represents the observed first-order rate constant at which backbone amides incorporate deuterium under the experimental conditions. It is not a pure measure of chemical exchange, but an apparent constant that integrates several processes: the intrinsic chemical exchange rate (k_{int}), the stability of local hydrogen bonding, transient structural opening events and solvent accessibility. A higher k_{ex} therefore indicates faster exchange, typically associated with greater flexibility or reduced protection, whereas lower k_{ex} reflects structural stabilisation and persistent hydrogen bonding.

The fitted k_{ex} values were very similar across the fragment series, with rates of $\sim 5 \times 10^{-2}$ s^{-1} for c4-c6 and slightly higher values approaching 8×10^{-2} s^{-1} for longer fragments extending to the C-terminus (c9–c11). This trend suggests that the additional residues near the end of the peptide contribute greater conformational mobility, resulting in faster apparent exchange. Representative fits are shown in Figure 4.20, with correlation coefficients in the range $R^2 = 0.63$-0.77.

Interpreting these results requires consideration of the structural context. The PBL is a loop region predicted to be intrinsically disordered and is therefore expected to exchange rapidly and homogeneously. The fact that we still observe measurable protection and residue to residue variation indicates that, even within a disordered segment, local structural fluctuations and transient hydrogen-bonding networks modulate exchange behaviour. The fitted k_{ex} values therefore provide a

kinetic window into how this disordered loop samples protected and flexible states, information that can be refined using the residue-level analysis.

4.6.3 Protection factors (PFs)

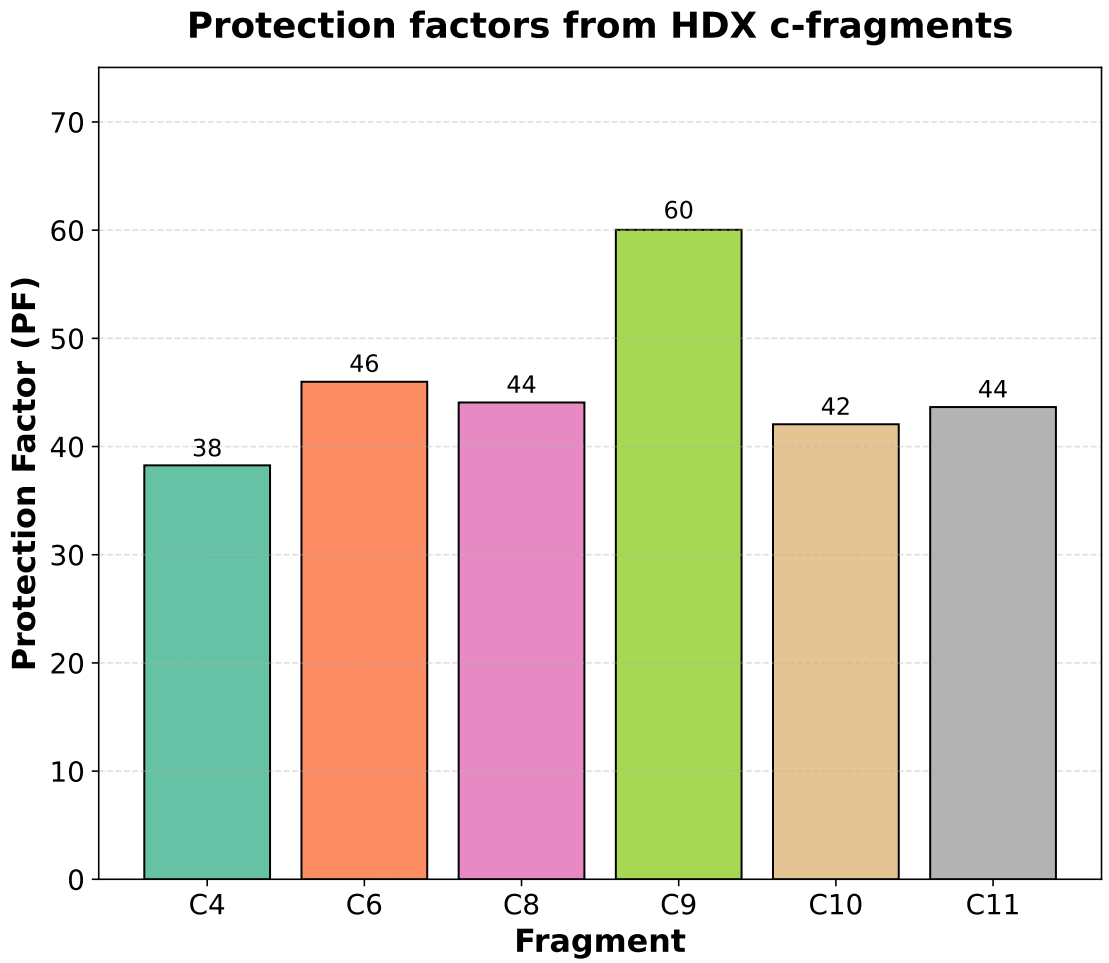


Figure 4.21: Protection factors calculated for *c*-ion fragments. k_{int} values were averaged across exchangeable residues within each fragment. PFs fall in a narrow window (40–60), indicative of moderate protection throughout the sequence.

Protection factors quantify the extent to which local structure suppresses exchange relative to the fully unfolded state and are defined as the ratio of the intrinsic exchange rate constant to the experimentally observed exchange rate constant:

$$PF = \frac{k_{\text{int}}}{k_{\text{ex}}}.$$

Across the fragment series, PFs range from about 38 to 60, indicating consistently low protection across the PBL. The lowest value (c4, $PF \approx 38$) and the highest (c9, $PF \approx 60$) differ only slightly, suggesting that the loop shows similar flexibility along its length. These values suggest that the PBL is not fully disordered, but neither is it rigidly structured. It behaves as a flexible, solvent-exposed region that retains some transient stabilisation, consistent with its role in light-dependent conformational change.

4.6.4 Residue-level localisation

Fragment-level PFs indicated that the PBL peptide is only weakly protected, with values within a narrow range of about 38–60. This uniformity suggests that the loop remains consistently flexible rather than adopting distinct stable or disordered segments. However, averaging across multiple residues inevitably conceals local variation and the aim of the ECD analysis was to resolve such differences. To achieve this, a pairwise subtraction approach was applied between consecutive *c*-ions. When multiple residues were introduced (for example, c4→c6), the observed uptake increment was divided equally between them to yield per-residue k_{ex} values. This assumption provides a practical route to residue-level information, though it inevitably smooths over fine differences between neighbouring sites. Non-exchangeable positions (F0, P3, P7) were retained in the plot at zero to preserve sequence context (Figure 4.22).

To clarify which positions are more or less directly defined, Table 4.2 summarises the fragment sources used for each residue. Positions derived from single-residue increments (e.g. N8, S9, L10, L11) are well defined, whereas those obtained by dividing increments between two or more residues (e.g. T5, I6) or averaged across an entire fragment (e.g. T1, K2, R4) are less specific.

At this higher resolution, differences across the sequence become clear. The per-residue PFs span nearly two orders of magnitude (from ∼5 to ∼120). Ser9 shows the strongest protection ($PF \sim 120$), supported by a single-residue increment, while Thr5 also appears more protected ($PF \sim 80$), though this estimate is less precise

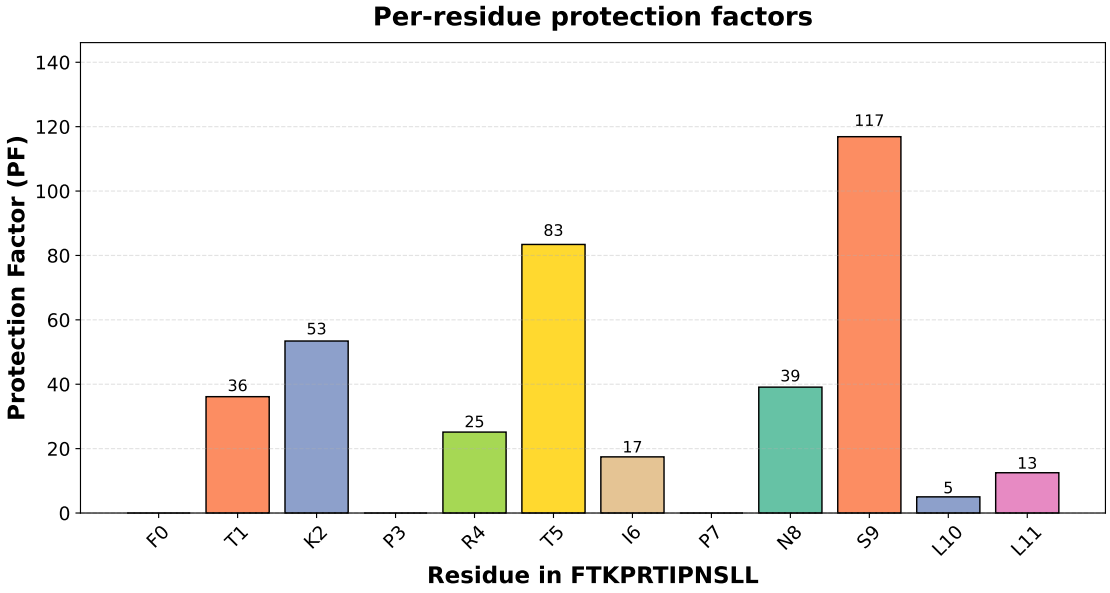


Figure 4.22: Per-residue PFs obtained by pairwise subtraction, using equal division of uptake increments when multiple residues were introduced. Elevated protection is evident at T5 and especially S9, whereas L10 exhibits markedly lower protection, consistent with increased flexibility at the C terminus. Non-exchangeable positions (F0, P3, P7) are retained at zero to preserve context.

Residue	Fragment source(s)	Averaged across (residues)
F0	c4 (present; non-exchangeable)	0
T1	c4	3 (T1, K2, R4)
K2	c4	3 (T1, K2, R4)
P3	c4 (present; non-exchangeable)	0
R4	c6–c4 difference	2 (R4, T5)
T5	c6–c4 difference	2 (R4, T5)
I6	c8–c6 difference	2 (I6, N8)
P7	c8 (present; non-exchangeable)	0
N8	c9–c8 difference	1 (N8)
S9	c10–c9 difference	1 (S9)
L10	c10–c9 difference	1 (L10)
L11	c11–c10 difference	1 (L11)

Table 4.2: Residue-level PF derivation for `FTKPRTIPNSLL`. For each residue, the fragment contrast used to estimate k_{ex} is listed, together with the number of residues across which the observed increment was distributed. Zeros indicate non-exchangeable positions (F0, P3, P7) that were included for context but excluded from PF estimation.

because it was obtained by equal division over multiple residues. By contrast, Leu10 is markedly less protected ($PF \sim 5$), consistent with a flexible, solvent-exposed terminus. The remaining positions fall between these extremes, forming a band of weak protection consistent with the fragment-level analysis. These results show that the PBL is not uniformly disordered, most sites display modest stabilisation, with S9 emerging as the most clearly protected position and L10 as a flexible terminus.

Although PFs are convenient ratios, their interpretation becomes clearer on an energetic scale. Conversion to $\Delta G_{\mathrm{op}} = RT \ln(PF)$ estimates the free energy penalty required to transiently open the local structure and permit exchange. In this framework, a higher ΔG_{op} reflects an amide that is stabilised by persistent interactions, while a lower value corresponds to a site that is easily accessible to solvent.

The observed PFs of 5-117 correspond to ΔG_{op} values between $\sim$1.0 and 2.8 kcal mol^{-1}. This span highlights the subtle energetic landscape of the PBL. Thr5 ($\sim$2.6 kcal mol^{-1}) and Ser9 ($\sim$2.8 kcal mol^{-1}) are the most stabilised positions, approaching the range expected for transient secondary-structural elements. By contrast, Leu10 drops to only $\sim$1.0 kcal mol^{-1}, indicating that its backbone exchanges with little energetic cost, consistent with a solvent-exposed and mobile terminus. Most other positions cluster in the middle of this range (1.5–2.3 kcal mol^{-1}), reflecting modest protection relative to a random coil.

These results give an energetic view of the PBL showing that the loop is not completely disordered, but is also not tightly folded. Most residues exchange with only small energy barriers, while a few positions such as Thr5 and Ser9 show slightly higher resistance and the C-terminal end (Leu10) remains flexible. This weak stability may be functionally important, allowing the loop to adjust to movements around the flavin pocket and to respond to light-induced structural changes.

4.6.5 Interpretation

The HDX–ECD data reveals that [FTKPRTIPNSLL] does not behave as a completely unstructured random coil, nor does it form a rigid secondary structure. Instead, the peptide exhibits moderate, position-dependent protection consistent

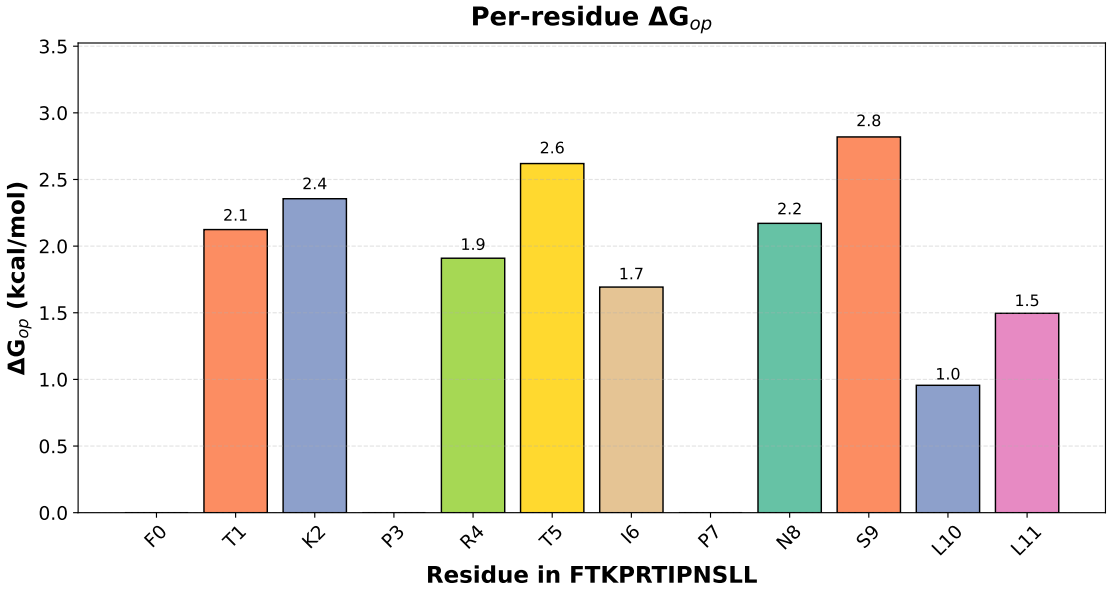


Figure 4.23: Per-residue opening free energies $\Delta G_{\mathrm{op}} = RT\ln(PF)$. Values span 1.0–2.8 kcal mol^{-1}, reflecting modest stabilisation. S9 shows the highest ΔG_{op}, while L10 falls to the lowest end of the scale, highlighting the balance between stabilised and flexible positions within the PBL.

with transient local structuring. The N-terminal residues (Thr1–Arg4) show PFs in the 25–53 range, compatible with dynamic but stabilised conformations. Protection peaks at Thr5 and Ser9, suggesting involvement in transient hydrogen bonding networks or local clustering, whereas Leu10 is comparatively unprotected, consistent with terminal flexibility.

The conversion of PFs into ΔG_{op} emphasises that the energetic cost of locally unfolding the backbone lies in the low range of 1–3 kcal mol^{-1}. This is substantially lower than the stability of canonical secondary-structure elements, where α-helices typically show 5–8 kcal mol^{-1} per residue and β-sheets 6–10 kcal mol^{-1} or higher [78]. Against this benchmark, the PBL is only marginally stabilised. Yet the stabilisation at Thr5 and Ser9, approaching 2.6–2.8 kcal mol^{-1}, sits at the lower end of helix-like stability, implying that the loop is capable of transiently sampling ordered conformations.

This interpretation is consistent with structural predictions. As stated previously, AF2 models the PBL as largely unstructured, whereas AF3 predicts additional local order centred on Pro235 (Pro3 here), which introduces a kink that could

cause transient secondary-structure formation. The HDX–ECD data suggest that the experimental ensemble lies between these structures: generally flexible, but with embedded positions capable of stabilisation. Comparable behaviour has been observed in molecular dynamics simulations of pigeon Cry4, where the PBL was found to act as a dynamic gate controlling access to the FAD pocket [188]. In those simulations, loop mobility responded to the redox state of the flavin, supporting the idea that marginal stabilisation allows the PBL to shift rapidly between conformational states in response to photoreduction.

This stability is advantageous from a functional standpoint: it permits the PBL to respond rapidly to conformational cues without requiring large-scale unfolding, while still allowing transient structuring that could modulate cofactor accessibility. In this way, the energetic profile observed here aligns with computational and structural predictions, reinforcing the role of the PBL as a responsive gating element in cryptochrome signalling.

Finally, several limitations must be acknowledged. Single-exponential fits average over multiple microscopic processes and may obscure biphasic kinetics. The pairwise subtraction approach assumes equal contribution from simultaneously added residues and is sensitive to the precise ECD fragmentation pattern. Nonetheless, by combining fragment-level and residue-level analysis with position-specific intrinsic rates, we obtain a coherent energetic picture: the PBL peptide is moderately protected, with subtle hotspots of stabilisation and incurs an energetic penalty of only $\sim$1–3 kcal mol^{-1} to transiently open for exchange.

4.7 Magnet-Induced Differences

To assess whether a static magnetic field alters the light-activated conformational dynamics of *Er*Cry4a, differential HDX–MS analysis was performed on samples incubated with and without a permanent magnet during labelling. As shown in Figure 4.24, differences between the two states were minimal ($\pm$3% RFU) and displayed no consistent magnet-dependent stabilisation or destabilisation. Statistical analysis using the hybrid significance test (99% confidence interval; ΔHDX threshold

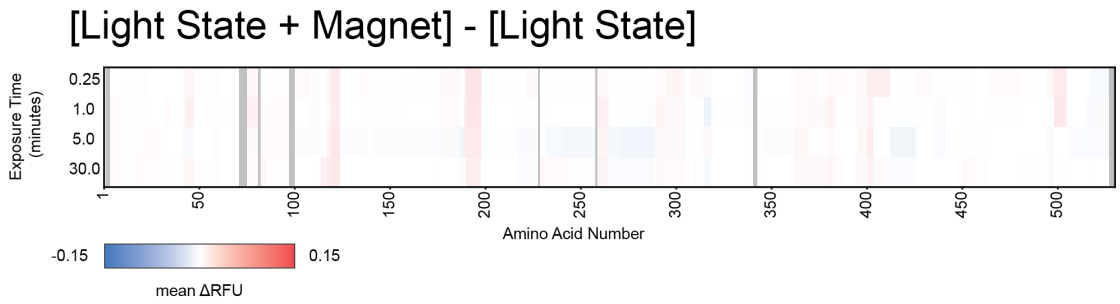


Figure 4.24: Differential HDX–MS heatmap comparing the light state in the presence of a static magnetic field (LSM) with the control light state (LS). Colour coding represents the difference in relative fractional uptake (ΔRFU), plotted along the primary sequence. White indicates no change, while red and blue correspond to relative increases or decreases in uptake, respectively. Grey indicates regions without coverage. The heatmap is largely white indicating that exposure to a static magnetic field did not measurably alter the backbone dynamics of *Er*Cry4a under the conditions tested.

0.18 Da; $p < 0.01$) confirmed the absence of significant effects. Across all time points, none of the 116 peptides exceeded threshold values, with the volcano plots clustering tightly around zero (Figure 4.25).

The absence of significant differences indicates that a static magnetic field does not measurably alter the backbone dynamics of *Er*Cry4a under the conditions tested. This result contrasts with the clear light-induced changes, confirming that the experimental workflow was sufficiently sensitive to detect structural responses when present. It is therefore unlikely that the lack of a magnetic effect reflects limitations in peptide coverage or data quality. Instead, these findings support the view that the primary influence of the magnetic field in the radical-pair mechanism lies at the level of spin chemistry in transient flavin–tryptophan radical pairs, rather than in large-scale conformational rearrangements detectable by HDX–MS. These quantum-level interactions may not translate into measurable differences in solvent accessibility or hydrogen bonding within the timescales examined.

An alternative explanation is that magnet-induced structural effects may depend on cofactors or interaction partners absent in the purified protein. *In vivo*, Cry4a may associate with membranes or interact with downstream signalling partners that modulate conformational changes following radical-pair formation [182, 191]. The absence of an effect *in vitro* therefore does not exclude a role for magnetic fields in

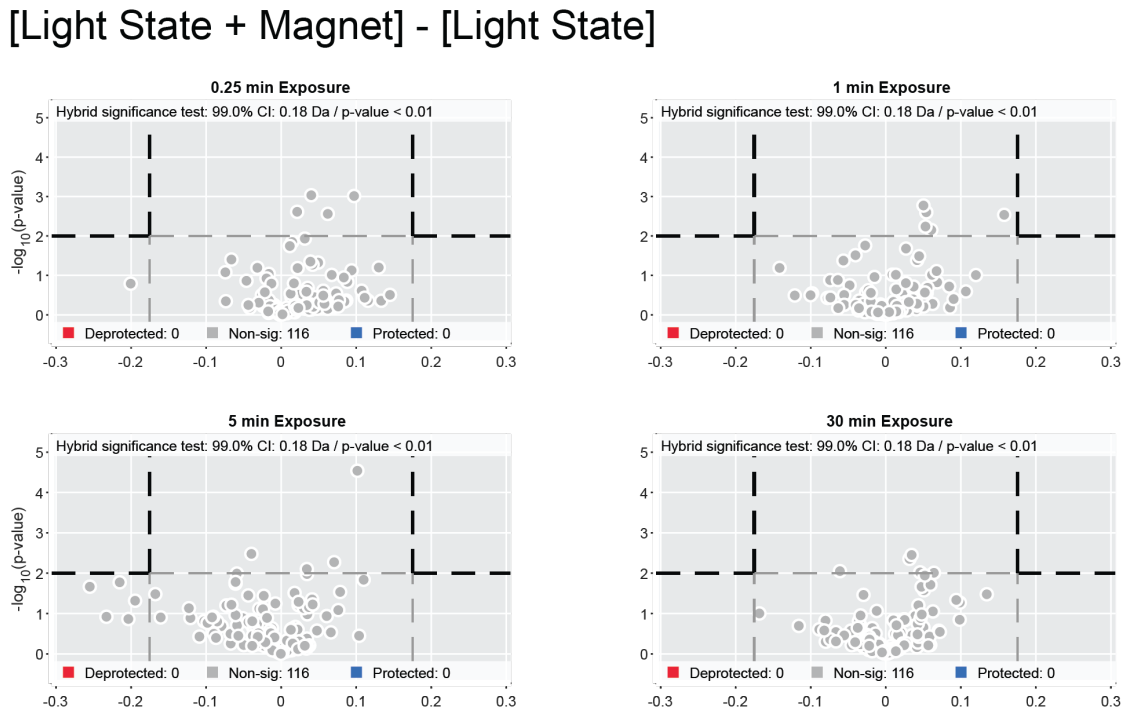


Figure 4.25: Volcano plot of differential HDX–MS results comparing the light state in the presence of a static magnetic field (LSM) with the control light state (LS). Each point represents a peptide, plotted by the difference in uptake (ΔHDX, x-axis) against significance ($-\log_{10} p$, y-axis). The vertical lines indicate the ΔHDX threshold of 0.18 Da and the horizontal line marks the 99% confidence level ($p < 0.01$). Data points are deemed as significnt if they fall within the top right or left quadrants. Axes are scaled to the data range. All peptides clustered near zero and below the significance cutoff, confirming that magnet exposure did not produce measurable conformational changes in *Er*Cry4a.

regulating Cry4a activity *in vivo*, but rather suggests that any such influences do not manifest as backbone dynamics detectable by HDX–MS in the isolated protein.

Effect of reducing agents and the use of BME

The absence of measurable magnetic field effects in these experiments is likely to be influenced by the reducing conditions employed. In order for a magnetic field effect to arise, the system must cycle through multiple radical pair formation and recombination events, allowing differences in singlet-triplet interconversion rates to accumulate. Under strongly reducing conditions, particularly in the presence of β-mercaptoethanol (BME), the photochemistry of avian cryptochromes is altered such that the system no longer undergoes efficient radical pair cycling. Instead,

BME promotes rapid formation and stabilisation of the semiquinone state (FADH·), effectively trapping the flavin in this state and preventing repeated passage around the radical pair mechanism.

Reducing agents such as BME and DTT have been reported to increase both the yield and stability of the FADH· state in avian Cry4a proteins. This behaviour may attributed to quenching of tryptophan-derived radicals within the electron transfer chain, which suppresses radical recombination and thereby favours accumulation of $FAD^{\bullet -}$ and subsequently FADH·. Although this leads to a larger radical yield, it also alters the natural photocycle and can substantially slow the regeneration of the ground state. As a result, the radical pair dynamics become limited, reducing the opportunity for repeated radical pair cycling that is required to generate a detectable magnetic field effect under typical experimental conditions.

Consequently, although reducing conditions may more closely resemble aspects of the intracellular environment and keep the sample monomeric, the use of BME in these experiments likely constrained the radical pair chemistry to a regime in which magnetically sensitive processes could not manifest as measurable spectral or structural signals. This provides a plausible explanation for the absence of detectable magnetic field effects under the conditions tested.

4.8 Conclusions

This chapter establishes *Er*Cry4a as a model system for probing the structural dynamics of avian cryptochromes. Using HDX–MS as the principal tool, complemented by pulsed-labelling and ECD experiments, I have characterised the conformational behaviour of the wild-type protein under dark, light and magnetic-field conditions.

The data confirms that *Er*Cry4a shares the canonical organisation of stable and dynamic regions seen across the cryptochrome–photolyase family. The most dynamic element is the CTT, which exchanges rapidly throughout and reinforces its status as a flexible signalling domain.

Illumination induces reproducible, statistically significant changes in defined regions. The PBL, PL and helix α22 consistently exhibit light-dependent protection

and an additional cysteine-containing peptide (404–412) also stabilises under light, linking this region to previously proposed dimerisation sites. These changes demonstrate that photoexcitation alters local dynamics without perturbing the global fold, providing structural signatures for potential signal propagation following flavin photoreduction.

By contrast, static magnetic fields produced no measurable changes in backbone dynamics. The indistinguishable HDX profiles of magnet-exposed and control samples suggest that magnetic effects act primarily at the level of radical-pair spin chemistry, rather than through conformational rearrangements detectable by HDX. It remains possible, however, that magnetically modulated responses require cofactors or partners absent in the isolated protein system.

Pulsed-labelling experiments revealed the reversibility of these light-induced changes. Both the PBL and PL remained protected immediately after illumination but progressively relaxed back to dark-state dynamics over minutes to hours. This demonstrates that cryptochrome conformations are not locked states but transient equilibria that reset upon removal of light, consistent with the physiological requirement to cycle between signalling-competent and basal states.

Residue-level localisation with ECD further refined the picture of the PBL. Protection factor analysis across *c*-ion fragments showed a variation in protection, suggesting that the loop adopts partial structure rather than behaving as uniformly disordered. Although the kinetic fits are approximate and limited by the assumptions of single-exponential modelling, this approach illustrates the potential of combining HDX with gas-phase fragmentation to extract near-residue resolution.

In summary, these findings establish a detailed reference for the structural dynamics of avian cryptochromes. The experiments define which regions of *Er*Cry4a respond to light and how these changes evolve over time, showing that local structural adjustments rather than global rearrangements underlie activation. This behaviour supports the view that photoreduction within the FAD pocket is transmitted through selective stabilisation of gating loops and terminal helices, providing a pathway for structural signalling. The results therefore place *Er*Cry4a at the centre of a

mechanistic framework that connects photochemistry to conformational change, forming the basis for the mutant and comparative studies that follow.

4.9 Materials and Methods

4.9.1 Materials

All reagents and chemicals were purchased from Sigma Aldrich (Gillingham, UK) unless otherwise stated. Recombinant cryptochrome proteins were expressed in *E. coli* and purified by collaborators in the laboratory of Henrik Mouritsen at the Carl von Ossietzky University of Oldenburg, Germany, using established protocols [17]. Samples were shipped on ice in storage buffer containing 20 mM Tris, 250 mM NaCl, 2 mM DTT and 20% (v/v) glycerol and stored at −80 °C until required for experiments. For HDX-MS, three buffers were prepared: an equilibration buffer consisting of 5 mM potassium phosphate in H_2O at pH 7.0, a labelling buffer consisting of 5 mM potassium phosphate in D_2O at pD 7.0 and a quench buffer consisting of 50 mM potassium phosphate in H_2O adjusted to pH 1.9.

4.9.2 HDX-MS

Initial continuous labelling experiments were performed by Dr Angela Gehrckens. HDX-MS experiments were carried out under carefully controlled conditions. All protein handling was performed under dim red illumination in an otherwise dark environment to prevent unwanted photoactivation. Protein aliquots were thawed immediately prior to analysis and diluted to volumes between 10 and 16 μL. Before labelling, each sample was equilibrated for at least 20 min at 20 °C within a temperature-controlled chamber. The light state was generated by continuous exposure to 450 nm blue light at intensities ranging from 0.03 to 0.06 ± 0.001 mW cm^{-2} , while the dark state was maintained in complete darkness (Figure 4.26). To generate magnet states, samples were placed in custom-built holders positioned above neodymium-iron-boron magnets (10 mm × 1.5 mm, N42 grade, Magnet Expert Ltd.) with a nominal surface field strength of 160 mT. Measurements confirmed that

the magnetic field at the sample position corresponded to approximately 18–25 mT at a distance of 2–3 mm from the magnet face (Figure 4.27).

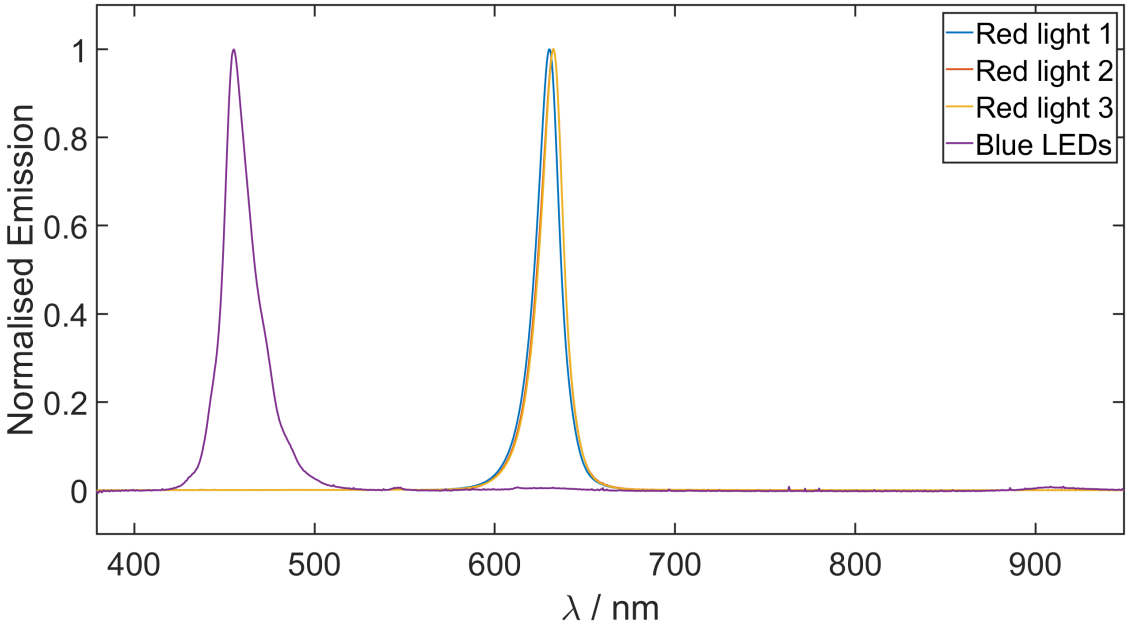


Figure 4.26: Emission spectra of all lights used during experiments conducted by Dr Angela Gehrckens

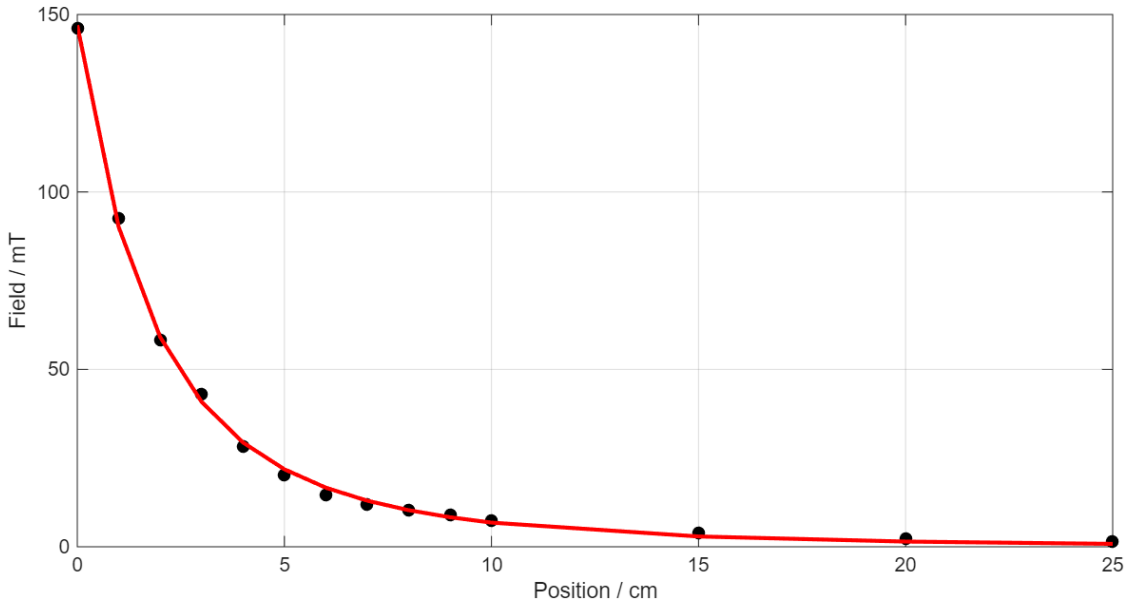


Figure 4.27: Magnet strength over distance away from sample holder as determined by Daniel Cubbin

Labelling reactions were initiated by diluting the protein with deuterated buffer. 55 μL of labelling buffer was added to 5 μL of protein, producing a final solution

of approximately 92% D_2O. For wild-type *Er*Cry4a, 54 μL of labelling buffer was combined with 1 μL of protein, yielding a final deuterium content of approximately 98%. Exchange was stopped by mixing the sample with an equal volume of ice-cold quench buffer. Quenched solutions were immediately injected into the HDX Manager (Waters, Milford, MA, USA) and maintained at 0 °C until reaching the Enzymate Pepsin digestion column (Waters), which was held at 20 °C. Digestion was performed with an isocratic flow of 0.1% formic acid in H_2O at 100 μL min^{-1}. Peptides were collected and desalted on a BEH C18 trapping column (Waters) for 2 min before separation on a reversed-phase analytical column operated at 0 °C with a flow rate of 40 μL min^{-1}. The chromatographic gradient began with 97% H_2O and 3% MeCN, shifted to 65% H_2O and 35% MeCN over 7 min, then decreased to 5% H_2O within 1 min and was held for an additional 2 min.

Peptides were analysed on a Synapt G2Si Q-ToF mass spectrometer (Waters) by electrospray ionisation. Instrument parameters included a capillary voltage of 2.8 kV, sample cone voltage of 100 V, source offset of 30 V, source temperature of 80 °C and desolvation temperature of 150 °C. Leucine enkephalin (m/z 556.2771) was infused every 30 seconds as a lock mass for internal calibration. To minimise carryover between runs, a saw-tooth gradient cleaning cycle was applied using 4% acetonitrile and 0.1% formic acid in water supplemented with 0.5 M guanidinium hydrochloride, with intermittent blank injections included as further quality control. The emission spectra of all light sources, including the red bench lights and the blue LEDs used for photoactivation, were independently verified to confirm spectral separation and avoid unintended activation.

4.9.3 Native Mass Spectrometry

Native mass spectrometry experiments employed the same *Er*Cry4a preparations used in HDX-MS. Samples were buffer exchanged into 200 mM ammonium acetate at pH 8.0 using Zeba^{TM} Micro Spin desalting columns with a 40 kDa molecular weight exclusion limit (ThermoFisher Scientific). Measurements were conducted at the University of Oxford on a Q Exactive^{TM} mass spectrometer (ThermoFisher

Scientific) using custom-fabricated gold-coated capillaries for nano-electrospray ionisation. Protein samples were introduced at a concentration of approximately 8 μM. The source temperature was maintained at 150 °C and the capillary voltage was set to 1.0 kV. In-source trapping was applied at −200 V to assist in desolvation and to disrupt weakly bound adducts. The higher-energy collisional dissociation (HCD) cell was operated at 5 V and ion optics were adjusted empirically to maximise transmission of intact protein ions.

4.9.4 Data Analysis

Peptides were identified by MSE fragmentation of non-deuterated controls and processed with ProteinLynx Global Server 3.0 (Waters) for database searching. The results were imported into DynamX 3.0 (Waters) for automated peak picking and assignment. To ensure reliability, stringent filtering criteria were applied: peptides were required to display at least 0.2 fragment ions per amino acid, have a precursor mass accuracy within 5 ppm, contain no more than 25 residues and be detected reproducibly in at least three replicate analyses. Peptides that did not meet these standards, or that showed ambiguous or noisy isotopic distributions, were excluded. Deuterium incorporation was quantified by comparing centroid mass shifts of labelled peptides relative to undeuterated controls.

Native mass spectra were processed using MassLynx V4.2 (Waters, Wilmslow, UK) and structural mapping of differential deuterium uptake was visualised in PyMOL (Schrödinger, New York, USA).

"Holy mutant, batman"

— Robin via Kiera Obi

5

The Effect of Mutations on Robin Cryptochrome 4a

Contents

5.1 Abstract 122
5.2 Apo Protein (R356E) 123
5.2.1 Global Dynamics 124
5.2.2 Response to Stimuli 126
5.3 TrpD Mutant (W369F) 129
5.3.1 Response to Stimuli 131
5.4 Triple Mutant (C317R/Y319F/W369F) 133
5.4.1 Global Dynamics 133
5.4.2 Response to Stimuli 135
5.5 Comparative Discussion 136
5.5.1 Phosphate Binding Loop 136
5.5.2 Protrusion Loop 138
5.5.3 α22 139
5.5.4 Putative Dimer Region 140
5.5.5 Mutation Region 141
5.5.6 Discussion 141
5.6 Conclusions 143
5.7 Materials and Methods 144
5.7.1 Materials 144
5.7.2 HDX-MS 145
5.7.3 Native Mass Spectrometry 146
5.7.4 Data Analysis 146

5.1 Abstract

This chapter examines how specific residues within the flavin-binding pocket and the tryptophan electron-transfer chain control the light-dependent conformational behaviour of European robin cryptochrome 4a (*Er*Cry4a) (Figure 5.1). Building on the wild-type characterisation presented in Chapter 4.9.4, three mutants were analysed using HDX–MS to disentangle the structural roles of FAD binding and distal electron donors.

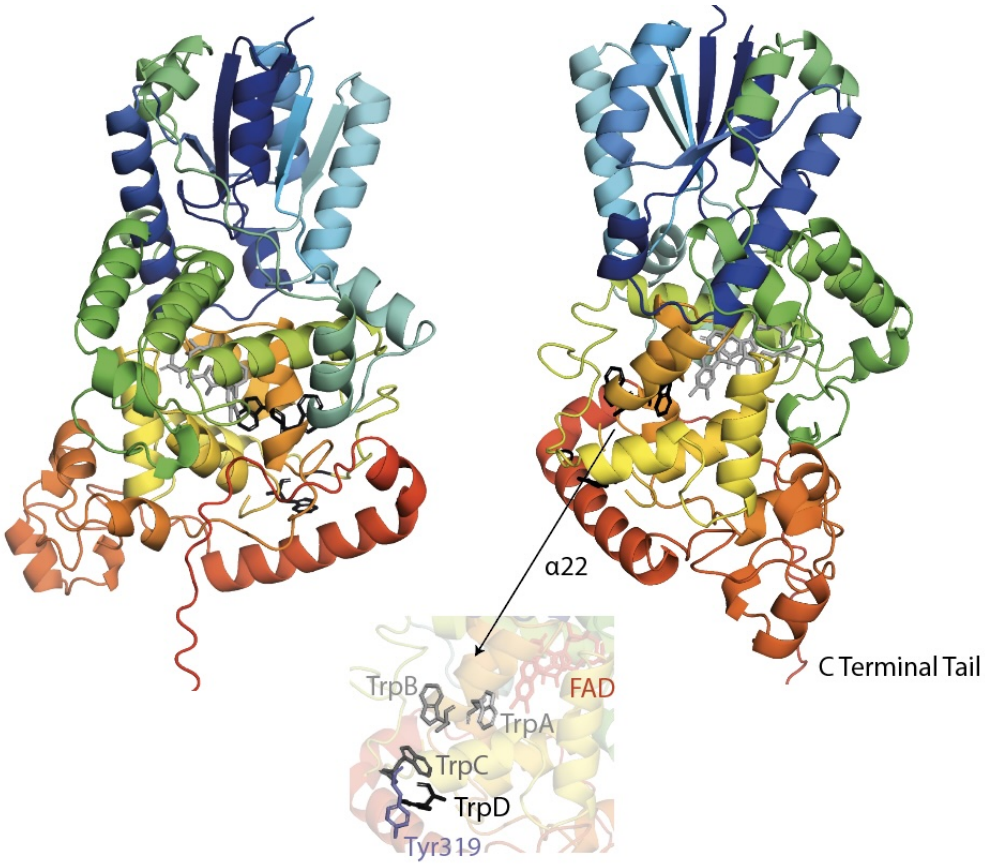


Figure 5.1: Cartoon representation of *Er*Cry4a using AlphaFold2. The FAD shown in orange and the residues involved in the radical-pair mechanism coloured from grey to black along the chain.

An apo mutant (R356E) was generated to prevent FAD binding and assess whether conformational responses are intrinsic to the protein or dependent on cofactor excitation. A single mutant (W369F) was produced to interrupt the

terminal residue of the tryptophan tetrad (TrpD) and test how truncation of the electron-transfer pathway affects structural signalling. Finally, a triple mutant (C317R/Y319F/W369F) was designed to remove both TrpD and Y319 while introducing the arginine residue found at the equivalent position in chicken Cry4a.

HDX–MS revealed that the apo protein retains the overall fold but is unresponsive to light, confirming that FAD binding is essential for initiating structural change. The W369F mutant displayed the same pattern of light-induced protection seen in the wild type, most notably in the PBL, PL and helix α22, but with reduced magnitude, demonstrating that TrpD enhances the amplitude rather than the presence of conformational responses. The triple mutant showed no detectable differences between light and dark conditions, establishing that both TrpD and Y319 are required to propagate the photochemical signal from the flavin pocket to distal structural elements.

These results provide a direct experimental link between flavin photochemistry and protein motion in *Er*Cry4a. They demonstrate that FAD acts as both the structural anchor and the photochemical trigger, while electron transfer through TrpD and Y319 is essential for transmitting the conformational response. The C317R substitution, found naturally in chicken Cry4a, suggests a potential mechanism by which species-specific variations may tune the strength or kinetics of the light-driven response. Data for the W369F mutant were collected in collaboration with Dr Angela Gehrckens. The following sections describe the results for each mutant in turn and compare their dynamic behaviour with the wild-type protein.

5.2 Apo Protein (R356E)

The first mutant tested was the apo protein where FAD binding is prevented. In the WT protein, R356 lies within the flavin pocket in a position where it can directly interact with the ribityl and pyrophosphate groups of FAD. Although no crystal structure is available for *Er*Cry4a, comparable cryptochrome and photolyase structures show conserved arginine residues that have similar interactions with FAD [192, 193]. By homology, it is expected that R356 in robin Cry4a would carry

out a comparable role in stabilising the anionic phosphate groups of the cofactor, validated through its conservation across the cryptochrome/photolyase family [59, 183]. Substitution with glutamic acid was expected to prevent flavin binding by reversing the charge environment. This meant that rather than the strong positive electrostatic stabilisation provided by arginine, the pocket now contains a negatively charged residue that repels the phosphate group.

By generating this mutant, the question of whether light-induced conformational dynamics are an intrinsic property of the protein or strictly dependent on flavin excitation could be directly tested. In addition, the apo protein provides a baseline control for assessing how much of the HDX behaviour observed in WT derives from inherent backbone flexibility rather than cofactor-driven structural responses.

Native MS analysis confirmed that the R356E protein lacked bound FAD, as indicated by the absence of the 785 Da mass increment corresponding to the cofactor.

5.2.1 Global Dynamics

The global uptake profile of the apo protein was compared with WT to assess whether overall folding was preserved (Figure 5.2). Both proteins reached a similar maximum uptake, however, the apo protein showed a larger proportion of peptides at or near saturation, indicating that in the absence of FAD, local flexibility is increased in multiple regions.

Several regions stood out in this comparison, most strikingly, the PBL in the apo protein reached maximal uptake at the first time point (0.25 min) and remained saturated at all later times. In the WT, this loop interacts with the phosphate of FAD and shows robust light-dependent protection. Its immediate saturation in the apo protein indicates that these interactions are lost without the cofactor, leaving the loop highly dynamic and solvent exposed. The PL also showed elevated uptake in the apo protein, in agreement with the idea that contacts with the flavin help to constrain its flexibility in WT. Peptide 404-412, located at a putative dimer interface, exchanged similarly in both proteins but at slightly higher RFU in the apo protein, suggesting a subtle long-range effect of flavin absence. Finally, the

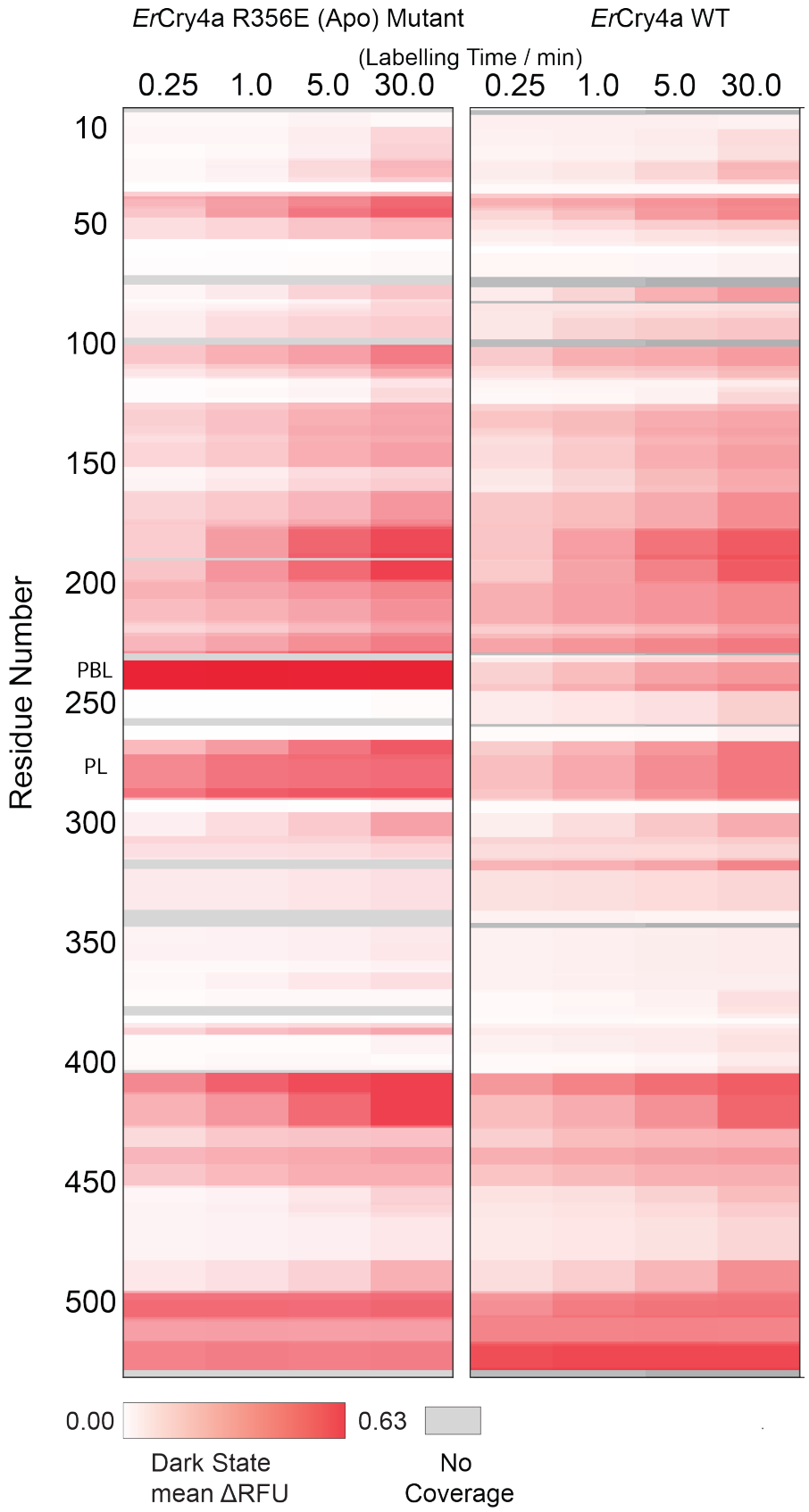


Figure 5.2: Heatmap comparison of uptake in the apo mutant (R356E) (left) and wild type (right) across four labelling times. Regions of lower uptake are shown in white, whilst a higher uptake is indicated in red. Whilst global uptake capacity is similar, the apo protein shows a broader distribution of saturated peptides, particularly in the PBL and PL.

CTT remained highly dynamic in both apo and WT, saturating almost instantly, as expected for an intrinsically disordered region.

These observations indicate that although the overall fold is preserved, FAD contributes strongly to the local stability of flavin-proximal loops.

5.2.2 Response to Stimuli

To test whether any conformational responses remained, the apo protein was examined under LS, DS, LSM and DSM conditions.

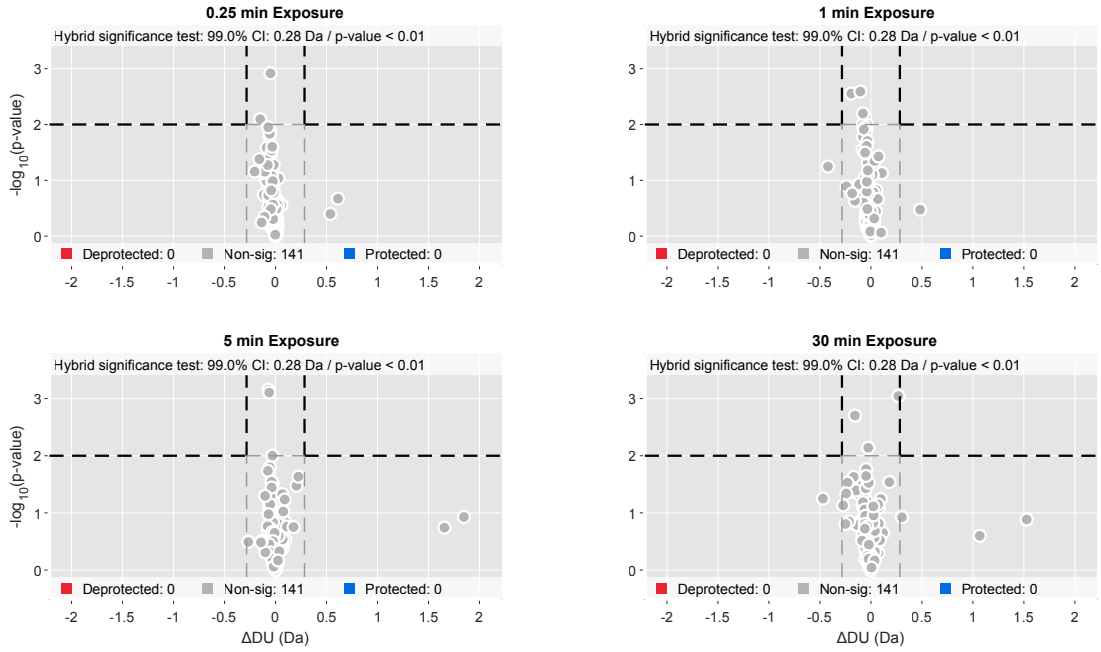


Figure 5.3: Volcano plots comparing LS and DS in the apo protein. None of the 141 peptides tested crossed the significance threshold, confirming absence of light-induced responses.

No significant uptake differences were detected between any of the conditions (Figures 5.3, 5.4, 5.5). The only variations observed were in the CTT, with differences up to ∼4% RFU, but these were inconsistent across replicates and within the expected experimental error. Importantly, the PBL was already saturated in both LS and DS, meaning that even if light-sensitive differences existed, they would be masked. The lack of detectable changes in other regions, however, makes it clear that the apo protein is unresponsive to illumination.

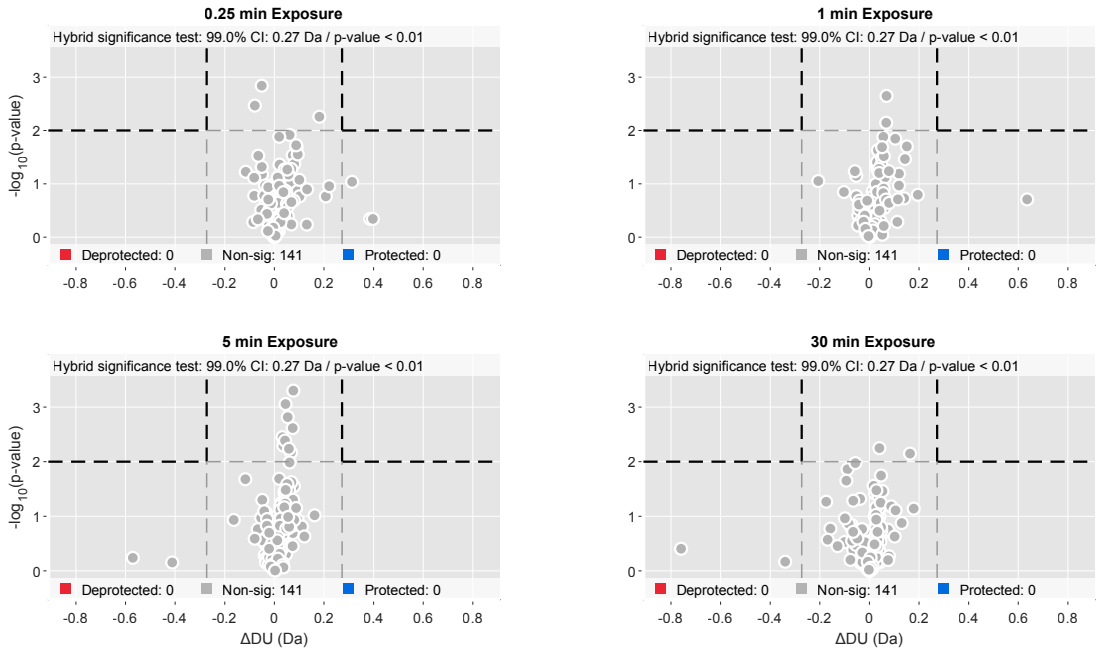


Figure 5.4: Volcano plots comparing LSM and LS for the apo mutant. No reproducible differences were observed, consistent with loss of cofactor-driven responses.

The absence of any measurable light- or magnet-dependent effects in the apo protein reinforces the role of FAD. Without the cofactor, photoexcitation cannot occur, the radical pair cannot form and the protein structure remains insensitive to light. These results also rule out the possibility that conformational changes in WT are driven by intrinsic backbone fluctuations alone and instead are coupled to flavin excitation.

From a mechanistic perspective, this experiment sets the precedent that the protein can fold without FAD, but it cannot respond to stimuli. The apo protein therefore provides a critical negative control, confirming that FAD acts as both the photochemical trigger and a structural base.

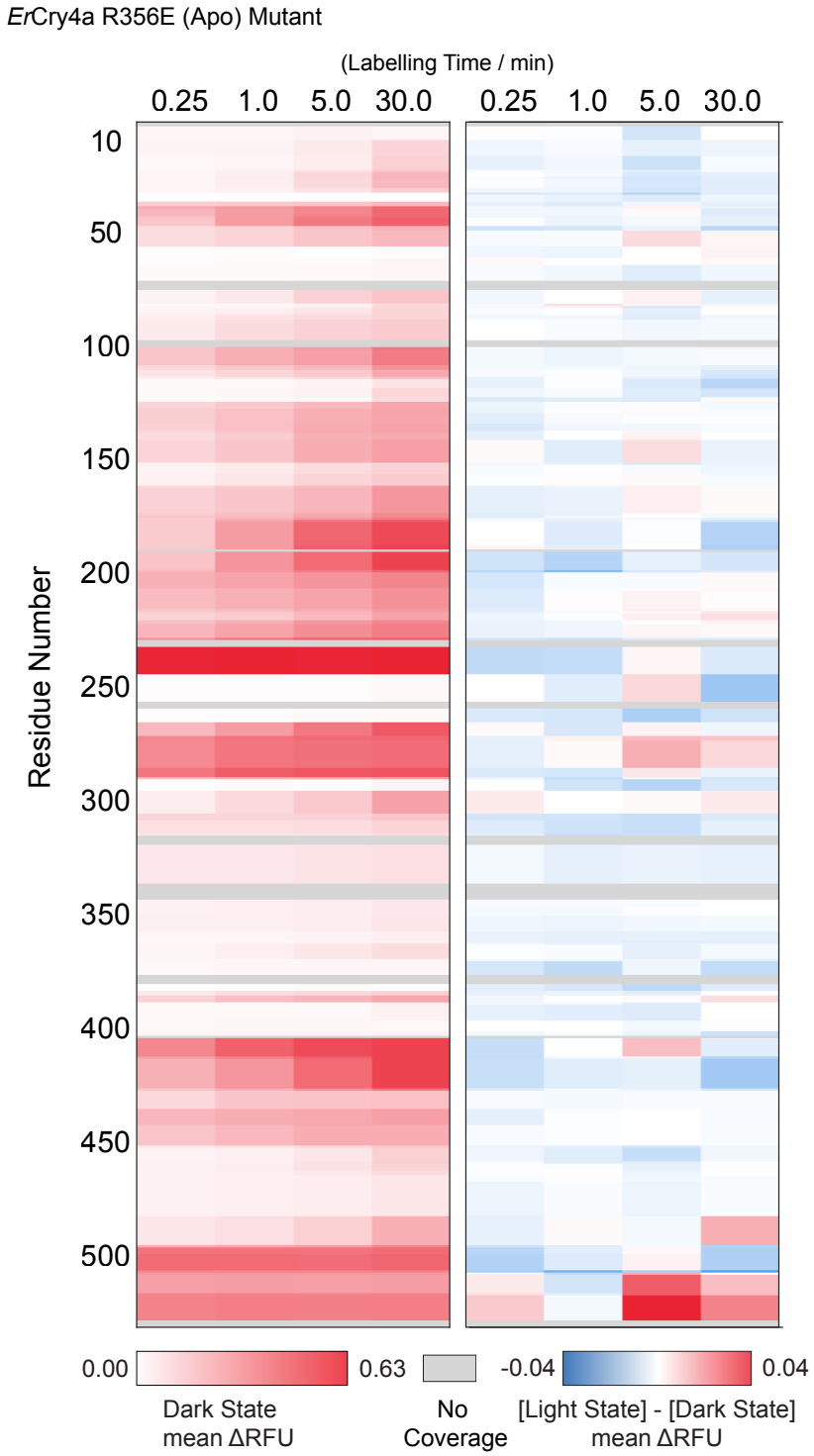


Figure 5.5: Heatmap of the global dynamics of *Er*Cry4a R356E in the DS (left). Uptake is shown on a white to red scale, with regions coloured red taking up more deuterium. LS-DS differences are shown on the second heatmap (right). Regions that are more protected are shown in blue, those that show no difference are white and regions that take up more deuterium in the light are shown in red. The PBL (peptide covering residues 232-243 is saturated from the first time point)

5.3 TrpD Mutant (W369F)

The second mutation investigated was W369F, which disrupts the terminal residue of the electron-transfer chain (TrpD). In WT cryptochromes, TrpD forms the terminal residue of the tryptophan tetrad, positioned furthest from the photoexcited FAD toward the protein surface. Its indole side chain can stabilise a radical through resonance delocalisation and when electron transfer proceeds through the complete tetrad, TrpD defines the maximum FAD–tryptophan radical separation distance achievable via this pathway. Substitution with phenylalanine removes this function because, unlike tryptophan, phenylalanine has unfavourable redox properties and cannot act as an efficient electron donor. Consequently, electron transfer is truncated at TrpC, shortening the effective chain length and limiting radical separation.

The rationale for generating this mutation stems from the hypothesis that TrpC and TrpD have distinct roles. TrpC has been suggested to act as the 'sensing' residue, while TrpD has been implicated in conformational change as the 'signalling' residue [181].

The global HDX profile of the W369F mutant (Figure 5.6) closely resembled that of WT (Figure 4.5). Exchange was higher in the same regions as the WT: the PBL, PL, peptide 404-412 and the CTT, indicating that the fold and overall dynamics of the protein remained similar. Importantly, the PBL in W369F did not display the immediate saturation seen in the apo protein, but instead exchanged more like WT, confirming that disruption of the chain does not destabilise the pocket to the same degree as loss of FAD.

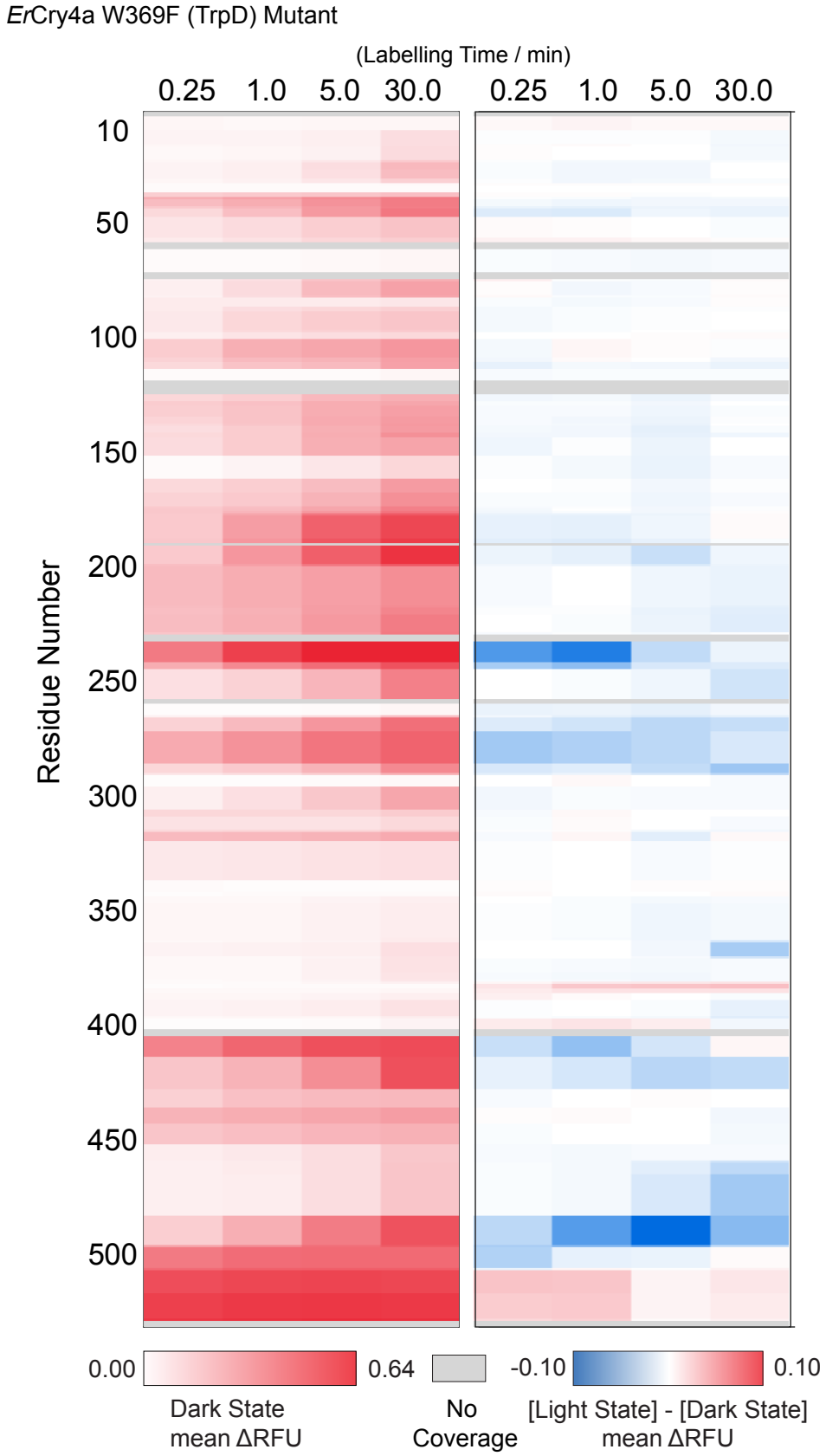


Figure 5.6: *Er*Cry4a W369F in the DS (left). Uptake is shown on a white to red scale, with red regions indicating higher deuterium incorporation. LS-DS differences are shown on the second heatmap (right). Regions more protected in the light are coloured blue, unchanged regions are white and regions with greater uptake in the light are red. Overall behaviour resembles WT, but the magnitude of protection is reduced.

5.3.1 Response to Stimuli

The Woods plots of LS vs DS (Figure 5.7) revealed differences in several key regions. The PBL and PL both showed light-induced protection, but the uptake difference was smaller than in WT. The number of protected peptides increased over time, suggesting these changes represent cumulative conformational stabilisation rather than transient fluctuations. Protection was also seen around peptide 404–412 and immediately before the CTT.

Interestingly, this mutant showed a small, transient deprotection in the CTT at the earliest labelling times, which disappeared by 5 min. This behaviour was absent in WT and apo proteins and may reflect altered initial dynamics of the tail when TrpD is missing. By contrast, α22, located just upstream of the CTT, remained protected in the light, mirroring WT behaviour.

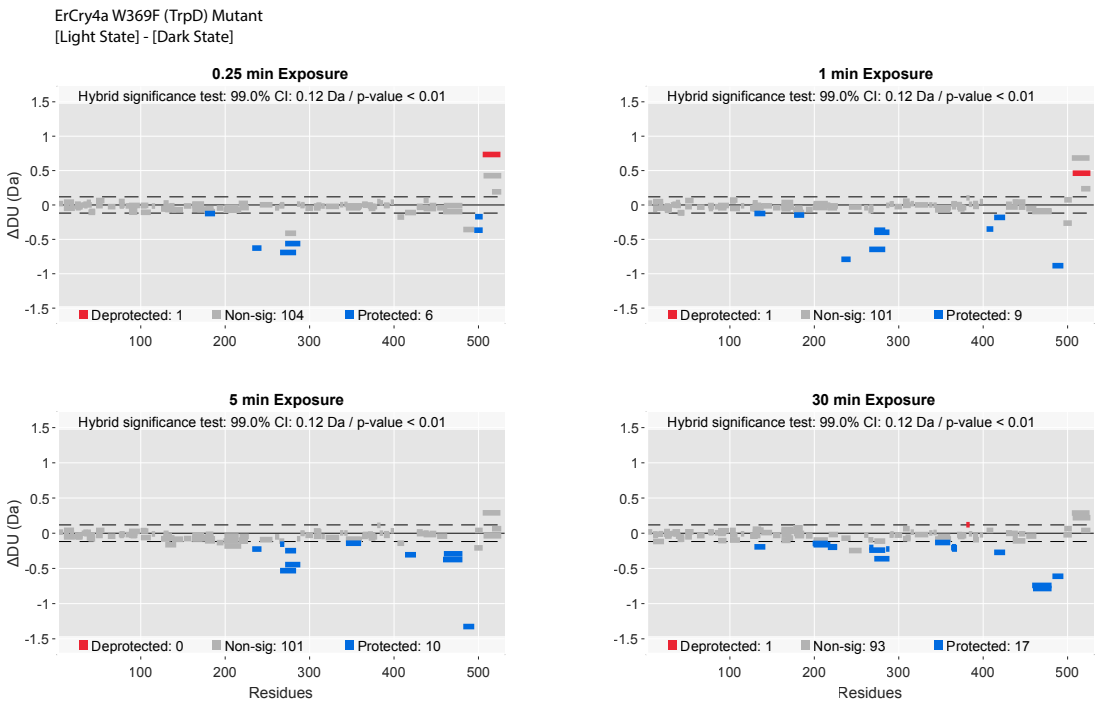


Figure 5.7: Woods plots of LS-DS differences in W369F. Peptides that show statistically significant protection in the light are shown in blue whilst those that are deprotected are shown in red. PBL and PL retain light-induced protection, though with reduced magnitude compared to WT. Transient deprotection is seen in the CTT at early times.

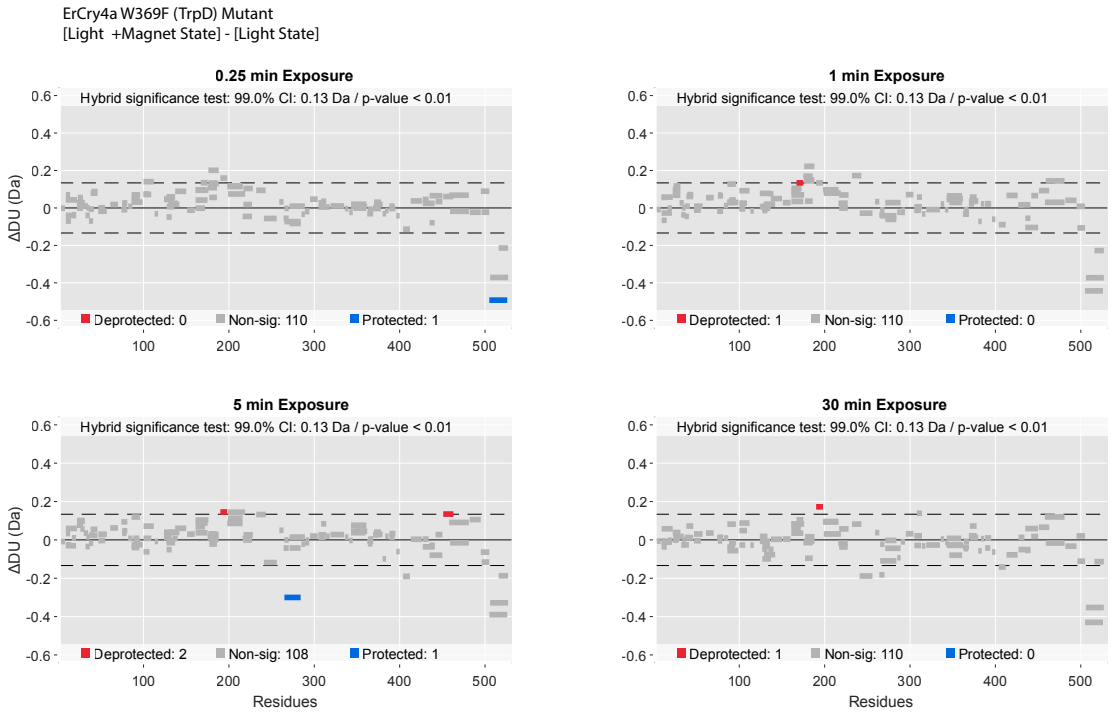


Figure 5.8: Woods plots comparing LSM-LS differences in W369F. No reproducible magnet effects were observed.

No magnet-dependent differences were detected when LSM and LS were compared (Figure 5.8), consistent with both the apo protein and WT. The few peptides deemed significant are likely artefacts as they are not reproducible and are only just above the significance thresholds.

The W369F mutant demonstrates that light-induced protection is not abolished by removal of TrpD, but the magnitude of these changes is consistently lower than in WT. This supports the idea that the radical pair can still form on TrpC, but TrpD enhances the stability and propagation of conformational responses. The transient early deprotection of the CTT suggests that TrpD may also contribute to the timing or coordination of tail rearrangements. Overall, these findings reinforce the model in which TrpD is not essential for sensing, but triggers the magnitude of the signalling process.

5.4 Triple Mutant (C317R/Y319F/W369F)

The final construct combined three substitutions to examine how alternative electron donors and sequence context influence Cry4a. C317 was mutated to arginine (C317R), matching the residue found at the equivalent position in chicken and quail Cry4a. Sequence analyses have identified position 320 as a site of positive selection within passerines, whereas position 317 shows increased conservation in migratory clades [194]. Cysteine at 317 and lysine at 320 are characteristic of many migratory songbirds, while both chicken and quail possess arginine and glutamic acid at these sites. Spectroscopic characterisation of chicken Cry4a has shown that introducing the robin-like substitution R317C had little effect on radical-pair kinetics or magnetic field sensitivity *in vitro*, suggesting that these residues may influence magnetic signalling rather than the primary sensing step [71]. Although C317 is not directly adjacent to the FAD, its replacement alters the polarity near the TrpC/TrpD region and may subtly affect redox connectivity within the protein.

Y319F removes a tyrosine located near the end of the electron-transfer chain to test whether this residue contributes to radical formation. Tyrosine can contribute to the electron transfer chain, whereas phenylalanine can also participate but usually with considerably reduced efficiency and not as the terminal donor [195]. W369F eliminates the terminal tryptophan (TrpD), truncating the chain; in chicken Cry4a this substitution produces a larger magnetic field effect than in the wild-type protein, consistent with similar behaviour in the robin homologue [71]. The triple mutant, therefore, provides a means to test whether combining C317R with loss of the terminal donors alters Cry4a stability or magnetic field sensitivity.

5.4.1 Global Dynamics

The global HDX profile of the triple mutant closely resembled that of WT, with β-sheets and α-helices consistently exchanging less than the connecting loops (Figure 5.9). This demonstrates that the overall fold and solvent accessibility remains similar to the WT despite the multiple substitutions. Importantly, this

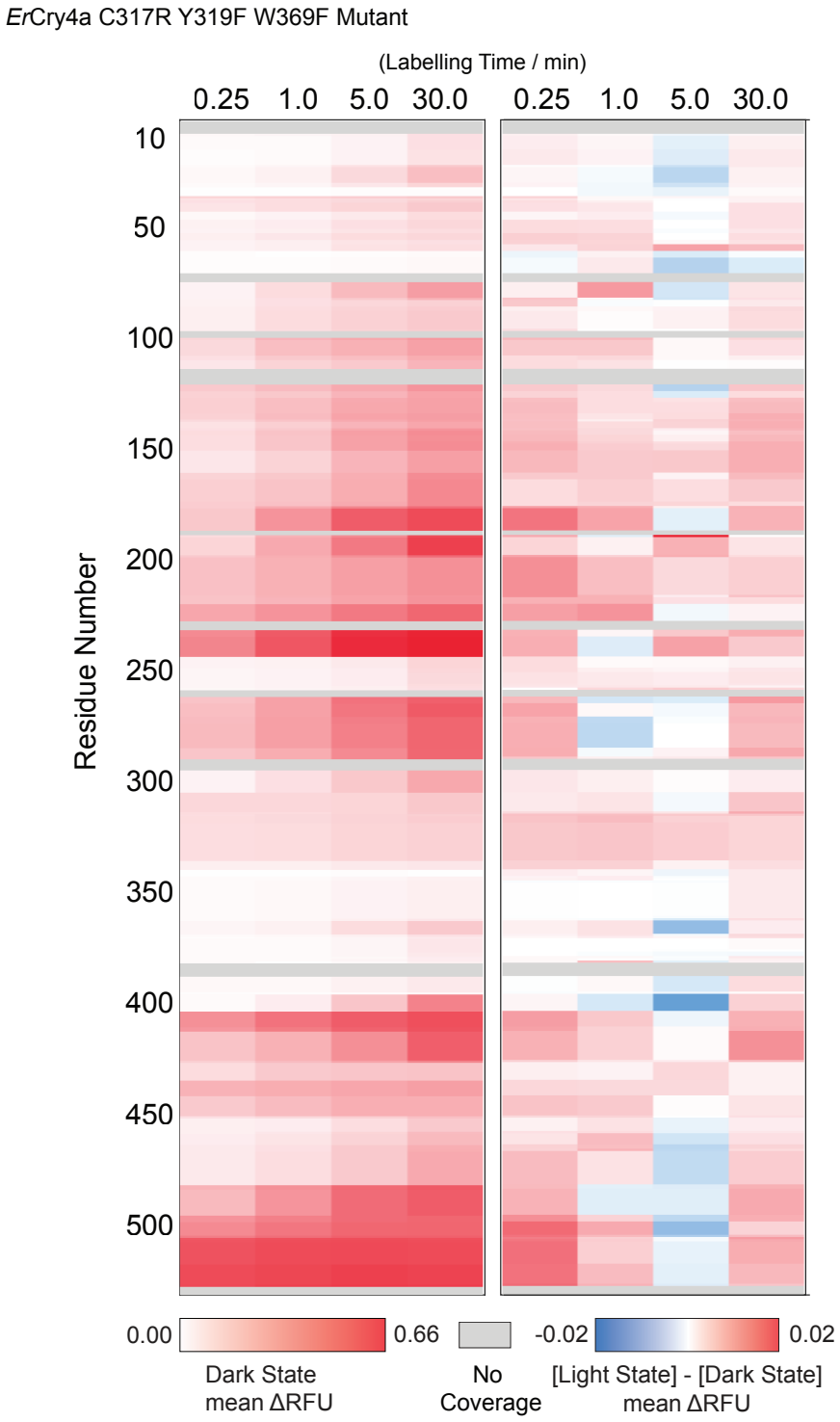


Figure 5.9: *Er*Cry4a C317R/Y319F/W369F in the DS (left). Uptake is shown on a white to red scale, with red regions indicating higher deuterium incorporation. LS-DS differences are shown on the second heatmap (right). Regions more protected in the light are coloured blue, unchanged regions are white and regions with greater uptake in the light are red. The overall fold is preserved, but no regions show reproducible protection in response to light.

means that any lack of responses to stimuli does not arise from misfolding or destabilisation of the protein backbone.

5.4.2 Response to Stimuli

The Woods plots for LS vs DS (Figure 5.10) revealed that protection normally observed in the PBL and PL was almost completely absent. Minor fluctuations were detected but were beneath the significance threshold and were not reproducible across replicates.

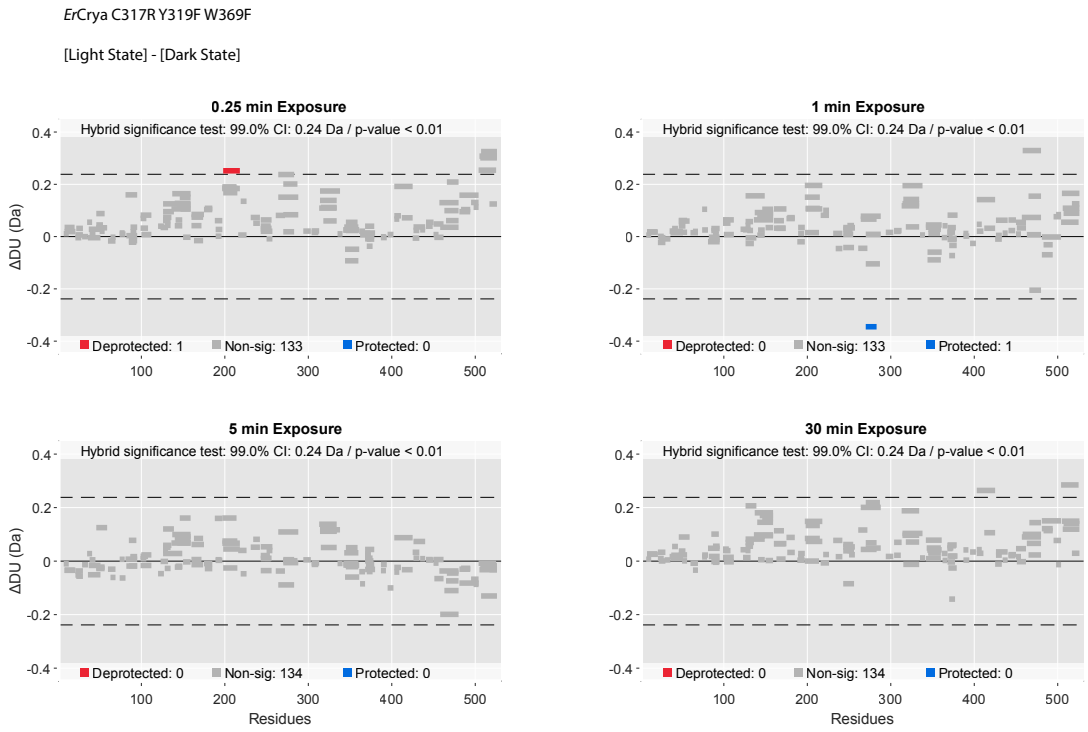


Figure 5.10: Woods plots of LS–DS uptake differences for the C317R/Y319F/W369F mutant. Protection in the PBL and PL is effectively abolished, indicating that both distal donors are required for light-dependent responses.

The absence of light-induced changes in the triple mutant confirms that both TrpD and Y319 are necessary for conformational signalling. Either residue alone can partially support the response, as seen in W369F, but both must be removed for the effect to be lost entirely. The addition of C317R, while not directly responsible for the loss of signalling, reproduces the sequence context found in chicken Cry4a and

alters the environment around TrpC. The lack of detectable differences in residues 404–412 suggests that this substitution does not perturb dimerisation dynamics but may influence how charge redistribution propagates through the Trp chain.

These results provide strong evidence that electron transfer beyond TrpC is essential for propagating the chemistry of FAD excitation into structural responses and that local sequence differences may modulate this coupling between species.

5.5 Comparative Discussion

The collective behaviour of the three mutants provides a progressive view of how FAD binding and the final electron donors shape the conformational dynamics of *Er*Cry4a (Figure 5.11). The apo, W369F and C317R/Y319F/W369F variants each display characteristic uptake patterns, which when considered side by side, demonstrate the contribution of individual residues and cofactor contacts to light-dependent stabilisation.

5.5.1 Phosphate Binding Loop

The PBL is the most sensitive region across the WT and all mutants (Figure 5.12). In the WT, it displays strong protection that occurs early on and continues across the full time course. This effect is absent in the apo protein, where the loop is saturated from the earliest time point, supporting the loss of stabilising phosphate–loop interactions in the absence of FAD. In W369F, after statistical analysis, protection is still observed but at a noticeably reduced magnitude, showing that electron transfer through TrpD enhances the response but is not strictly essential. In the triple mutant, uptake traces for LS and DS overlap almost completely, confirming that either TrpD or Y319 must be unchanged for the PBL to stabilise under illumination.

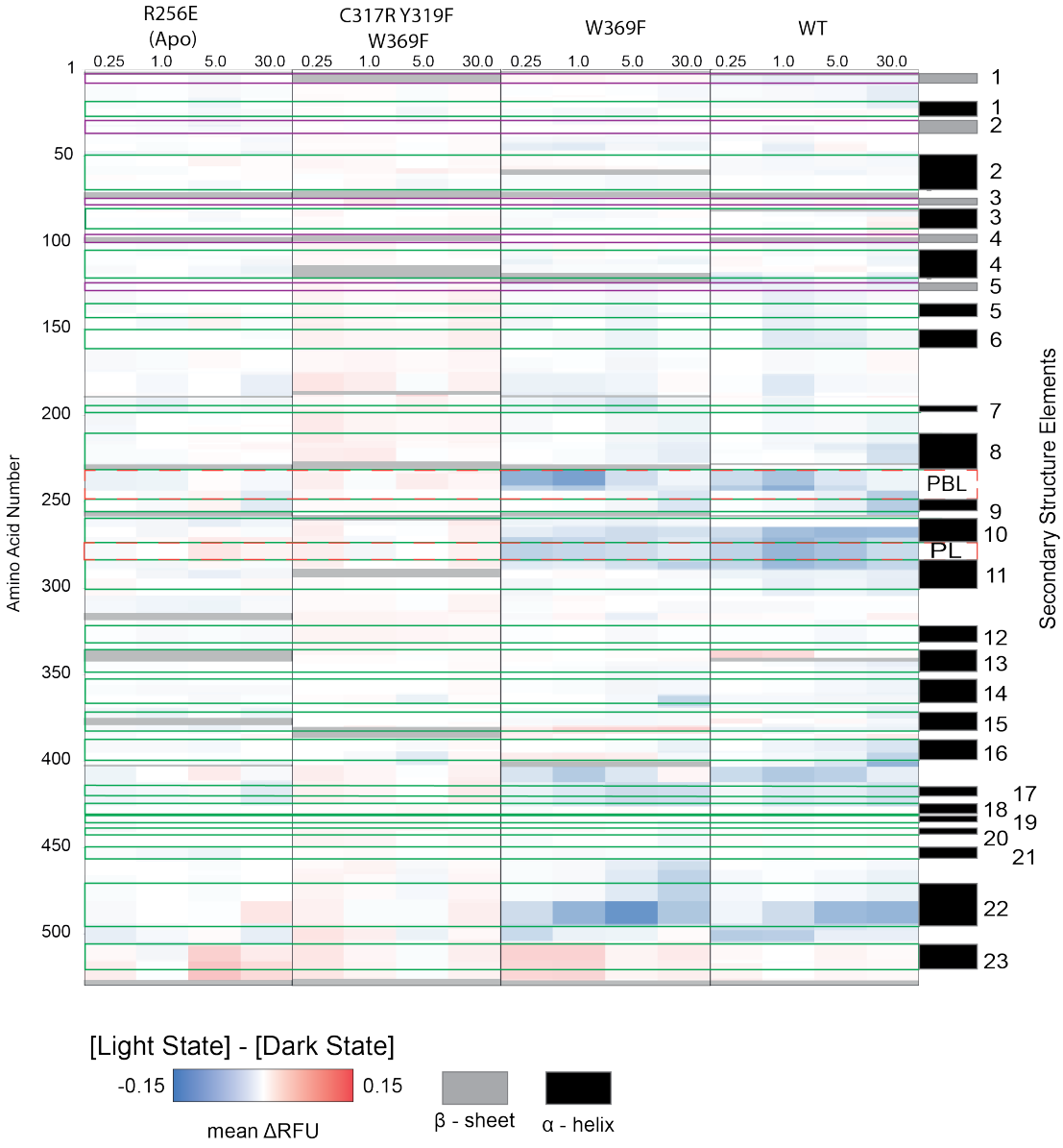


Figure 5.11: Heatmap of LS-DS uptake differences for WT and all mutants. Regions showing greater protection in the light are coloured blue, unchanged regions are white and regions with greater uptake in the light are red. Secondary structure is indicated by purple lines and grey boxes for β-sheets and by green lines and black boxes for α-helices.

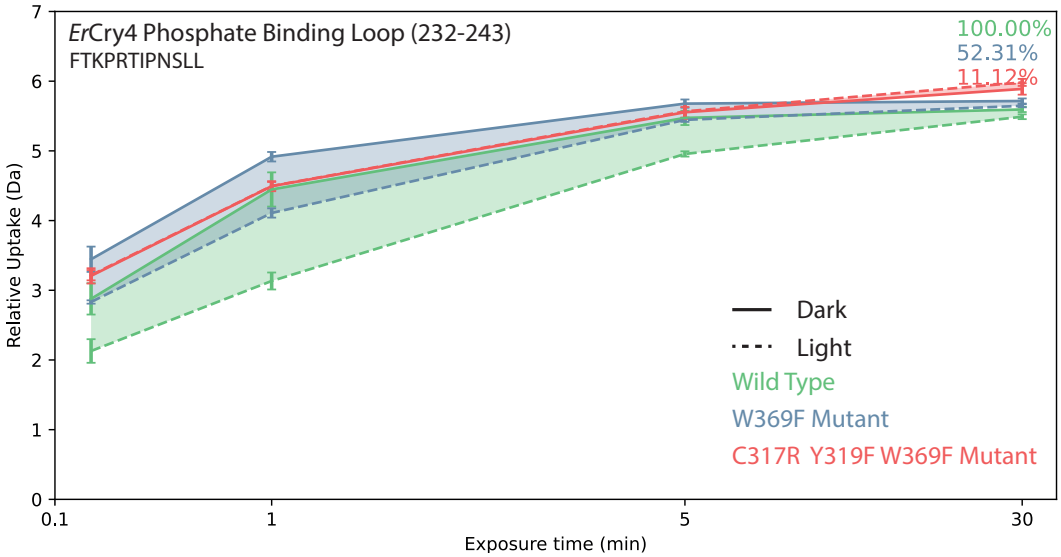


Figure 5.12: Deuterium uptake plots for the PBL (232–243). WT (green), W369F (blue) and C317R/Y319F/W369F (red) are shown with DS as solid lines and LS as dashed lines. WT displays strong light-induced protection, W369F retains a weaker response and the triple mutant shows no detectable difference.

5.5.2 Protrusion Loop

A similar pattern is seen in the PL (Figure 5.13). In WT, this loop shows strong light-induced protection, whereas the apo protein remains unresponsive, confirming that its behaviour depends on FAD. The W369F mutant retains a detectable response but with a smaller separation between LS and DS, corroborating partial compensation through Y319. Once both TrpD and Y319 are removed, light-induced protection is lost entirely, leaving the PL essentially unresponsive to light. Together with the PBL data, this indicates that both loops act as sensitive structural readouts of distal donor activity.

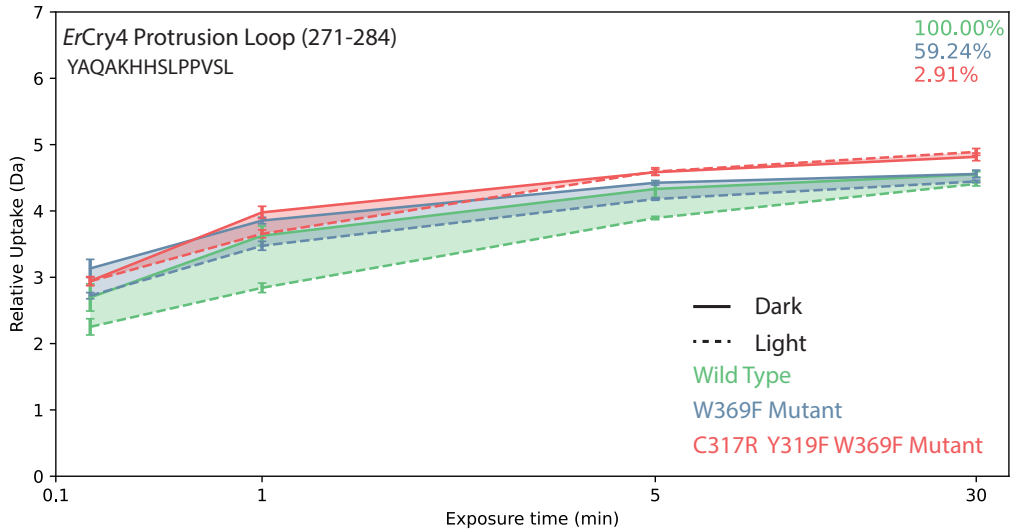


Figure 5.13: Deuterium uptake plots for the PL (271–284). WT (green), W369F (blue) and C317R/Y319F/W369F (red) are shown with DS as solid lines and LS as dashed lines. WT shows strong protection in LS, W369F retains a weaker response and the triple mutant shows almost no difference.

5.5.3 α22

α22 follows the same order of effects (Figure 5.14). In the WT, there is clear protection under illumination, whereas in W369F the effect persists but at reduced strength. In the triple mutant, no reproducible difference between LS and DS is detected. This indicates that α22 remains coupled to flavin excitation but requires at least one of the final donors to transmit stabilisation effectively. Interestingly, the mutations seem to increase uptake in both the DS and LS, with the TrpD mutant states being slightly above the WT and the triple mutants uptake being even higher. Notably, the adjacent CTT remains highly dynamic across all mutants, reinforcing that the effect is specific to the helix rather than a general shift in tail behaviour.

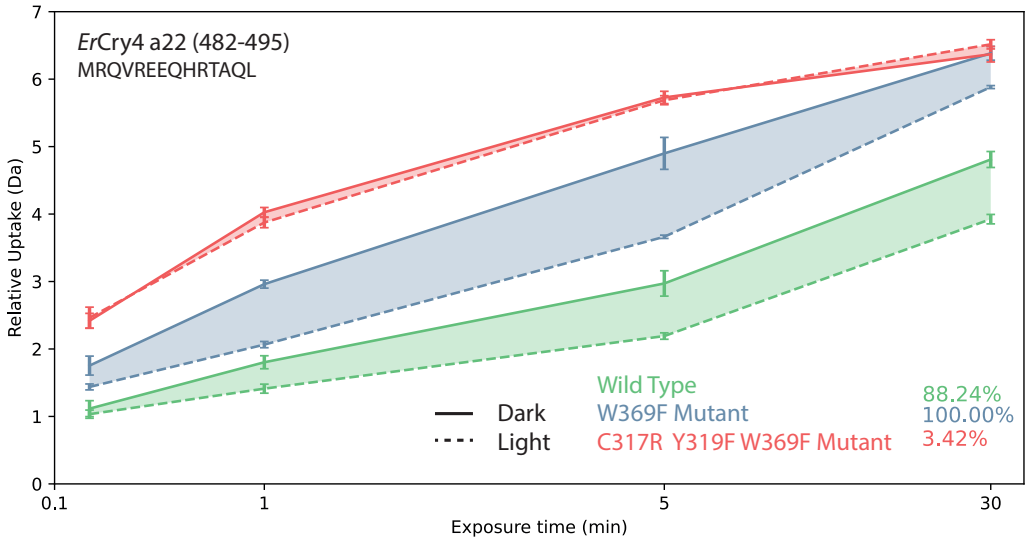


Figure 5.14: Deuterium uptake of α22 (residues 482–495). WT shows strong protection, W369F retains a reduced response and the triple mutant shows no detectable light dependence.

5.5.4 Putative Dimer Region

The peptide spanning 404-412, positioned near the proposed dimer interface, shows low level protection in the WT and a slightly weaker response in W369F, but in the triple mutant the uptake difference is close to zero (Figure 5.15).

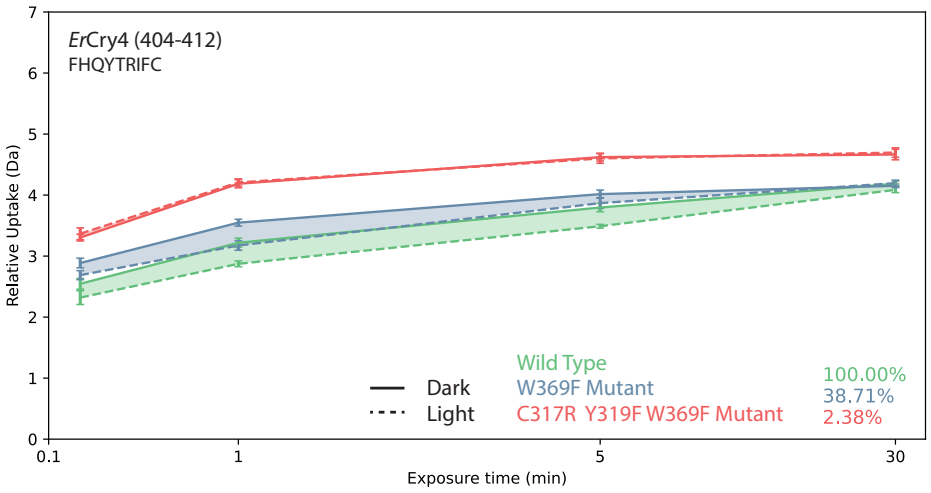


Figure 5.15: HDX uptake of peptide 404-412. WT shows modest light-induced protection, W369F retains a weaker effect and the triple mutant shows no difference, while baseline uptake is consistent across all mutants.

5.5.5 Mutation Region

The peptide containing the TrpD site itself (362-369) displays comparable uptake profiles across WT, W369F and the triple mutant, confirming that the substitutions do not create artefacts at the mutation site (Figure 5.16). These observations strengthen the interpretation that the altered responses in PBL, PL and α22 are genuine consequences of disrupted electron transfer rather than indirect effects of misfolding.

5.5.6 Discussion

The mutation series reveals a clear progression in structural responses to light. The apo form shows no detectable light-induced changes, confirming that FAD binding is required to initiate conformational switching. In the wild type, illumination produces reproducible protection within the PBL, PL and α22, indicating that photoexcitation of the flavin drives local stabilisation across these regions. The W369F mutant retains the same qualitative pattern but with weaker effects, suggesting that disruption of TrpD partially limits electron transfer, while residual coupling may occur through Y319. When both TrpD and Y319 are removed, protection is almost completely lost, showing that electron transfer along the Trp chain is essential

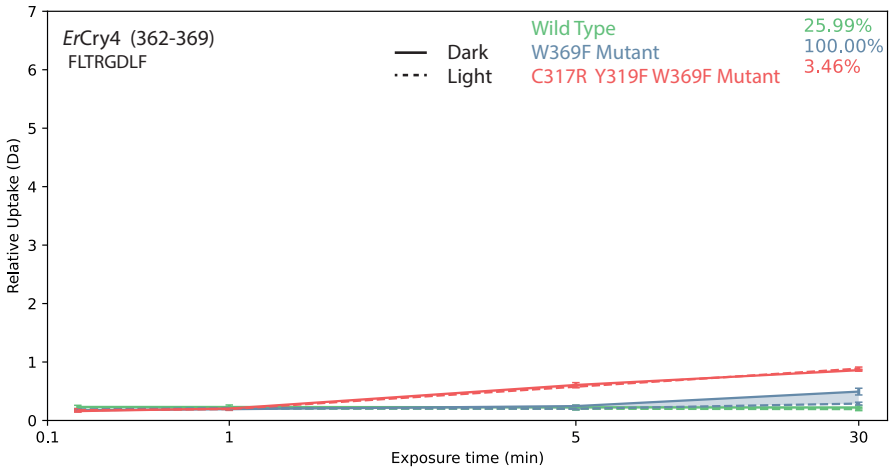


Figure 5.16: HDX uptake of peptide 362-369 across WT, W369F and C317R/Y319F/W369F. Uptake remains consistent across all mutants, confirming that substitutions do not destabilise the local backbone at the mutation site.

to connect flavin photochemistry with conformational change and that Y319 can act as an auxiliary redox extension.

Although *Er*Cry4a can fold without its cofactor, the absence of FAD prevents any light-dependent response, demonstrating that the flavin is not merely a structural component but the trigger for conformational change. This differs from *Drosophila* cryptochrome, where FAD has been shown to contribute directly to folding stability [192]. In that system, the isoalloxazine–ribityl–monophosphate portion of the cofactor alone was sufficient to stabilise the native fold, highlighting the strong coupling between cofactor binding and protein integrity. Structural studies on *Dm*Cry place the phosphate-binding loop (residues 249–263) and Arg237 in the same FAD-proximal region [178, 190, 192], a configuration shared across CPF proteins where basic residues stabilise anionic cofactors through electrostatic interactions. A clear example occurs in the (6-4) photolyase–DNA complex, where a conserved arginine forms a key Coulombic contact with the DNA phosphate backbone [193]. By analogy, conserved residues such as R356 in *Er*Cry4a are expected to anchor the phosphate groups of FAD, ensuring high-affinity binding within an already folded protein.

Native-MS analysis of the R356E mutant supports this interpretation: the expected 785 Da FAD increment is absent, indicating loss of cofactor binding. Replacing the positively charged arginine with glutamate would be expected to repel the phosphate groups of FAD and destabilise the binding pocket, explaining the lack of light-induced effects in the apo state. This highlights the dependence of cryptochrome function, though not necessarily its folding, on FAD incorporation.

Comparable behaviour is observed in plant cryptochromes, where mutations in the Trp chain reduce the efficiency of photoreduction but do not entirely abolish signalling *in vivo* [196]. These studies reinforce the view that electron transfer modulates the magnitude of the response, while the presence of FAD is indispensable for activation. Within avian cryptochromes, conserved FAD-pocket geometry and electrostatics [59] suggest that these same stabilising principles apply across species. Together, the results presented here establish that in *Er*Cry4a both cofactor binding and an intact electron-transfer pathway are required to couple photoexcitation to conformational change.

5.6 Conclusions

The mutant series described here sets out a clear progression of how FAD and the electron transfer chain shape the behaviour of *Er*Cry4a. The apo protein shows that the overall fold can be preserved without the cofactor, but no light responses are detectable. In other words, the protein can be made, but without FAD it is essentially unresponsive. This confirms that conformational changes seen in the WT are not just the product of an intrinsically flexible scaffold, but require the photochemistry of the flavin.

Disrupting the chain at TrpD (W369F) gives a different picture. Protection in the PBL, PL and α22 is still present, but weaker. This suggests that TrpC alone can sustain the radical pair and trigger downstream stabilisation, while TrpD helps to amplify or prolong the effect. The small, early deprotection of the CTT points to an additional role for TrpD in timing the tail response, something that is lost when the indole side chain is replaced.

Once both TrpD and Y319 are removed and the local environment altered by C317R, the response disappears almost entirely. The protein is folded and soluble, but the regions that normally show light protection are flat. This shows that at least one distal donor is required to carry the signal beyond the flavin pocket and that the presence of FAD alone is not enough.

Across the series, the PBL, PL and α22 emerge as the most sensitive reporters of these changes. They behave as local readouts of whether the radical pair has formed and been transmitted into the structure. The fact that these effects scale with the mutations, from absent in the apo, to reduced in W369F, to lost in the triple mutant, provides a direct experimental link between the chemistry at the flavin and the conformational dynamics of the protein.

The C317R substitution also raises the possibility that species differences tune how strongly the flavin pocket is coupled to the rest of the scaffold. In robin Cry4a, the substitution is artificial, but in chicken it is the natural sequence, hinting at an evolutionary route by which light-driven responses might be adjusted in strength or timing across species.

5.7 Materials and Methods

5.7.1 Materials

All reagents and chemicals were purchased from Sigma Aldrich (Gillingham, UK) unless otherwise stated. Recombinant cryptochrome proteins were expressed in *E. coli* and purified by collaborators in the laboratory of Henrik Mouritsen at the Carl von Ossietzky University of Oldenburg, Germany, using established protocols [17]. Samples were shipped on ice in storage buffer containing 20 mM Tris, 250 mM NaCl, 2 mM DTT and 20% (v/v) glycerol and stored at $-80\,^{\circ}\mathrm{C}$ until required for experiments. For HDX-MS, three buffers were prepared: an equilibration buffer consisting of 5 mM potassium phosphate in H_2O at pH 7.0, a labelling buffer consisting of 5 mM potassium phosphate in D_2O at pD 7.0 and a quench buffer consisting of 50 mM potassium phosphate in H_2O adjusted to pH 1.9.

5.7.2 HDX-MS

*Er*Cry4 W369F was performed in collaboration with Dr Angela Gehrckens. HDX-MS experiments were carried out under carefully controlled conditions. All protein handling was performed under dim red illumination in an otherwise dark environment to prevent unwanted photoactivation. Protein aliquots were thawed immediately prior to analysis and diluted to volumes between 10 and 16 μL. Before labelling, each sample was equilibrated for at least 20 min at 20 °C within a temperature-controlled chamber. The light state was generated by continuous exposure to 450 nm blue light at intensities ranging from 0.03 to 0.06 mW cm^{-2}, while the dark state was maintained in complete darkness. To generate magnet states, samples were placed in custom-built holders positioned above neodymium-iron-boron magnets (10 mm $\times$ 1.5 mm, N42 grade, Magnet Expert Ltd.) with a nominal surface field strength of 160 mT. Measurements confirmed that the magnetic field at the sample position corresponded to approximately 18–25 mT at a distance of 2–3 mm from the magnet.

Labelling reactions were initiated by diluting the protein with deuterated buffer. 55 μL of labelling buffer was added to 5 μL of protein, producing a final solution of approximately 92% D_2O. For *Er*Cry4a, 54 μL of labelling buffer was combined with 1 μL of protein, yielding a final deuterium content of approximately 98%. Exchange was stopped by mixing the sample with an equal volume of ice-cold quench buffer. Quenched solutions were immediately injected into the HDX Manager (Waters, Milford, MA, USA) and maintained at 0 °C until reaching the Enzymate Pepsin digestion column (Waters), which was held at 20 °C. Digestion was performed with an isocratic flow of 0.1% formic acid in H_2O at 100 μL min^{-1}. Peptides were collected and desalted on a BEH C18 trapping column (Waters) for 2 min before separation on a reversed-phase analytical column operated at 0 °C with a flow rate of 40 μL min^{-1}. The chromatographic gradient began with 97% H_2O and 3% MeCN, shifted to 65% H_2O and 35% MeCN over 7 min, then decreased to 5% H_2O within 1 min and was held for an additional 2 min.

Peptides were analysed on a Synapt G2Si Q-ToF mass spectrometer (Waters) by electrospray ionisation. Instrument parameters included a capillary voltage of

2.8 kV, sample cone voltage of 100 V, source offset of 30 V, source temperature of 80 °C and desolvation temperature of 150 °C. Leucine enkephalin (m/z 556.2771) was infused every 30 seconds as a lock mass for internal calibration. To minimise carryover between runs, a saw-tooth gradient cleaning cycle was applied using 4% acetonitrile and 0.1% formic acid in water supplemented with 0.5 M guanidinium hydrochloride, with intermittent blank injections included as further quality control. The emission spectra of all light sources, including the red bench lights and the blue LEDs used for photoactivation, were independently verified to confirm spectral separation and avoid unintended activation.

5.7.3 Native Mass Spectrometry

Native mass spectrometry experiments employed the same *Er*Cry4a preparations used in HDX-MS. Samples were buffer exchanged into 200 mM ammonium acetate at pH 8.0 using Zeba^{TM} Micro Spin desalting columns with a 40 kDa molecular weight exclusion limit (ThermoFisher Scientific). Measurements were conducted at the University of Oxford on a Q Exactive^{TM} mass spectrometer (ThermoFisher Scientific) using custom-fabricated gold-coated capillaries for nano-electrospray ionisation. Protein samples were introduced at a concentration of approximately 8 μM. The source temperature was maintained at 150 °C and the capillary voltage was set to 1.0 kV. In-source trapping was applied at 200 V to assist in desolvation and to disrupt weakly bound adducts. The higher-energy collisional dissociation (HCD) cell was operated at 5 V and ion optics were adjusted empirically to maximise transmission of intact protein ions.

5.7.4 Data Analysis

Peptides were identified by MSE fragmentation of non-deuterated controls and processed with ProteinLynx Global Server 3.0 (Waters) for database searching. The results were imported into DynamX 3.0 (Waters) for automated peak picking and assignment. To ensure reliability, stringent filtering criteria were applied: peptides were required to display at least 0.2 fragment ions per amino acid, have a

precursor mass accuracy within 5 ppm, contain no more than 25 residues and be detected reproducibly in at least three replicate analyses. Peptides that did not meet these standards, or that showed ambiguous or noisy isotopic distributions, were excluded. Deuterium incorporation was quantified by comparing centroid mass shifts of labelled peptides relative to undeuterated controls.

Native mass spectra were processed using MassLynx V4.2 (Waters, Wilmslow, UK) and structural mapping of differential deuterium uptake was visualised in PyMOL (Schrödinger, New York, USA).

"Bird fact: Birds have distinct tastes in music.
Chickens, for instance, prefer Bach."

— Reddit via Sophia Sorana

6

Comparative Study of Avian Cryptochromes across Robin, Chicken and Quail (*Er*Cry4a, *Gg*Cry4a and *Cc*Cry4a)

Contents

6.1 Abstract 150
6.2 Introduction 150
6.2.1 Chicken Cryptochrome (*Gg*Cry4a) 152
6.2.2 Quail Cryptochrome (*Cc*Cry4a) 154
6.2.3 Structure and Sequence Similarity 155
6.3 Motivation 161
6.4 Comparisons of Wild Types 162
6.5 Comparisons of TrpD Mutants 165
6.6 Comparisons of TrpD / Y319F Mutants 169
6.7 Important Regions 170
6.7.1 Phosphate-Binding Loop 170
6.7.2 Protrusion Loop 174
6.7.3 α22 176
6.7.4 Potential Dimer Region 179
6.7.5 Mutation Region 181
6.8 Magnet-Induced Effects 183
6.9 Discussion 183
6.9.1 Residue Distances from FAD Across Species 184
6.9.2 Kinetics in the *Cc*Cry4a CTT 187
6.10 Conclusions 190
6.11 Materials and Methods 192
6.11.1 Materials 192
6.11.2 HDX-MS 192

6.11.3 Native Mass Spectrometry 194
6.11.4 Data Analysis 194

6.1 Abstract

This chapter compares the structural dynamics of cryptochrome 4a (Cry4a) from three avian species,the European robin (*Erithacus rubecula*), chicken (*Gallus gallus*)and common quail (*Coturnix coturnix*), using HDX–MS. By examining homologues across migratory and non-migratory birds, the study tests whether light-induced conformational behaviour is a conserved property of avian Cry4a and how subtle sequence differences modulate its magnitude or kinetics.

HDX–MS revealed that all three homologues share a common structural architecture with a protected β-sheet core and flexible loop regions surrounding the flavin-binding pocket. In each species, light-dependent changes localised reproducibly to the PBL, PL and helix α22, confirming these as conserved structural relays within the Cry4a activation pathway. However, the magnitude of protection varied systematically between species: robin Cry4a displayed the strongest photoresponse, while chicken and quail exhibited smaller light–dark differences, consistent with a more constrained conformational landscape.

These results establish that the light-responsive behaviour of Cry4a is an evolutionarily conserved feature, but its sensitivity and flexibility have been differentially tuned among species. The data gathered from the three species investigated provide insight into how ecological and evolutionary factors shape the structural dynamics of avian magnetoreceptors and form the basis for understanding species-specific adaptations in subsequent analyses.

6.2 Introduction

Chicken and quail cryptochrome 4 proteins provide valuable comparative systems for investigating the mechanisms underlying avian magnetoreception. Alongside the

European robin, which remains the principal model for light-dependent magnetic orientation in migratory birds, these species offer an opportunity to examine how evolutionary distance, ecological niche and migratory behaviour influence Cry4a structure and function. The chicken represents a non-migratory galliform that has undergone extensive selection under domesticated conditions, whereas the quail migrates seasonally between Europe and sub-Saharan Africa [197, 198]. Studying their Cry4a homologues alongside the robin therefore helps to disentangle which aspects of Cry4a behaviour are fundamental to its magnetosensory function and which represent lineage-specific adaptations.

Spectroscopic and biochemical studies have shown that Cry4a proteins from both migratory and non-migratory birds can form magnetically sensitive radical pairs *in vitro*, supporting the radical-pair hypothesis as a conserved molecular basis for magnetic sensing [17, 63, 194, 199]. This conservation suggests that the capacity for light-induced radical-pair formation is ancestral among birds, whereas sequence variations and dynamic differences may modulate how efficiently the protein couples photochemistry to structural rearrangement and downstream signalling.

As members of the Galliformes, chickens and quails diverged from passerines (including robins) over 60 million years ago [200, 201]. Both groups retain functional magnetic compasses, demonstrating that magnetoreception is not an innovation of migratory species but a conserved sensory capability [202]. Their contrasting ecologies provide complementary evolutionary contexts: the quail's migratory lifestyle demands a magnetosensory system responsive to seasonal and geomagnetic cues, whereas the chicken's domestication under stable environmental conditions may have relaxed selective pressure on these mechanisms. Comparing Cry4a homologues across these species thus provides a framework for understanding how conserved photochemical mechanisms are tuned by evolution to match distinct behavioural and ecological demands.

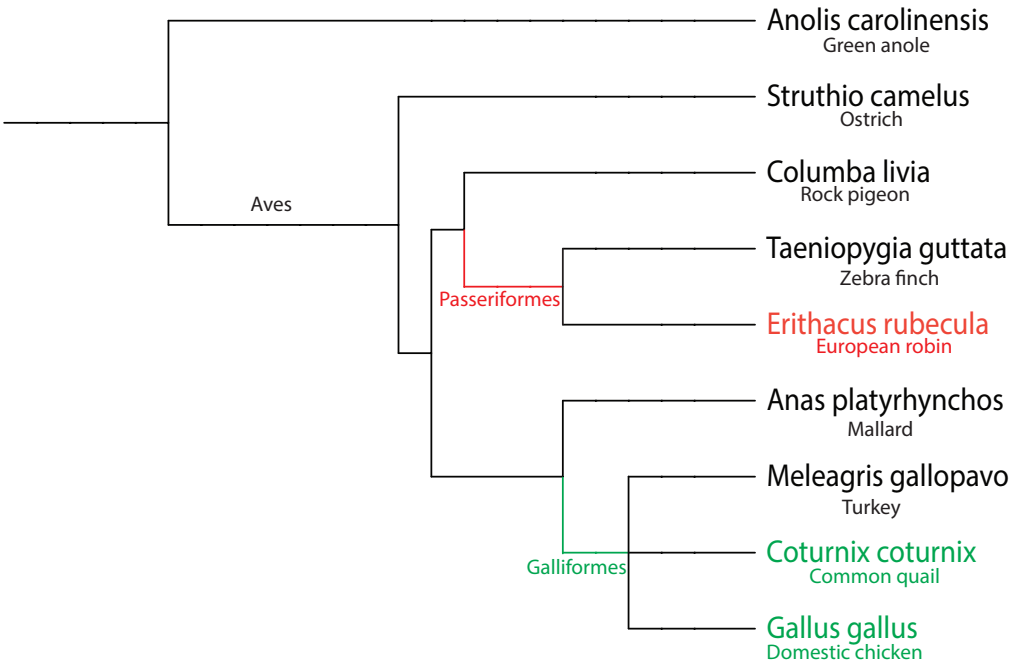


Figure 6.1: Phylogenetic tree showing the evolutionary relationships of the three species analysed in this chapter: European robin (*Erithacus rubecula*), common quail (*Coturnix coturnix*) and domestic chicken (*Gallus gallus*). Additional taxa were included to provide context, with the reptile green anole used as an outgroup. Higher-level clades are annotated for Passeriformes (robin and zebra finch) and Galliformes (chicken, quail, turkey).

6.2.1 Chicken Cryptochrome (*Gg*Cry4a)

*Gg*Cry4a was first cloned from chicken pineal tissue by Kubo and colleagues in 2006 [66]. They reported high expression of *Gg*Cry4a in photosensitive organs, with particularly strong levels in the pineal gland and retina. Interestingly, expression displayed daily oscillations in the pineal but remained stable in the retina, suggesting that Cry4a could act as a light-sensing molecule independent of circadian control.

Further evidence for a photoreceptive role came from the work of Watari *et al.*, who produced monoclonal antibodies specific to chicken Cry4a [199]. Using *in situ* hybridisation and immunohistochemistry, they localised the protein to multiple retinal cell layers, including ganglion cells and discovered that the C-terminal region undergoes a reversible, light-dependent conformational change. Illumination with blue light at physiologically relevant intensities altered antibody

accessibility, demonstrating that Cry4a responds directly to light under natural conditions. This provided the first experimental indication that avian Cry4a acts as a photoreceptive protein within the retina.

Recent work by Gravell et al. extended the characterisation of avian cryptochromes by directly probing purified chicken Cry4a (*Gg*Cry4a) using transient EPR, out-of-phase ESEEM, transient absorption spectroscopy and broadband cavity-enhanced absorption spectroscopy [71]. These complementary approaches confirmed that *Gg*Cry4a forms singlet-born $FAD^{\bullet-}/TrpH^{\bullet+}$ radical pairs along the canonical tryptophan tetrad, exhibiting magnetic-field-sensitive recombination kinetics. Mutations at positions 317 and 320, which differ between migratory passerines (C317/K320) and galliforms (R317/E320), produced no measurable effect on radical-pair lifetimes or magnetic-field dependence, suggesting that these substitutions do not determine magnetosensitivity. By contrast, replacement of the terminal tryptophan (W369F) markedly altered the photochemistry, increasing radical-pair persistence and enhancing magnetic-field sensitivity. These findings point to different functional roles for individual tryptophan residues, with W369 playing a specific role in modulating radical-pair dynamics and magnetic sensitivity.

Behavioural experiments have confirmed that chickens possess a functional magnetic compass. Freire *et al.* demonstrated that domestic chicks could be trained to locate a social imprinting object using magnetic directional cues and that their orientation shifted predictably when the field was rotated [202]. Wiltschko *et al.* later characterised the same response in greater depth, revealing that it depends on light wavelength (orientation under blue but not red light) and is disrupted by weak radiofrequency fields [203].

These studies show that chicken Cry4a exhibits all the photochemical features required for magnetically sensitive radical pair formation and that its overall behaviour differs little from that of migratory species, even though chickens themselves are not migratory and arguably have no need for a magnetic compass. The limited impact of the R317C and E320K substitutions implies that sequence variation alone cannot explain the differences in Cry4a photoresponse observed

between migratory and non-migratory species. Instead, functional differences likely arise from how the protein operates within the retinal environment, through altered membrane interactions, redox coupling, or downstream signalling rather than through intrinsic changes in the protein's photochemistry. In this respect, *Gg*Cry4a provides a valuable non-migratory reference point as a form in which the radical-pair mechanism is conserved, but where specifics of its nature may differ from that of its migratory homologues.

6.2.2 Quail Cryptochrome (*Cc*Cry4a)

The common quail (*Coturnix coturnix*) serves as an especially informative comparative model to the chicken. In captivity, they exhibit pronounced *Zugunruhe*, the nocturnal restlessness characteristic of migratory species and display directional preferences in orientation cage experiments [198, 204]. These well-defined behavioural traits, together with their suitability for captive breeding and the feasibility of producing transgenic lines, make the quail a particularly valuable model for exploring the physiological basis of migration and for identifying molecular components that might differ between migratory and non-migratory lineages.

Despite its behavioural importance, quail Cry4a remains relatively uncharacterised at the molecular level. No direct structural or spectroscopic analyses of *Cc*Cry4a have yet been reported. Early molecular work focused instead on Cry1 and Cry2 from Japanese quail (*Coturnix coturnix japonica*), demonstrating their involvement in circadian regulation rather than magnetoreception [205]. Nevertheless, given the exceptionally high sequence conservation within Galliformes, it is very likely that *Cc*Cry4a retains all canonical Cry4a motifs, including the FAD-binding pocket, the conserved Trp-tetrad (TrpA–TrpD) and the terminal tyrosine implicated in electron transfer. On this basis, quail Cry4a most likely shares the core photochemical mechanism identified in its chicken counterpart, providing a bridge between molecular conservation and behavioural divergence.

The absence of direct biochemical evidence makes *Cc*Cry4a an ideal candidate for comparative analysis using methods such as HDX–MS. Its migratory lifestyle

implies that, despite its close phylogenetic proximity to the chicken, the protein may display dynamic features more similar to those of the robin. For example, its flexible loops or CTT might be tuned for photoresponsiveness, enabling more efficient signal transduction during migration. Investigating whether such structural or kinetic properties parallel those seen in migratory songbirds will help clarify whether light-dependent conformational switching is a general property of Cry4a or a specialisation linked to migratory demands.

Recent transcriptomic studies have begun to contextualise quail migration within broader physiological pathways. Marasco *et al.* used RNA sequencing to examine quail brain gene expression during *Zugunruhe*, identifying transcriptional networks associated with circadian timing, photoperiodic responses and metabolic regulation [206]. Although Cry4a itself was not directly profiled, the data highlight the molecular systems that might interact with or modulate Cry4a activity *in vivo*. Integrating Cry4a structural dynamics with these expression patterns could therefore reveal how photoreception, magnetoreception and metabolic state work together during migration.

The quail, therefore, presents a promising but under-explored opportunity for cryptochrome research. As a migratory member of the Galliformes, it combines the genetic tractability and experimental accessibility of domestic species with the ecological and behavioural relevance of long-distance navigation. Comparative characterisation of *Cc*Cry4a alongside chicken and robin homologues will help determine whether the molecular features underpinning light-dependent conformational change are conserved across birds or have been evolutionarily refined in species that rely on magnetic cues for seasonal migration.

6.2.3 Structure and Sequence Similarity

Multiple sequence alignment of the three species (Figure 6.2) confirms the strong overall conservation of Cry4a across birds. Over the full-length proteins, *Er*Cry4a shares 88.05% identity with chicken Cry4a and 87.86% with quail Cry4a, while chicken and quail are most similar to one another at 95.65% (Table 6.1). These

values reflect the deep evolutionary relationship between galliforms and the more distant, yet structurally similar, passerine Cry4a sequences.

Table 6.1: Pairwise sequence similarity (%) between full-length Cry4a proteins from European robin (*Er*Cry4a), chicken (*Gg*Cry4a) and quail (*Cc*Cry4a).

	*Er*Cry4a	*Gg*Cry4a	*Cc*Cry4a
*Er*Cry4a	—	88.05%	87.86%
*Gg*Cry4a	88.05%	—	95.65%
*Cc*Cry4a	87.86%	95.65%	—

Most of this conservation arises from the PHR, which forms the structured catalytic core. When analysis is restricted to this region, the identities rise to 89.31% between robin and chicken, 89.11% between robin and quail and 96.44% between chicken and quail (Table 6.2). Key residues within the FAD-binding pocket, including the four tryptophans (TrpA–TrpD) that constitute the electron transfer chain and the terminal tyrosine are conserved across all three species, emphasising their functional indispensability.

Table 6.2: Pairwise sequence similarity (%) within the photolyase homology region (PHR).

	*Er*Cry4a	*Gg*Cry4a	*Cc*Cry4a
*Er*Cry4a	—	89.31%	89.11%
*Gg*Cry4a	89.31%	—	96.44%
*Cc*Cry4a	89.11%	96.44%	—

By contrast, the CTT shows markedly lower conservation. When restricted to the final 22–24 residues, robin Cry4a shares only 59.09% identity with both chicken and quail, whereas the galliform sequences remain more closely matched at 79.17% (Table 6.3). This pronounced divergence underlines the CTT as the most variable region across avian Cry4a proteins, consistent with its proposed role as within flexible signalling rather than a fixed structural component.

Examination of the predicted AlphaFold 3 structures reveals that several conserved motifs are retained (Figure 6.3). The PBL maintains its backbone geometry in all three species, though subtle substitutions, typically involving conservative

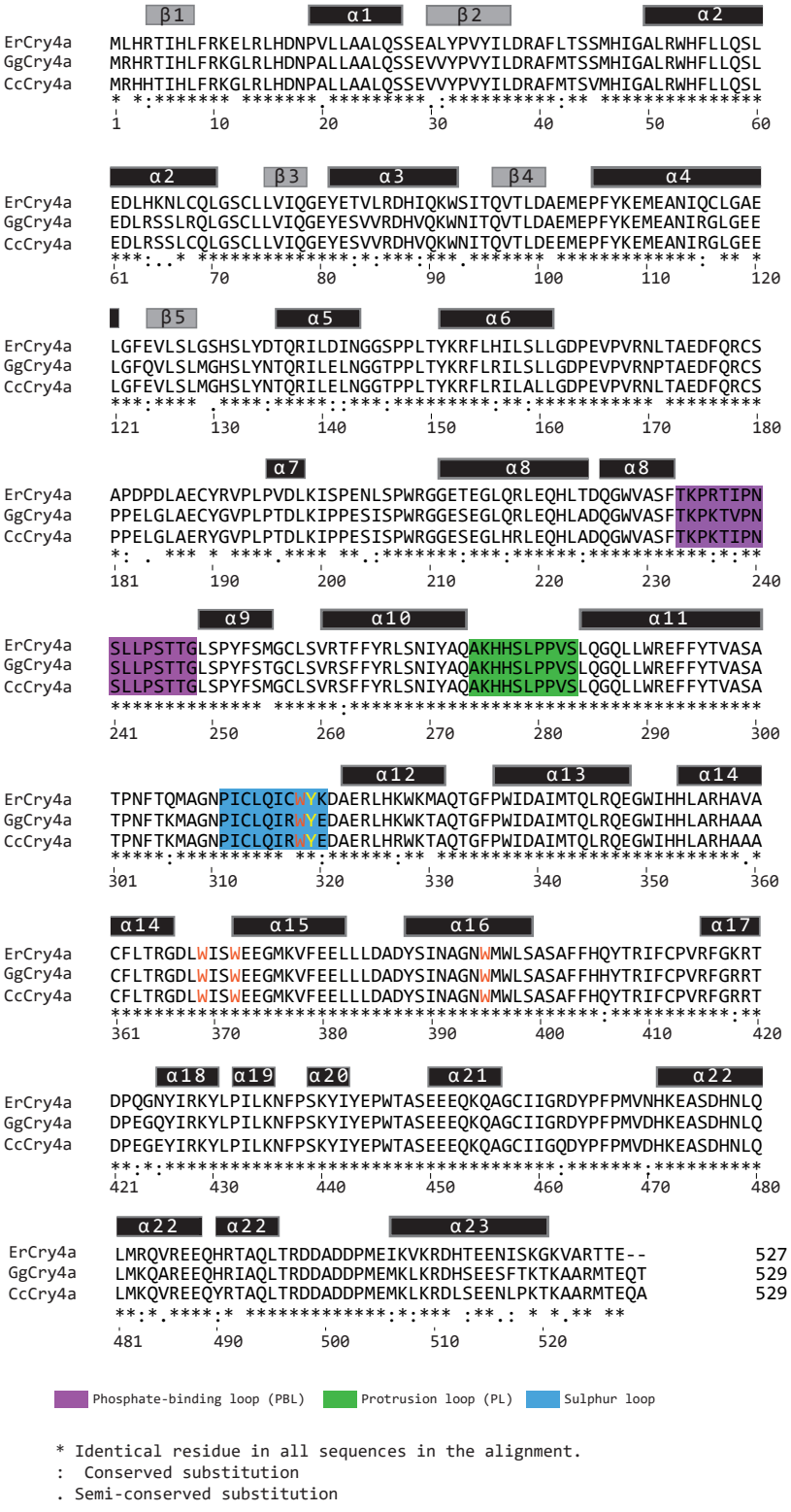


Figure 6.2: Sequence alignment of *Er*Cry4a, *Gg*Cry4a and *Cc*Cry4a. β-sheets are shown in black, α-helices in grey and three annotated loops, the phosphate-binding loop (PBL), protrusion loop (PL) and sulphur loop are highlighted in purple, green and blue, respectively. Positions where all three species share the same residue are marked with an asterisk (*), residues conserved with *Er*Cry4a with a colon (:) and semi-conserved positions with a dot (.).

Table 6.3: Pairwise sequence similarity (%) restricted to the CTT of Cry4a. Robin Cry4a shows lower similarity to both galliform sequences, whereas chicken and quail remain more closely aligned.

	*Er*Cry4a	*Gg*Cry4a	*Cc*Cry4a
*Er*Cry4a	—	59.09%	59.09%
*Gg*Cry4a	59.09%	—	79.17%
*Cc*Cry4a	59.09%	79.17%	—

polarity shifts such as arginine for lysine or isoleucine for valine, introduce small changes in local charge distribution and solvent accessibility.The PL, by contrast, is completely conserved at both sequence and structural levels, reinforcing its essential role as a rigid architectural element adjoining the FAD pocket.

The sulphur loop (residues 311–320) presents a more nuanced picture, its overall position within the fold is conserved, but residue-level substitutions subtly modify the local chemical environment. Robins possess a cysteine–lysine pair at positions 317 and 320, while chickens and quails carry an arginine–glutamic acid combination. These replacements switch the local electrostatic landscape from mixed redox-capable and basic (C–K) to a strongly ionic (R–E) environment. Although mutagenesis of these sites in chicken Cry4a did not significantly affect magnetic-field sensitivity or radical-pair kinetics, the substitutions could still influence local flexibility, loop mobility, or transient hydrogen-bonding networks around TrpC [71]. Subtle variations of this kind may underlie species-specific HDX differences in the vicinity of the sulphur loop, linking small-scale sequence variation to measurable changes in dynamic stability.

Residues where the backbone trajectory remains conserved but side-chain chemistry differs are of particular interest for HDX–MS, as such sites are sensitive indicators of conformational breathing and solvent exposure. The PBL and sulphur loop thus provide informative probes for testing whether Cry4a dynamics are universally conserved across species or display fine-tuned adaptations in light-dependent behaviour.

The comparative AlphaFold3 models provide a complementary structural view of these patterns. In all three species, the PHR is predicted with high confidence



Figure 6.3: AlphaFold3 models of *Er*Cry4a (red), *Gg*Cry4a (blue) and *Cc*Cry4a (green), aligned to illustrate conservation of the photolyase homology region and relative divergence of the C-terminal extension. Models produced by Navoneel Sen.

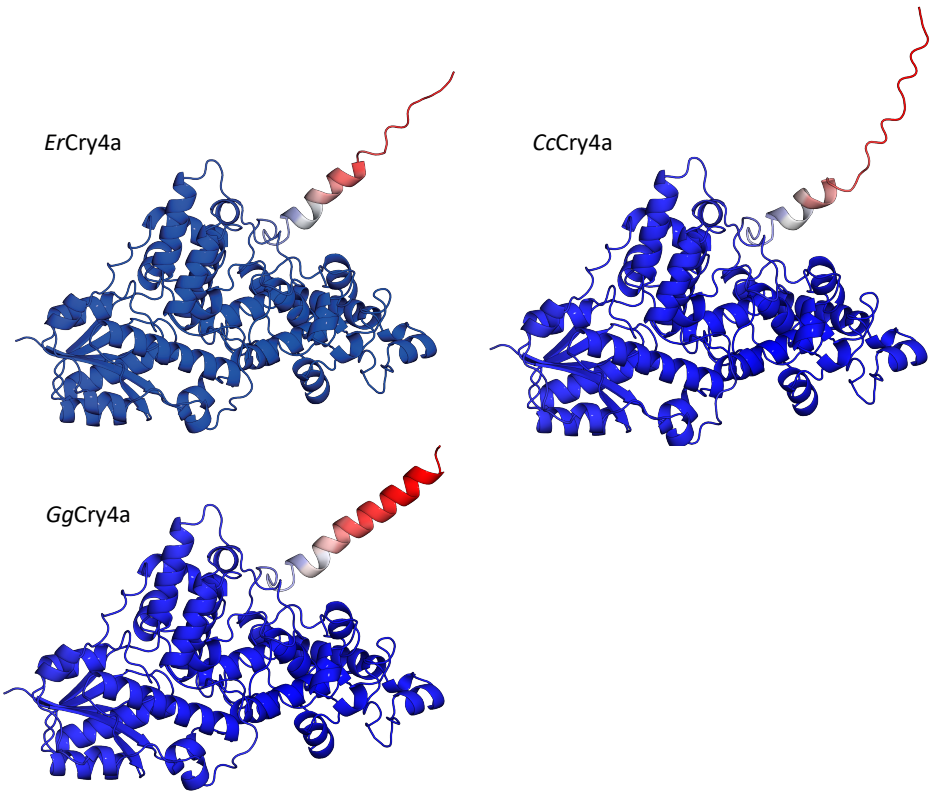


Figure 6.4: AlphaFold3 models of *Er*Cry4a, *Gg*Cry4a and *Cc*Cry4a, coloured by model confidence (blue = high, red = low). The PHR is predicted with high confidence and consistent architecture, whereas the CTT is low-confidence and variably organised, reflecting its intrinsic disorder. Models generated by Navoneel Sen.

(blue), reflecting the evolutionary conservation of its secondary structure elements surrounding the FAD-binding cavity (Figure 6.4). The FAD pocket and the TrpA–TrpD electron-transfer chain display near identical geometries, consistent with their preserved photochemical functions. The CTT, in contrast, is predicted with low confidence (red), signalling intrinsic disorder. Interestingly, AlphaFold predicts distinct secondary-structural propensities across species: in chicken, the CTT forms a comparatively stable α-helix extending from the PHR, whereas in robin and quail it is more fragmented, with a helical region which becomes unstructured towards the end. This diversity suggests that while the region remains disordered overall, its transient structure may be modulated by local sequence context or post-translational environment.

These computational predictions correspond well with experimental findings.

Immunolabelling of chicken Cry4a identified reversible light-dependent conformational changes within the C-terminal region [199], while HDX–MS experiments on robin Cry4a revealed very high uptake consistent with a predominantly disordered but dynamically responsive tail. The juxtaposition of a conserved, stable PHR with a flexible, species-variable CTT therefore represents a unifying structural principle of avian Cry4as. The core provides the photochemical scaffold necessary for radical-pair formation, whereas the variable extensions likely confer regulatory plasticity through altered flexibility, partner binding, or membrane association.

These comparisons demonstrate that Cry4a proteins from robin, chicken and quail share an almost identical folded architecture, anchored by the well-conserved PHR. Evolutionary differences are concentrated in the CTT and surface loops, regions that may influence the kinetics or localisation of photoactivation. Such variation provides a mechanistic framework for understanding how Cry4a can retain its universal light-sensing chemistry while evolving diverse dynamic and regulatory properties suited to the ecological demands of each species.

6.3 Motivation

The preceding chapters have established European robin Cry4a as a central model for exploring light-dependent structural dynamics in a migratory songbird. These studies revealed reproducible conformational responses to illumination, providing molecular evidence consistent with a role in magnetoreception. What remains uncertain, however, is whether these light-induced behaviours are characteristic of avian Cry4a in general, or whether they reflect specialisations that have evolved in migratory lineages such as the robin.

To address this question, the present chapter broadens the scope of analysis to include two additional species: the domestic chicken (*Gg*Cry4a) and the common quail (*Cc*Cry4a). These were examined in direct parallel with the robin protein using identical HDX–MS methodologies, labelling conditions and data-processing workflows. Applying a standardised experimental framework across all three species enables meaningful cross-comparison of hydrogen–deuterium uptake, both globally

and at the level of individual motifs. This approach makes it possible to determine whether the conformational changes characterised in the robin are conserved across avian Cry4a, or whether subtle differences in sequence or structure have given rise to species-specific responses.

Including both wild-type and mutant variants further extends this comparison. Mutations targeting the terminal tryptophan (W369F) and the combined Y319F/W369F substitutions were investigated for chicken and quail in direct analogy to the robin mutants described in Chapter 5.7.4. These perturbations disrupt successive steps of the electron-transfer chain, allowing the resulting HDX patterns to be interpreted in terms of how electron flow influences structural dynamics and solvent accessibility. By examining the impact of these same mutations across species, this study tests whether equivalent photochemical mechanisms underlie the observed light-dependent protection in each system.

These data sets permit a direct comparison between a non-migratory species (chicken) and two migratory species (robin and quail). This provides a framework for asking whether migration-linked behaviour correlates with specific differences in Cry4a flexibility or conformational switching. The analysis focuses particularly on recurring structural motifs, the PBL, PL and CTT, to assess whether these regions respond similarly to light activation in all three species or display lineage-specific modulation of dynamics.

In this way, the comparative approach serves not only to identify conserved elements of Cry4a structure but also to trace how they may have diversified during avian evolution.

The HDX–MS datasets for wild-type *Gg*Cry4a and *Cc*Cry4a were acquired by Dr Angela Gehrckens, while data for the corresponding W369F variants were collected in collaboration with Dr Gehrckens.

6.4 Comparisons of Wild Types

HDX–MS measurements on wild-type *Er*Cry4a, *Gg*Cry4a and *Cc*Cry4a reveal broadly similar exchange profiles, consistent with their conserved tertiary organisa-

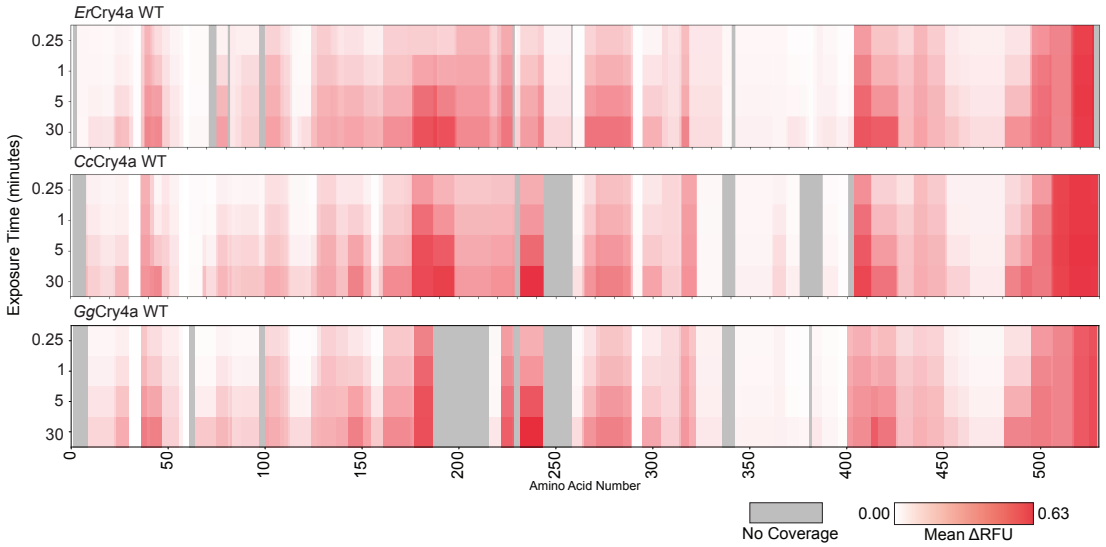


Figure 6.5: Comparison of relative fractional uptake (RFU, expressed as Δ relative to the undeuterated reference) across all three wild-type Cry4a proteins (*Er*Cry4a, *Gg*Cry4a and *Cc*Cry4a). Each panel shows uptake across all time points (0.25–30 min), with white indicating low deuterium incorporation, red indicating higher uptake and grey indicating regions of no coverage.

tion. Across all three species, the PHR is strongly protected, particularly within the central β-sheet core and surrounding helices that form the FAD-binding pocket (Figure 6.5). Exchange increases across flexible loop segments and rises sharply beyond residue 400, reflecting the transition into the disordered, solvent-exposed CTT. The only clear experimental difference lies in the coverage map, where chicken shows slightly reduced peptide recovery between residues 180–220, nevertheless, all structurally and functionally important regions are adequately sampled.

Light-dependent conformational responses are evident in all three species and cluster reproducibly within three motifs, the PBL, the PL and the segment immediately preceding the CTT (Figure 6.6). These regions correspond to the same sites previously identified as light-sensitive in robin Cry4a, indicating that they represent conserved elements of the activation mechanism. Among the three, the PBL in chicken exhibits the most pronounced protection upon illumination, whereas robin shows the weakest magnitude. Quail displays an intermediate behaviour, implying that the strength of light-induced stabilisation does not scale directly

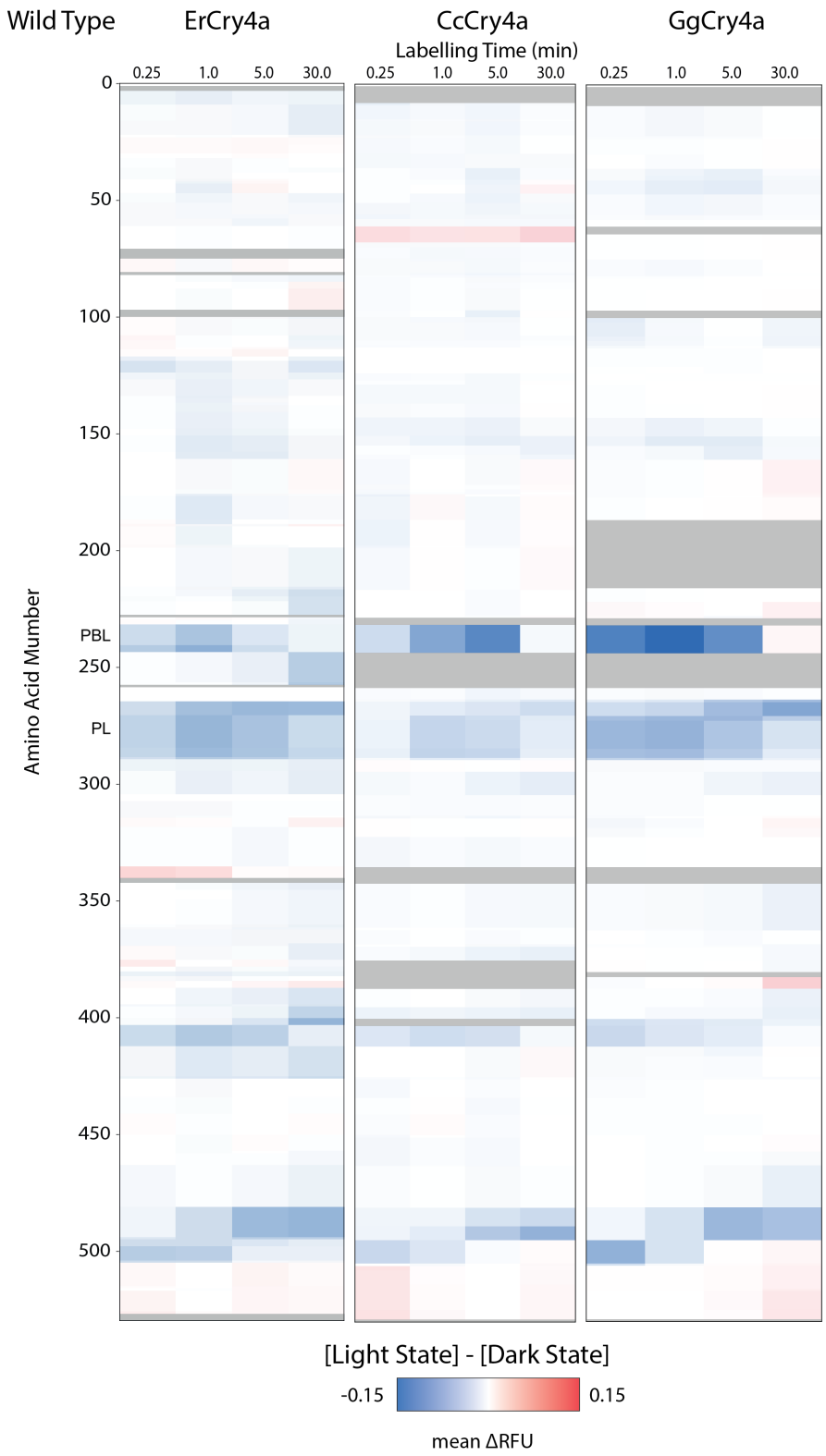


Figure 6.6: ΔRFU heatmaps for wild-type Cry4a from robin, chicken and quail, showing differences between light and dark states. Blue indicates decreased uptake (greater protection under illumination) and red indicates increased uptake (deprotection). Grey indicates no coverage.The phosphate binding loop (PBL) and the protrusion loop (PL) are indicared and experience the largest light induced difference.

with migratory status but may instead reflect subtle sequence or electrostatic differences affecting loop mobility.

The PL exhibits a consistent light-induced protection across all species, aligning with its complete sequence conservation. This protection likely reflects a concerted rearrangement within the solvent-exposed surface near the FAD pocket that transiently restricts solvent accessibility following photoexcitation.

Meanwhile, the region encompassing residues 404–412, situated near the proposed dimerisation interface of other cryptochromes, also displays a modest but reproducible protection, suggesting that light activation may trigger small local reorganisations within otherwise stable secondary-structural elements.

As expected, the CTT shows uniformly high uptake in both light and dark states, confirming its intrinsic disorder and rapid exchange kinetics. However, a reproducible and statistically significant difference emerges in the transition region bridging the PHR and CTT (residues 490–505). This segment encompasses a conserved set of amino acids between the three species and likely acts as a structural hinge sensitive to illumination. Although the amplitude of this change is modest compared to the PBL or PL, its persistence across all three species suggests that conformational modulation at the PHR–CTT junction is a core feature of Cry4a photodynamics.

This data demonstrates that the overall pattern of Cry4a dynamics is strongly conserved across avian lineages. Each protein retains a rigid, well-protected PHR core flanked by flexible loops and a dynamic C-terminal region, forming a shared scaffold for light-driven rearrangements. The primary interspecies differences arise not from the location but from the magnitude of these responses, particularly within the PBL and the hinge adjoining the CTT. These variations likely stem from subtle shifts in local polarity or charge distribution, rather than any large-scale change in tertiary structure.

6.5 Comparisons of TrpD Mutants

HDX–MS measurements of the TrpD (W369F) mutants show that the overall pattern of light-induced changes remains broadly conserved between robin, chicken

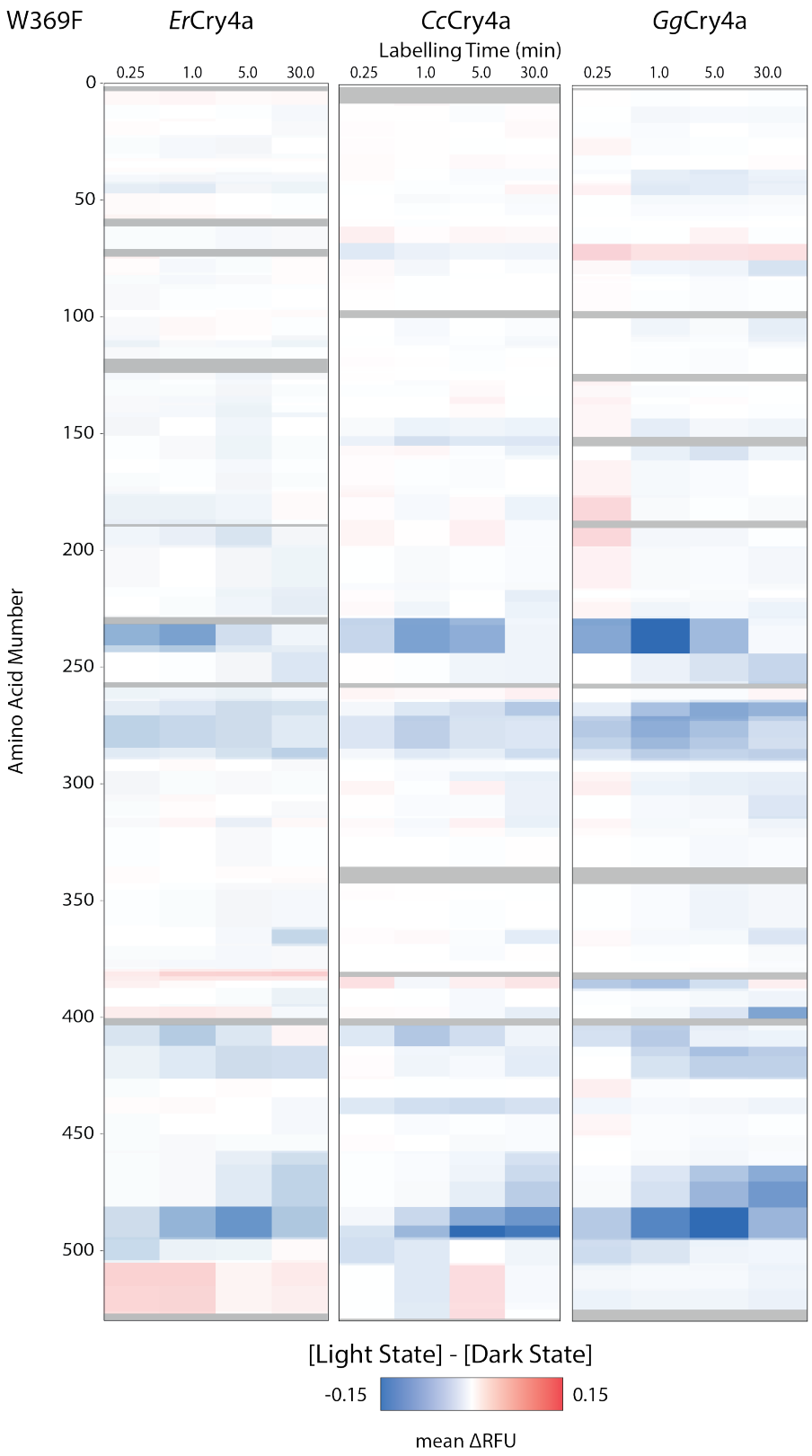


Figure 6.7: Comparison of light-induced uptake differences in the W369F (TrpD) mutants of European robin, quail and chicken. Blue indicates decreased uptake (greater protection under illumination) and red indicates increased uptake (deprotection). Grey indicates no coverage.

and quail (Figure 6.7). Protection is concentrated within the same structural regions identified in the wild types. Despite this overall similarity, each species displays distinct differences in the extent and direction of change, suggesting species-specific modulation of the underlying dynamics.

The most noticeable divergence occurs within the CTT. In the robin, this region exhibits a mild deprotection upon illumination, implying that photoexcitation increases solvent exposure or transient disorder near the tail junction. By contrast, chicken Cry4a shows modest protection within the same region, while quail displays negligible light–dark difference. This inverse behaviour may indicate that the light-activated states are stabilised through subtly different rearrangements across species, potentially reflecting variations in charge distribution or CTT flexibility.

The Woods plots (Figure 6.8) provide a temporal perspective on these changes, showing that the significant differences cluster within the same structural elements but emerge on different timescales across species. In the robin and quail mutants, protection within the PBL, PL and the 404–412 loop is already apparent at the earliest labelling time (15 s), indicating a rapid, light-triggered rearrangement near the FAD pocket. In chicken Cry4a, however, no significant differences are detected at this early point; protection appears only after one minute and increases thereafter, suggesting a slower transition or a higher energetic barrier for stabilising the light-adapted conformation.

The strongest protection is centred on the PBL and PL across all three proteins. These motifs flank the FAD-binding cavity and control access to the cofactor, so their protection under illumination likely reflects loop closure or tightening around the reduced flavin. Smaller, delayed changes near residues 404–412 and the adjoining helices (α17–α22) suggest that this motion extends into the C-terminal portion of the PHR.

Although the overall pattern of responsive regions is conserved, the magnitude and kinetics of protection differ among species. The robin and quail exhibit a rapid and pronounced stabilisation that may facilitate efficient conformational switching, whereas the slower onset in chicken indicates a more constrained network

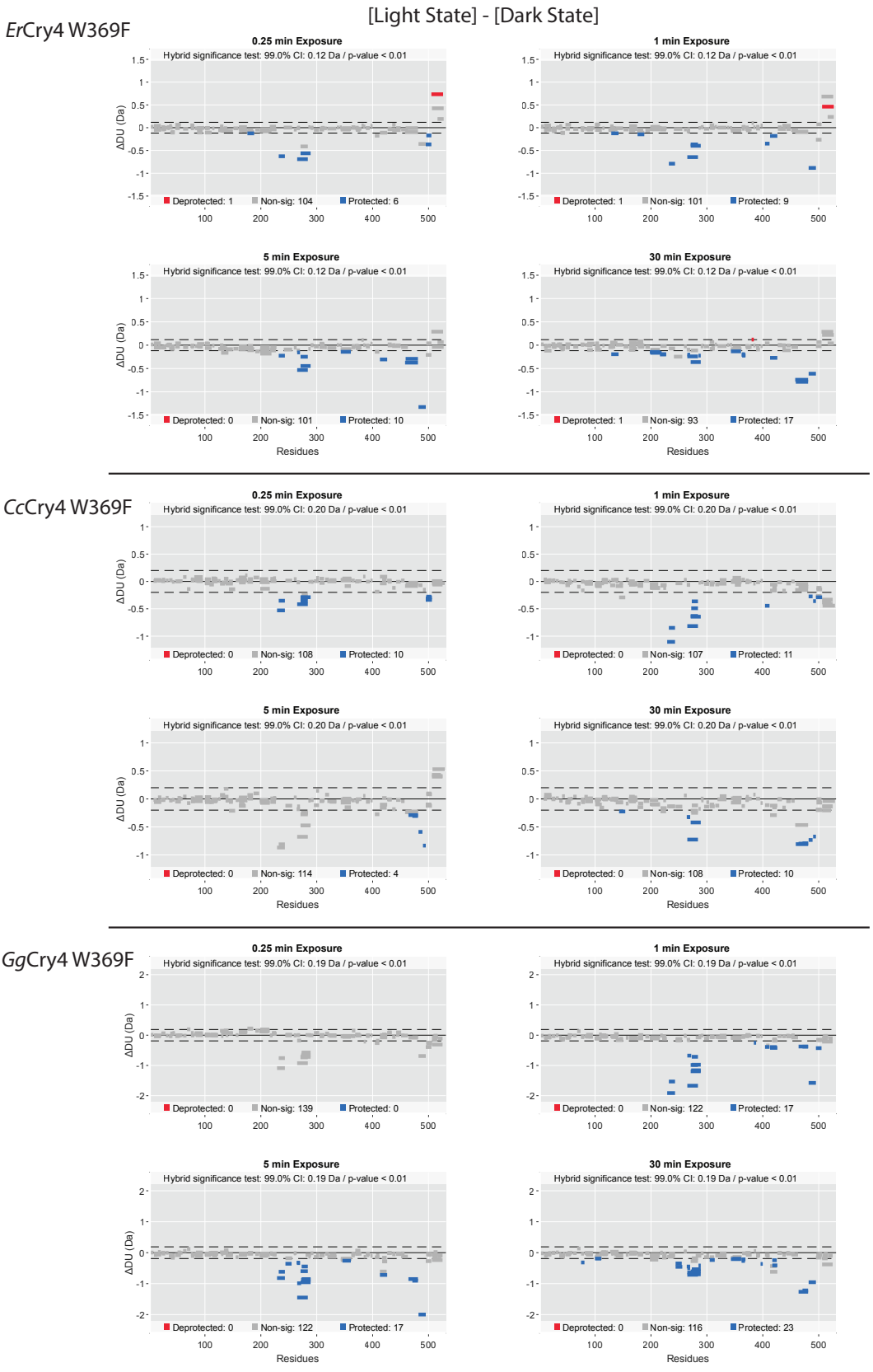


Figure 6.8: Woods plots comparing light–dark differences for W369F mutants. Each plot shows the change in uptake (ΔD_U)for peptides across the sequence at different labelling times (0.25, 1, 5 and 30 min), analysed using the hybrid significance test (99% CI, $p < 0.01$). Protected peptides (blue) indicate statistically significant decreased exchange under illumination.

of interactions around the FAD cavity. Such kinetic differences are consistent with subtle sequence and electrostatic variations, including those within the sulphur loop (C317 in robin versus R317 in chicken and quail), which could modulate the ease of electron redistribution and loop motion.

6.6 Comparisons of TrpD / Y319F Mutants

Across all three Cry4a homologues, the combined W369F/Y319F (and C317R in robin) substitution completely suppresses the light-induced structural response normally observed in the wild-type proteins. HDX–MS analysis reveals no statistically significant uptake differences between light and dark conditions, indicating that photoactivation no longer produces measurable changes in backbone flexibility or solvent accessibility (Figure 6.9).

This loss of light sensitivity stands in contrast to the behaviour of the wild-type proteins, where distinct regions exhibit reproducible protection upon illumination. In the Y319F/W369F variants, these same motifs display identical uptake profiles under both conditions, suggesting that the conformational network that normally transmits the FAD redox signal has been disrupted. The absence of responsive peptides implies that the coupling between photochemistry and protein dynamics is critically dependent on these residues.

Crucially, this loss of responsiveness is consistent across robin, chicken and quail Cry4a, indicating that the Tyr–Trp coupling forms a universally conserved structural switch within the Cry4a family. Its disruption effectively traps the protein in a conformational state resembling the dark-adapted ensemble, in which the tertiary structure remains relaxed and solvent exposure unaltered by illumination. This behaviour shows that maintaining the Y319–W369 pair is crucial for coupling flavin photochemistry to light-driven structural rearrangements across the protein.

From a mechanistic perspective, these findings highlight the combination of Y319–W369 as a pivotal element in the Cry4a activation pathway. The conserved response across all species implies that this coupling has been maintained throughout avian evolution to ensure efficient communication between the flavin redox centre

and distal structural motifs such as the PBL and CTT. Disrupting this relay not only abolishes measurable light sensitivity but also demonstrates how specific aromatic interactions underpin the conformational plasticity that enables Cry4a to function as a light-dependent signalling molecule.

6.7 Important Regions

Having established that the overall pattern of light-induced protection is conserved across species and largely dependent on the integrity of the electron-transfer chain, it is helpful to examine the behaviour of specific peptides in more detail. Focusing on the regions identified as statistically significant by Deuteros analysis allows direct comparison of how individual structural elements respond to mutation and illumination. This analysis reveals trends across the PBL, PL, α22 and the putative dimer region, which show how alterations at TrpD and Y319 modulate local flexibility, solvent accessibility and coupling between the FAD-binding site and the protein surface. In this section, each region is considered in turn, with comparisons made across wild-type and mutant forms of robin, chicken and quail Cry4a to highlight both conserved and divergent aspects of their dynamic behaviour.

6.7.1 Phosphate-Binding Loop

The PBL, (residues 232–243) is a conserved and strongly light-responsive element in all Cry4a homologues studied. Figure 6.10 compares the deuterium uptake profiles for wild-type and mutant forms of (*Er*Cry4a),(*Gg*Cry4a) and (*Cc*Cry4a). In every case, illumination produces a measurable decrease in deuterium incorporation, indicating transient stabilisation or reduced solvent accessibility of this flexible loop upon photoactivation.

In the robin wild type, this light-dependent protection is particularly pronounced, producing the largest difference between light and dark uptake curves among the three species. The magnitude of protection reflects an increase in the structuring of the loop or reduced solvent exposure upon flavin photoreduction. Introduction of the TrpD mutation (W369F) markedly reduces this effect, approximately halving

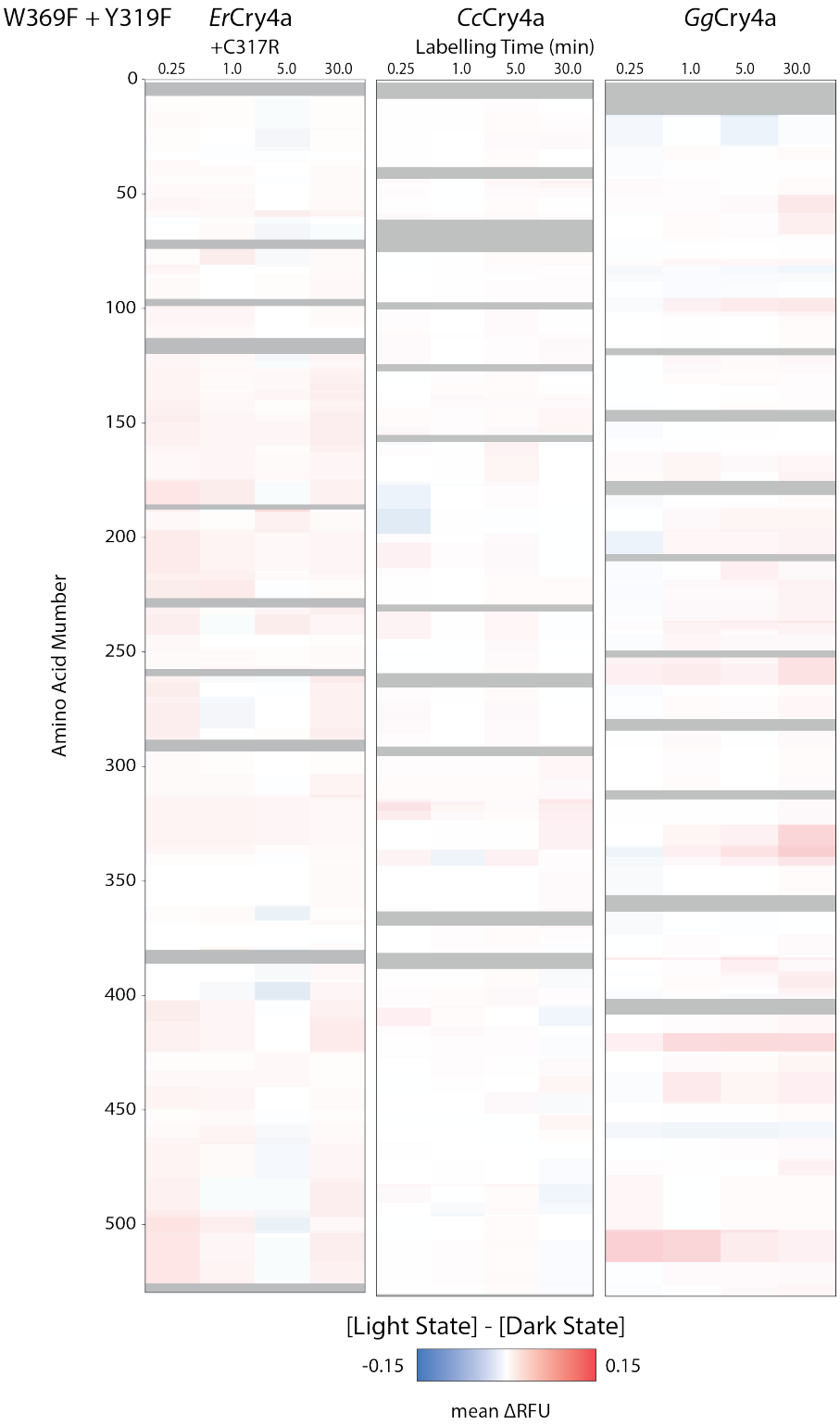


Figure 6.9: Summary of HDX-MS results for the Y319F/W369F double / triple (C317R) mutants across *Er*Cry4a, *Gg*Cry4a and *Cc*Cry4a. No statistically significant differences are observed between light and dark states.

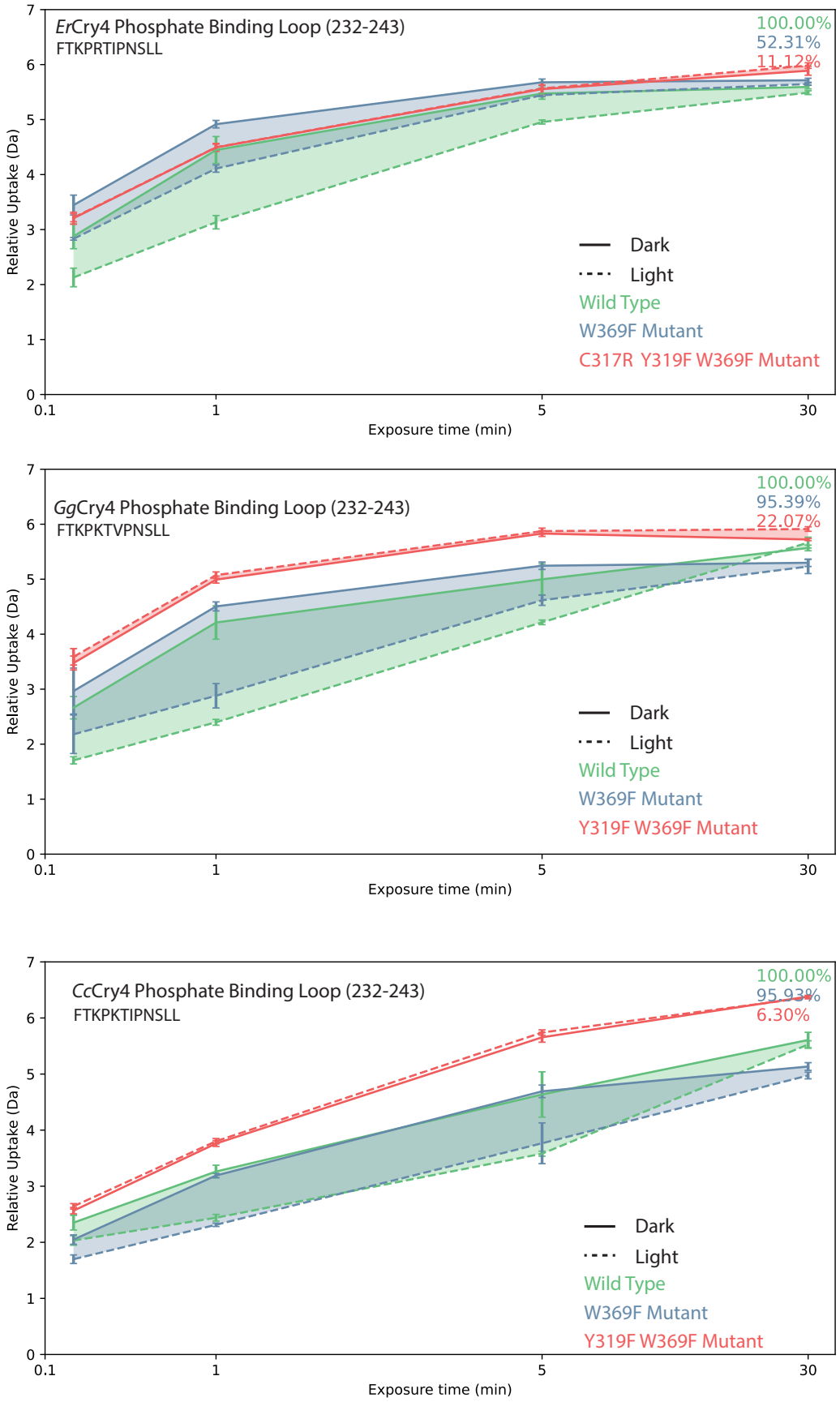


Figure 6.10: Relative deuterium uptake of the PBL for *Er*Cry4a (top), *Gg*Cry4a (middle) and *Cc*Cry4a (bottom) wild-type and mutant proteins under light (dashed) and dark (solid) conditions. The shaded area represents the magnitude of light-induced protection.

the amplitude of the response, implying that the terminal electron-transfer step from TrpD to FAD is central to the conformational coupling that stabilises the PBL. The double mutant (Y319F/W369F) eliminates the response almost entirely, demonstrating that disruption of either the terminal tryptophan or its adjacent tyrosine breaks the allosteric communication pathway linking the flavin pocket to this loop.

In both chicken and quail, mutation of TrpD only slightly decreases the light–dark difference, with the W369F mutants retaining approximately 90–95% of the wild-type protection amplitude. This persistence suggests that the PBL in these species is less tightly coupled to the redox chemistry of the flavin, perhaps reflecting altered electrostatic connectivity or differences in local hydrogen-bonding networks that mediate the propagation of charge redistribution through the protein. As with robin, the Y319F/W369F double mutation largely abolishes protection, reducing the response to roughly 20% of the wild-type amplitude in chicken and to background levels in quail.

Interestingly, in the galliforms the uptake curves for the double mutants do not overlap with those of either the wild type or TrpD mutant. Instead, both display consistently higher overall uptake across all time points, indicating an intrinsically more solvent-exposed and flexible loop even before illumination. This suggests that, in addition to removing light sensitivity, the mutations also shift the equilibrium towards a more disordered conformational ensemble, possibly by destabilising transient interactions between the loop and the surrounding β-sheet.

Overall, the robin Cry4a PBL demonstrates the strongest functional coupling between FAD photoreduction and loop stabilisation, consistent with rapid and efficient transmission of redox changes through the electron-transfer chain. In contrast, the corresponding loops in chicken and quail retain similar structural response but less clearly, implying that the coupling between the FAD pocket and surface loops has become partially attenuated. This attenuation may stem from subtle sequence differences that stabilise the flavin cavity and dampen allosteric propagation. Consequently, while the overall structural scaffold of Cry4a remains

conserved, the PBL illustrates how species-specific tuning of electrostatics and flexibility can modulate the dynamic range of the photoactivation response.

6.7.2 Protrusion Loop

The PL (residues 271–284) represents another flexible, solvent-exposed region that shows light-dependent structural responses in all Cry4a homologues. Figure 6.11 compares the relative deuterium uptake profiles for this region under both light and dark conditions.

In the robin wild type, illumination leads to a clear reduction in deuterium uptake within the PL, reflecting stabilisation or restricted solvent access upon photoactivation. The magnitude of this protection decreases substantially in the W369F mutant, approximately 60% of the wild-type magnitude, indicating that the terminal electron-transfer step from TrpD is critical for transmitting redox-linked structural changes into this region. The combined Y319F/W369F substitution almost completely abolishes the response, reducing the light–dark difference to less than 3% of the wild-type value. This near-total loss of sensitivity reinforces the idea that the PL is dynamically coupled to the FAD redox state, responding directly to charge redistribution and local reorganisation within the PHR.

The behaviour in chicken and quail diverges notably from that seen in robin. In both galliforms, the largest difference between light and dark states occurs not in the wild type but in the TrpD mutant. For *Cc*Cry4a, the integrated area between the light and dark uptake curves of the wild type is around 92% of that of the W369F variant, indicating that substitution at this position only slightly alters the photoresponse. In chicken, the disparity is more pronounced, with the wild-type response reaching only about two-thirds of the difference observed for the TrpD mutant. Therefore, while robin Cry4a exhibits a progressive reduction in light sensitivity with successive mutations, chicken and quail show a plateau or even a reversal of this trend. The Y319F/W369F double mutant, however, once again eliminates measurable light dependence in both species and exhibits a

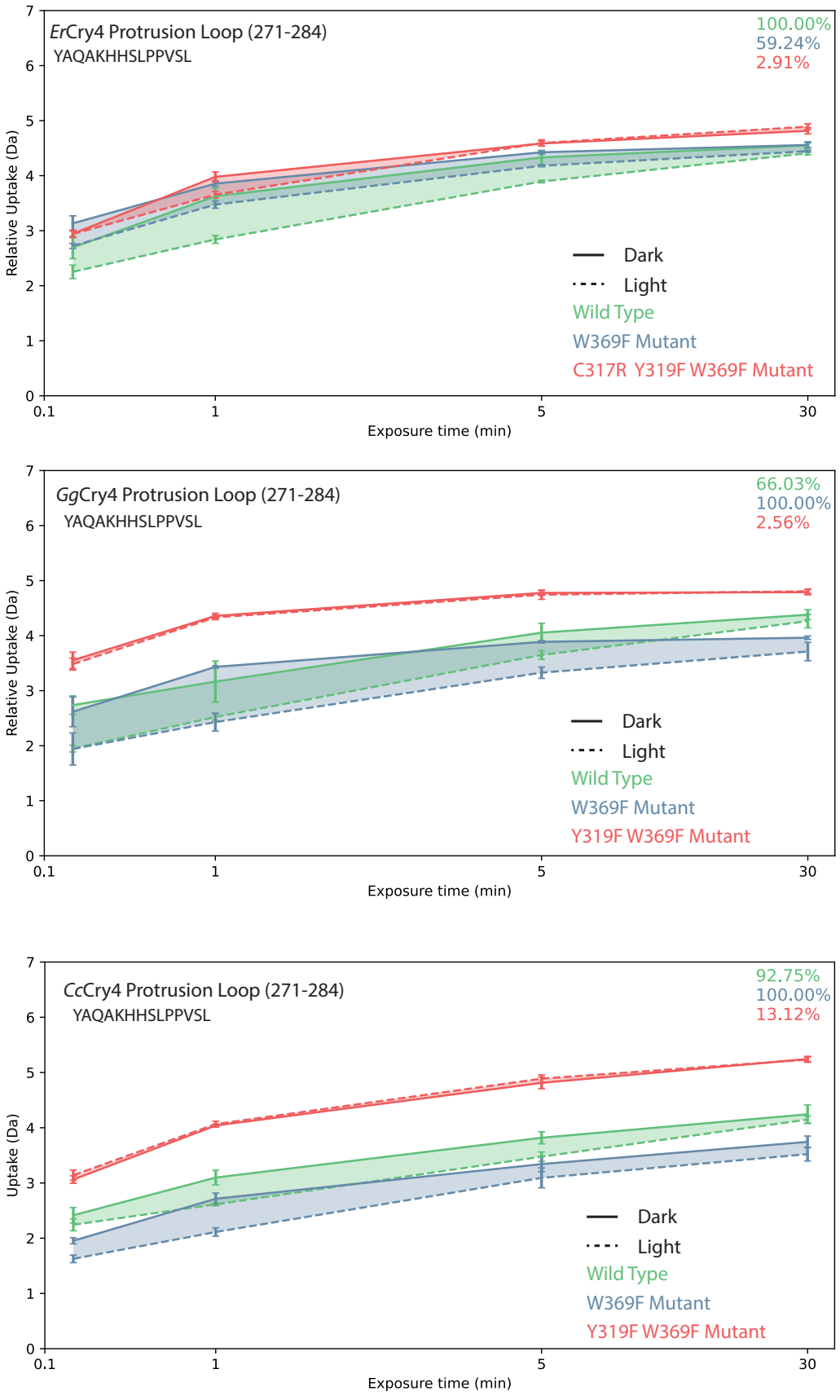


Figure 6.11: Relative deuterium uptake of the PL for *Er*Cry4a (top), *Gg*Cry4a (middle) and *Cc*Cry4a (bottom) wild-type and mutant proteins under light (dashed) and dark (solid) conditions. Shaded areas represent the difference between the two states

consistently higher baseline uptake across time points, suggesting increased intrinsic flexibility or solvent exposure of the loop.

Across all three species, the PL emerges as a conserved site of light-responsive motion, yet the way this motion is coupled to electron transfer appears to differ. In robin Cry4a, the response scales directly with the integrity of the electron-transfer chain, consistent with tight coupling between redox state and local conformational dynamics. In chicken and quail, the persistence or even amplification of the response following TrpD substitution suggests that the PL is influenced by a broader network of structural interactions rather than by direct electron transfer alone. These interspecies contrasts imply that the overall mechanism of activation is conserved, but the structural pathways through which redox changes are communicated to the PL have diverged subtly between lineages.

6.7.3 α22

Helix α22 (residues 482–495) lies at the boundary between the structured PHR and the disordered CTT, placing it in an ideal position to sense and transmit conformational changes associated with light activation. Figure 6.12 compares the deuterium uptake behaviour of this region across *Er*Cry4a, *Gg*Cry4a and *Cc*Cry4a wild-type and mutant proteins under dark and illuminated conditions.

The α22 segment exhibits a distinct pattern from the other light-responsive regions of Cry4a. Across all three species, the most pronounced changes occur in the TrpD mutant, indicating that replacement of the terminal tryptophan substantially perturbs the dynamics of this helix. In every case, a clear sequential increase in uptake of the light and dark states is observed across the mutant series, the wild type shows the lowest uptake, the W369F mutant higher and the double or triple mutants progressively greater uptake. This consistent progression suggests that disruption of the electron-transfer chain systematically enhances solvent accessibility and mobility within α22.

In robin and chicken Cry4a, the uptake curves for the light and dark states are well separated, showing little overlap between conditions. This indicates that

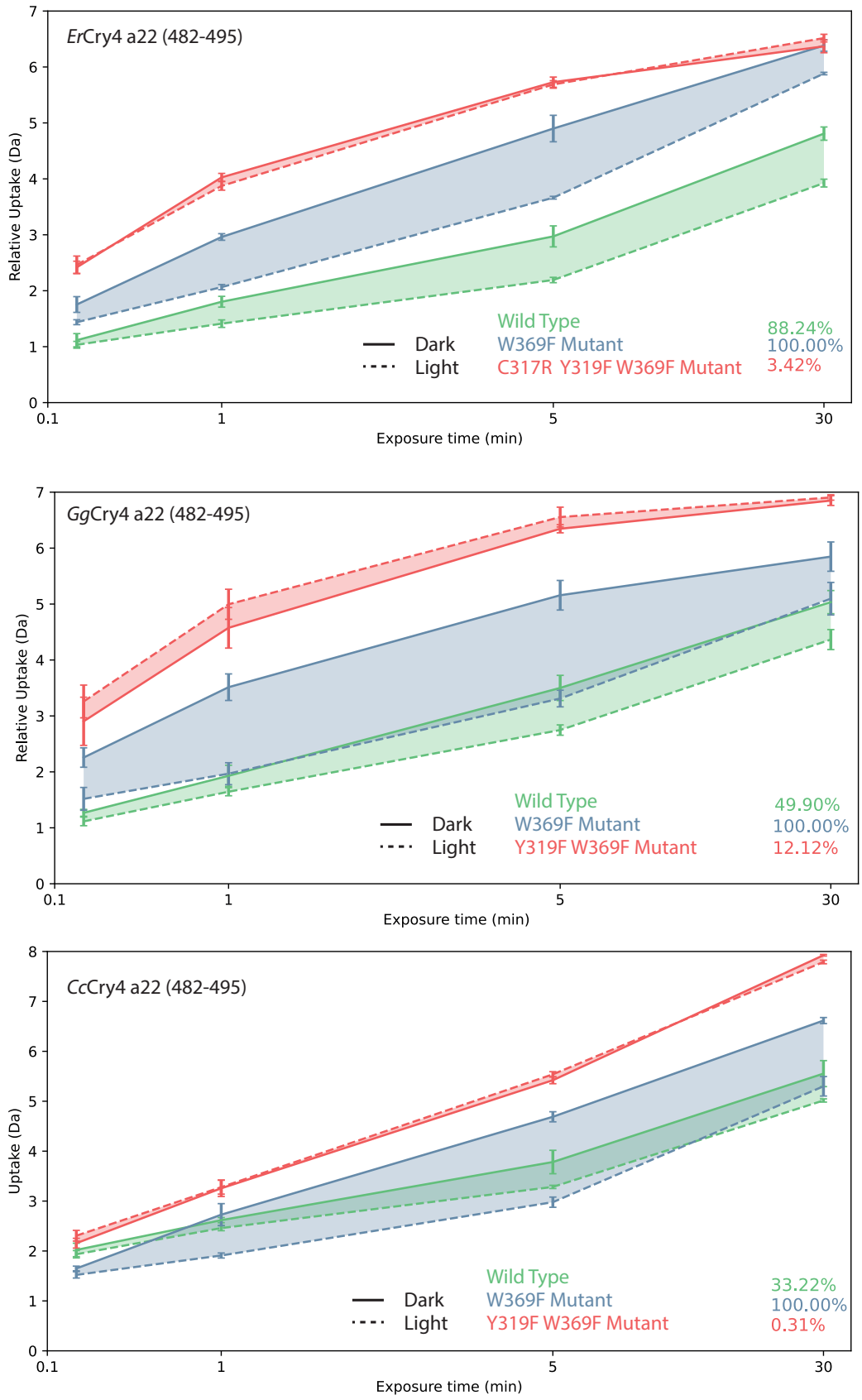


Figure 6.12: Relative deuterium uptake of helix α22 for *Er*Cry4a (top), *Gg*Cry4a (middle) and *Cc*Cry4a (bottom) wild-type and mutant proteins under dark (solid) and light (dashed) conditions. Shaded areas represent the differences between the two states

mutation affects not only the magnitude of the photoresponse but also the baseline stability of the region. In quail, the same general trend is observed, although with greater overlap between the wild-type and TrpD curves. Interestingly, quail displays the largest absolute difference in uptake between the light and dark states when comparing the wild type and the TrpD mutant.These data reveal that α22 is particularly sensitive to alterations in the local redox environment, with mutations at TrpD and Y319 shifting its conformational equilibrium towards increased flexibility and solvent exposure regardless of illumination.

The behaviour of α22 suggests that this helix functions as a dynamic relay linking the FAD-binding pocket to the solvent-exposed surface. Positioned near the terminus of the PHR, it may act as a hinge that modulates access to the C-terminal tail or influences interactions with regulatory partners. The progressive increase in uptake observed upon disruption of the electron-transfer chain indicates that this region becomes increasingly mobile as stabilising interactions are lost, likely those involving electrostatic and hydrogen-bonding contacts with the flavin pocket and the adjacent sulphur loop that restrain α22 in the dark state.

The clear separation between light and dark uptake curves in robin and chicken shows that photoactivation still drives rearrangement within this region even when the terminal tryptophan electron donor is absent. This persistence implies that α22 does not respond solely to the electron-transfer step, but to broader redox-linked reorganisation within the FAD cavity. The gradual rise in solvent exposure across the mutant series supports a model in which α22 acts as a flexible hinge that accommodates and dissipates light-induced structural strain while partially transmitting conformational change to the disordered CTT. Such behaviour would be consistent with its position at a key mechanical junction in the protein and may represent an early step in coupling photoactivation to downstream signalling in avian Cry4a.

6.7.4 Potential Dimer Region

Residues 404–412, form part of a surface-exposed segment proposed to contribute to dimerisation in avian Cry4a [72]. Although this region exhibits less pronounced light-dependent protection than the major responsive motifs, its exchange kinetics differ consistently between species and mutants (Figure 6.13).

The 404–412 region displays relatively subtle but reproducible light-induced behaviour compared with the more strongly responsive loops of Cry4a. In the robin wild type, illumination produces a small yet measurable reduction in uptake, indicating limited stabilisation or restricted solvent exposure upon photoactivation. This effect likely represents transient ordering within a local interface that becomes partially more compact when the FAD is reduced. Substitution of the terminal tryptophan (W369F) attenuates this behaviour, reducing the light–dark difference to less than half of the wild-type value, while the triple mutant (C317R/Y319F/W369F) abolishes the response almost completely.

In chicken Cry4a, the corresponding segment displays an even weaker effect. The wild type shows only slight separation between light and dark curves, consistent with minimal photoinduced structural change. The W369F variant marginally enhances this difference, though the magnitude remains low and the Y319F/W369F double mutant again exhibits negligible light sensitivity. In quail, the wild type and TrpD mutant display similar degrees of protection under illumination, whereas the double mutant fully suppresses this response.

Across all three species, the double and triple mutants consistently show higher absolute uptake values than either the wild type or TrpD mutant. This uniform increase suggests that disruption of the electron-transfer chain enhances local flexibility or solvent exposure, possibly by breaking transient contacts that stabilise this segment in the native state. Such contacts could involve weak side-chain hydrogen bonding or packing interactions with adjacent helices or subunits.

These observations indicate that residues 404–412 constitute a semi-structured region whose stability is subtly influenced by the redox state of the FAD. The modest protection observed in the wild type likely reflects weak allosteric coupling between

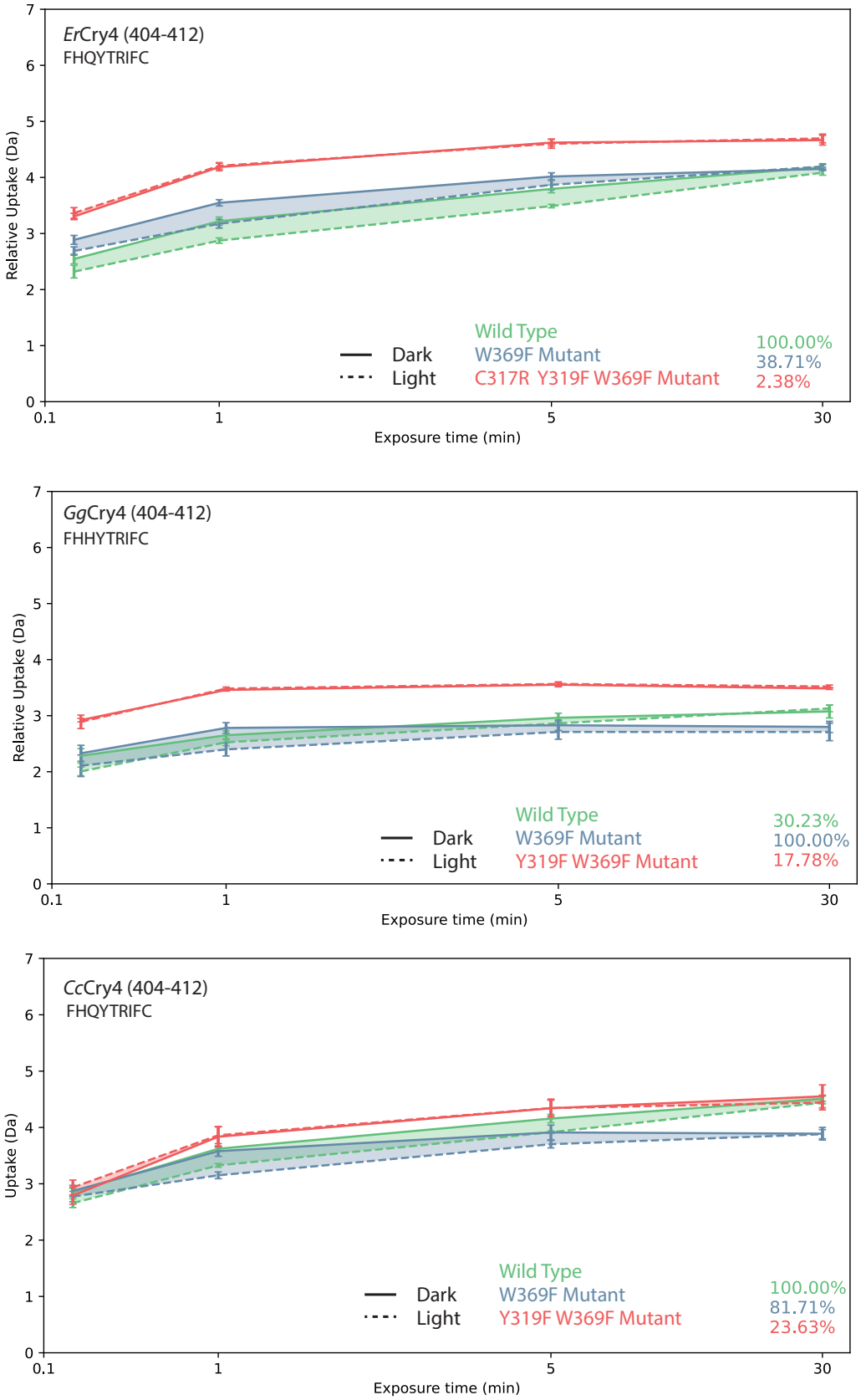


Figure 6.13: Relative deuterium uptake of residues 404–412 for *Er*Cry4a (top), *Gg*Cry4a (middle) and *Cc*Cry4a (bottom) wild-type and mutant proteins under dark (solid) and light (dashed) conditions. Shaded regions represent the differences between the two states.

this site and the flavin cavity, leading to slight restructuring upon photoexcitation. Successive disruption of the electron-transfer chain progressively decouples this interaction, resulting in greater dynamic freedom and higher baseline uptake. This behaviour aligns with models in which Cry4a dimerisation, or local domain rearrangement, is modulated indirectly by photoactivation through small shifts in local packing and electrostatics rather than by large-scale structural transitions.

6.7.5 Mutation Region

To ensure that the introduced mutations do not induce large-scale structural rearrangements, the peptide encompassing residue 369, tryptophan in the wild type and phenylalanine in the mutants, was analysed across all species (Figure 6.14). This region lies within the C-terminal portion of the FAD-proximal domain and directly hosts the terminal residue of the electron-transfer chain (TrpD).

Across all variants, the uptake profiles of this peptide show no statistically significant difference between light and dark states and the overall deuterium incorporation remains highly similar among species. These consistent patterns demonstrate that substitution at position 369 does not cause major conformational reorganisation or destabilisation of the local structure. Instead, the changes observed elsewhere in the protein likely arise from altered photochemical or dynamic coupling rather than from structural distortion induced by mutation.

In the robin wild type, a minor decrease in uptake under illumination is detectable, consistent with weak light-dependent stabilisation at the TrpD site, but this difference is completely absent in the W369F mutant. The same behaviour is mirrored in both chicken and quail Cry4a, where the mutation has minimal structural effect but abolishes any residual light-linked difference. These data confirm that the W369F substitution preserves the global integrity of the protein fold while interrupting the terminal step of the electron-transfer chain, isolating photochemical changes from structural artefacts.

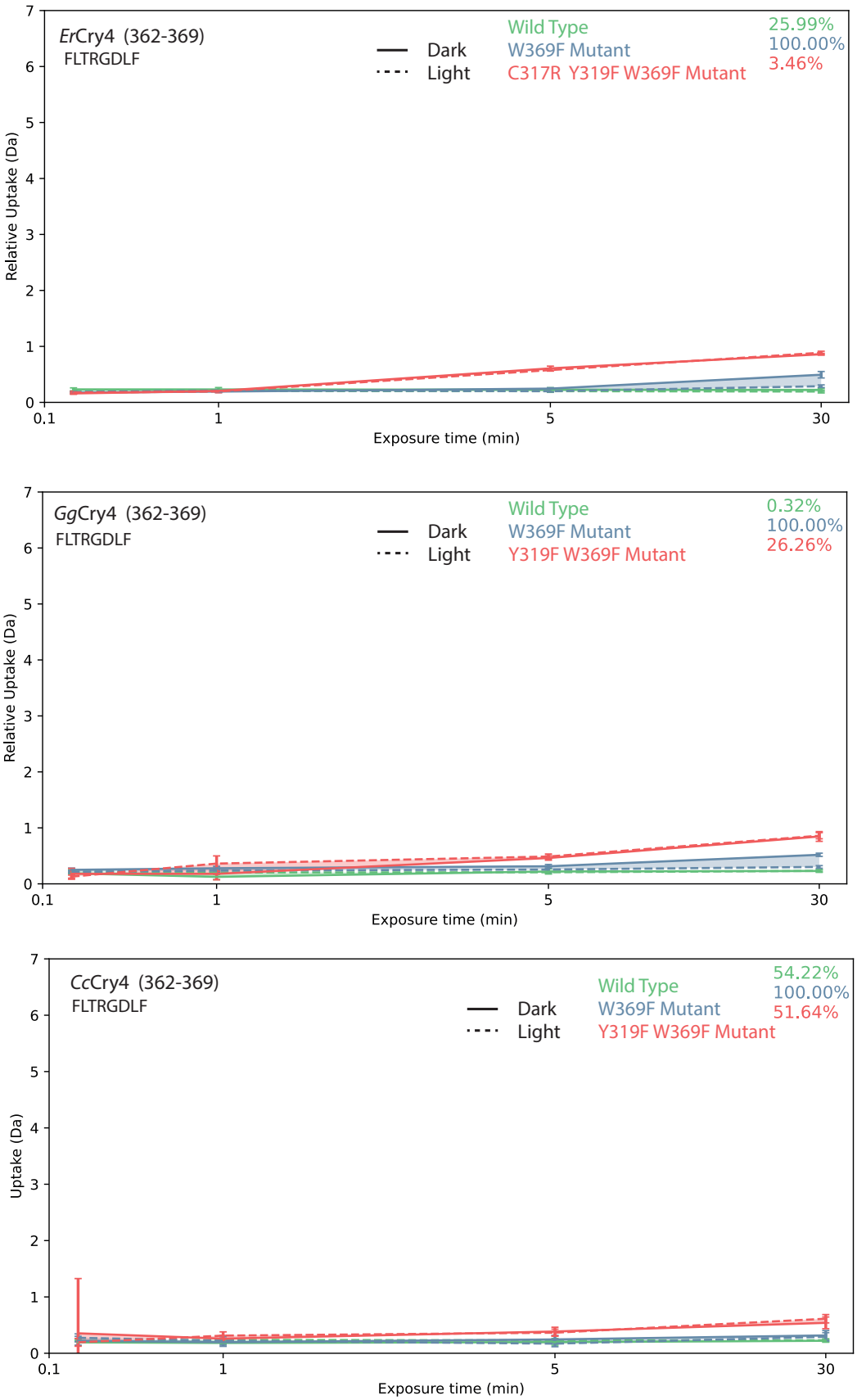


Figure 6.14: Relative deuterium uptake of residues 362–369 (FLTRGDLF) for *Er*Cry4a (top), *Gg*Cry4a (middle) and *Cc*Cry4a (bottom) wild-type and mutant proteins under dark (solid) and light (dashed) conditions. Shaded regions represent the differences between the two states.

6.8 Magnet-Induced Effects

Across all three species and their respective mutants, no statistically significant magnetic field effects were observed under the experimental conditions employed. Comparison of deuterium uptake profiles between magnetic and non-magnetic light exposures revealed no reproducible differences in either direction, indicating that the conformational responses detected by HDX–MS are driven predominantly by illumination.

These results suggest that, if magnetically sensitive steps do occur within the Cry4a photocycle, they operate on a timescale or structural level not directly accessible to the present HDX–MS workflow. The technique captures ensemble-averaged backbone exchange events over seconds to minutes, whereas magnetically induced effects are expected to arise as transient population shifts within radical-pair intermediates on the nanosecond to microsecond scale. Such shifts could, in principle, be inherited by longer-lived conformational states, but under the conditions employed here, no evidence for these downstream effects was detected.

The absence of a magnetic effect in both wild-type and mutant proteins therefore indicates that the mutations investigated do not disrupt or enhance a magnetically coupled conformational state. Instead, the structural changes resolved by HDX–MS reflect intrinsic photoactivation dynamics, those directly linked to redox events within the FAD-binding pocket rather than downstream magnetoreceptive modulation. This outcome aligns with spectroscopic observations that magnetic field sensitivity in Cry4a arises primarily from radical-pair spin dynamics rather than large-scale structural rearrangements.

6.9 Discussion

To interpret the differences observed between species and experimental states, it is important to consider the underlying structural and sequence variations between the proteins. These may arise from subtle amino acid substitutions that modify local electrostatics, or from small shifts in backbone conformation that alter the

geometry of regions positioned near the FAD cofactor or along the electron-transfer pathway. These structural adjustments, while often undetectable in static models, can have measurable consequences for HDX behaviour, particularly in flexible loops or redox-active motifs.

6.9.1 Residue Distances from FAD Across Species

To explore whether structural differences between species could underlie the variation in light-induced protection observed by HDX–MS, residue-wise distances from the isoalloxazine ring of the FAD cofactor were compared for *Er*Cry4a, *Gg*Cry4a and *Cc*Cry4a (Figure 6.15). This analysis highlights the proximity of individual residues to the flavin-binding pocket and provides a framework for assessing how subtle sequence or conformational differences might influence photoactivation and dynamic coupling.

Residues within 20 Å of the flavin, those most likely to interact directly or indirectly with the cofactor, were examined in more detail. A notable cluster spans residues 201–262, which contains 11 substitutions between robin and the two galliform species. Furthermore, within this stretch, residue 254 is conserved in identity but displaced by more than 1 Å in the galliforms relative to robin, suggesting a small but measurable local rearrangement. This segment lies approximately 30 residues upstream of the PBL, positioning it close enough to influence the local electrostatic field or the flexibility of the FAD-adjacent surface. Although the PBL itself shows minimal sequence divergence (Figure 6.16), with only two conservative substitutions (R/K and I/V), such flanking differences could modulate its mobility or solvent exposure, potentially contributing to the species-dependent variation in light-induced protection observed by HDX–MS.

A second region of interest spans residues 317–330, encompassing the sulphur loop and the terminal section of the electron-transfer chain near TrpD. This region contains four sequence differences among the three species (Figure 6.17). As mentioned above, positions 317 and 320, in robin, residue 317 is a cysteine (C317), whereas in chicken and quail it is replaced by arginine; residue 320 is a lysine

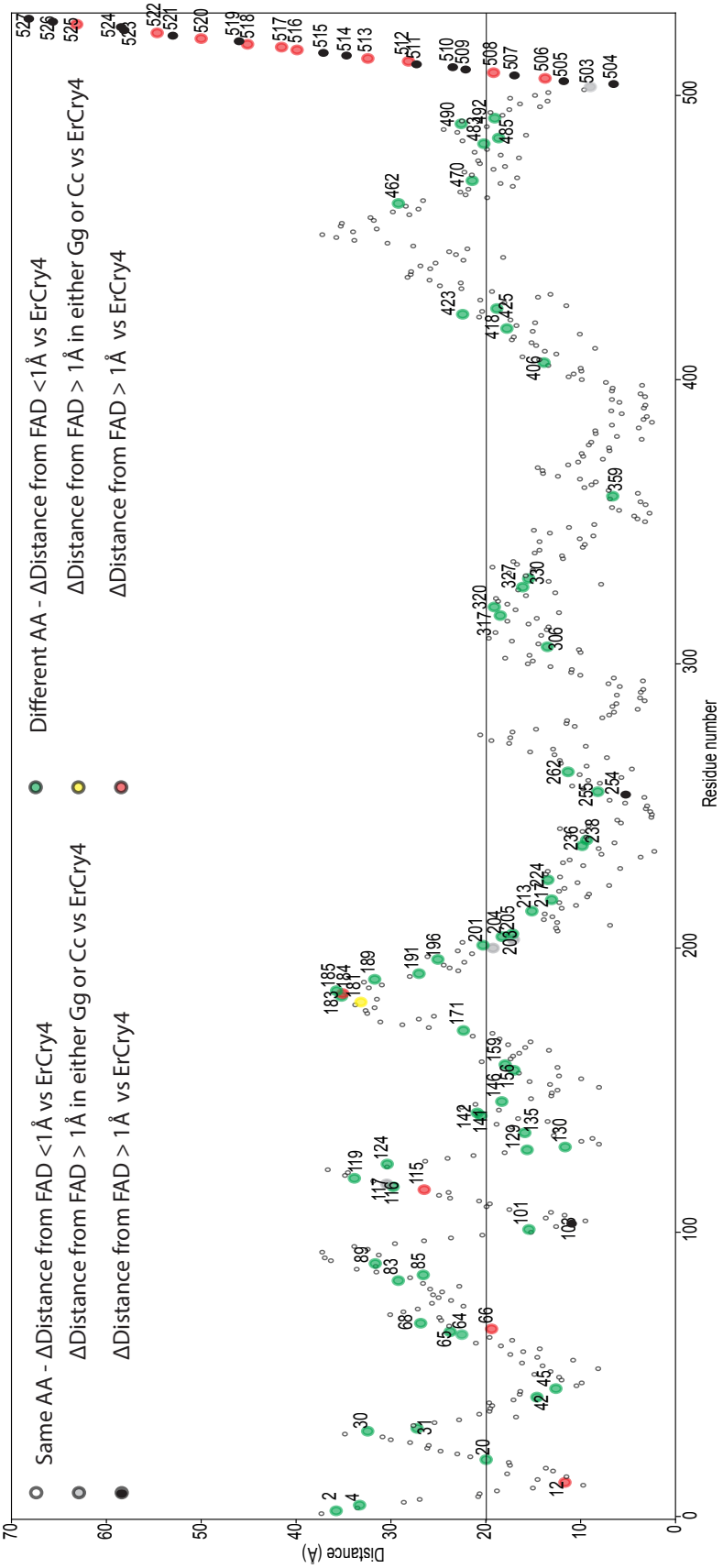


Figure 6.15: Residue-wise distance of each amino acid to the FAD cofactor in *Er*Cry4a, *Gg*Cry4a and *Cc*Cry4a. Horizontal dashed lines indicate 20 Å thresholds from the FAD isoalloxazine ring. Coloured circles represent different amino acids / positions in robin compared to chicken and quail. Figure adapted from Navoneel Sen

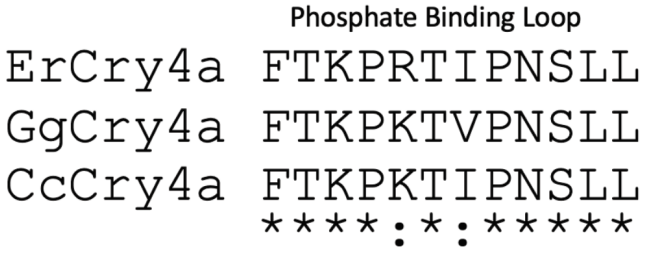


Figure 6.16: Residue composition of the PBL in *Er*Cry4a, *Gg*Cry4a and *Cc*Cry4a.

in robin and a glutamic acid in both galliforms. Although, these mutants have been shown not to affect the radical pair behaviour, they may still cause an alteration of HDX within the protein [71]. These opposing substitutions invert the local electrostatic potential, replacing a redox-sensitive Cys–Lys pair with a more electrostatically stabilised Arg–Glu pair.

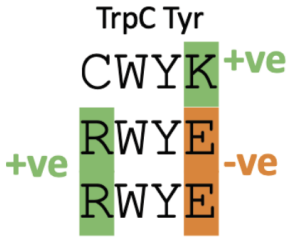


Figure 6.17: Residue variation between *Er*Cry4a (top), *Gg*Cry4a (middle) and *Cc*Cry4a (bottom). Amino acids that differ between species are coloured by chemical property: green (positively charged) and orange (negatively charged).

The substitution of cysteine with arginine at position 317 is particularly significant, as it replaces a small, potentially redox-active residue with a bulkier, positively charged side chain. This change alters the local chemical environment and could influence nearby electrostatic interactions or solvent accessibility. In contrast, the arginine present in chicken and quail would form stronger, persistent electrostatic interactions, reducing loop flexibility and dampening sensitivity to light-induced charge redistribution. The accompanying reversal at position 320, from lysine (positive) to glutamate (negative), further stabilises the galliform loop electrostatically while diminishing its capacity for transient rearrangement.

These local variations offer a plausible molecular basis for the species-specific HDX behaviour observed experimentally. The presence of C317 in robin may enhance coupling between flavin redox changes and conformational shifts in adjacent loops, producing stronger light-induced protection. In the galliform homologues, the Arg–Glu substitution pair imposes a more rigid, charge-balanced environment that constrains local motion, thereby limiting the amplitude of the conformational response. Although the overall fold and FAD geometry remain conserved, these subtle differences in local charge distribution and hydrogen-bonding potential appear sufficient to modulate the degree of dynamic flexibility detected by HDX–MS.

This interpretation is further supported by the convergence of mutant behaviour across species. In the engineered variants, the cysteine in robin Cry4a is replaced with an arginine, effectively rendering the local environment more similar to that of chicken and quail. Correspondingly, the HDX response in the robin mutants resembles that of the galliform proteins, with reduced light-induced protection and a dampened overall dynamic range. These observations reinforce the view that small, chemically specific residue substitutions near the TrpC–TrpD junction can fine-tune the sensitivity of Cry4a to photoactivation, providing a molecular explanation for the interspecies differences in HDX–MS patterns without invoking large-scale structural divergence.

6.9.2 Kinetics in the *Cc*Cry4a CTT

HDX–MS analysis of the quail Cry4a CTT revealed complex exchange kinetics within the peptide spanning residues 505–527 (Figure 6.18). Instead of the clear bimodal isotopic envelopes expected for classical EX1 behaviour, the spectra show a gradual rightward shift of the more protected, lower-mass population accompanied by a steady rise in intensity of the higher-mass, more exchanged population. The isotopic distribution therefore broadens without distinct separation, pointing to an intermediate kinetic regime-often described as EXX, where the rates of conformational opening and amide exchange are of similar magnitude [207, 208].

Under these conditions, exchange proceeds through partially coupled structural fluctuations rather than discrete unfolding events. Protected regions begin to sample more open conformations while already exposed residues continue to incorporate deuterium, leading to the simultaneous evolution of both species. This mixed pattern differs from the cooperative transitions typical of EX1 kinetics, where one population replaces the other and from the residue-by-residue behaviour of EX2 exchange. The data thus suggest that the CTT of *Cc*Cry4a does not undergo a single concerted transition but instead samples a heterogeneous ensemble of states in which local and global motions occur on comparable timescales.

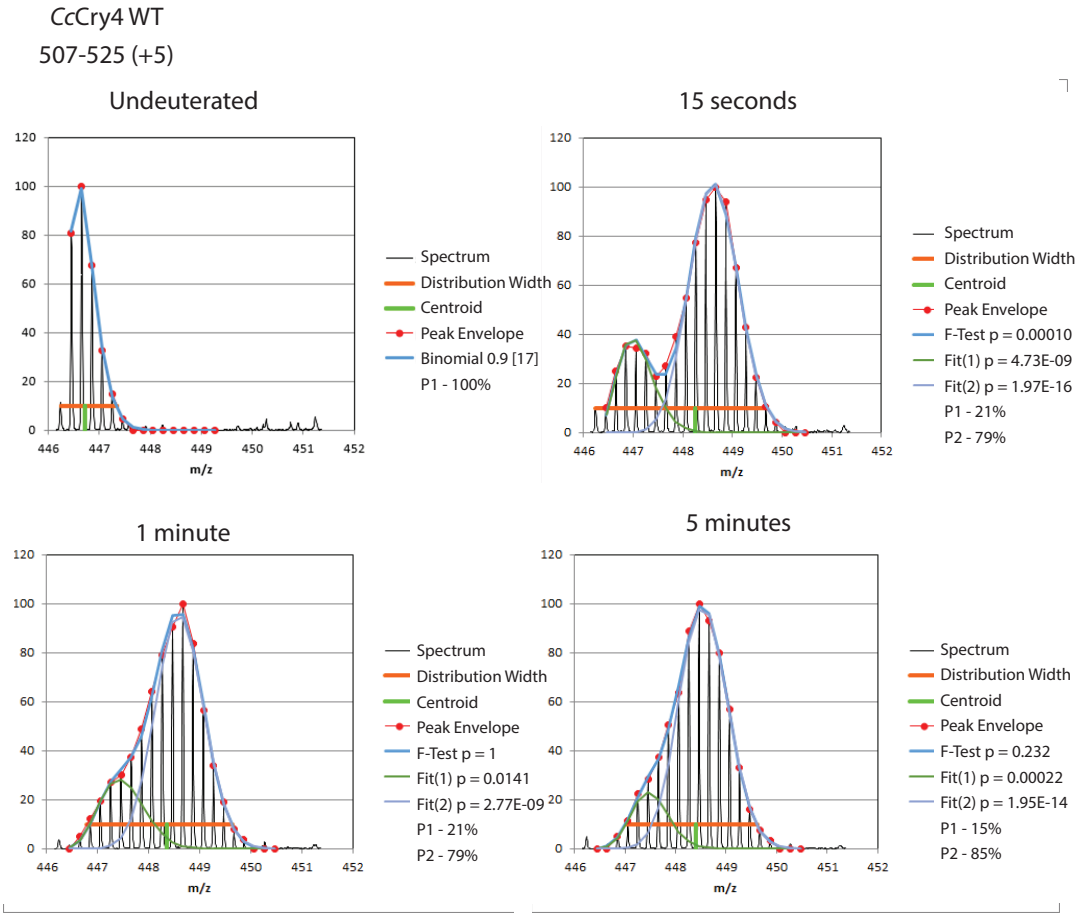


Figure 6.18: Fitted mass spectra of peptide 507–525 from *Cc*Cry4a wild type, showing a gradual shift of the isotopic centroid consistent with intermediate EXX kinetics. The progressive increase in average mass without distinct bimodality indicates exchange through interconverting conformers rather than cooperative unfolding.[208]

Structurally, this peptide corresponds to the final segment of the CTT, which is

predicted by AlphaFold3 to possess partial secondary structure. In the quail model, this region forms a short α-helical segment that transitions into a disordered coil (see Figure 6.4). This prediction aligns closely with the EXX behaviour observed by HDX–MS: the helical portion provides transient protection, while the adjacent disordered residues permit rapid solvent access. The interplay between these two conformational states yields an intermediate exchange profile reflecting continual interconversion on the HDX timescale.

This dynamic equilibrium likely represents a finely balanced competition between stabilising and destabilising forces within the CTT. Partial structuring may arise from transient electrostatic interactions between acidic residues of the tail and basic patches on the PHR surface, while the disordered termini allow flexibility for transient disengagement. Such reversible structuring could play a regulatory role, modulating interaction surfaces or the positioning of the CTT relative to the protein core.

Comparable behaviour has been reported in *Drosophila melanogaster* cryptochrome (*Dm*Cry), where the CTT undergoes light-induced EX1 exchange upon FAD photoreduction [56]. In that protein, illumination triggers cooperative unfolding or unstructuring of the final part of the CTT. In contrast, the exchange behaviour of *Cc*Cry4a appears intrinsic and illumination-independent, suggesting that the quail CTT samples these conformations spontaneously rather than switching in response to light. This distinction may reflect an evolutionary divergence in regulatory coupling. While both proteins retain a structurally responsive tail, the linkage between the CTT and the FAD redox state appears relaxed in the avian Cry4a family.

Interestingly, no comparable EXX or EX1 behaviour is observed in the equivalent CTT peptides of *Er*Cry4a or *Gg*Cry4a. In both cases, the isotopic envelopes broaden gradually but remain unimodal, consistent with rapid EX2-type exchange characteristic of highly dynamic, solvent-exposed regions. The absence of intermediate or cooperative kinetics in these species likely reflects differences in the intrinsic stability of their CTTs. In robin and chicken Cry4a, the CTT is predicted to be

almost fully disordered, providing no opportunity for transient secondary structure to persist long enough to generate intermediate exchange behaviour.

By contrast, the partial α-helical propensity predicted in quail may create a structural element capable of reversible ordering, allowing it to sample both protected and exposed states on the HDX timescale. This structural heterogeneity provides a compelling explanation for why quail alone exhibits EXX-like kinetics within the CTT, whereas robin and chicken tails exchange rapidly and uniformly. Such species-specific tuning of CTT stability may represent an evolutionary adjustment in how the tail interacts with other cellular components or the membrane environment, subtly modulating Cry4a's conformational plasticity without altering its conserved photochemical core.

6.10 Conclusions

The comparative HDX–MS analyses of *Er*Cry4a, *Gg*Cry4a and *Cc*Cry4a demonstrate that avian cryptochromes share a conserved structural and photochemical framework while exhibiting species-specific modulation of flexibility and light responsiveness. Across all three homologues, the PHR forms a stable, highly protected scaffold centred around the FAD-binding pocket and the tryptophan electron-transfer chain. Light-induced changes localise reproducibly several regions confirming these as conserved structural relays within the Cry4a activation pathway.

Although the same regions respond to illumination across species, the amplitude and kinetics of protection vary systematically. The European robin displays the strongest photoresponse, with pronounced protection in the PBL and PL and measurable stabilisation at the PHR–CTT junction. By contrast, chicken and quail exhibit smaller light–dark differences, consistent with a more constrained conformational landscape. These variations likely arise from subtle sequence-dependent effects, such as altered local electrostatics or loop mobility, rather than differences in overall fold.

Mutation of the terminal tryptophan (W369F) and the adjacent tyrosine (Y319F) confirms that both residues are essential for transmitting the redox-driven

conformational signal from the flavin pocket to distal regions. Disruption of this Tyr–Trp coupling progressively attenuates light sensitivity, culminating in complete loss of the response in the double mutant. This effect is conserved across all three species, indicating that conformational changes in this region are coupled to the redox state of the flavin and represent an intrinsic feature of the Cry4a fold.

Residue-level comparison of sequences and AlphaFold3 models provide a structural rationale for the species-specific dynamics observed. While the PHR remains nearly identical among species, subtle substitutions near the TrpC/TrpD junction, notably the presence of cysteine at position 317 in robin, replaced by arginine in chicken and quail, alter local polarity and flexibility around the FAD cavity. These differences may influence how structural or electrostatic changes induced by photoreduction are transmitted through the surrounding matrix, potentially contributing to the greater light responsiveness of the robin protein.

Within the CTT, HDX–MS reveals uniformly rapid exchange consistent with intrinsic disorder, yet distinct behaviour emerges between species. Only quail Cry4a exhibits intermediate EXX kinetics within residues 505–527, indicative of partial and reversible structuring. This behaviour aligns with AlphaFold3 predictions of a hybrid configuration containing both helical and disordered elements. The predicted secondary structure of the CTT differs among species, with chicken forming a continuous helical segment, whereas robin and quail show only partial ordering, consistent with a mixed helical–disordered character (Figure 6.4). This pattern suggests that CTT flexibility is conserved but modulated across species, potentially influencing how the tail engages in transient interactions.

No magnetically induced effects were detected in any of the species or mutants examined, suggesting that the conformational changes observed by HDX–MS arise primarily from photochemical activation. Magnetically sensitive events, if present, may be too subtle or transient to resolve on current HDX–MS timescales, or could require protein–protein interactions not captured in the isolated systems studied here.

Overall, these findings reveal that the molecular framework underlying Cry4a photoactivation is deeply conserved across avian lineages, yet individual species

differ in how their dynamic elements respond to light. The robin Cry4a exhibits the strongest and most finely tuned photoresponse, whereas the galliform homologues display more restrained and less tightly coupled dynamics. Evolutionary divergence therefore appears to have acted not on the conserved photochemical core, but on the dynamic and electrostatic properties of peripheral loops and the disordered CTT, providing a mechanism for fine-tuning Cry4a's conformational plasticity while preserving its underlying radical-pair photochemistry.

6.11 Materials and Methods

6.11.1 Materials

All reagents and chemicals were purchased from Sigma Aldrich (Gillingham, UK) unless otherwise stated. Recombinant cryptochrome proteins were expressed in *E. coli* and purified by collaborators in the laboratory of Henrik Mouritsen at the Carl von Ossietzky University of Oldenburg, Germany, using established protocols [17]. Samples were shipped on ice in storage buffer containing 20 mM Tris, 250 mM NaCl, 2 mM DTT and 20% (v/v) glycerol and stored at −80 °C until required for experiments. For HDX-MS, three buffers were prepared: an equilibration buffer consisting of 5 mM potassium phosphate in H_2O at pH 7.0, a labelling buffer consisting of 5 mM potassium phosphate in D_2O at pD 7.0 and a quench buffer consisting of 50 mM potassium phosphate in H_2O adjusted to pH 1.9.

6.11.2 HDX-MS

Experiments on *Cc*Cry4a WT and *Gg*Cry4a WT were by Dr Angela Gehrckens and *Cc*Cry4a W369F and *Gg*Cry4a W369F were performed in collaboration. HDX-MS experiments were carried out under carefully controlled conditions. All protein handling was performed under dim red illumination in an otherwise dark environment to prevent unwanted photoactivation. Protein aliquots were thawed immediately prior to analysis and diluted to volumes between 10 and 16 μL. Before labelling, each sample was equilibrated for at least 20 min at 20 °C within a temperature-controlled chamber. The light state was generated by continuous exposure to 450 nm blue

light at intensities ranging from 0.03 to 0.06 mW cm^{-2}, while the dark state was maintained in complete darkness. To generate magnet states, samples were placed in custom-built holders positioned above neodymium-iron-boron magnets (10 mm × 1.5 mm, N42 grade, Magnet Expert Ltd.) with a nominal surface field strength of 160 mT. Measurements confirmed that the magnetic field at the sample position corresponded to approximately 18–25 mT at a distance of 2–3 mm from the magnet.

Labelling reactions were initiated by diluting the protein with deuterated buffer. 55 μL of labelling buffer was added to 5 μL of protein, producing a final solution of approximately 92% D_2O. For *Er*Cry4a, 54 μL of labelling buffer was combined with 1 μL of protein, yielding a final deuterium content of approximately 98%. Exchange was stopped by mixing the sample with an equal volume of ice-cold quench buffer. Quenched solutions were immediately injected into the HDX Manager (Waters, Milford, MA, USA) and maintained at 0 °C until reaching the Enzymate Pepsin digestion column (Waters), which was held at 20 °C. Digestion was performed with an isocratic flow of 0.1% formic acid in H_2O at 100 μL min^{-1}. Peptides were collected and desalted on a BEH C18 trapping column (Waters) for 2 min before separation on a reversed-phase analytical column operated at 0 °C with a flow rate of 40 μL min^{-1}. The chromatographic gradient began with 97% H_2O and 3% MeCN, shifted to 65% H_2O and 35% MeCN over 7 min, then decreased to 5% H_2O within 1 min and was held for an additional 2 min.

Peptides were analysed on a Synapt G2Si Q-ToF mass spectrometer (Waters) by electrospray ionisation. Instrument parameters included a capillary voltage of 2.8 kV, sample cone voltage of 100 V, source offset of 30 V, source temperature of 80 °C and desolvation temperature of 150 °C. Leucine enkephalin (m/z 556.2771) was infused every 30 seconds as a lock mass for internal calibration. To minimise carryover between runs, a saw-tooth gradient cleaning cycle was applied using 4% acetonitrile and 0.1% formic acid in water supplemented with 0.5 M guanidinium hydrochloride, with intermittent blank injections included as further quality control. The emission spectra of all light sources, including the red bench lights and the

blue LEDs used for photoactivation, were independently verified to confirm spectral separation and avoid unintended activation.

6.11.3 Native Mass Spectrometry

Native mass spectrometry experiments employed the same *Er*Cry4a preparations used in HDX-MS. Samples were buffer exchanged into 200 mM ammonium acetate at pH 8.0 using Zeba^{TM} Micro Spin desalting columns with a 40 kDa molecular weight exclusion limit (ThermoFisher Scientific). Measurements were conducted at the University of Oxford on a Q Exactive^{TM} mass spectrometer (ThermoFisher Scientific) using custom-fabricated gold-coated capillaries for nano-electrospray ionisation. Protein samples were introduced at a concentration of approximately 8 μM. The source temperature was maintained at 150 °C and the capillary voltage was set to 1.0 kV. In-source trapping was applied at −200 V to assist in desolvation and to disrupt weakly bound adducts. The higher-energy collisional dissociation (HCD) cell was operated at 5 V and ion optics were adjusted empirically to maximise transmission of intact protein ions.

6.11.4 Data Analysis

Peptides were identified by MSE fragmentation of non-deuterated controls and processed with ProteinLynx Global Server 3.0 (Waters) for database searching. The results were imported into DynamX 3.0 (Waters) for automated peak picking and assignment. To ensure reliability, stringent filtering criteria were applied: peptides were required to display at least 0.2 fragment ions per amino acid, have a precursor mass accuracy within 5 ppm, contain no more than 25 residues and be detected reproducibly in at least three replicate analyses. Peptides that did not meet these standards, or that showed ambiguous or noisy isotopic distributions, were excluded. Deuterium incorporation was quantified by comparing centroid mass shifts of labelled peptides relative to undeuterated controls.

Native mass spectra were processed using MassLynx V4.2 (Waters, Wilmslow, UK) and structural mapping of differential deuterium uptake was visualised in PyMOL (Schrödinger, New York, USA).

"Cause I'm as free as a bird now
And this bird you cannot change."

— Lynyrd Skynyrd via Bryan Kidd

7 Final Conclusions and Outlook

Contents

7.1 Summary of Principal Findings 198
7.2 Insights from Mutational Studies 198
7.2.1 R356E (Apo Protein) 199
7.2.2 W369F (TrpD Mutant) 199
7.2.3 C317R/Y319F/W369F (Triple Mutant) 199
7.3 Comparative Dynamics Across Species 200
7.4 Mechanistic Interpretation 201
7.5 Future Directions 201
7.5.1 Membrane Association 202
7.5.2 Interaction Partners 203
7.5.3 Post-Translational Modifications 203
7.5.4 Residue-Level Experiments 204
7.6 Concluding Remarks 204

This thesis has explored the structural dynamics of avian cryptochrome 4a using HDX-MS as the principal experimental approach. Through a series of light–dark comparisons, mutational studies and cross-species analyses, it establishes a detailed experimental framework describing how illumination modulates local flexibility across various domains of the protein. Collectively, these studies reveal that photoactivation triggers reproducible, region-specific rearrangements rather than global unfolding and that these conformational changes are conserved across avian species but modulated by both cofactor state and sequence context.

7.1 Summary of Principal Findings

The wild-type European robin cryptochrome provided the foundation for this investigation. HDX-MS revealed a well-defined pattern of solvent protection where the central β-sheet core and FAD-binding pocket remain highly protected, while peripheral helices and loops show elevated exchange. Upon illumination, a few regions exhibited reproducible light-dependent decreases in deuterium uptake such as the PBL, the PL and α22. These sites consistently reported local stabilisation in the light state, confirming them as important regions within the Cry4a signalling pathway. The PBL displayed rapid yet reversible protection consistent with closure over the cofactor following photoexcitation. The PL, which may interact dynamically with the PBL, also exhibited decreased uptake, implying coupled rearrangement between the two loops. α22, showed slower but sustained protection, suggesting that this helix acts as a hinge transmitting conformational change from the flavin pocket towards the solvent-exposed C-terminal interface.

Pulsed-labelling HDX experiments confirmed that these structural shifts were reversible within minutes of returning to the dark, demonstrating that Cry4a returns to its initial conformation rather than forming an irreversibly altered state. ECD analysis of fragments from the PBL provided residue-level resolution, revealing moderate protection factors and corresponding ΔG_{op} values, compatible with transient stabilisation. This data suggests a model in which Cry4a remains largely ordered yet accommodates local redox-driven rearrangements upon illumination.

7.2 Insights from Mutational Studies

Building upon the wild-type characterisation, three *Er*Cry4a mutants were examined to examine the structural contributions of key residues within the flavin-binding and electron-transfer regions. Each provided distinct mechanistic insight into how Cry4a couples photochemistry to conformational response.

7.2.1 R356E (Apo Protein)

The R356E mutation removes the electrostatic contact that stabilises FAD binding, generating an apo form without bound FAD. HDX-MS showed increased flexibility across the PHR, with a larger proportion of peptides reaching saturation, reflecting the loss of the cofactor's structural constraint. In this mutant, none of the light-sensitive peptides observed in the wild type displayed measurable differences between illumination states. Notably, the PBL saturated immediately in both light and dark conditions, masking any potential light-dependent behaviour, while the PL and α22 showed no detectable response. This confirms that FAD is indispensable for mediating conformational signalling and that the light-induced protection patterns originate from photochemical changes within the cofactor pocket rather than non-specific photoeffects.

7.2.2 W369F (TrpD Mutant)

Substitution of the terminal tryptophan in the electron-transfer chain (TrpD) with phenylalanine produced a protein that remained photochemically active but showed attenuated light-dark differences. The same regions as in the wild type still responded to illumination, but the magnitude of protection was markedly reduced. This finding demonstrates that conformational responses can occur even when electron transfer terminates at TrpC, indicating that radical pair formation at this site is sufficient to initiate structural changes, though TrpD enhances their magnitude and stability. The transient early deprotection observed in the CTT suggests that TrpD may also coordinate the timing of tail rearrangements.

7.2.3 C317R/Y319F/W369F (Triple Mutant)

The triple mutant combined alterations to the cysteine and tyrosine residues with loss of the final donors. This construct exhibited the weakest response of all variants, with effectively no reproducible protection in the PBL and near-complete loss of signal in α22. The results suggest cooperative coupling between the electron-transfer chain and adjacent residues surrounding the isoalloxazine ring. When

these stabilising interactions are disrupted, the conformational link between flavin redox chemistry and surface motion is effectively severed. The progression from wild type to R356E traces a clear reduction in light-driven conformational change, showing that Cry4a retains a degree of flexibility to sequence alteration while remaining responsive to photochemical cues.

7.3 Comparative Dynamics Across Species

Parallel HDX-MS experiments on chicken and quail revealed that the same structural motifs mediate light response across species (PBL, PL and α22), indicating conservation of the conformational mechanism within avian cryptochromes. All three homologues share a stable, highly protected core surrounding the FAD pocket, with light-dependent decreases in uptake localised to these loops and the short helix near the C-terminal interface.

Across species, the magnitude, kinetics and regional distribution of protection differ in characteristic ways. In European robin Cry4a, illumination produces clear stabilisation in the PBL and PL within the first minute, followed by a delayed response in α22. Chicken Cry4a exhibits the strongest PBL protection among the three species, whereas quail is intermediate and shows altered coupling in other regions. These kinetic nuances can also be distinguished from mutant behaviour. For *Gg*W369F, significant light-dark differences are not detected at the earliest time point (15 s) and emerge at later times, indicating a slower onset relative to wild type. Sequential differences offer potential explanations in differences between the species. Substitutions near the sulphur loop and around residues 316-320 and 404-41, highlighted by sequence/structure comparisons and AlphaFold models, can modulate local electrostatics and loop mobility, shifting the equilibrium between open and closed conformations while preserving the overall fold and pocket geometry.

7.4 Mechanistic Interpretation

The data indicate that avian Cry4a responds to light through local redox-driven changes rather than large-scale refolding. Photoexcitation of the FAD initiates electron transfer along the conserved tryptophan chain, leading to light-dependent differences in solvent exposure within several flexible regions. The PBL and PL show clear protection under illumination, consistent with altered interactions around the FAD cavity, while helix α22 and the CTT also display changes in stability. These effects suggest that photoactivation influences the structural connectivity between the flavin pocket and the outer regions of the protein, potentially modulating how the CTT is positioned or engaged with binding partners under light conditions.

The results therefore point to a direct relationship between photochemical changes in the flavin environment and conformational responses in the surrounding structural elements. The absence of magnetic-field effects on exchange implies that any geomagnetic influence acts by altering radical-pair lifetimes rather than by producing detectable rearrangements in the protein backbone. The light-dependent motions detected by HDX–MS provide a structural basis for the signalling-competent state proposed from spectroscopic and behavioural models of magnetoreception.

7.5 Future Directions

This work has focused on characterising the conformational dynamics of monomeric Cry4a in isolation. While this has provided detailed insight into the intrinsic stability and light-dependent flexibility of the protein, Cry4a functions within a complex cellular environment that includes membranes, signalling partners and regulatory modifications. Future work should therefore aim to contextualise these findings within physiological settings and determine how the observed conformational responses translate into cellular signalling. Among the directions outlined below, membrane reconstitution and residue-level HDX–ECD studies represent the most

immediate extensions, while identifying interaction partners and mapping post-translational modifications (PTMs) will be essential to connect structural dynamics with biological function.

7.5.1 Membrane Association

Cry4a is found in the photoreceptor outer segments, where its close position to the membrane suggests possible contact with lipid surfaces [65, 199]. The outer segment is a densely packed membrane enriched in polyunsaturated phospholipids and phototransduction proteins, providing extensive surfaces for peripheral proteins to interact with disc membranes [209–211]. Evidence from other systems supports this view. European robin Cry4a binds lipid bilayers in vitro and shows an electrostatic surface consistent with transient attachment, while in *Drosophila*, cryptochrome links blue light activation to membrane depolarisation through redox control of Kv channel complexes [182, 187, 212].

Charged regions around the CTT and along α22, together with amphipathic residues in nearby loops, appear well suited for transient membrane contact. Comparable arrangements of basic and hydrophobic side chains mediate peripheral association in other flavoproteins. In plant ferredoxin:$NADP^+$ reductase (FNR), a positively charged surface promotes thylakoid binding and is further stabilised by interactions with the membrane tethers Tic62 and TROL [213–215]. Molecular-dynamics simulations of pigeon and robin Cry4 variants reveal loop motion and C-terminal flexibility consistent with membrane proximity and light-dependent rearrangements [72, 188]. Such interactions may stabilise the CTT and restrict the movement of α22, reducing deuterium uptake in these regions and positioning Cry4a relative to the bilayer in a way that could support downstream signalling.

HDX–MS and native MS are increasingly used to study membrane proteins in native-like lipid assemblies, including nanodiscs and polymer-based systems. HX and HDX with nanodiscs allow quantitative mapping of membrane-induced protection [216, 217]. Polymer nanodiscs made with styrene maleic acid (SMALPs) permit HDX measurements in native lipid mixtures and newer materials such

as DIBMA and SMA–QA improve buffer and pH compatibility for subsequent MS [218, 219]. Native MS using nanodiscs or SMALPs can reveal lipid adduction, changes in collisional cross section and complexes that would otherwise dissociate in detergent [220, 221].

7.5.2 Interaction Partners

Proteomic and biochemical studies have identified prospective Cry4a partners, including $G_{t\alpha}$, opsins, transducins and other phototransduction components [222]. These proteins could mediate or respond to the conformational transitions characterised here by HDX–MS. Preliminary native-MS experiments conducted during this work sought Cry4a–$G_{t\alpha}$ assemblies under dark and illuminated conditions but revealed no stable or light-responsive complexes. The absence of a detectable complex may reflect a requirement for membrane association, cofactors or scaffolding proteins to stabilise binding. Similar challenges are common for transient photoreceptor assemblies, where weak affinities and condition-sensitive interfaces hamper detection in detergent or gas-phase environments [223]. Crosslinking and affinity-based MS under near-physiological conditions, ideally with membrane-reconstituted samples, could help capture such assemblies and define their interaction surfaces. Parallel co-expression and co-purification in heterologous systems would further test the composition and stoichiometry of Cry4a-containing complexes.

7.5.3 Post-Translational Modifications

PTMs are likely to regulate Cry4a *in vivo*, particularly phosphorylation of solvent-exposed loops and the CTT. In other cryptochromes and circadian proteins, phosphorylation modulates localisation, stability and partner recruitment [224–226]. Sequence inspection of Cry4a highlights serine and threonine residues within light-sensitive regions-such as Ser519, Thr523 and Ser540, that fit consensus motifs for casein kinase I/II. Modification at these positions could alter the dynamics or accessibility of the CTT, potentially explaining reversible protection patterns observed by HDX–MS. Identifying these PTMs by phosphopeptide enrichment or

top-down MS would directly link post-translational regulation to the conformational switching described here [227].

7.5.4 Residue-Level Experiments

While the present HDX–MS data define the major regions undergoing light-dependent change, residue-level resolution remains limited. Fragmentation-enabled HDX such as HDX–ECD can localise protection within individual peptides, identifying specific amide positions with altered exchange [228]. Extending this approach to membrane-reconstituted or mutant variants could reveal how local perturbations propagate through the protein. Combining HDX–ECD with complementary top-down fragmentation (for example UVPD) would further increase spatial resolution and help connect photochemical events within the flavin pocket to the structural dynamics underpinning Cry4a function [229].

7.6 Concluding Remarks

This thesis has explored the structural dynamics of avian cryptochromes, defining how light influences the conformation and stability of Cry4a proteins across species. The combined use of HDX–MS, mutagenesis and comparative analysis has revealed a consistent relationship between photochemical activation and protein dynamics, offering new insight into how these flavoproteins respond to environmental stimuli.

Beyond the detailed findings, this work demonstrates how dynamic structural methods can illuminate processes that lie at the intersection of photochemistry, redox biology and sensory perception. The results provide a foundation for future studies that place Cry4a within its native cellular and membrane environment, advancing our understanding of how molecular events within cryptochrome contribute to the magnetic orientation of birds and, more broadly, to light-dependent signalling in living systems.

Appendices

"Because fact into doubt won't go"

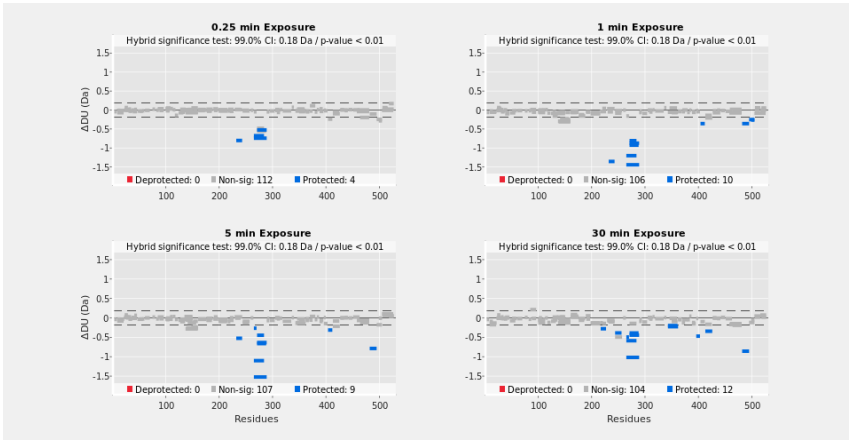
— The Day Today via Pip Benjamin

A Appendices

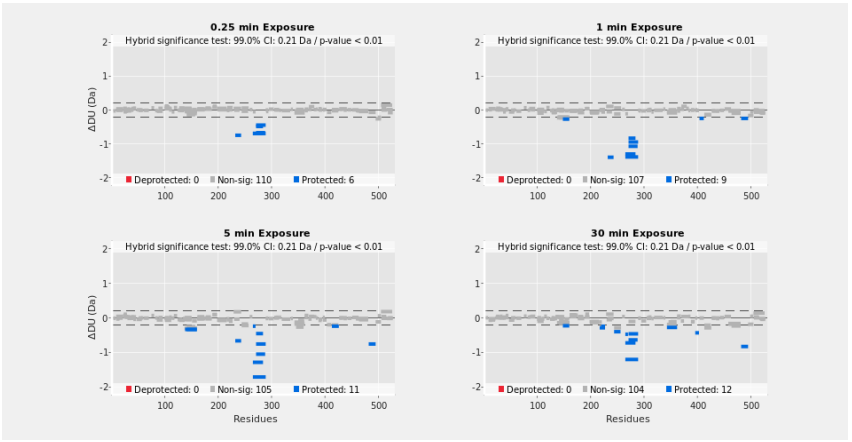
Contents

A.1 Chapter 4 207
A.2 Chapter 5 209
A.3 Chapter 6 213

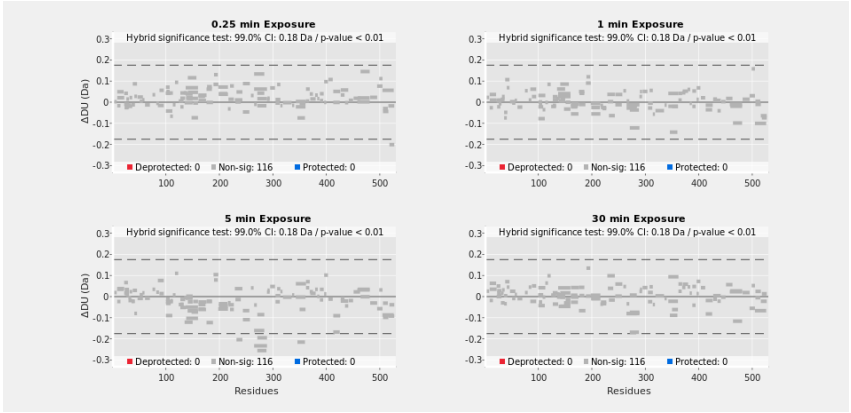
A.1 Chapter 4



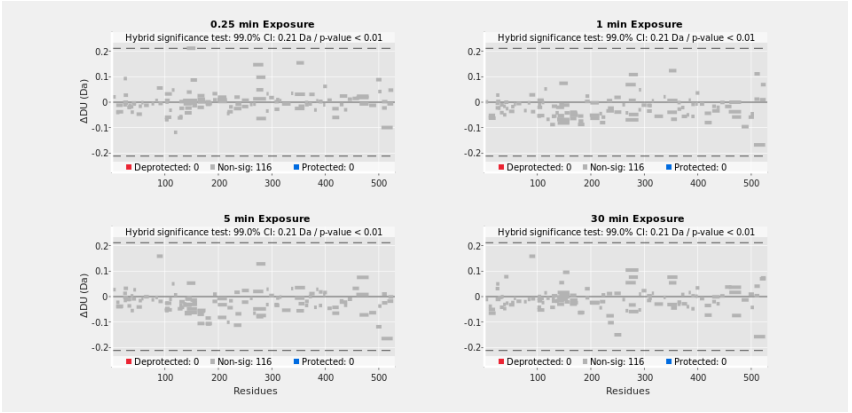
(a) L–D



(b) LSM–DSM



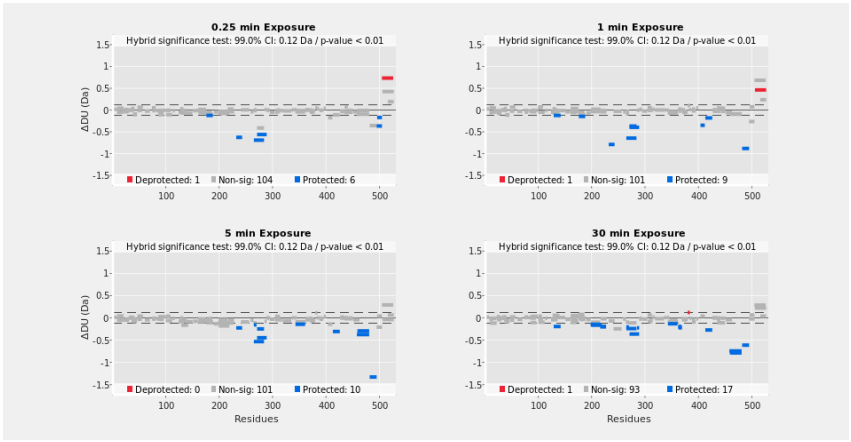
(c) LSM–LS



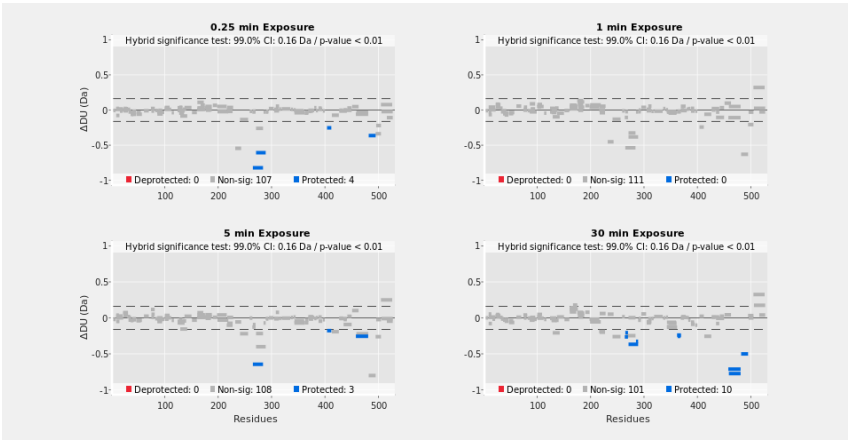
(d) DSM–DS

Figure A.1: Woods plots of *Er*Cry4a WT generated in Deuteros showing (A) light–dark, (B) light–state vs dark–state, (C) light–state, and (D) dark–state comparisons.

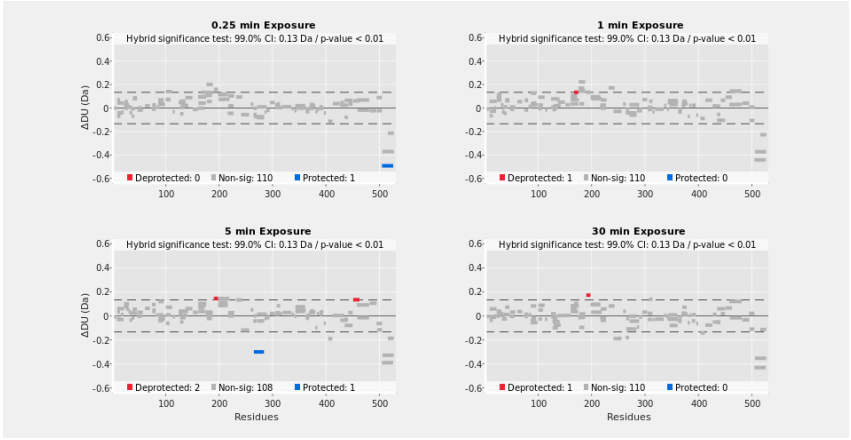
A.2 Chapter 5



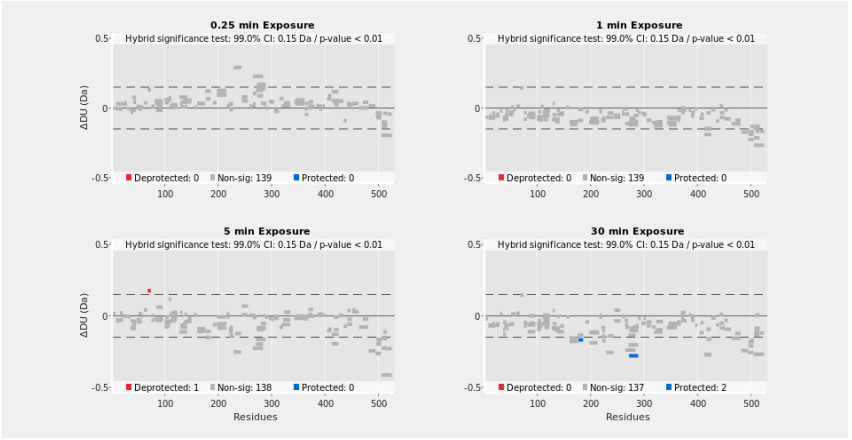
(a) L–D



(b) LSM–DSM

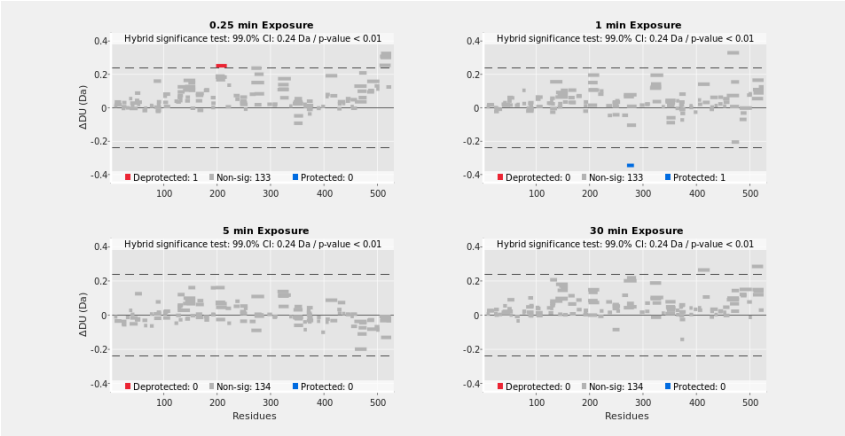


(c) LSM–LS

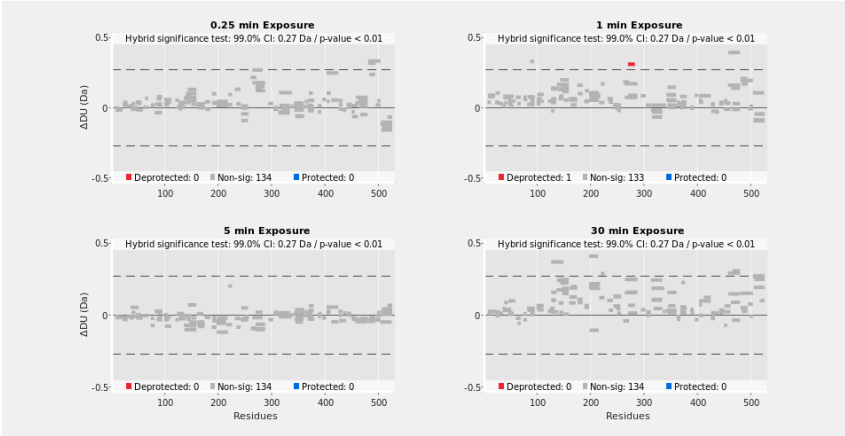


(d) DSM–DS

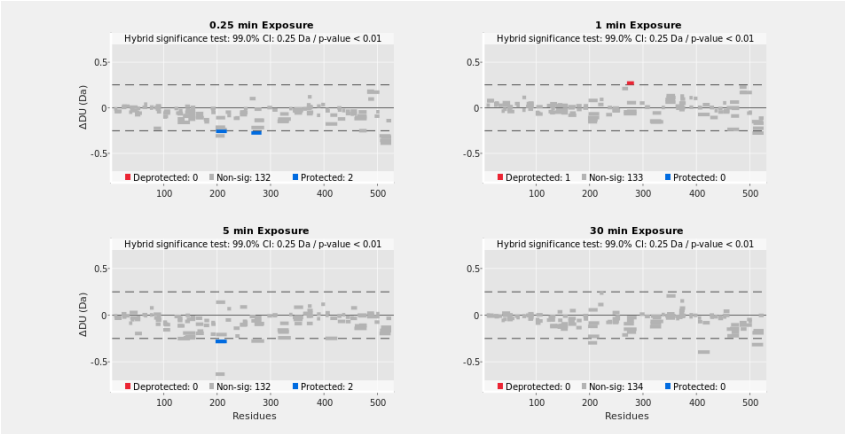
Figure A.2: Woods plots of *Er*Cry4a W369F generated in Deuteros showing (A) light–dark, (B) light–state vs dark–state, (C) light–state, and (D) dark–state comparisons.



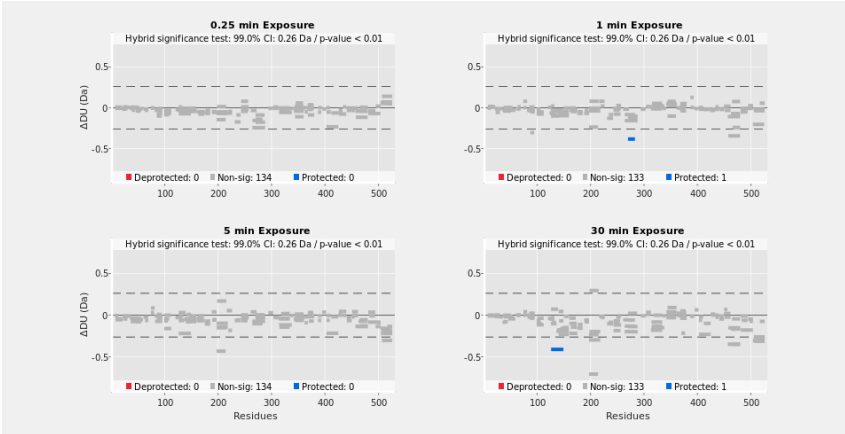
(a) L–D



(b) LSM–DSM

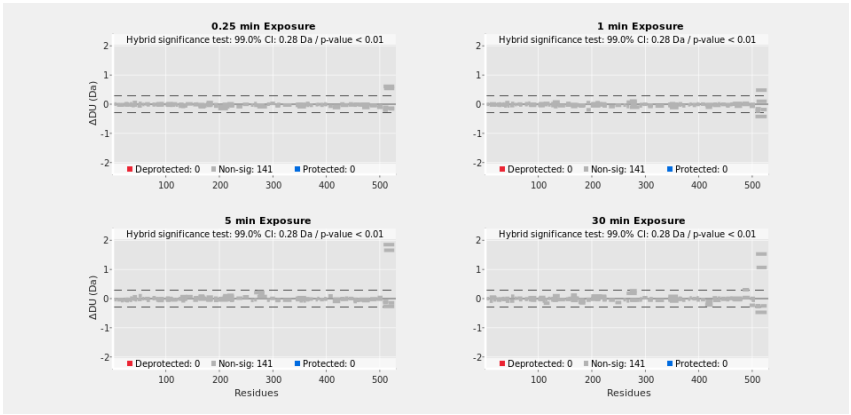


(c) LSM–LS

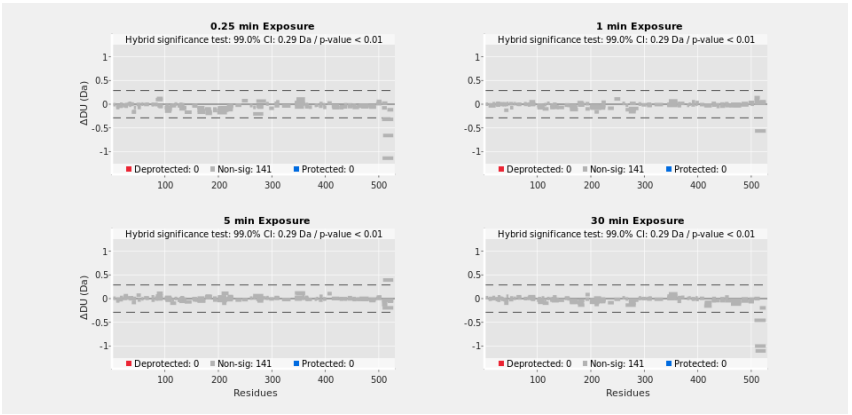


(d) DSM–DS

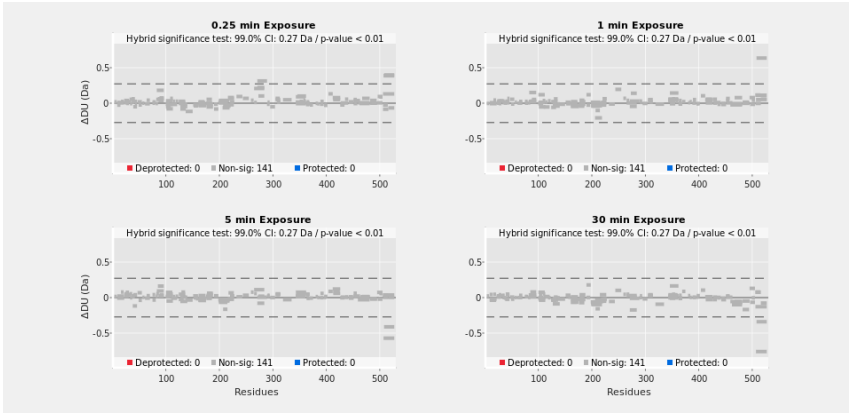
Figure A.3: Woods plots of *Er*Cry4a C317R/Y319F/W369F generated in Deuteros showing (A) light–dark, (B) light–state vs dark–state, (C) light–state, and (D) dark–state comparisons.



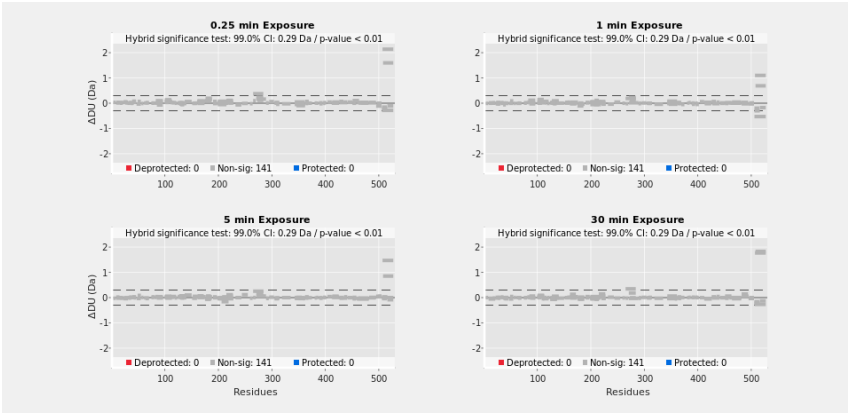
(a) Variant 1



(b) Variant 2



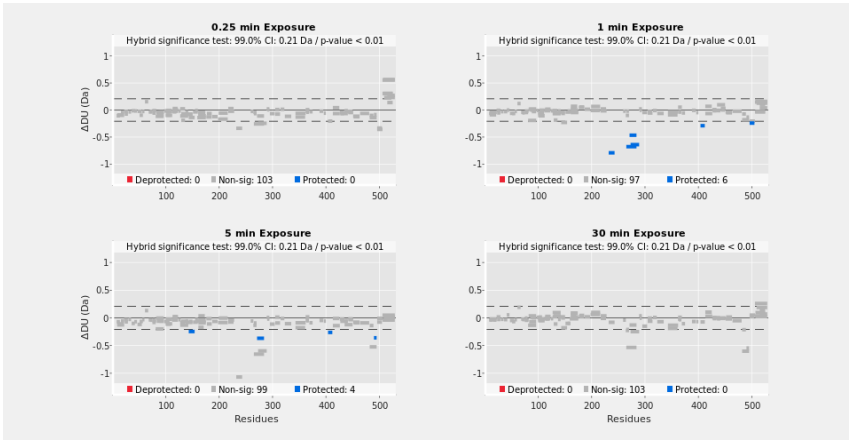
(c) LSM–LS



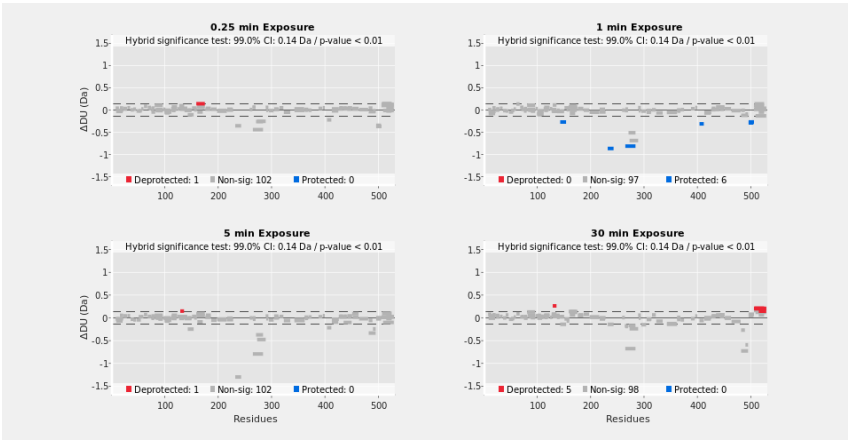
(d) DSM–DS

Figure A.4: Woods plots of *Er*Cry4a R356E generated in Deuteros showing (A) variant 1, (B) variant 2, (C) light–state, and (D) dark–state comparisons.

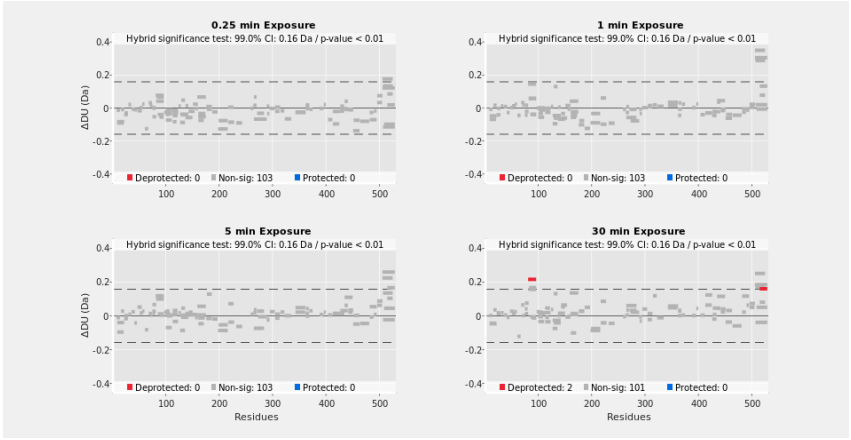
A.3 Chapter 6



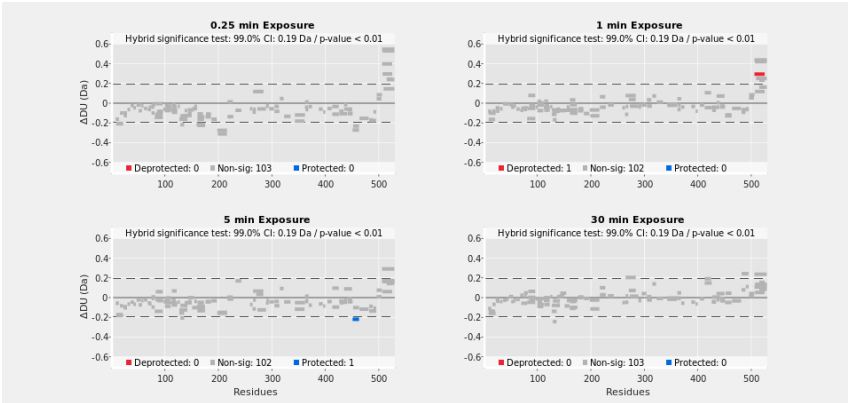
(a) L–D



(b) LSM–DSM

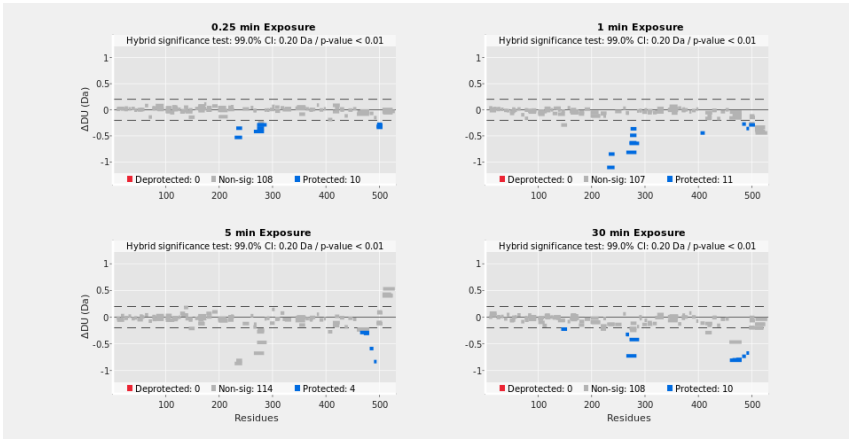


(c) LSM–LS

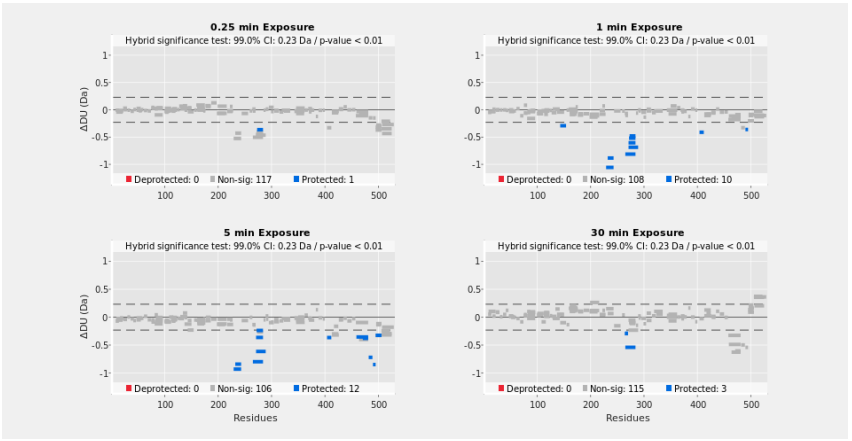


(d) DSM–DS

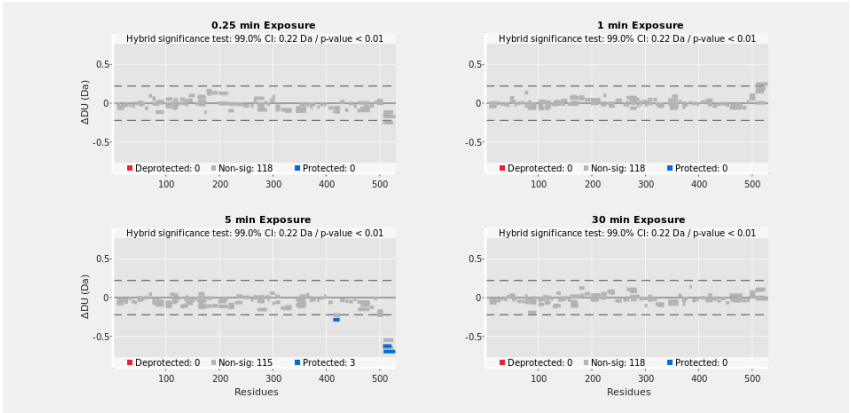
Figure A.5: Woods plots of *Cc*Cry4a WT generated in Deuteros showing (A) light–dark, (B) light–state vs dark–state, (C) light–state, and (D) dark–state comparisons.



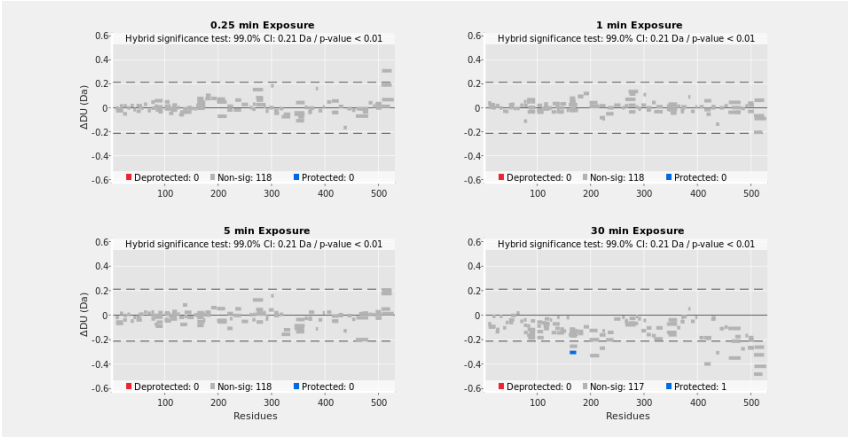
(a) L–D



(b) LSM–DSM

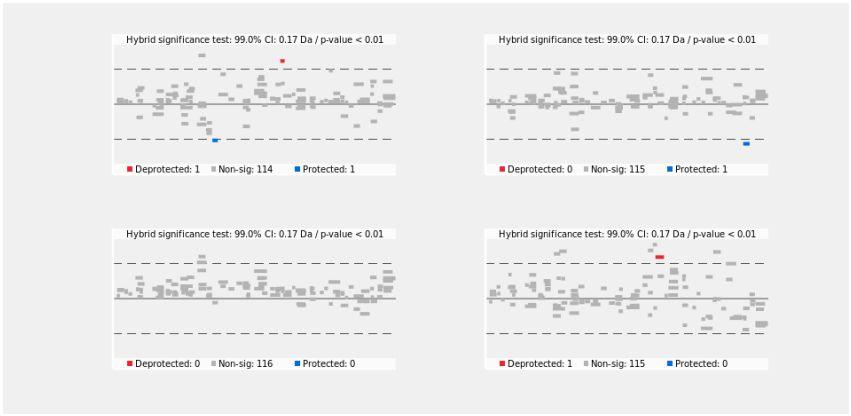


(c) LSM–LS

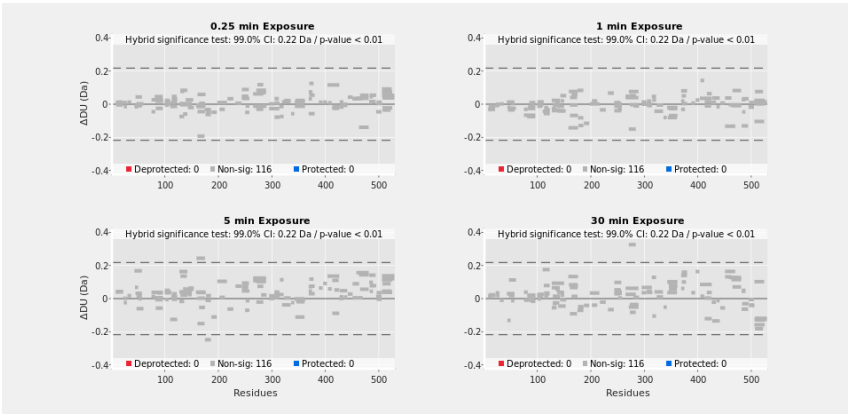


(d) DSM–DS

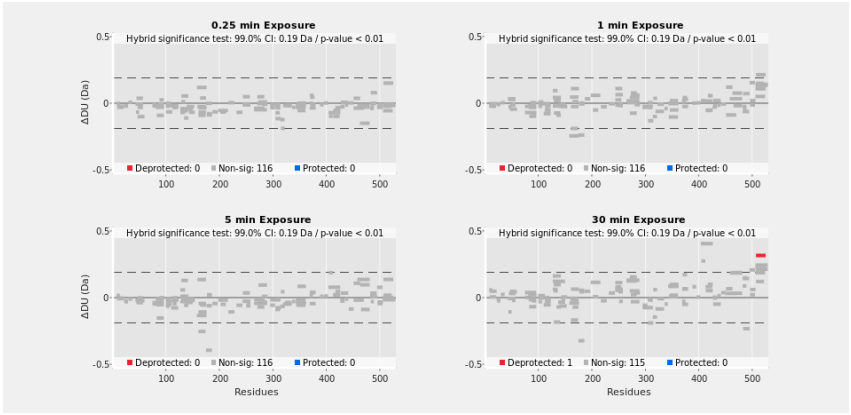
Figure A.6: Woods plots of *Cc*Cry4a W369F generated in Deuteros showing (A) light–dark, (B) light–state vs dark–state, (C) light–state, and (D) dark–state comparisons.



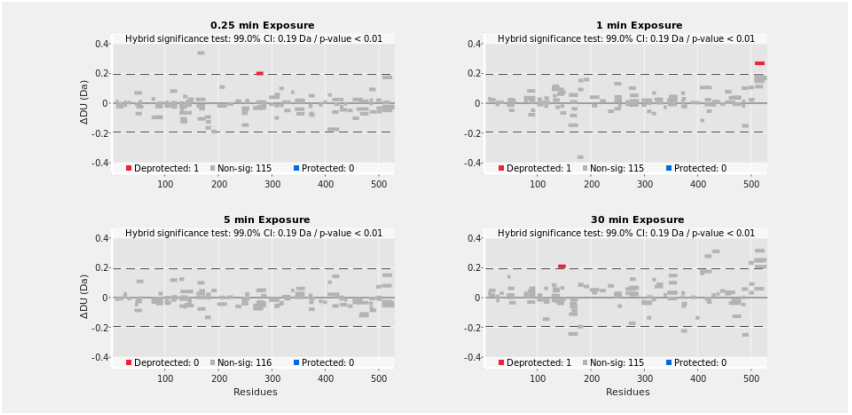
(a) LS–DS



(b) LSM–DSM

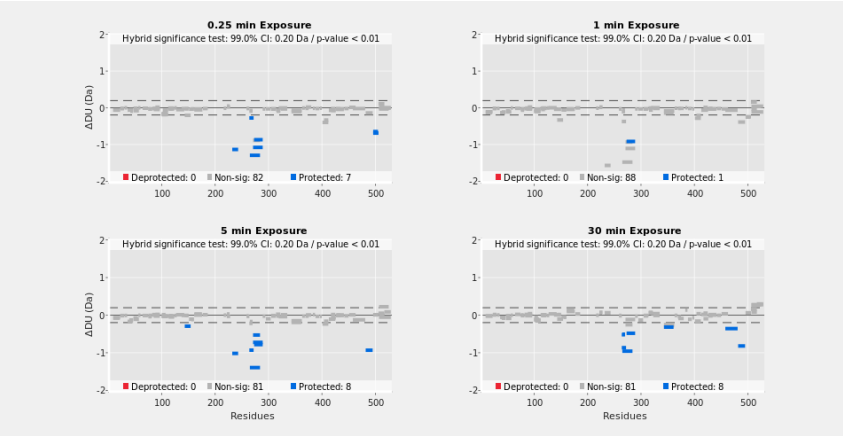


(c) LSM–LS

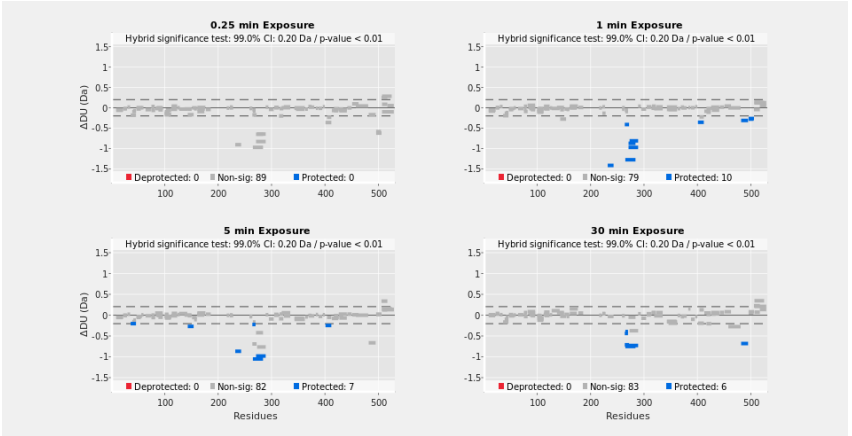


(d) DSM–DS

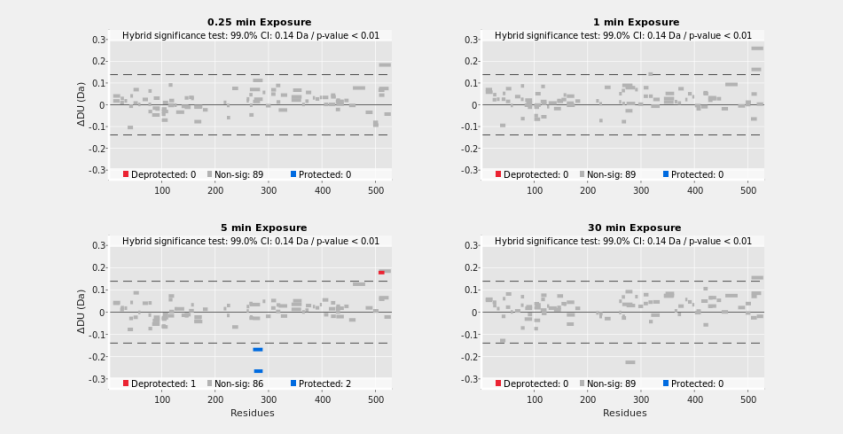
Figure A.7: Woods plots of *Cc*Cry4a Y319F/W369F generated in Deuteros showing (A) light–dark, (B) light–state vs dark–state, (C) light–state, and (D) dark–state comparisons.



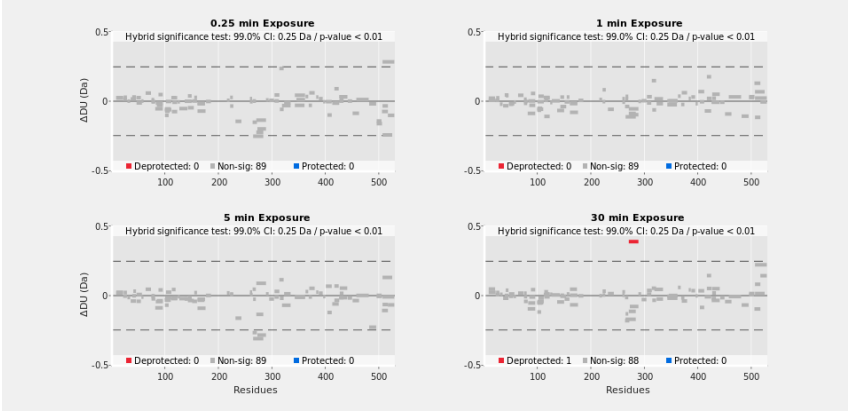
(a) L–D



(b) LSM–DSM

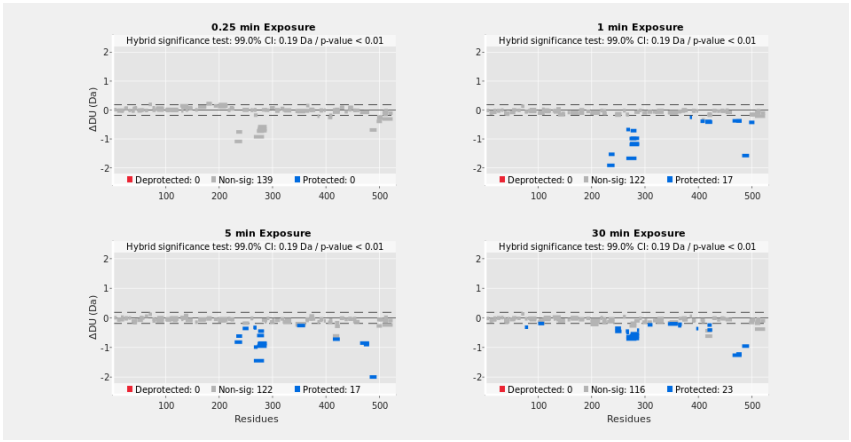


(c) LSM–LS

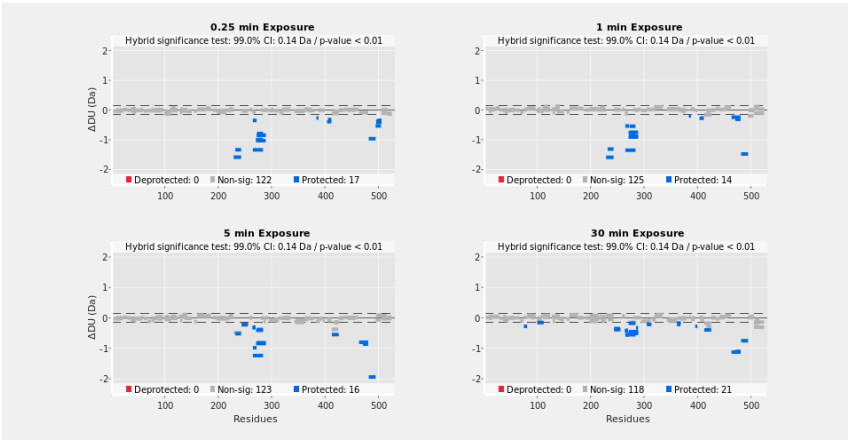


(d) DSM–DS

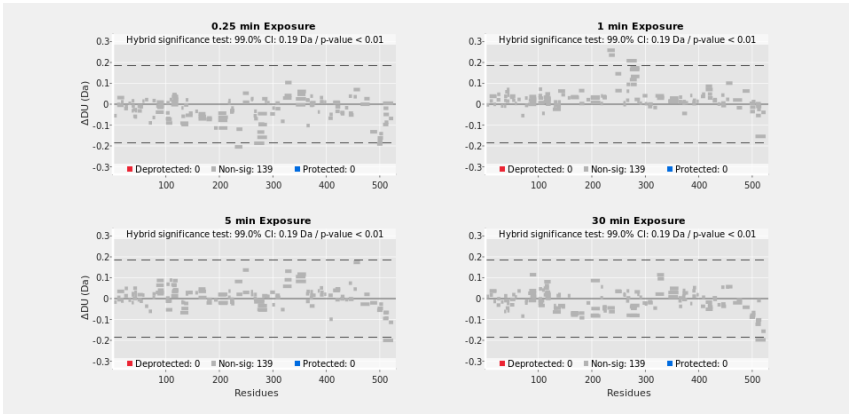
Figure A.8: Woods plots of *Gg*Cry4a WT generated in Deuteros showing (A) light–dark, (B) light–state vs dark–state, (C) light–state, and (D) dark–state comparisons.



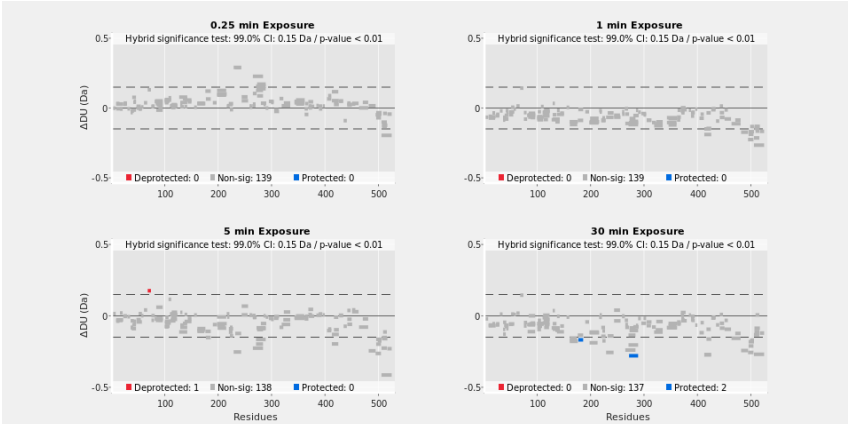
(a) L–D



(b) LSM–DSM

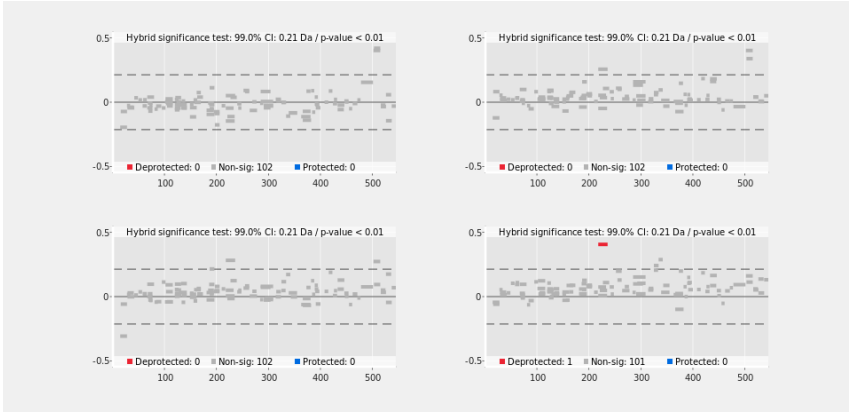


(c) LSM–LS

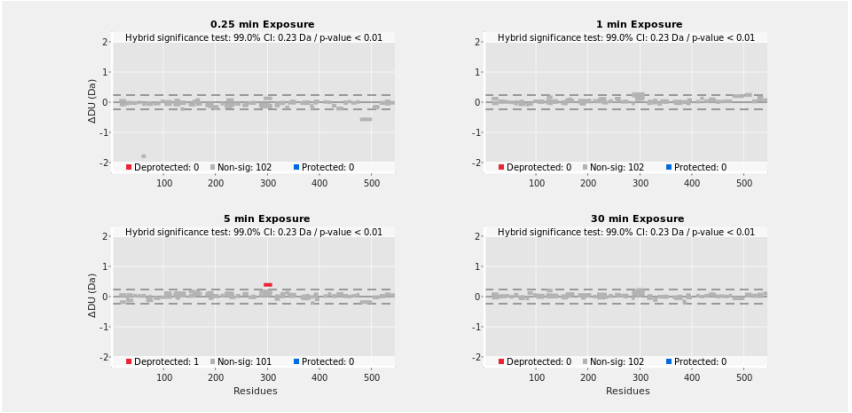


(d) DSM–DS

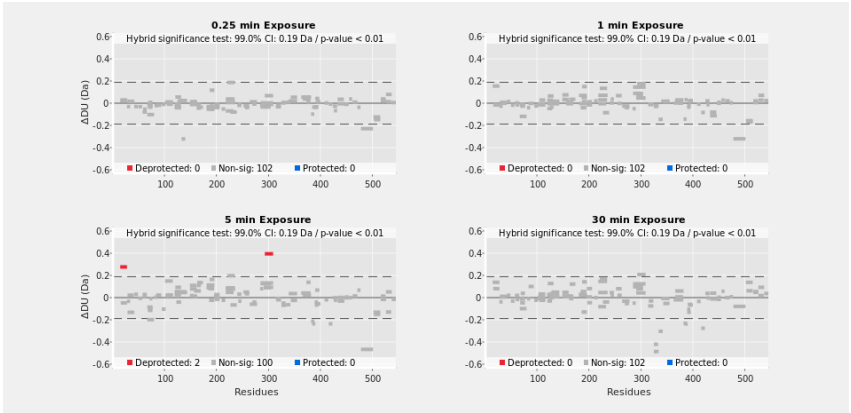
Figure A.9: Woods plots of *Gg*Cry4a W369F generated in Deuteros showing (A) light–dark, (B) light–state vs dark–state, (C) light–state, and (D) dark–state comparisons.



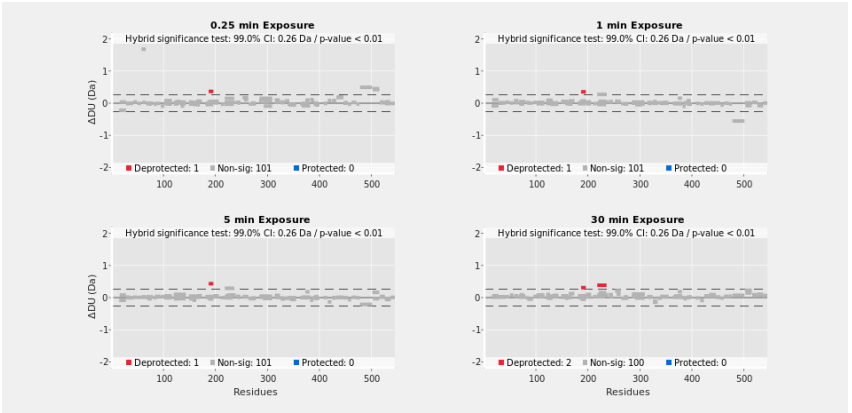
(a) LS–DS



(b) LSM–DSM



(c) LSM–LS



(d) DSM–DS

Figure A.10: Woods plots of *Gg*Cry4a Y319F/W369F generated in Deuteros showing (A) light–dark, (B) light–state vs dark–state, (C) light–state, and (D) dark–state comparisons.

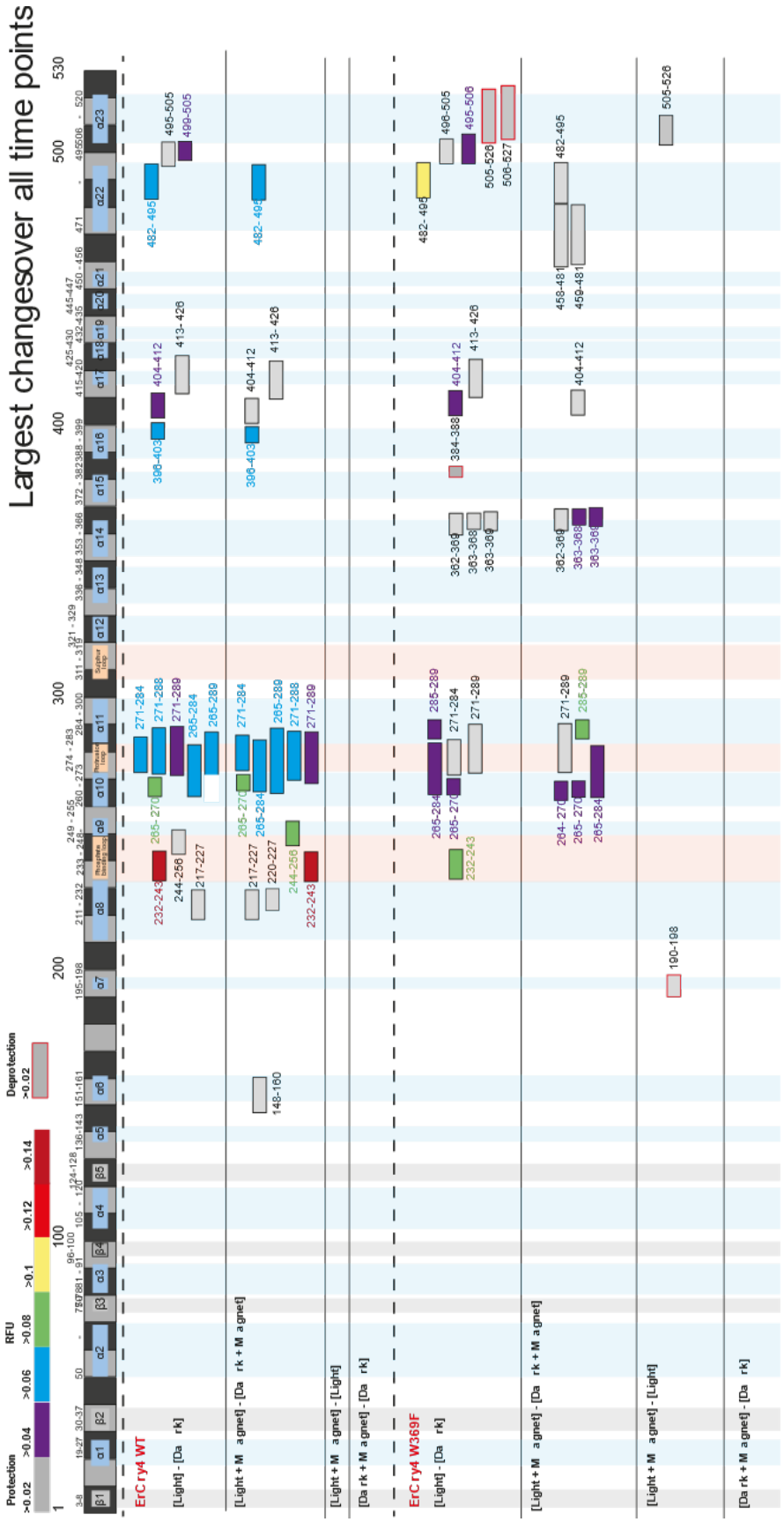


Figure A.11: Relative fractional uptake (RFU) of *Er*Cry4a WT and W369F significant peptides across all time points. Blue corresponds to α-helices, grey to β-sheets, and red to loops. RFU values above each peptide indicate the degree of protection.

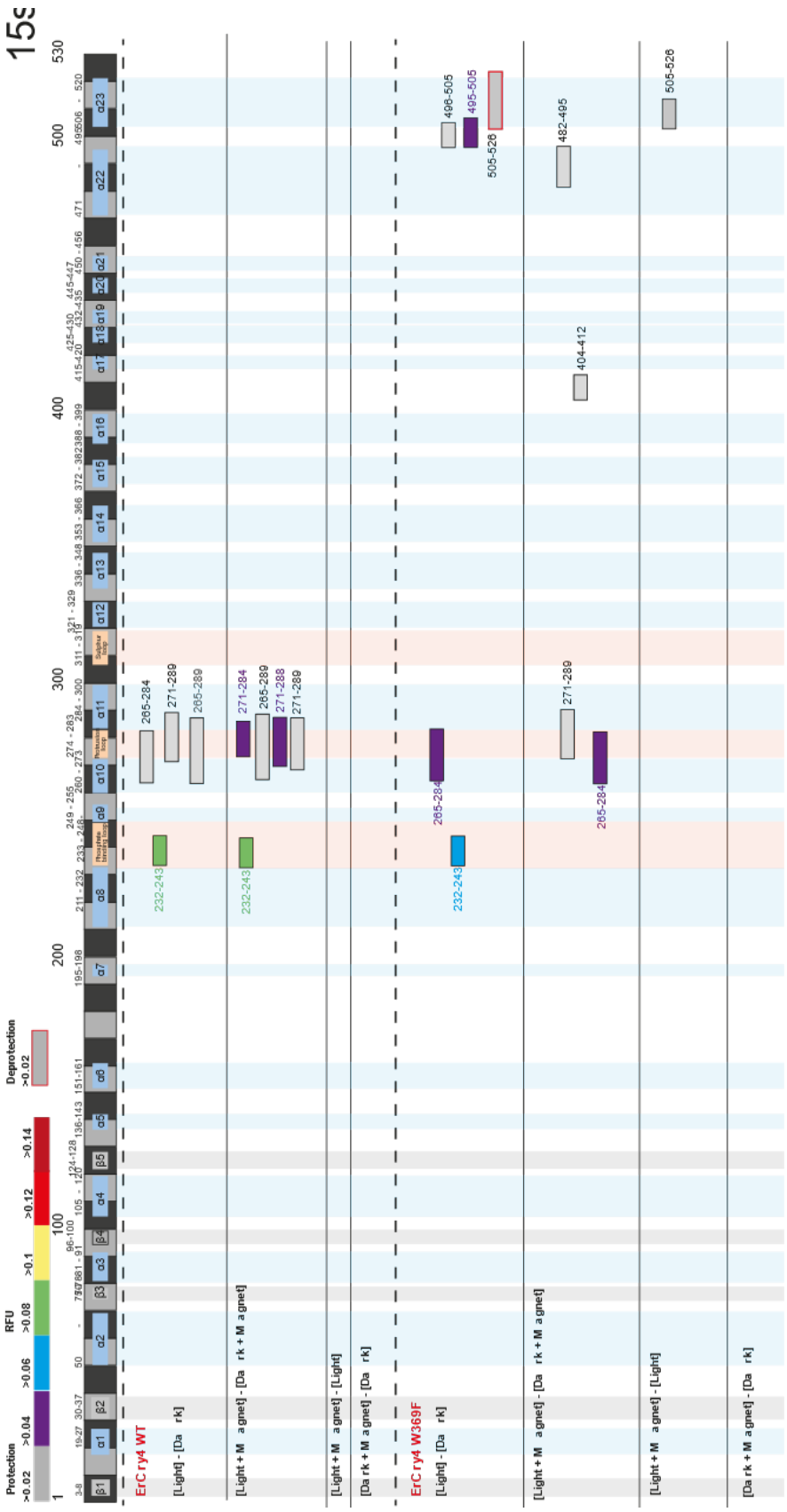


Figure A.12: RFU of *Er*Cry4a WT and W369F at 15 s.

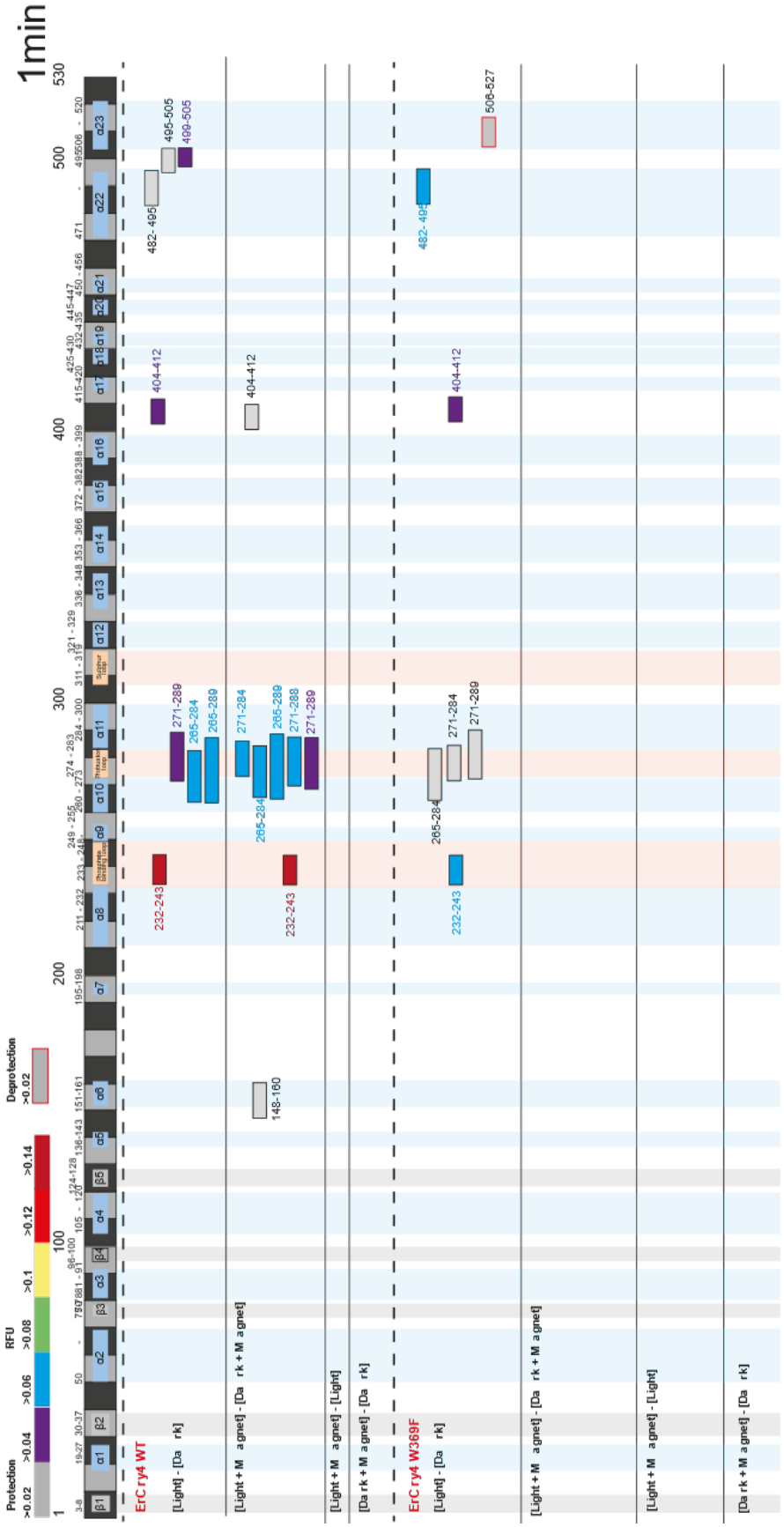


Figure A.13: RFU of *Er*Cry4a WT and W369F at 1 min.

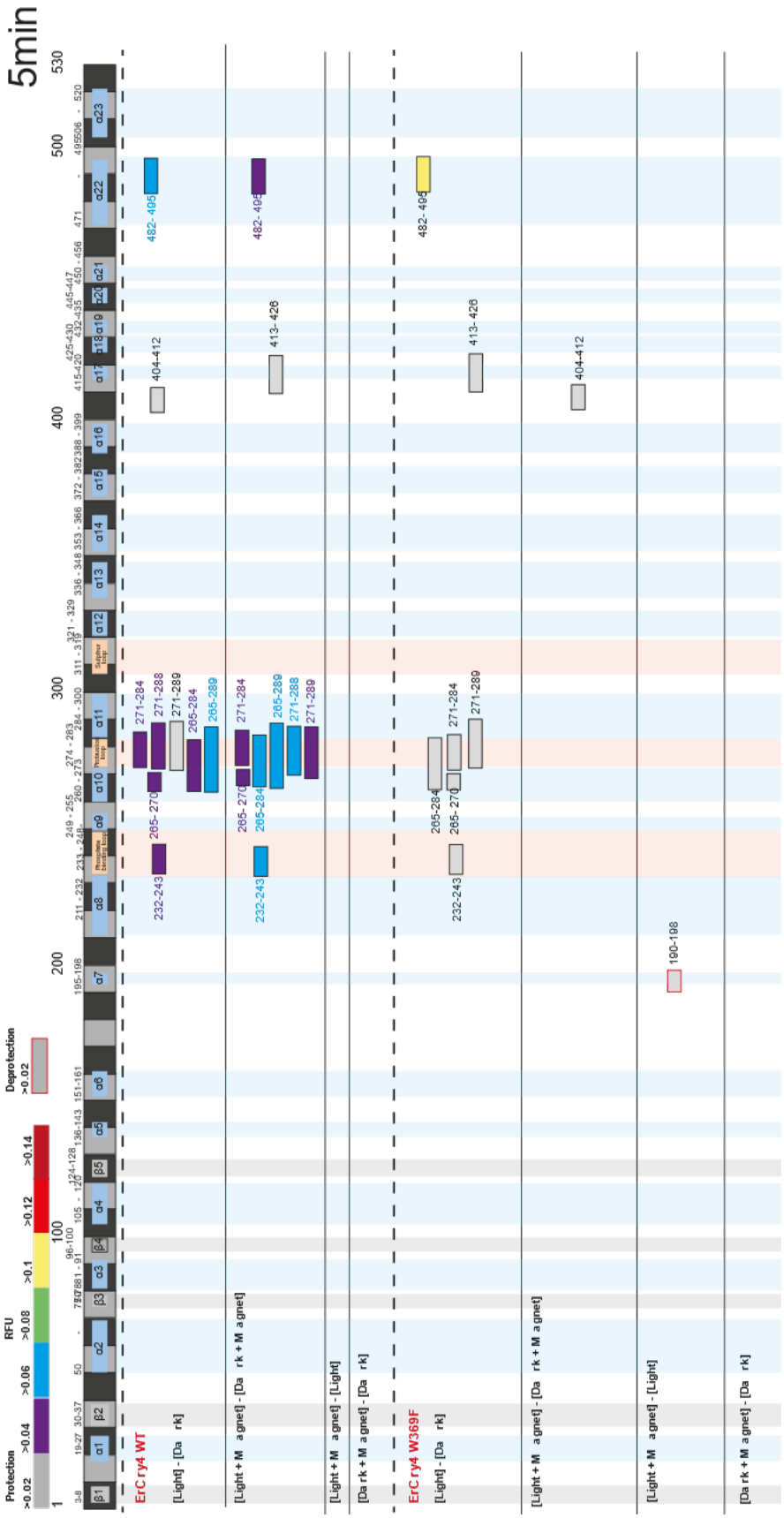


Figure A.14: RFU of *Er*Cry4a WT and W369F at 5 min.

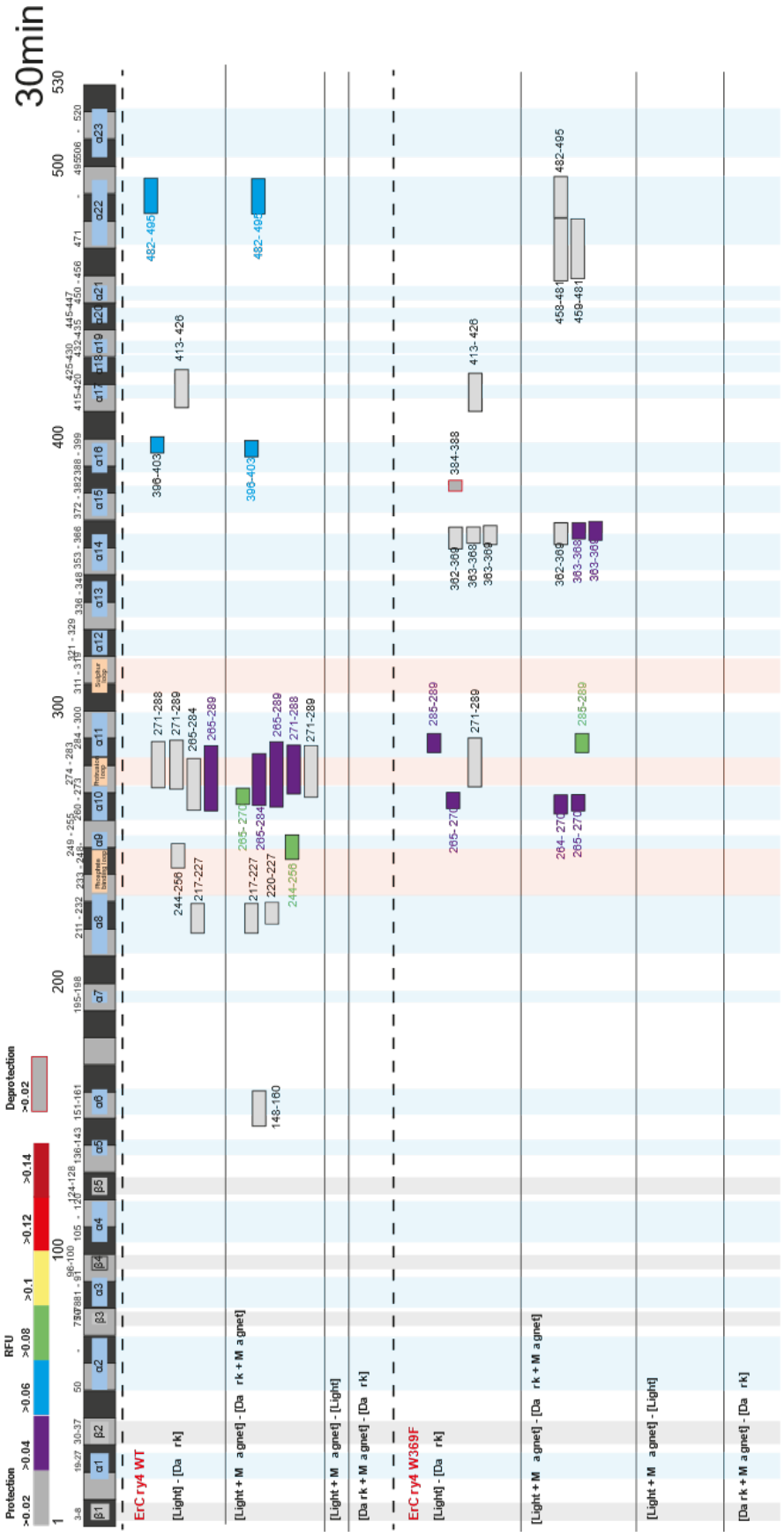


Figure A.15: RFU of *Er*Cry4a WT and W369F at 30 min.

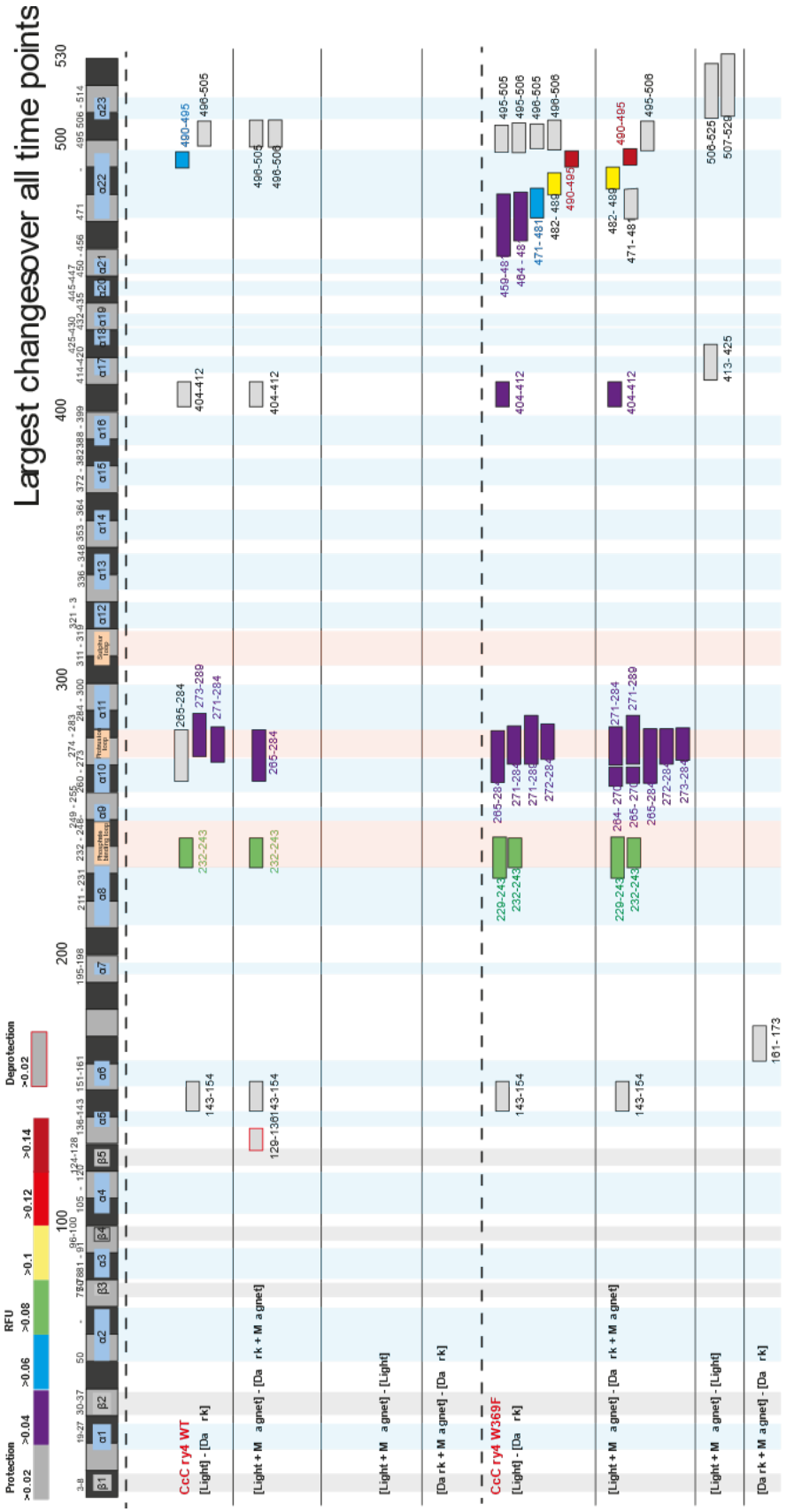


Figure A.16: Relative fractional uptake (RFU) of *Cc*Cry4a WT and W369F significant peptides across all time points. Blue corresponds to α-helices, grey to β-sheets, and red to loops. RFU values above each peptide indicate the degree of protection.

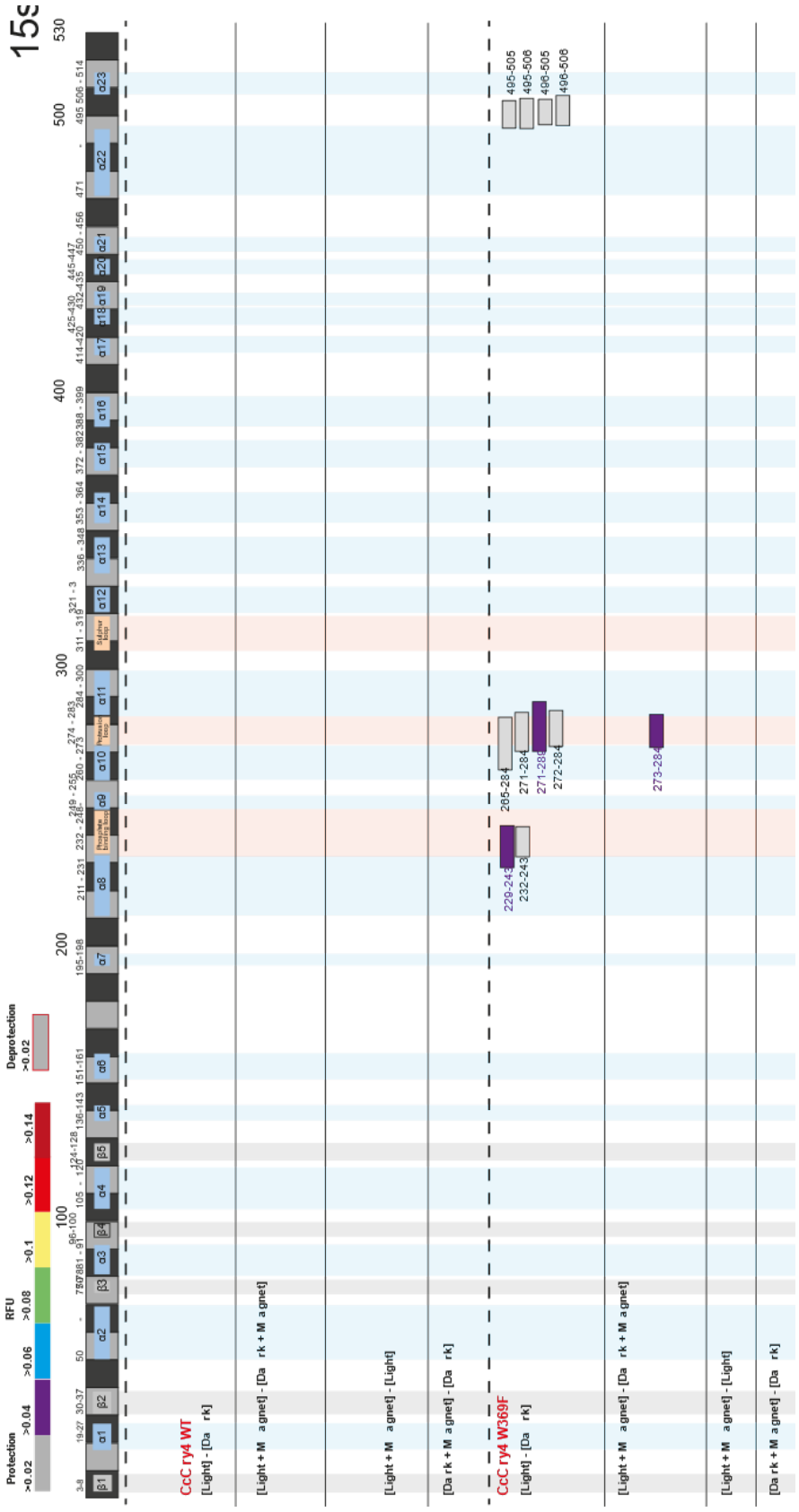


Figure A.17: RFU of *Cc*Cry4a WT and W369F at 15 s.

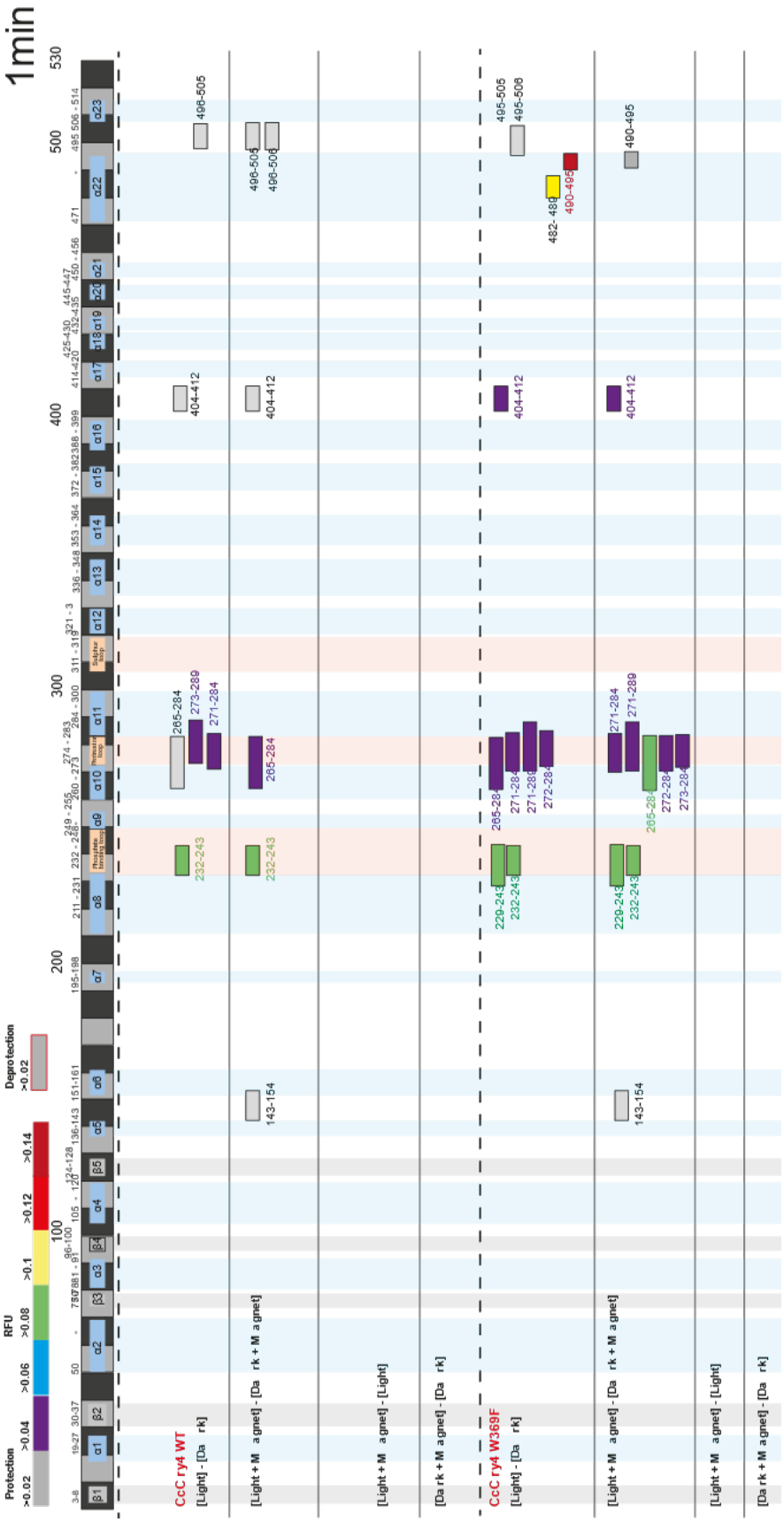


Figure A.18: RFU of *Cc*Cry4a WT and W369F at 1 min.

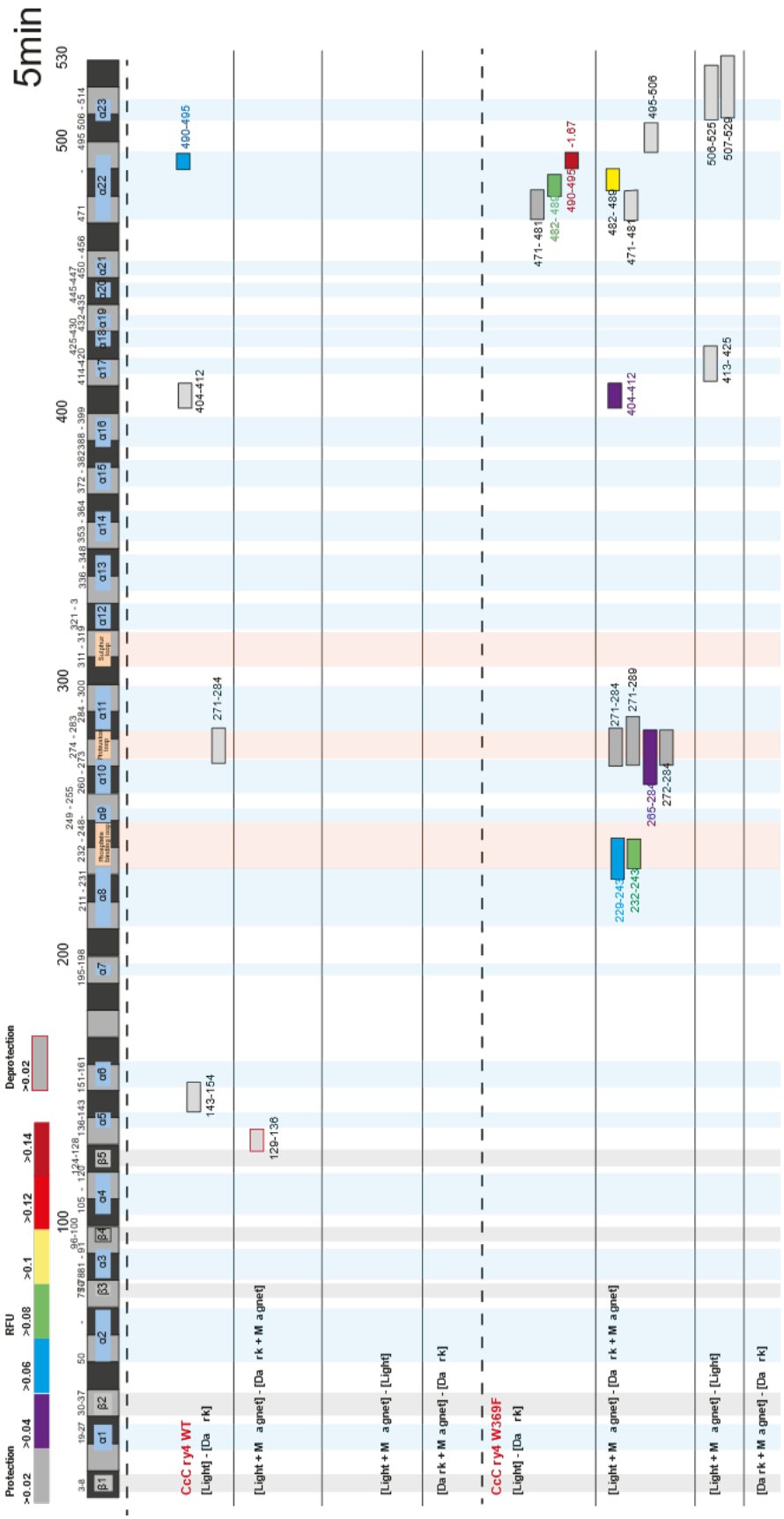


Figure A.19: RFU of *Cc*Cry4a WT and W369F at 5 min.

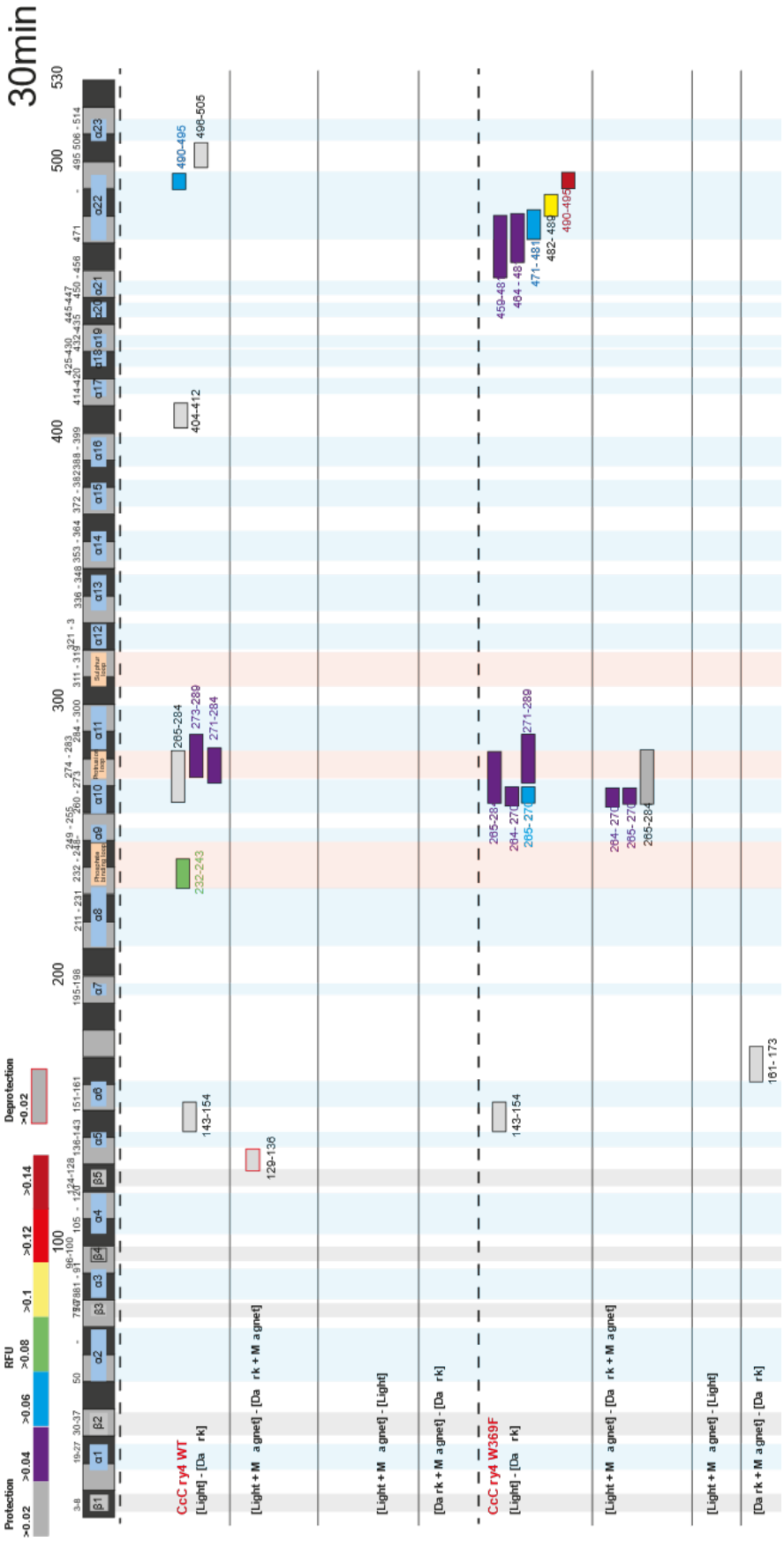


Figure A.20: RFU of *Cc*Cry4a WT and W369F at 30 min.

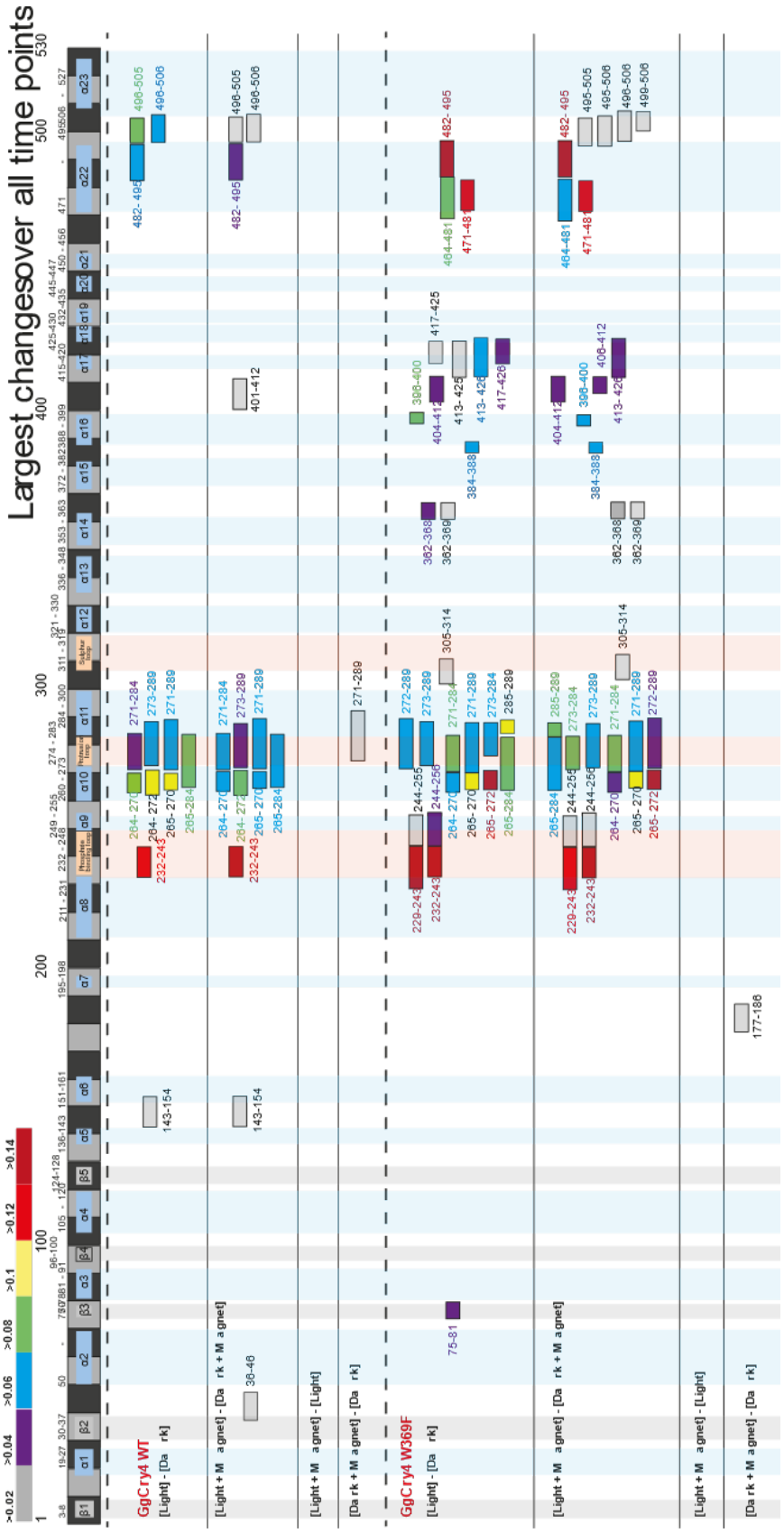


Figure A.21: Relative fractional uptake (RFU) of *Gg*Cry4a WT and W369F significant peptides across all time points. Blue corresponds to α-helices, grey to β-sheets, and red to loops. RFU values above each peptide indicate the degree of protection.

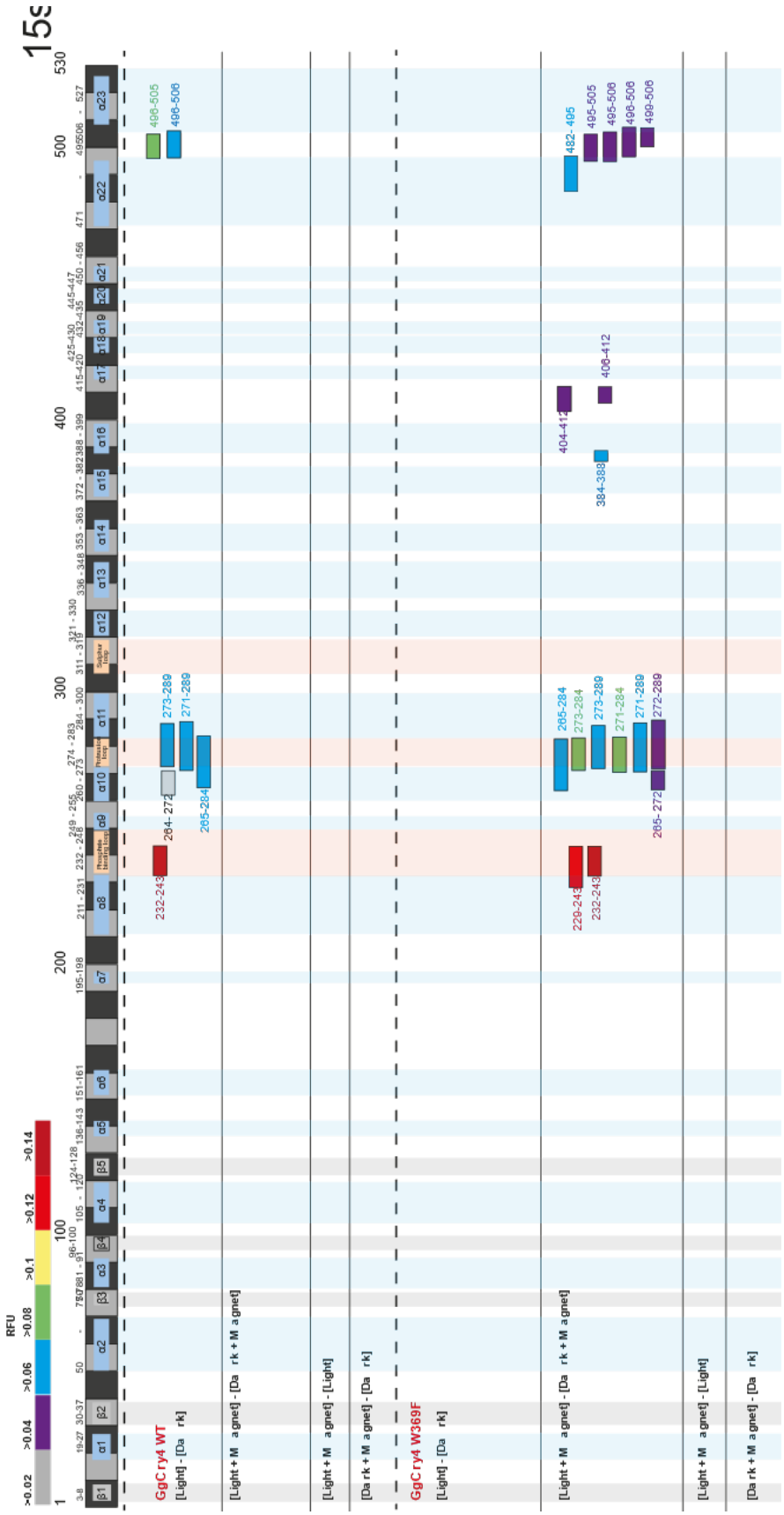


Figure A.22: RFU of *Gg*Cry4a WT and W369F at 15 s.

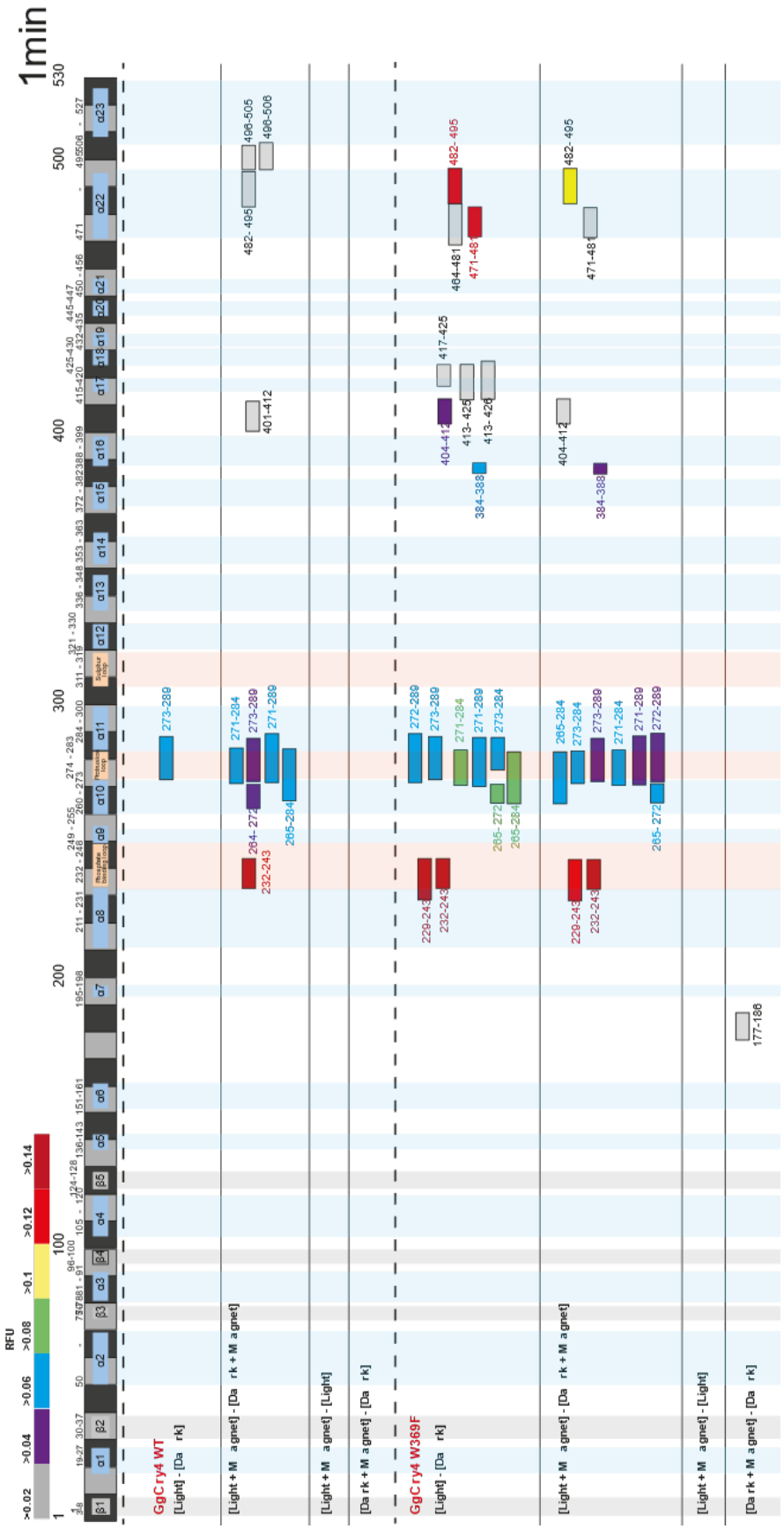


Figure A.23: RFU of *Gg*Cry4a WT and W369F at 1 min.

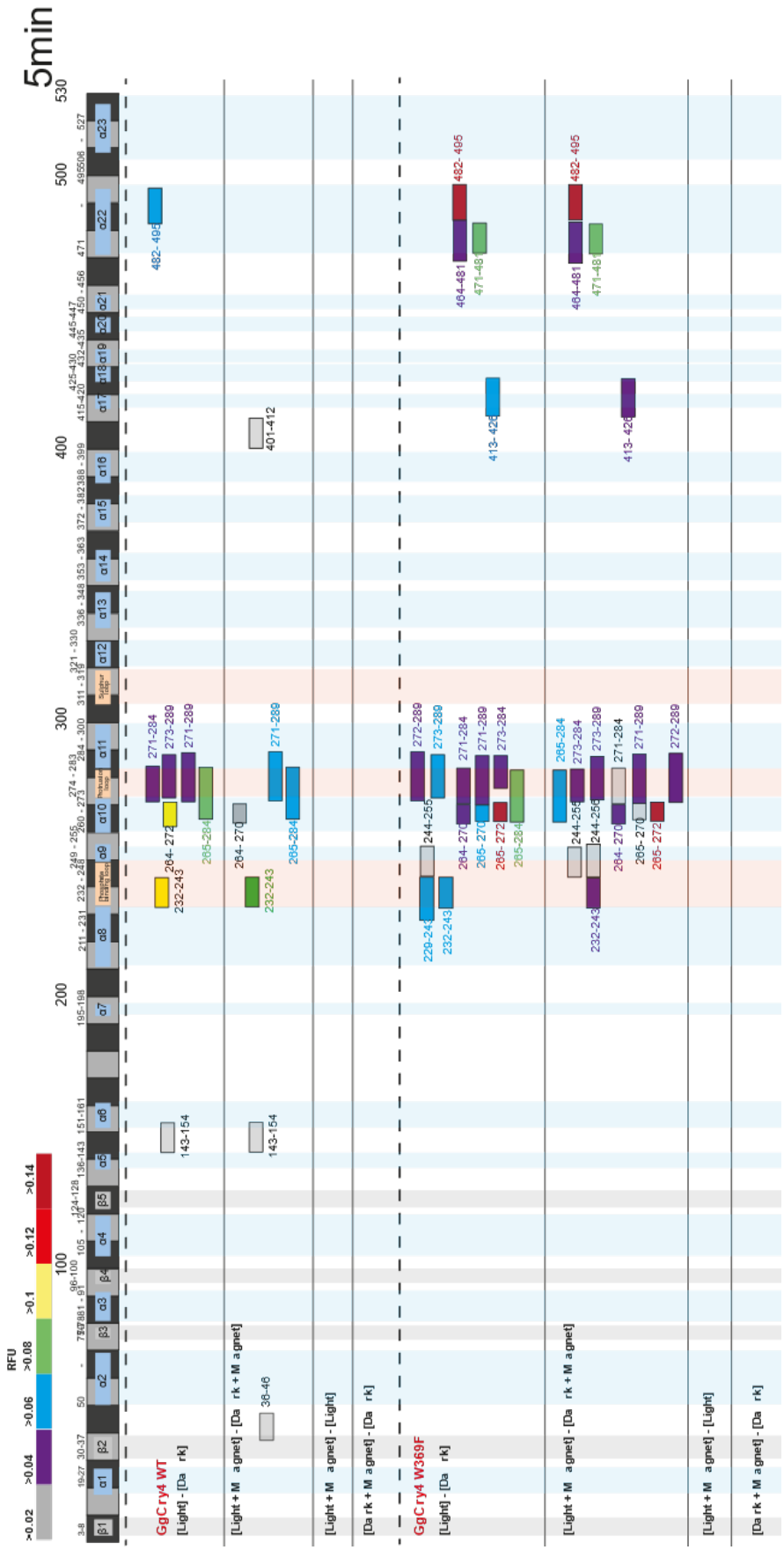


Figure A.24: RFU of *Gg*Cry4a WT and W369F at 5 min.

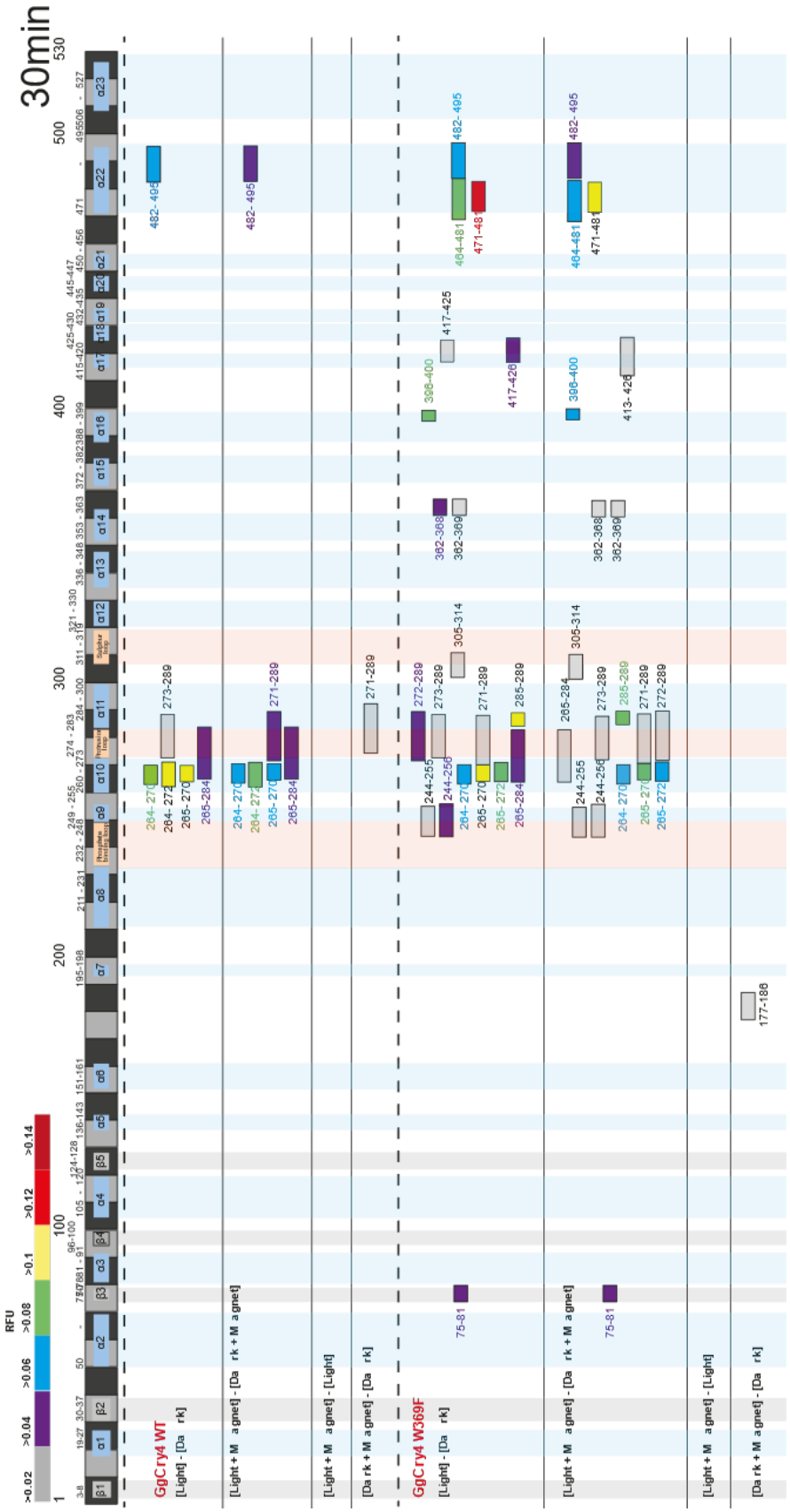


Figure A.25: RFU of *Gg*Cry4a WT and W369F at 30 min.

References

[1] Hugh Dingle and V. Alistair Drake. “What Is Migration?” In: *BioScience* 57.2 (Feb. 2007), pp. 113–121.

[2] Thomas Alerstam, Anders Hedenström, and Susanne Åkesson. “Long-distance migration: evolution and determinants”. en. In: *Oikos* 103.2 (2003). _eprint: https://nsojournals.onlinelibrary.wiley.com/doi/pdf/10.1034/j.1600-0706.2003.12559.x, pp. 247–260.

[3] Roswitha Wiltschko and Wolfgang Wiltschko. “Avian navigation: from historical to modern concepts”. In: *Animal Behaviour* 65.2 (Feb. 2003), pp. 257–272.

[4] W. Wiltschko and R. Wiltschko. “Magnetic compass of European robins”. eng. In: *Science (New York, N.Y.)* 176.4030 (Apr. 1972), pp. 62–64.

[5] Kenneth J. Lohmann et al. “Magnetic maps in animal navigation”. en. In: *Journal of Comparative Physiology A* 208.1 (Jan. 2022), pp. 41–67.

[6] Sönke Johnsen and Kenneth J. Lohmann. “The physics and neurobiology of magnetoreception”. eng. In: *Nature Reviews. Neuroscience* 6.9 (Sept. 2005), pp. 703–712.

[7] Will T. Schneider, Richard A. Holland, and Oliver Lindecke. “Over 50 years of behavioural evidence on the magnetic sense in animals: what has been learnt and how?” en. In: *The European Physical Journal Special Topics* 232.2 (Mar. 2023), pp. 269–278.

[8] Florian Packmor et al. “Migratory birds can extract positional information from magnetic inclination and magnetic declination alone”. In: *Proceedings of the Royal Society B: Biological Sciences* 291.2034 (Nov. 2024). Publisher: Royal Society, rspb20241363.

[9] Henrik Mouritsen and Thorsten Ritz. “Magnetoreception and its use in bird navigation”. In: *Current Opinion in Neurobiology.* Sensory systems 15.4 (Aug. 2005), pp. 406–414.

[10] Rachel Muheim, Frank R. Moore, and John B. Phillips. “Calibration of magnetic and celestial compass cues in migratory birds–a review of cue-conflict experiments”. eng. In: *The Journal of Experimental Biology* 209.Pt 1 (Jan. 2006), pp. 2–17.

[11] James L. Gould. “Animal navigation: the evolution of magnetic orientation”. eng. In: *Current biology: CB* 18.11 (June 2008), R482–484.

[12] R. A. Holland. “True navigation in birds: from quantum physics to global migration”. en. In: *Journal of Zoology* 293.1 (2014). _eprint: https://zslpublications.onlinelibrary.wiley.com/doi/pdf/10.1111/jzo.12107, pp. 1–15.

[13] K. J. Lohmann et al. “Regional magnetic fields as navigational markers for sea turtles”. eng. In: *Science (New York, N.Y.)* 294.5541 (Oct. 2001), pp. 364–366.

[14] Nathan F. Putman et al. “An Inherited Magnetic Map Guides Ocean Navigation in Juvenile Pacific Salmon”. English. In: *Current Biology* 24.4 (Feb. 2014). Publisher: Elsevier, pp. 446–450.

[15] Wolfgang Wiltschko et al. “Magnetite-based magnetoreception in birds: the effect of a biasing field and a pulse on migratory behavior”. In: *Journal of Experimental Biology* 205.19 (Oct. 2002), pp. 3031–3037.

[16] P. J. Hore and Henrik Mouritsen. “The Radical-Pair Mechanism of Magnetoreception”. en. In: *Annual Review of Biophysics* 45.Volume 45, 2016 (July 2016). Publisher: Annual Reviews, pp. 299–344.

[17] Jingjing Xu et al. “Magnetic sensitivity of cryptochrome 4 from a migratory songbird”. en. In: *Nature* 594.7864 (June 2021). Publisher: Nature Publishing Group, pp. 535–540.

[18] Gregory C. Nordmann, Tobias Hochstoeger, and David A. Keays. “Magnetoreception—A sense without a receptor”. en. In: *PLOS Biology* 15.10 (Oct. 2017). Publisher: Public Library of Science, e2003234.

[19] Kenneth J. Lohmann, Catherine M. F. Lohmann, and Nathan F. Putman. “Magnetic maps in animals: nature’s GPS”. In: *Journal of Experimental Biology* 210.21 (Nov. 2007), pp. 3697–3705.

[20] Ian P. Howard. “Animal Navigation”. In: *Perceiving in Depth: Volume 3 Other Mechanisms of Depth Perception*. Ed. by Ian P. Howard. Oxford University Press, Feb. 2012, p. 0.

[21] W. Wiltschko and R. Wiltschko. “Magnetic orientation in birds”. eng. In: *The Journal of Experimental Biology* 199.Pt 1 (1996), pp. 29–38.

[22] K.J. Lohmann, P. Luschi, and G.C. Hays. “Goal navigation and island-finding in sea turtles”. en. In: *Journal of Experimental Marine Biology and Ecology* 356.1-2 (Mar. 2008), pp. 83–95.

[23] Larry C. Boles and Kenneth J. Lohmann. “True navigation and magnetic maps in spiny lobsters”. eng. In: *Nature* 421.6918 (Jan. 2003), pp. 60–63.

[24] David Dreyer et al. “The Earth’s Magnetic Field and Visual Landmarks Steer Migratory Flight Behavior in the Nocturnal Australian Bogong Moth”. eng. In: *Current biology: CB* 28.13 (July 2018), 2160–2166.e5.

[25] J. B. Phillips. “Magnetic compass orientation in the Eastern red-spotted newt (Notophthalmus viridescens)”. eng. In: *Journal of Comparative Physiology. A, Sensory, Neural, and Behavioral Physiology* 158.1 (Jan. 1986), pp. 103–109.

[26] F. W. Merkel and Wolfgang Wiltschko. “Magnetismus und Richtungsfinden zugunruhiger Rotkehlchen (Erithacus rubecula)”. German. In: *Vogelwarte, Die* 23 (1965), pp. 71–77.

[27] Patrick A. Guerra, Robert J. Gegear, and Steven M. Reppert. “A magnetic compass aids monarch butterfly migration”. en. In: *Nature Communications* 5.1 (June 2014). Publisher: Nature Publishing Group, p. 4164.

[28] K. P. Able. “Orientation cues used by migratory birds: A review of cue-conflict experiments”. eng. In: *Trends in Ecology & Evolution* 8.10 (Oct. 1993), pp. 367–371.

[29] Anna Gagliardo. “Forty years of olfactory navigation in birds”. In: *Journal of Experimental Biology* 216.12 (June 2013), pp. 2165–2171.

[30] J. L. Kirschvink, M. M. Walker, and C. E. Diebel. “Magnetite-based magnetoreception”. eng. In: *Current Opinion in Neurobiology* 11.4 (Aug. 2001), pp. 462–467.

[31] R. Blakemore. “Magnetotactic bacteria”. eng. In: *Science (New York, N.Y.)* 190.4212 (Oct. 1975), pp. 377–379.

[32] Dennis A. Bazylinski and Richard B. Frankel. “Magnetosome formation in prokaryotes”. en. In: *Nature Reviews Microbiology* 2.3 (Mar. 2004). Publisher: Nature Publishing Group, pp. 217–230.

[33] Damien Faivre and Dirk Schüler. “Magnetotactic Bacteria and Magnetosomes”. In: *Chemical Reviews* 108.11 (Nov. 2008). Publisher: American Chemical Society, pp. 4875–4898.

[34] M. M. Walker et al. “Production of single-domain magnetite throughout life by sockeye salmon, Oncorhynchus nerka”. eng. In: *The Journal of Experimental Biology* 140 (Nov. 1988), pp. 51–63.

[35] Carol E. Diebel et al. “Magnetite defines a vertebrate magnetoreceptor”. en. In: *Nature* 406.6793 (July 2000). Publisher: Nature Publishing Group, pp. 299–302.

[36] M. Renee Bellinger et al. “Conservation of magnetite biomineralization genes in all domains of life and implications for magnetic sensing”. In: *Proceedings of the National Academy of Sciences of the United States of America* 119.3 (Jan. 2022), e2108655119.

[37] Lewis C. Naisbett-Jones et al. “Magnetoreception in fishes: the effect of magnetic pulses on orientation of juvenile Pacific salmon”. In: *Journal of Experimental Biology* 223.10 (May 2020), jeb222091.

[38] Christoph Daniel Treiber et al. “Clusters of iron-rich cells in the upper beak of pigeons are macrophages not magnetosensitive neurons”. en. In: *Nature* 484.7394 (Apr. 2012). Publisher: Nature Publishing Group, pp. 367–370.

[39] Gerta Fleissner et al. “Ultrastructural analysis of a putative magnetoreceptor in the beak of homing pigeons”. en. In: *Journal of Comparative Neurology* 458.4 (2003). _eprint: https://onlinelibrary.wiley.com/doi/pdf/10.1002/cne.10579, pp. 350–360.

[40] Dominik Heyers et al. “Magnetic field changes activate the trigeminal brainstem complex in a migratory bird”. eng. In: *Proceedings of the National Academy of Sciences of the United States of America* 107.20 (May 2010), pp. 9394–9399.

[41] Hervé Cadiou and Peter A. McNaughton. “Avian magnetite-based magnetoreception: a physiologist’s perspective”. In: *Journal of the Royal Society Interface* 7.Suppl 2 (Apr. 2010), S193–S205.

[42] Nathaniel B. Edelman et al. “No evidence for intracellular magnetite in putative vertebrate magnetoreceptors identified by magnetic screening”. In: *Proceedings of the National Academy of Sciences* 112.1 (Jan. 2015). Publisher: Proceedings of the National Academy of Sciences, pp. 262–267.

[43] Kirill Kavokin. “Can a hybrid chemical-ferromagnetic model of the avian compass explain its outstanding sensitivity to magnetic noise?” en. In: *PLOS ONE* 12.3 (Mar. 2017). Publisher: Public Library of Science, e0173887.

[44] Lü Yan and Song Tao. “Avian magnetoreception model realized by coupling a magnetite-based mechanism with a radical-pair-based mechanism”. In: *Chinese Physics B* 22.4 (2013).

[45] Wolfgang Wiltschko et al. “Magnetic Orientation in Birds: Non-Compass Responses under Monochromatic Light of Increased Intensity”. In: *Proceedings: Biological Sciences* 270.1529 (2003). Publisher: The Royal Society, pp. 2133–2140.

[46] Inês Chaves et al. “The cryptochromes: blue light photoreceptors in plants and animals”. eng. In: *Annual Review of Plant Biology* 62 (2011), pp. 335–364.

[47] Aziz Sancar. “Structure and function of DNA photolyase and cryptochrome blue-light photoreceptors”. eng. In: *Chemical Reviews* 103.6 (June 2003), pp. 2203–2237.

[48] Milena Damulewicz and Gabriella M. Mazzotta. “One Actor, Multiple Roles: The Performances of Cryptochrome in Drosophila”. In: *Frontiers in Physiology* 11 (Mar. 2020), p. 99.

[49] Khushbeer Malhotra et al. “Putative Blue-Light Photoreceptors from Arabidopsis thaliana and Sinapis alba with a High Degree of Sequence Homology to DNA Photolyase Contain the Two Photolyase Cofactors but Lack DNA Repair Activity”. In: *Biochemistry* 34.20 (May 1995). Publisher: American Chemical Society, pp. 6892–6899.

[50] P. Emery et al. “CRY, a Drosophila clock and light-regulated cryptochrome, is a major contributor to circadian rhythm resetting and photosensitivity”. eng. In: *Cell* 95.5 (Nov. 1998), pp. 669–679.

[51] R. Stanewsky et al. “The cryb mutation identifies cryptochrome as a circadian photoreceptor in Drosophila”. eng. In: *Cell* 95.5 (Nov. 1998), pp. 681–692.

[52] Taishi Yoshii, Margaret Ahmad, and Charlotte Helfrich-Förster. “Cryptochrome Mediates Light-Dependent Magnetosensitivity of Drosophila’s Circadian Clock”. en. In: *PLOS Biology* 7.4 (Apr. 2009). Publisher: Public Library of Science, e1000086.

[53] Robert J. Gegear et al. “Cryptochrome mediates light-dependent magnetosensitivity in Drosophila”. en. In: *Nature* 454.7207 (Aug. 2008). Publisher: Nature Publishing Group, pp. 1014–1018.

[54] Steven M. Reppert. “Magnetic field effects on behaviour in Drosophila”. en. In: *Nature* 629.8010 (May 2024). Publisher: Nature Publishing Group, E1–E2.

[55] Marco Bassetto et al. “No evidence for magnetic field effects on the behaviour of Drosophila”. en. In: *Nature* 620.7974 (Aug. 2023). Publisher: Nature Publishing Group, pp. 595–599.

[56] Shane A. Chandler et al. “Light-induced conformational switching and magnetic sensitivity of *Drosophila* cryptochrome”. In: *Structure* (Aug. 2025).

[57] Nuri Ozturk. “Phylogenetic and Functional Classification of the Photolyase/Cryptochrome Family”. en. In: *Photochemistry and Photobiology* 93.1 (2017). _eprint: https://onlinelibrary.wiley.com/doi/pdf/10.1111/php.12676, pp. 104–111.

[58] Li Zhang and E. Pascal Malkemper. “Cryptochromes in mammals: a magnetoreception misconception?” English. In: *Frontiers in Physiology* 14 (Aug. 2023). Publisher: Frontiers.

[59] Cristina C. DeOliveira and Brian R. Crane. “A structural decryption of cryptochromes”. English. In: *Frontiers in Chemistry* 12 (Aug. 2024). Publisher: Frontiers.

[60] Ronald Brudler et al. “Identification of a New Cryptochrome Class: Structure, Function, and Evolution”. In: *Molecular Cell* 11.1 (Jan. 2003), pp. 59–67.

[61] Stephan Kiontke et al. “DASH-type cryptochromes – solved and open questions”. en. In: *Biological Chemistry* 401.12 (Nov. 2020). Publisher: De Gruyter, pp. 1487–1493.

[62] Peter Deppisch, Charlotte Helfrich-Förster, and Pingkalai R. Senthilan. “The Gain and Loss of Cryptochrome/Photolyase Family Members during Evolution”. en. In: *Genes* 13.9 (Sept. 2022). Publisher: Multidisciplinary Digital Publishing Institute, p. 1613.

[63] Atticus Pinzon-Rodriguez, Staffan Bensch, and Rachel Muheim. “Expression patterns of cryptochrome genes in avian retina suggest involvement of Cry4 in light-dependent magnetoreception”. In: *Journal of The Royal Society Interface* 15.140 (Mar. 2018). Publisher: Royal Society, p. 20180058.

[64] Angelika Einwich et al. “A novel isoform of cryptochrome 4 (Cry4b) is expressed in the retina of a night-migratory songbird”. en. In: *Scientific Reports* 10.1 (Sept. 2020). Publisher: Nature Publishing Group, p. 15794.

[65] Anja Günther et al. “Double-Cone Localization and Seasonal Expression Pattern Suggest a Role in Magnetoreception for European Robin Cryptochrome 4”. eng. In: *Current biology: CB* 28.2 (Jan. 2018), 211–223.e4.

[66] Yoko Kubo et al. “Molecular cloning, mRNA expression, and immunocytochemical localization of a putative blue-light photoreceptor CRY4 in the chicken pineal gland”. eng. In: *Journal of Neurochemistry* 97.4 (May 2006), pp. 1155–1165.

[67] Takahiro Takeuchi et al. “Identification and characterization of cryptochrome4 in the ovary of western clawed frog Xenopus tropicalis”. eng. In: *Zoological Science* 31.3 (Mar. 2014), pp. 152–159.

[68] Klaus Schulten, Charles E. Swenberg, and Albert Weiler. “A Biomagnetic Sensory Mechanism Based on Magnetic Field Modulated Coherent Electron Spin Motion”. In: *Zeitschrift fur Physikalische Chemie* 111.1 (1978), pp. 1–5.

[69] T. Ritz, S. Adem, and K. Schulten. “A model for photoreceptor-based magnetoreception in birds”. eng. In: *Biophysical Journal* 78.2 (Feb. 2000), pp. 707–718.

[70] Thorsten Ritz et al. “Photoreceptor-based magnetoreception: optimal design of receptor molecules, cells, and neuronal processing”. In: *Journal of The Royal Society Interface* 7.suppl_2 (Feb. 2010). Publisher: Royal Society, S135–S146.

[71] Jamie Gravell et al. “Spectroscopic Characterization of Radical Pair Photochemistry in Nonmigratory Avian Cryptochromes: Magnetic Field Effects in GgCry4a”. eng. In: *Journal of the American Chemical Society* 147.28 (July 2025), pp. 24286–24298.

[72] Maja Hanić et al. “Dimerization of European Robin Cryptochrome 4a”. eng. In: *The Journal of Physical Chemistry. B* 127.28 (July 2023), pp. 6251–6264.

[73] Sophie Franz-Badur et al. “Structural changes within the bifunctional cryptochrome/photolyase CraCRY upon blue light excitation”. en. In: *Scientific Reports* 9.1 (July 2019). Publisher: Nature Publishing Group, p. 9896.

[74] Rene Zangl et al. “Time-Resolved Ion Mobility Mass Spectrometry to Solve Conformational Changes in a Cryptochrome”. In: *Journal of the American Chemical Society* 146.21 (May 2024). Publisher: American Chemical Society, pp. 14468–14478.

[75] Nertila Siuti and Neil L. Kelleher. “Decoding protein modifications using top-down mass spectrometry”. eng. In: *Nature Methods* 4.10 (Oct. 2007), pp. 817–821.

[76] Adam D. Catherman, Owen S. Skinner, and Neil L. Kelleher. “Top Down proteomics: Facts and perspectives”. In: *Biochemical and Biophysical Research Communications*. Advances in OMICs-based disciplines 445.4 (Mar. 2014), pp. 683–693.

[77] Albert J. R. Heck. “Native mass spectrometry: a bridge between interactomics and structural biology”. en. In: *Nature Methods* 5.11 (Nov. 2008). Publisher: Nature Publishing Group, pp. 927–933.

[78] S. Walter Englander and Neville R. Kallenbach. “Hydrogen exchange and structural dynamics of proteins and nucleic acids”. en. In: *Quarterly Reviews of Biophysics* 16.4 (Nov. 1983), pp. 521–655.

[79] Glenn Masson. *HDX-MS explained: Principles, applications, and best practices*. 2023.

[80] Cong Wu et al. “A Protease for Middle Down Proteomics”. In: *Nature methods* 9.8 (June 2012), pp. 822–824.

[81] Alba Cristobal et al. “Toward an Optimized Workflow for Middle-Down Proteomics”. In: *Analytical Chemistry* 89.6 (Mar. 2017). Publisher: American Chemical Society, pp. 3318–3325.

[82] Ruedi Aebersold and Matthias Mann. “Mass-spectrometric exploration of proteome structure and function”. en. In: *Nature* 537.7620 (Sept. 2016). Publisher: Nature Publishing Group, pp. 347–355.

[83] Upneet Kaur et al. “Evolution of Structural Biology through the Lens of Mass Spectrometry”. In: *Analytical chemistry* 91.1 (Jan. 2019), pp. 142–155.

[84] A. Konijnenberg, A. Butterer, and F. Sobott. “Native ion mobility-mass spectrometry and related methods in structural biology”. eng. In: *Biochimica Et Biophysica Acta* 1834.6 (June 2013), pp. 1239–1256.

[85] Helena Hernández and Carol V Robinson. “Determining the stoichiometry and interactions of macromolecular assemblies from mass spectrometry”. en. In: *Nature Protocols* 2.3 (Mar. 2007), pp. 715–726.

[86] Sem Tamara, Maurits A. den Boer, and Albert J. R. Heck. “High-Resolution Native Mass Spectrometry”. In: *Chemical Reviews* 122.8 (Apr. 2022). Publisher: American Chemical Society, pp. 7269–7326.

[87] Justin LP Benesch and Brandon T Ruotolo. “Mass spectrometry: come of age for structural and dynamical biology”. In: *Current Opinion in Structural Biology.* Carbohydrates and glycoconjugates/Biophysical methods 21.5 (Oct. 2011), pp. 641–649.

[88] Marie Barth and Carla Schmidt. “Native mass spectrometry—A valuable tool in structural biology”. en. In: *Journal of Mass Spectrometry* 55.10 (2020). _eprint: https://analyticalsciencejournals.onlinelibrary.wiley.com/doi/pdf/10.1002/jms.4578, e4578.

[89] Albert J. R. Heck and Robert H. H. Van Den Heuvel. “Investigation of intact protein complexes by mass spectrometry”. eng. In: *Mass Spectrometry Reviews* 23.5 (2004), pp. 368–389.

[90] J. B. Fenn et al. “Electrospray ionization for mass spectrometry of large biomolecules”. eng. In: *Science (New York, N.Y.)* 246.4926 (Oct. 1989), pp. 64–71.

[91] M. Karas et al. “Matrix-assisted ultraviolet laser desorption of non-volatile compounds”. In: *International Journal of Mass Spectrometry and Ion Processes* 78 (Sept. 1987), pp. 53–68.

[92] Koichi Tanaka et al. “Protein and polymer analyses up to m/z 100 000 by laser ionization time-of-flight mass spectrometry”. en. In: *Rapid Communications in Mass Spectrometry* 2.8 (1988). _eprint: https://analyticalsciencejournals.onlinelibrary.wiley.com/doi/pdf/10.1002/rcm.1290020802, pp. 151–153.

[93] Bruce Ganem, Yu Tsyr Li, and Jack D. Henion. “Detection of noncovalent receptor-ligand complexes by mass spectrometry”. In: *Journal of the American Chemical Society* 113.16 (July 1991). Publisher: American Chemical Society, pp. 6294–6296.

[94] Joseph A. Loo. “Studying noncovalent protein complexes by electrospray ionization mass spectrometry”. en. In: *Mass Spectrometry Reviews* 16.1 (1997). _eprint: https://analyticalsciencejournals.onlinelibrary.wiley.com/doi/pdf/10.1002/%28SICI%291098-2787%281997%2916%3A1%3C1%3A%3AAID-MAS1%3E3.0.CO%3B2-L, pp. 1–23.

[95] Frank Sobott et al. “A Tandem Mass Spectrometer for Improved Transmission and Analysis of Large Macromolecular Assemblies”. In: *Analytical Chemistry* 74.6 (Mar. 2002). Publisher: American Chemical Society, pp. 1402–1407.

[96] Robert H. H. van den Heuvel and Albert J. R. Heck. “Native protein mass spectrometry: from intact oligomers to functional machineries”. eng. In: *Current Opinion in Chemical Biology* 8.5 (Oct. 2004), pp. 519–526.

[97] J. Mitchell Wells and Scott A. McLuckey. “Collision-induced dissociation (CID) of peptides and proteins”. eng. In: *Methods in Enzymology* 402 (2005), pp. 148–185.

[98] Roman A. Zubarev, Neil L. Kelleher, and Fred W. McLafferty. “Electron Capture Dissociation of Multiply Charged Protein Cations. A Nonergodic Process”. In: *Journal of the American Chemical Society* 120.13 (Apr. 1998). Publisher: American Chemical Society, pp. 3265–3266.

[99] Fred W. McLafferty et al. “Electron capture dissociation of gaseous multiply charged ions by Fourier-transform ion cyclotron resonance”. In: *Journal of the American Society for Mass Spectrometry* 12.3 (Mar. 2001). Publisher: American Society for Mass Spectrometry. Published by the American Chemical Society. All rights reserved., pp. 245–249.

[100] Michael T. Marty et al. “Bayesian Deconvolution of Mass and Ion Mobility Spectra: From Binary Interactions to Polydisperse Ensembles”. In: *Analytical Chemistry* 87.8 (Apr. 2015). Publisher: American Chemical Society, pp. 4370–4376.

[101] Aneika C. Leney and Albert J. R. Heck. “Native Mass Spectrometry: What is in the Name?” In: *Journal of the American Society for Mass Spectrometry* 28.1 (2017), pp. 5–13.

[102] Kentaro Ishii, Min Zhou, and Susumu Uchiyama. “Native mass spectrometry for understanding dynamic protein complex”. eng. In: *Biochimica Et Biophysica Acta. General Subjects* 1862.2 (Feb. 2018), pp. 275–286.

[103] Geoffrey Ingram Taylor. “Disintegration of water drops in an electric field”. In: *Proceedings of the Royal Society of London. Series A. Mathematical and Physical Sciences* 280.1382 (Jan. 1997). Publisher: Royal Society, pp. 383–397.

[104] Lord Rayleigh. “XX. On the equilibrium of liquid conducting masses charged with electricity”. In: *The London, Edinburgh, and Dublin Philosophical Magazine and Journal of Science* 14.87 (Sept. 1882). Publisher: Taylor & Francis _eprint: https://doi.org/10.1080/14786448208628425, pp. 184–186.

[105] CS Ho et al. “Electrospray Ionisation Mass Spectrometry: Principles and Clinical Applications”. In: *The Clinical Biochemist Reviews* 24.1 (Feb. 2003), pp. 3–12.

[106] J. V. Iribarne and B. A. Thomson. “On the evaporation of small ions from charged droplets”. In: *Journal of Chemical Physics* 64 (Mar. 1976). Publisher: AIP ADS Bibcode: 1976JChPh..64.2287I, pp. 2287–2294.

[107] Malcolm Dole et al. “Gas Phase Macroions”. In: *Macromolecules* 1.1 (Jan. 1968). Publisher: American Chemical Society, pp. 96–97.

[108] J Fernandez de la Mora. “Electrospray ionization of large multiply charged species proceeds via Dole’s charged residue mechanism”. In: *Analytica Chimica Acta* 406.1 (Feb. 2000), pp. 93–104.

[109] Lars Konermann et al. “Unraveling the Mechanism of Electrospray Ionization”. In: *Analytical Chemistry* 85.1 (Jan. 2013). Publisher: American Chemical Society, pp. 2–9.

[110] Wai Siang Law et al. “On the mechanism of extractive electrospray ionization”. eng. In: *Analytical Chemistry* 82.11 (June 2010), pp. 4494–4500.

[111] M. Karas, U. Bahr, and T. Dülcks. “Nano-electrospray ionization mass spectrometry: addressing analytical problems beyond routine”. eng. In: *Fresenius’ Journal of Analytical Chemistry* 366.6-7 (2000), pp. 669–676.

[112] Reinhard Juraschek, Thomas Dülcks, and Michael Karas. "Nanoelectrospray—more than just a minimized-flow electrospray ionization source". In: *Journal of the American Society for Mass Spectrometry* 10.4 (Apr. 1999), pp. 300–308.

[113] Ryan T. Kelly et al. "The Ion Funnel: Theory, Implementations, and Applications". In: *Mass spectrometry reviews* 29.2 (2010), pp. 294–312.

[114] Raymond E. March. "An Introduction to Quadrupole Ion Trap Mass Spectrometry". en. In: *Journal of Mass Spectrometry* 32.4 (1997). _eprint: https://analyticalsciencejournals.onlinelibrary.wiley.com/doi/pdf/10.1002/%28SICI%291096-9888%28199704%2932%3A4%3C351%3A%3AAID-JMS512%3E3.0.CO%3B2-Y, pp. 351–369.

[115] Eugen Damoc et al. *Advancing native top-down MS analysis of non-covalent protein complexes: The Thermo Scientific Q Exactive UHMR mass spectrometer.* Technical Note 65379. Bremen, Germany; San Jose, CA; Eindhoven, Netherlands: Thermo Fisher Scientific, Dec. 2018.

[116] Steven D. Pringle et al. "An investigation of the mobility separation of some peptide and protein ions using a new hybrid quadrupole/travelling wave IMS/oa-ToF instrument". In: *International Journal of Mass Spectrometry* 261.1 (Mar. 2007), pp. 1–12.

[117] D. J. Douglas and J. B. French. "Collisional focusing effects in radio frequency quadrupoles". In: *Journal of the American Society for Mass Spectrometry* 3.4 (May 1992), pp. 398–408.

[118] Jesper V. Olsen et al. "Higher-energy C-trap dissociation for peptide modification analysis". eng. In: *Nature Methods* 4.9 (Sept. 2007), pp. 709–712.

[119] Annette Michalski et al. "Mass Spectrometry-based Proteomics Using Q Exactive, a High-performance Benchtop Quadrupole Orbitrap Mass Spectrometer *". English. In: *Molecular & Cellular Proteomics* 10.9 (Sept. 2011). Publisher: Elsevier.

[120] John C. Jurchen and Evan R. Williams. "Origin of Asymmetric Charge Partitioning in the Dissociation of Gas-Phase Protein Homodimers". In: *Journal of the American Chemical Society* 125.9 (Mar. 2003). Publisher: American Chemical Society, pp. 2817–2826.

[121] Rebecca J. Rose et al. "High-sensitivity Orbitrap mass analysis of intact macromolecular assemblies". en. In: *Nature Methods* 9.11 (Nov. 2012). Publisher: Nature Publishing Group, pp. 1084–1086.

[122] Jennifer S. Brodbelt. "Photodissociation mass spectrometry: new tools for characterization of biological molecules". en. In: *Chemical Society Reviews* 43.8 (Mar. 2014). Publisher: The Royal Society of Chemistry, pp. 2757–2783.

[123] Dalton T. Snyder, Sophie R. Harvey, and Vicki H. Wysocki. "Surface-induced dissociation mass spectrometry as a structural biology tool". In: *Chemical reviews* 122.8 (Apr. 2022), pp. 7442–7487.

[124] Alexander Makarov. "Electrostatic Axially Harmonic Orbital Trapping: A High-Performance Technique of Mass Analysis". In: *Analytical Chemistry* 72.6 (Mar. 2000). Publisher: American Chemical Society, pp. 1156–1162.

[125] Qizhi Hu et al. “The Orbitrap: a
new mass spectrometer”. en. In: *Journal of Mass Spectrometry* 40.4 (2005). _eprint: https://analyticalsciencejournals.onlinelibrary.wiley.com/doi/pdf/10.1002/jms.856, pp. 430–443.

[126] Robert J. Cotter. “Time-of-Flight Mass Spectrometry for the Structural Analysis of Biological Molecules”. In: *Analytical Chemistry* 64.21 (Nov. 1992). Publisher: American Chemical Society, 1027A–1039A.

[127] Kevin Giles et al. “Applications of a travelling wave-based radio-frequency-only stacked ring ion guide”. en. In: *Rapid Communications in Mass Spectrometry* 18.20 (2004). _eprint: https://analyticalsciencejournals.onlinelibrary.wiley.com/doi/pdf/10.1002/rcm.1641, pp. 2401–2414.

[128] Alexandre A. Shvartsburg and Richard D. Smith. “Fundamentals of Traveling Wave Ion Mobility Spectrometry”. In: *Analytical Chemistry* 80.24 (Dec. 2008). Publisher: American Chemical Society, pp. 9689–9699.

[129] Martin F. Jarrold. “Applications of Charge Detection Mass Spectrometry in Molecular Biology and Biotechnology”. In: *Chemical Reviews* 122.8 (Apr. 2022). Publisher: American Chemical Society, pp. 7415–7441.

[130] Linus Pauling, Robert B. Corey, and H. R. Branson. “The structure of proteins: Two hydrogen-bonded helical configurations of the polypeptide chain”. en. In: *Proceedings of the National Academy of Sciences* 37.4 (Apr. 1951), pp. 205–211.

[131] S. Walter Englander. “Hydrogen Exchange and Mass Spectrometry: A Historical Perspective”. In: *Journal of the American Society for Mass Spectrometry* 17.11 (Nov. 2006), pp. 1481–1489.

[132] A. Hvidt and K. Linderstrøm-Lang. “Exchange of hydrogen atoms in insulin with deuterium atoms in aqueous solutions”. eng. In: *Biochimica Et Biophysica Acta* 14.4 (Aug. 1954), pp. 574–575.

[133] A. Hvidt and S. O. Nielsen. “Hydrogen exchange in proteins”. eng. In: *Advances in Protein Chemistry* 21 (1966), pp. 287–386.

[134] G. Wagner and K. Wüthrich. “Sequential resonance assignments in protein 1H nuclear magnetic resonance spectra. Basic pancreatic trypsin inhibitor”. eng. In: *Journal of Molecular Biology* 155.3 (Mar. 1982), pp. 347–366.

[135] Zhongqi Zhang and David L. Smith. “Determination of amide hydrogen exchange by mass spectrometry: A new tool for protein structure elucidation”. en. In: *Protein Science* 2.4 (1993). _eprint: https://onlinelibrary.wiley.com/doi/pdf/10.1002/pro.5560020404, pp. 522–531.

[136] R. S. Johnson and K. A. Walsh. “Mass spectrometric measurement of protein amide hydrogen exchange rates of apo- and holo-myoglobin”. eng. In: *Protein Science: A Publication of the Protein Society* 3.12 (Dec. 1994), pp. 2411–2418.

[137] John R. Engen. “Analysis of Protein Conformation and Dynamics by Hydrogen/Deuterium Exchange MS”. In: *Analytical chemistry* 81.19 (Oct. 2009), pp. 7870–7875.

[138] Glenn R. Masson et al. “Recommendations for performing, interpreting and reporting hydrogen deuterium exchange mass spectrometry (HDX-MS) experiments”. eng. In: *Nature Methods* 16.7 (July 2019), pp. 595–602.

[139] Dominic Narang, Cristina Lento, and Derek J. Wilson. “HDX-MS: An Analytical Tool to Capture Protein Motion in Action”. en. In: *Biomedicines* 8.7 (July 2020), p. 224.

[140] Kerene A. Brown and Derek J. Wilson. “Bottom-up hydrogen deuterium exchange mass spectrometry: data analysis and interpretation”. en. In: *The Analyst* 142.16 (2017), pp. 2874–2886.

[141] Arieh Berger and K. Linderstrøm-Lang. “Deuterium exchange of poly-dl-alanine in aqueous solution”. en. In: *Archives of Biochemistry and Biophysics* 69 (1957), pp. 106–118.

[142] D. L. Smith, Y. Deng, and Z. Zhang. “Probing the non-covalent structure of proteins by amide hydrogen exchange and mass spectrometry”. eng. In: *Journal of mass spectrometry: JMS* 32.2 (Feb. 1997), pp. 135–146.

[143] David D. Weis et al. “Identification and Characterization of EX1 Kinetics in H/D Exchange Mass Spectrometry by Peak Width Analysis”. In: *Journal of the American Society for Mass Spectrometry* 17.11 (Nov. 2006), pp. 1498–1509.

[144] Thomas E. Wales and John R. Engen. “Hydrogen exchange mass spectrometry for the analysis of protein dynamics”. eng. In: *Mass Spectrometry Reviews* 25.1 (2006), pp. 158–170.

[145] Lars Konermann and Pablo M. Scrosati. “Hydrogen/Deuterium Exchange Mass Spectrometry: Fundamentals, Limitations, and Opportunities”. eng. In: *Molecular & cellular proteomics: MCP* 23.11 (Nov. 2024), p. 100853.

[146] Y. Bai et al. “Primary structure effects on peptide group hydrogen exchange”. eng. In: *Proteins* 17.1 (Sept. 1993), pp. 75–86.

[147] David Nguyen et al. “Reference Parameters for Protein Hydrogen Exchange Rates”. In: *Journal of the American Society for Mass Spectrometry* 29.9 (Sept. 2018). Publisher: American Society for Mass Spectrometry. Published by the American Chemical Society. All rights reserved., pp. 1936–1939.

[148] Kasper Rand. *Pepsin column repacking*. en-US. 2018.

[149] Jeffrey C. Silva et al. “Absolute quantification of proteins by LCMSE: a virtue of parallel MS acquisition”. eng. In: *Molecular & cellular proteomics: MCP* 5.1 (Jan. 2006), pp. 144–156.

[150] Andy M. Lau et al. “Deuteros 2.0: peptide-level significance testing of data from hydrogen deuterium exchange mass spectrometry”. eng. In: *Bioinformatics (Oxford, England)* 37.2 (Apr. 2021), pp. 270–272.

[151] B. L. Welch. “The Generalization of ‘Student’s’ Problem when Several Different Population Variances are Involved”. In: *Biometrika* 34.1/2 (1947). Publisher: [Oxford University Press, Biometrika Trust], pp. 28–35.

[152] Kasper D. Rand et al. “Protein Hydrogen Exchange Measured at Single-Residue Resolution by Electron Transfer Dissociation Mass Spectrometry”. In: *Analytical Chemistry* 81.14 (July 2009). Publisher: American Chemical Society, pp. 5577–5584.

[153] Ellie I. James et al. “Advances in Hydrogen/Deuterium Exchange Mass Spectrometry and the Pursuit of Challenging Biological Systems”. In: *Chemical Reviews* 122.8 (Apr. 2022). Publisher: American Chemical Society, pp. 7562–7623.

[154] Daniel T. Weltz Wollenberg et al. “Avoiding H/D Scrambling with Minimal Ion Transmission Loss for HDX-MS/MS-ETD Analysis on a High-Resolution Q-TOF Mass Spectrometer”. eng. In: *Analytical Chemistry* 92.11 (June 2020), pp. 7453–7461.

[155] R. Latter et al. “Evidence of an activity-enhancing conformational shift in Arabidopsis thaliana Plant Cysteine Oxidase 4 induced by binding of substrate or substrate-mimics”. English. In: *Journal of Biological Chemistry* 0.0 (Sept. 2025). Publisher: Elsevier.

[156] Daan A. Weits et al. “An apical hypoxic niche sets the pace of shoot meristem activity”. eng. In: *Nature* 569.7758 (May 2019), pp. 714–717.

[157] Mohamad Abbas et al. “Oxygen Sensing Coordinates Photomorphogenesis to Facilitate Seedling Survival”. In: *Current Biology* 25.11 (June 2015), pp. 1483–1488.

[158] Manuela Hinz et al. “Arabidopsis RAP2.2: an ethylene response transcription factor that is important for hypoxia survival”. eng. In: *Plant Physiology* 153.2 (June 2010), pp. 757–772.

[159] Angelika Mustroph et al. “Profiling translatomes of discrete cell populations resolves altered cellular priorities during hypoxia in Arabidopsis”. eng. In: *Proceedings of the National Academy of Sciences of the United States of America* 106.44 (Nov. 2009), pp. 18843–18848.

[160] Daan A. Weits et al. “Plant cysteine oxidases control the oxygen-dependent branch of the N-end-rule pathway”. en. In: *Nature Communications* 5.1 (Mar. 2014). Publisher: Nature Publishing Group, p. 3425.

[161] Daniel J. Gibbs et al. “Homeostatic response to hypoxia is regulated by the N-end rule pathway in plants”. eng. In: *Nature* 479.7373 (Oct. 2011), pp. 415–418.

[162] Francesco Licausi et al. “Oxygen sensing in plants is mediated by an N-end rule pathway for protein destabilization”. eng. In: *Nature* 479.7373 (Oct. 2011), pp. 419–422.

[163] James F. White et al. “Rhizophagy Cycle: An Oxidative Process in Plants for Nutrient Extraction from Symbiotic Microbes”. In: *Microorganisms* 6.3 (Sept. 2018), p. 95.

[164] Norma Masson et al. “Conserved N-terminal cysteine dioxygenases transduce responses to hypoxia in animals and plants”. eng. In: *Science (New York, N.Y.)* 365.6448 (July 2019), pp. 65–69.

[165] Mark D. White et al. “Structures of Arabidopsis thaliana oxygen-sensing plant cysteine oxidases 4 and 5 enable targeted manipulation of their activity”. eng. In: *Proceedings of the National Academy of Sciences of the United States of America* 117.37 (Sept. 2020), pp. 23140–23147.

[166] Zhenzhen Chen et al. “Molecular basis for cysteine oxidation by plant cysteine oxidases from Arabidopsis thaliana”. eng. In: *Journal of Structural Biology* 213.1 (Mar. 2021), p. 107663.

[167] Dona M. Gunawardana, Karen C. Heathcote, and Emily Flashman. “Emerging roles for thiol dioxygenases as oxygen sensors”. en. In: *The FEBS Journal* 289.18 (2022). _eprint: https://febs.onlinelibrary.wiley.com/doi/pdf/10.1111/febs.16147, pp. 5426–5439.

[168] Leah J. Taylor-Kearney and Emily Flashman. “Targeting plant cysteine oxidase activity for improved submergence tolerance”. eng. In: *The Plant Journal: For Cell and Molecular Biology* 109.4 (Feb. 2022), pp. 779–788.

[169] Guillermina M. Mendiondo et al. “Enhanced waterlogging tolerance in barley by manipulation of expression of the N-end rule pathway E3 ligase PROTEOLYSIS6”. eng. In: *Plant Biotechnology Journal* 14.1 (Jan. 2016), pp. 40–50.

[170] Mikel Lavilla-Puerta et al. “Identification of novel plant cysteine oxidase inhibitors from a yeast chemical genetic screen”. eng. In: *The Journal of Biological Chemistry* 299.12 (Dec. 2023), p. 105366.

[171] Sjon Hartman et al. “Ethylene-mediated nitric oxide depletion pre-adapts plants to hypoxia stress”. en. In: *Nature Communications* 10.1 (Sept. 2019). Publisher: Nature Publishing Group, p. 4020.

[172] Stephen T. Emlen and John T. Emlen. “A Technique for Recording Migratory Orientation of Captive Birds”. en. In: *The Auk* 83.3 (July 1966), pp. 361–367.

[173] Wolfgang Wiltschko et al. “Red light disrupts magnetic orientation of migratory birds”. en. In: *Nature* 364.6437 (Aug. 1993). Publisher: Nature Publishing Group, pp. 525–527.

[174] Rachel Muheim, Johan Bäckman, and Susanne Akesson. “Magnetic compass orientation in European robins is dependent on both wavelength and intensity of light”. eng. In: *The Journal of Experimental Biology* 205.Pt 24 (Dec. 2002), pp. 3845–3856.

[175] W. Wiltschko, M. Gesson, and R. Wiltschko. “Magnetic compass orientation of European robins under 565 nm green light”. eng. In: *Die Naturwissenschaften* 88.9 (Sept. 2001), pp. 387–390.

[176] Henrik Mouritsen. “Long-distance navigation and magnetoreception in migratory animals”. en. In: *Nature* 558.7708 (June 2018). Publisher: Nature Publishing Group, pp. 50–59.

[177] Chad A. Brautigam et al. “Structure of the photolyase-like domain of cryptochrome 1 from Arabidopsis thaliana”. In: *Proceedings of the National Academy of Sciences* 101.33 (Aug. 2004). Publisher: Proceedings of the National Academy of Sciences, pp. 12142–12147.

[178] Brian D. Zoltowski et al. “Chemical and structural analysis of a photoactive vertebrate cryptochrome from pigeon”. In: *Proceedings of the National Academy of Sciences* 116.39 (Sept. 2019). Publisher: Proceedings of the National Academy of Sciences, pp. 19449–19457.

[179] Anthony R. Cashmore. “Cryptochromes”. en. In: *PHOTOMORPHOGENESIS IN PLANTS AND BACTERIA*. Ed. by EBERHARD SCHÁFER and FERENC NAGY. Dordrecht: Springer Netherlands, 2006, pp. 199–221.

[180] Andrea Cellini et al. “Directed ultrafast conformational changes accompany electron transfer in a photolyase as resolved by serial crystallography”. en. In: *Nature Chemistry* 16.4 (Apr. 2024). Publisher: Nature Publishing Group, pp. 624–632.

[181] Siu Ying Wong et al. “Cryptochrome magnetoreception: four tryptophans could be better than three”. In: *Journal of The Royal Society Interface* 18.184 (Nov. 2021). Publisher: Royal Society, p. 20210601.

[182] Marta Majewska et al. “European Robin Cryptochrome-4a Associates with Lipid Bilayers in an Ordered Manner, Fulfilling a Molecular-Level Condition for Magnetoreception”. In: *ACS Chemical Biology* 20.3 (Mar. 2025). Publisher: American Chemical Society, pp. 592–606.

[183] Kenichi Hitomi et al. “Functional motifs in the (6-4) photolyase crystal structure make a comparative framework for DNA repair photolyases and clock cryptochromes”. eng. In: *Proceedings of the National Academy of Sciences of the United States of America* 106.17 (Apr. 2009), pp. 6962–6967.

[184] Yadi Chen et al. “Regulation of Arabidopsis photoreceptor CRY2 by two distinct E3 ubiquitin ligases”. en. In: *Nature Communications* 12.1 (Apr. 2021). Publisher: Nature Publishing Group, p. 2155.

[185] Ling Ma et al. “Structural insights into BIC-mediated inactivation of Arabidopsis cryptochrome 2”. en. In: *Nature Structural & Molecular Biology* 27.5 (May 2020). Publisher: Nature Publishing Group, pp. 472–479.

[186] Oskar Berntsson et al. “Photoactivation of Drosophila melanogaster cryptochrome through sequential conformational transitions”. eng. In: *Science Advances* 5.7 (July 2019), eaaw1531.

[187] Lisa S. Baik et al. “Distinct mechanisms of Drosophila CRYPTOCHROME-mediated light-evoked membrane depolarization and in vivo clock resetting”. In: *Proceedings of the National Academy of Sciences* 116.46 (Nov. 2019). Publisher: Proceedings of the National Academy of Sciences, pp. 23339–23344.

[188] Fabian Schuhmann, Daniel R. Kattnig, and Ilia A. Solov’yov. “Exploring Post-activation Conformational Changes in Pigeon Cryptochrome 4”. In: *The Journal of Physical Chemistry B* 125.34 (Sept. 2021). Publisher: American Chemical Society, pp. 9652–9659.

[189] Malathy Palayam et al. “Structural insights into photoactivation of plant Cryptochrome-2”. en. In: *Communications Biology* 4.1 (Jan. 2021). Publisher: Nature Publishing Group, p. 28.

[190] Anna Czarna et al. “Structures of Drosophila cryptochrome and mouse cryptochrome1 provide insight into circadian function”. eng. In: *Cell* 153.6 (June 2013), pp. 1394–1405.

[191] Haijia Wu et al. “Protein-protein interaction of the putative magnetoreceptor cryptochrome 4 expressed in the avian retina”. en. In: *Scientific Reports* 10.1 (Apr. 2020). Publisher: Nature Publishing Group, p. 7364.

[192] Sahar Foroutannejad et al. “The cofactor-dependent folding mechanism of Drosophila cryptochrome revealed by single-molecule pulling experiments”. en. In: *Nature Communications* 14.1 (Feb. 2023). Publisher: Nature Publishing Group, p. 1057.

[193] Yuma Terai et al. “Coulomb and CH–π interactions in (6–4) photolyase–DNA complex dominate DNA binding and repair abilities”. In: *Nucleic Acids Research* 46.13 (May 2018). tex.eprint: https://academic.oup.com/nar/article-pdf/46/13/6761/25228146/gky364.pdf, pp. 6761–6772.

[194] Corinna Langebrake et al. “Adaptive evolution and loss of a putative magnetoreceptor in passerines”. eng. In: *Proceedings. Biological Sciences* 291.2016 (Feb. 2024), p. 20232308.

[195] Christiane R Timmel. *Viva*. Personal Communication. University of Oxford, Jan. 2025.

[196] Jie Gao et al. “Trp triad-dependent rapid photoreduction is not required for the function of Arabidopsis CRY1”. In: *Proceedings of the National Academy of Sciences* 112.29 (July 2015). Publisher: Proceedings of the National Academy of Sciences, pp. 9135–9140.

[197] D. W. Burt. “Emergence of the chicken as a model organism: implications for agriculture and biology”. eng. In: *Poultry Science* 86.7 (July 2007), pp. 1460–1471.

[198] Aline Bertin et al. “Stable Individual Profiles of Daily Timing of Migratory Restlessness in European Quail”. EN. In: *Chronobiology International* (Jan. 2007). Publisher: Taylor & Francis.

[199] Ryuji Watari et al. “Light-dependent Structural Change of Chicken Retinal Cryptochrome4”. en. In: *Journal of Biological Chemistry* 287.51 (Dec. 2012), pp. 42634–42641.

[200] Sergio L. Pereira and Allan J. Baker. “A molecular timescale for galliform birds accounting for uncertainty in time estimates and heterogeneity of rates of DNA substitutions across lineages and sites”. In: *Molecular Phylogenetics and Evolution* 38.2 (Feb. 2006), pp. 499–509.

[201] De Chen et al. “Divergence time estimation of Galliformes based on the best gene shopping scheme of ultraconserved elements”. In: *BMC Ecology and Evolution* 21.1 (Nov. 2021), p. 209.

[202] Rafael Freire et al. “Chickens orient using a magnetic compass”. English. In: *Current Biology* 15.16 (Aug. 2005). Publisher: Elsevier, R620–R621.

[203] Wolfgang Wiltschko et al. “The magnetic compass of domestic chickens, Gallus gallus”. eng. In: *The Journal of Experimental Biology* 210.Pt 13 (July 2007), pp. 2300–2310.

[204] J. D. Rodríguez-TeijeiroJ D. Rodríguez-Teijeiro et al. “Orientation-cage experiments with the European Quail during the breeding season and autumn migration”. en. In: *Canadian Journal of Zoology* (July 2006).

[205] Zhengwei Fu et al. “Molecular cloning and circadian regulation of cryptochrome genes in Japanese quail (Coturnix coturnix japonica)”. eng. In: *Journal of Biological Rhythms* 17.1 (Feb. 2002), pp. 14–27.

[206] Valeria Marasco et al. “Brain gene expression reveals pathways underlying nocturnal migratory restlessness”. en. In: *Scientific Reports* 14.1 (Sept. 2024). Publisher: Nature Publishing Group, p. 22420.

[207] Hui Xiao et al. “Mapping protein energy landscapes with amide hydrogen exchange and mass spectrometry: I. A generalized model for a two-state protein and comparison with experiment”. en. In: *Protein Science* 14.2 (2005). _eprint: https://onlinelibrary.wiley.com/doi/pdf/10.1110/ps.041001705, pp. 543–557.

[208] Miklos Guttman et al. “Analysis of Overlapped and Noisy Hydrogen/Deuterium Exchange Mass Spectra”. In: *Journal of the American Society for Mass Spectrometry* 24.12 (Dec. 2013). Publisher: American Society for Mass Spectrometry. Published by the American Chemical Society. All rights reserved., pp. 1906–1912.

[209] Andrew F. X. Goldberg, Orson L. Moritz, and David S. Williams. “Molecular basis for photoreceptor outer segment architecture”. In: *Progress in Retinal and Eye Research* 55 (Nov. 2016), pp. 52–81.

[210] Christopher L. Sander et al. “Nano-scale resolution of native retinal rod disk membranes reveals differences in lipid composition”. In: *The Journal of Cell Biology* 220.8 (June 2021), e202101063.

[211] Martin-Paul Agbaga et al. “Differential composition of DHA and very-long-chain PUFAs in rod and cone photoreceptors”. In: *Journal of Lipid Research* 59.9 (Sept. 2018), pp. 1586–1596.

[212] Keri J. Fogle et al. “CRYPTOCHROME is a blue-light sensor that regulates neuronal firing rate”. eng. In: *Science (New York, N.Y.)* 331.6023 (Mar. 2011), pp. 1409–1413.

[213] Anja Dorowski et al. “Crystal Structure of Paprika Ferredoxin-NADP+Reductase”. In: *Journal of Biological Chemistry* 276.12 (Mar. 2001), pp. 9253–9263.

[214] Ferdinand Alte et al. “Ferredoxin:NADPH oxidoreductase is recruited to thylakoids by binding to a polyproline type II helix in a pH-dependent manner”. In: *Proceedings of the National Academy of Sciences of the United States of America* 107.45 (Nov. 2010), pp. 19260–19265.

[215] J. P. Benz et al. “Arabidopsis Tic62 and ferredoxin-NADP(H) oxidoreductase form light-regulated complexes that are integrated into the chloroplast redox poise”. eng. In: *The Plant Cell* 21.12 (Dec. 2009), pp. 3965–3983.

[216] Christine M. Hebling et al. “Conformational Analysis of Membrane Proteins in Phospholipid Bilayer Nanodiscs by Hydrogen Exchange Mass Spectrometry”. In: *Analytical Chemistry* 82.13 (July 2010). Publisher: American Chemical Society, pp. 5415–5419.

[217] Michelle Redhair, Amanda F. Clouser, and William M. Atkins. “Hydrogen-deuterium exchange mass spectrometry of membrane proteins in lipid nanodiscs”. eng. In: *Chemistry and Physics of Lipids* 220 (May 2019), pp. 14–22.

[218] Eamonn Reading et al. “Interrogating Membrane Protein Conformational Dynamics within Native Lipid Compositions”. eng. In: *Angewandte Chemie (International Ed. in English)* 56.49 (Dec. 2017), pp. 15654–15657.

[219] Thirupathi Ravula and Ayyalusamy Ramamoorthy. “Synthesis, Characterization, and Nanodisc Formation of Non-ionic Polymers”. en. In: *Angewandte Chemie International Edition* 60.31 (2021). _eprint: https://onlinelibrary.wiley.com/doi/pdf/10.1002/anie.202101950, pp. 16885–16888.

[220] Marius M. Kostelic et al. “Assembly of Model Membrane Nanodiscs for Native Mass Spectrometry”. eng. In: *Analytical Chemistry* 93.14 (Apr. 2021), pp. 5972–5979.

[221] Michael T. Marty. “Nanodiscs and Mass Spectrometry: Making Membranes Fly”. In: *International journal of mass spectrometry* 458 (Dec. 2020), p. 116436.

[222] Katharina Görtemaker et al. “Direct Interaction of Avian Cryptochrome 4 with a Cone Specific G-Protein”. In: *Cells* 11.13 (June 2022), p. 2043.

[223] Alexander Leitner et al. “Crosslinking and Mass Spectrometry: An Integrated Technology to Understand the Structure and Function of Molecular Machines”. eng. In: *Trends in Biochemical Sciences* 41.1 (Jan. 2016), pp. 20–32.

[224] Erik J. Eide et al. “The Circadian Regulatory Proteins BMAL1 and Cryptochromes Are Substrates of Casein Kinase Iε”. In: *The Journal of biological chemistry* 277.19 (May 2002), pp. 17248–17254.

[225] Qing Liu et al. “Molecular basis for blue light-dependent phosphorylation of Arabidopsis cryptochrome 2”. en. In: *Nature Communications* 8.1 (May 2017). Publisher: Nature Publishing Group, p. 15234.

[226] Peng Gao et al. “Phosphorylation of the Cryptochrome 1 C-terminal Tail Regulates Circadian Period Length”. en. In: *Journal of Biological Chemistry* 288.49 (Dec. 2013), pp. 35277–35286.

[227] Matthias Mann and Ole N. Jensen. “Proteomic analysis of post-translational modifications”. en. In: *Nature Biotechnology* 21.3 (Mar. 2003). Publisher: Nature Publishing Group, pp. 255–261.

[228] Rachelle R. Landgraf, Michael J. Chalmers, and Patrick R. Griffin. “Automated Hydrogen/Deuterium Exchange Electron Transfer Dissociation High Resolution Mass Spectrometry Measured at Single-Amide Resolution”. In: *Journal of the American Society for Mass Spectrometry* 23.2 (Feb. 2012), pp. 301–309.

[229] Jared B. Shaw et al. “Complete protein characterization using top-down mass spectrometry and ultraviolet photodissociation”. eng. In: *Journal of the American Chemical Society* 135.34 (Aug. 2013), pp. 12646–12651.